



Fractionation and characterization of nanoparticles by a hydrodynamic method : modelling and application to consumer products

Valentin de Carsalade Du Pont

► To cite this version:

Valentin de Carsalade Du Pont. Fractionation and characterization of nanoparticles by a hydrodynamic method : modelling and application to consumer products. Physics [physics]. Université Paris sciences et lettres, 2021. English. NNT : 2021UPSLS045 . tel-03320831

HAL Id: tel-03320831

<https://pastel.hal.science/tel-03320831>

Submitted on 16 Aug 2021

HAL is a multi-disciplinary open access archive for the deposit and dissemination of scientific research documents, whether they are published or not. The documents may come from teaching and research institutions in France or abroad, or from public or private research centers.

L'archive ouverte pluridisciplinaire **HAL**, est destinée au dépôt et à la diffusion de documents scientifiques de niveau recherche, publiés ou non, émanant des établissements d'enseignement et de recherche français ou étrangers, des laboratoires publics ou privés.



THÈSE DE DOCTORAT
DE L'UNIVERSITÉ PSL

Préparée à l'Ecole supérieure de physique et de chimie industrielle
Dans le cadre d'une cotutelle avec le laboratoire national de métrologie et
d'essais

**Fractionnement et caractérisation de nanoparticules par
une méthode hydrodynamique : modélisation et
application aux produits de consommation**

Fractionation and characterization of nanoparticles by a
hydrodynamic method: modelling and application to
consumer products.

Soutenue par

**Valentin DE CARSALADE DU
PONT**

Le 16 avril 2021

Ecole doctorale n° 564

EDPIF

Spécialité

Physique

Composition du jury :

Gaëtane, LESPES

Professeur d'université, université de Pau et des pays de
l'Adour *Présidente du jury*

Catia, CONTADO

Associate professor, université de Ferrara
Rapporteur

Jean-Luc, AIDER

Directeur de recherche, école supérieure de physique et de
chimie industrielle *Examineur*

Thierry, CAEBERGS

Ingénieur de recherche, SMD-ENS
Examineur

Mauricio, HOYOS

Chargé de recherche, école supérieure de physique et de
chimie industrielle *Directeur de thèse*

Paola, FISICARO

Directeur de recherche, laboratoire national de métrologie et
d'essais *Co-Directrice de thèse*

Remerciements

En premier lieu, je tiens à remercier mes directeurs de thèse, Paola Fisicaro et Mauricio Hoyos pour toute l'aide, la disponibilité et la confiance qu'ils m'ont accordé depuis avril 2018.

Je remercie également mes encadrants officiels, Enrica Alasonati et Michel Martin pour toutes les discussions sur les aspects théoriques et pratiques de la FFF ainsi que pour l'aide qu'ils m'ont apporté.

Je tenais également à remercier Sophie Vaslin-Reimann pour m'avoir accueilli au sein du pôle chimie. Au cours de ces trois ans, j'ai eu la chance de pouvoir travailler avec de nombreuses personnes appartenant à des domaines très différents tels que l'optique ou la programmation. Je remercie donc Clément Guibert, Joffray Guillory, Jabran Zaouli, Nicolas Fischer et Nicolas Feltin pour m'avoir fait découvrir leur domaines respectifs et apporter un regard extérieur sur certains problèmes ce qui a abouti à des solutions concrètes.

Pour la convivialité qu'ils apportent au laboratoire et les discussions scientifiques que nous avons eues je remercie les équipes de chimie organique et inorganique du LNE : Caroline O, Daniela S, Johanna N, Vincent R, Amandine B, Véronique L, Hélène V, Carine F, Vincent D, Mélissa C et Fanny G.

Je remercie mes amis et particulièrement Cédric Tricoche et Marc Da Costa pour les bons moments passés ensemble, que ce soit au LNE ou l'extérieur.

Je remercie également mon ami et collègue thésard Rémi Moulian pour les longues discussions sur nos résultats respectifs qui ont toujours été une source de bonne humeur.

Enfin, je remercie ma famille pour son soutien inconditionnel depuis toujours.

Table of Contents

Introduction	8
Chapter I. Nanotechnology, metrology and size characterization.....	14
1. Generalities about nanomaterials	14
1.1. History.....	14
1.2. Definitions.....	16
1.3. Classification of nanomaterials	17
1.3.1. Dimensional based classification.....	17
1.3.2. Classification based on chemical composition and structure	19
1.3.3. Origin based classification.....	19
1.4. Fabrication methods	20
1.4.1. Top-down method.....	21
1.4.2. Bottom-up method	22
1.5. Properties of nanoparticles	22
1.5.1. Surface effect	22
1.5.2. Quantum confinement effect	24
1.6. Applications	25
1.6.1. Catalysis.....	25
1.6.2. Environmental applications	25
1.6.3. Medical applications	26
1.6.4. Optical applications	26
2. Characterization of nanomaterials.....	26
2.1. Size characterization techniques	29
2.1.1. Equivalent diameter	30
2.1.2. Dynamic light scattering	31
2.1.3. Single particle inductive coupled plasma mass spectrometry SP-ICP-MS	32
2.1.4. Multi angle light scattering	33
2.1.5. Electronic microscopy	35
2.1.6. Atomic force microscopy	36
2.1.7. Particle tracking analysis	37
2.1.8. Small-angle X-ray scattering	38
2.1.9. Tunable resistive pulse sensing (TRPS)	38
2.1.10. Numerous techniques and numerous mesurands.....	39
3. Fractionations techniques	41

3.1. Field Flow Fractionation	41
3.2. Size exclusion chromatography	42
3.3. Analytical ultracentrifugation and centrifugal liquid sedimentation	42
4. Metrology	42
4.1. International system of units	43
4.2. Metrological Traceability	45
4.3. Measurement uncertainties	47
References	48
Chapter II. Field-Flow Fractionation techniques: state of the art	56
Abstract	57
1. FFF principle	58
1.1. Elution modes	59
1.2. Theoretical formalization	62
1.3. Working hypotheses of the FFF retention theory	65
1.4. Practice <i>versus</i> classical theory	69
1.5. Variants of the classical retention model	71
1.5.1. Steric model	71
1.5.2. Model taking into account the interaction particle-wall	72
1.5.3. Experimental correction for particle-wall interaction	74
1.5.4. Models based on different assumptions	75
2. Flow-FFF and Asymmetrical Flow-FFF	76
2.1. The different steps in AF4 analysis	78
2.2. AF4 applications	79
2.3. Strength and weakness of AF4-multidetector	80
Scope of the work	82
References	83
Chapter III. Materials and methods	102
Abstract	102
1. AF4-multidetector instrumentation	102
1.1. Determination of the effective channel thickness	105
1.2. Determination of the retention time	106
1.3. Determination of the void time	106
1.4. Determination of the focusing position	107
1.5. Determination of the recovery rate	108
2. Zeta potential analyses	108

2.1. Measurement of the zeta potential of particle suspensions.....	109
2.2. Measurement of the zeta potential of membranes	110
3. Scanning electron microscopy analyses	113
4. Particle standards.....	114
5. Experimental approach and method validation of AF4 method	116
References	119
Chapter IV: Study of the mechanisms governing the retention inside the AF4 channel and application of the δ_w model for the characterisation of nanoparticle hydrodynamic diameter.....	124
Abstract:	124
1. Study of the retention behaviour of spherical nanoparticles in AF4 channel using the classical model	125
1.1. Influence of the carrier ionic strength on the particle retention	128
1.2. Influence of the membrane nature on the particle retention and recovery rate....	130
1.3. Influence of the particle size on the particle retention	132
1.4. Influence of the particle nature on the particle retention	133
1.5. Lessons retained from preliminary tests on retention behaviour of spherical nanoparticles in AF4 channel	134
2. Application of the δ_w model to AF4 for the size characterization of nanoparticles	135
2.1. Determination of the channel thickness in the case of the δ_w model	136
2.2. Effect of the ionic strength and of the particle size on δ_w	137
2.3. Validation of the model	141
Conclusion.....	146
References	147
Chapter V. Implementation and evaluation of a retention model taking into account particle-wall interactions for the measurement of nanoparticle hydrodynamic diameter by asymmetrical flow field-flow fractionation.....	152
Abstract	152
1. Introduction	153
2. Theory	155
3. Materials and methods	158
3.1. Instrumentation	158
3.2. Reagents and Samples.....	159
4. Results and discussion.....	159
4.1. Zeta potential of the membrane	159
4.2. Characterization of the particles standard.....	160
4.3. Determination of the void time	161

4.4. Channel thickness determination	163
4.4.1. Effective channel thickness as a physical parameter.....	167
4.4.2. Effective thickness as a correction factor.....	170
Conclusion.....	172
Chapter VI. Metrological validation of a retention model taking in account particle-wall interactions for the measurement of nanoparticle hydrodynamic diameter by asymmetrical flow field-flow fractionation	182
Abstract:	182
1. Introduction	183
2. Theory	185
2.1 FFF theory	185
3. Materiel and methods	187
3.1. Nanoparticles Standards for size values	187
3.2. Instrumentation.....	188
4. Results and discussion.....	189
4.1. Program operation and uncertainty propagation	189
4.2. Determination of the standard uncertainty of the inputs parameters	189
4.3. Result of the r_h probability density function	193
4.4. Metrological traceability	197
Conclusion.....	197
References	198
Chapter VII: A novel approach to directly determine the channel thickness: feasibility study.....	206
Abstract	206
1. On the measurement of the effective channel thickness	206
2. Characteristics of the ideal method for the direct measurement of w_{eff}	208
2.1. Principle of chromatic confocal sensor.....	209
3. Evaluation of the experimental set-up.....	212
4. Future enhancements of the measurement set-up	217
Conclusion.....	219
References	220
Conclusions and perspectives	222
Résumé étendu en français	228
Annex I: Conference paper 19th International Congress of Metrology - CIM2019	251

Introduction

Engineered nanoparticles are defined as materials manufactured by man with a size inferior or equal to 100 nm in at least one of their dimensions (ISO/TS 80004-2:2015). They can either be in individual or agglomerated form. Their small size gives them different physico-chemical properties compared to the bulk material. These properties are particularly interesting for numerous applications in several fields (electronics, optics, medicine) which induced a great production of nanomaterials (NMs) during the last years. Due to the increasing use of NMs, a better understanding of their properties, their environmental fate, and their impact on human health becomes mandatory. To this end, a better characterization of NMs properties needs to be developed.

In 2012, the ISO and the OECD proposed a list of 11 characteristics that need to be known to define a nanomaterial ('Guidance on sample preparation and dosimetry for the safety testing of manufactured nanomaterials', 2012; 'ISO/TR 13014:2012):

- size
- size distribution
- agglomeration/aggregation state
- shape
- surface area/specific area
- chemical composition
- purity
- surface chemistry
- surface charge
- solubility
- dispersibility

Among these parameters, NMs size and size distribution are key parameters as they influence numerous properties of the NMs like their toxicological properties and behavior in the environment. Furthermore, since the European Commission (EC) definition of NM adopted by the Recommendation (2011/696/EU), the size measurement has become a strategic parameter in the regulatory framework of NMs characterization. A broad range of measurement techniques based on different physical principles are available to characterize the sample size and size distribution, each one having a specific working range in which the size can reliably be measured. Until now, several analytical techniques depending on different physical principles have been applied to characterize the sample size and size distribution (Mourdikoudis, Pallares and Thanh, 2018).

In recent years the measurement performances, quality assurance and traceability of common particle size measurement methods and techniques have been improved, thanks to the numerous international collaborative and standardization projects. Nevertheless, up today no single technique alone can cover, in a single measurement and for all the materials, the complete size range from 1 nm to well above 100 nm (Rauscher *et al.*, 2019). A combination of several techniques is necessary to ensure adequate characterization.

Among the size measurement techniques, the asymmetrical flow field-flow-fractionation (AF4) has become in recent years a method of choice for the separation and characterization of nano-objects. AF4 was selected by the CEN/TS 17273 amongst the most established approaches able to detect and identify nano-objects in a number of complex matrices. Despite the numerous applications of the FFF method for NM characterization documented in the literature, a real metrological approach that allows reliable, reproducible and SI traceable measurements is still missing and a specific chain of metrology traceability should be implemented at national and international level.

The principle of AF4 has been described by Giddings in 1966 (Giddings, 1966). An equation that describes the particle behavior inside the channel has been reported in 1970 (Hovingh, Thompson and Giddings, 1970) and allowed the determination of the particle size (hydrodynamic diameter) from its retention time in the channel. However, the validity of this equation is based on several assumptions linked to the channel geometry, the migration process, the cross sectional concentration distribution and flow profile, which need to be verified to be able to reliably apply the equation. In practical conditions, some assumptions like the absence of interaction between the particles and the channel wall are not verified. These interactions influence the particles retention, which can induce bias up to 40% when determining the particle

size. Improving the retention models would allow having a simple method to determine the particles size. Moreover, this approach would have the potentiality to characterise the particle size without referring to a standard of the same quantity of measurement, giving to the FFF method the characteristics of a potentially primary method.

This method would also be complementary to the MALS detection as the ratio of the measurand of each method is equal to the form factor, which give an indication on the particle shape.

The general objective of the thesis was therefore to develop an improved method for the characterization of the size and size distribution of NPs based on the retention theory in AF4 and eventually to evaluate its potentiality to be a primary method. To this end, the mechanisms governing the retention behaviour inside the AF4 channel have been studied and evaluated on different models.

Firstly, the influence of each parameter entering in an AF4 analysis on the particle retention time was studied. This study generated a data set to test the applicability of two models, namely the one proposed for the first time by *Williams et al.* (*Williams et al.*, 1997) and the one proposed by *Hansen et al.* (*Hansen and Giddings*, 1989) that used different approaches to estimate the interactions taking place in the channel. The advantage and limit of each model were evaluated in order to propose further improvement. The retention model based on *Hansen et al.* and called thereafter the “particle-wall model (p-w model)” has been selected as preferred approach because of its intent to improve the understanding on the retention mechanisms by including particle-walls interactions.

In the second step of the work, the performances of the p-w model have been evaluated. This included the evaluation of the repeatability and reproducibility of the measurand, as well as the verification of the range of validity by applying the model to standard particles of different chemical nature and different size. A complete uncertainty budget that includes the propagation of the contribution of all the input parameters of the model has been estimated and the metrological traceability of the results has been demonstrated.

Finally, a particular attention has been paid to the measurement of the AF4 channel thickness by a direct method. A novel method using a confocal sensor has been conceived and the feasibility of the method has been demonstrated. This method has the advantages to measure directly the thickness without the need for calibration with standards of size and can be used *in situ* giving a value of thickness representative of the real working conditions

This manuscript is divided in seven chapters:

In the **first chapter**, the definition of nanomaterial is given and NMs principal properties and applications are presented as well as an overview of the techniques commonly used to characterize the particle size. One section is dedicated to the explanation of the principal metrology concepts.

In the **second chapter**, the principle of the FFF method is presented as well as the different techniques belonging to this family of techniques. The different retention models developed to understand the analyte elution behavior inside an FFF channel are presented. The work hypotheses associated to the equations will also be discussed. Then the focus will be on the sub category technique of flow-FFF and especially on the asymmetrical version, the AF4 which is the technique studied in this work.

The **third chapter** explains the principles of the different analytical techniques used in this work. The methodology used to produce and compare the different data obtained, and the particles studied are described.

The **fourth chapter** presents the experimental approach used to characterize the AF4 system. The influence of the carrier ionic strength, size and nature of the particles on the retention time are presented. Then a retention model proposed by *Williams et al.* was applied to the AF4. The advantages and limits of the model as a characterization method are explained.

The **fifth chapter** presents the application of the p-w model, which describes the retention behavior by considering the two principal types of particle-wall interactions, the van der Waals and the electrostatic interactions. The advantages and limits of the model as a characterization method are explained and results were compared to well-known retention models. The issue of the channel thickness determination was also addressed by applying two different approaches.

The **sixth chapter** presents the validation of the p-w model. This includes the evaluation of the method performances, the uncertainties propagation and the sensibility analysis performed with the Monte Carlo approach, as well as a critical description of the approach applied to demonstrate the metrological traceability of the results.

The **seventh chapter** focuses on the determination of an important parameter in the FFF retention models: the channel thickness. A promising method based on optic measurements is presented.

Chapter I:
**Nanotechnology, metrology and size
characterization**

Chapter I. Nanotechnology, metrology and size characterization

1. Generalities about nanomaterials

1.1. History

Nanomaterials (NMs) have been conceived and used by mankind since long time. One of the first use of nanomaterials goes back from ancient Egypt where the Egyptians used to dye their hair in black with a mixture constituted of past from lime, lead oxide and water. Nanoparticles (NPs) of galenite (lead sulfide) were formed during the mixing and offered an even and steady dying.

Another example is the Lycurgus cup made by the Romans in fourth century. Gold and silver NPs have been added during the fabrication of the cup glass giving to the cup the particularity to change color under certain lighting conditions (Bayda *et al.*, 2020). Silver and gold NPs have also been used during the medieval age to give shining colors to the church windows. Figure 1 shows the effect of the size and the shape of NPs on the color reflected by the glass.

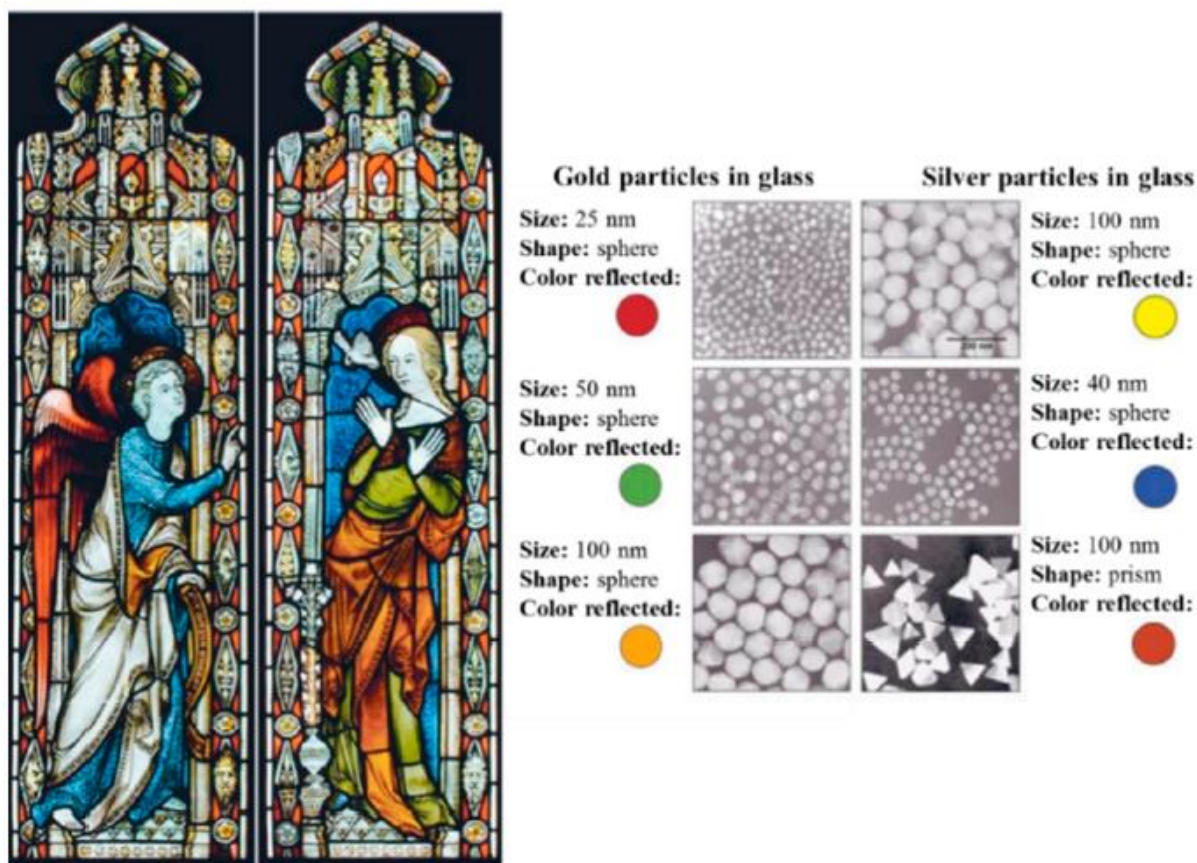


Figure 1. Effect of NPs size and shape on the colors of the stained glass windows(Bayda *et al.*, 2020)

The concept/idea of nanotechnology was introduced in 1959 by the physicist and Nobel laureate Richard Feynman during a talk called “There’s plenty of room at the bottom”. The term “nanotechnology” was not pronounced but Feynman suggested the possibility of manipulating precisely the atoms and molecules. In 1974 the physicist Norio Taniguchi employed for the first time the term nanotechnology in a paper where he described the manufacturing of nanomaterials by breaking bigger material down until the nanoscale was reached (Taniguchi, 1974). The invention of the scanning tunneling microscope (STM) by Gerd Binnig and Heinrich Rohrer in 1981 allowed visualizing clusters of atoms. A few years later in 1990, a STM was used to manipulate 35 xenon atoms on a nickel surface and form the logo of the American company IBM. The nanotechnologies became popular with the discovery of carbon nanotubes and fullerene also known as “buckyball”. Since then, nanotechnologies continued their development and numerous applications in different fields (Bayda *et al.*, 2020).

1.2.Definitions

The term **nano object** has been defined by the International Standards Organization (ISO) as “*a material which has one, two or three of their external dimensions in the nanoscale*”. The **nanoparticles** are a category of nano object and are defined as “*a nano object which have three of their external dimensions within the nanometric scale*” (ISO/TS 80004-2:2015).

In the case of **nanomaterials** there is not, at this moment, a single definition adopted yet. A technical definition proposed by the ISO is “*material with any external dimension in the nanoscale or having internal structure or surface structure in the nanoscale*”. However, this definition based on size only may be insufficient for regulation purposes from safety point of view.

Yet, until now, there is no agreement between the different regulation agencies and this leads to multiple definitions or recommendations with different criteria (Boverhof *et al.*, 2015). The recommendations proposed by the European Commission define a nanomaterial as “a natural, incidental or manufactured material containing particles, in an unbound state or as an aggregate or as an agglomerate and where, for 50% or more of the particles in the number size distribution, one or more external dimension is in the size range 1 nm-100 nm.” (Commission Recommendation of 18 October 2011 on the definition of nanomaterial Text with EEA relevance) The United States Environmental protection agency (EPA) chose a weight distribution criterion of 10%. EPA gives a list of criteria rather than a formal definition which is why it has not been quoted here (Boverhof *et al.*, 2015). From the toxicology point of view, this difference of criteria is less relevant as the large particles will have a higher contribution in the distribution than the small one and shift the mean towards high value while it is precisely small particles that need to be monitored. However, weight distribution has the advantage to be easier to obtain as most of the analytical methods give a weight distribution.

The debate goes even further with the question: should we even define the term nanomaterial? Andrew D. Maynard wrote a paper named “Don’t define nanomaterials” (Maynard, 2011) where he exposed the risks of having a strict regulatory definition as exception may slip through the regulatory net. He proposed as replacement to establish a list of 9 or 10 attributes, which can represent nanomaterials with the particularity to be flexible enough to be adapted quickly depending on scientific knowledge.

1.3. Classification of nanomaterials

Whatever the exact definition is, every material is made up of arrangements of particular atoms in a specific way, which define its properties and behavior. A classification can be made with respect to the properties of these materials. In the case of nanomaterials, numerous classifications have been established (Tervonen *et al.*, 2009; Stone *et al.*, 2010; Glezer, 2011; Saleh, 2020). This section presents three different ways to classify nanomaterials.

1.3.1. Dimensional based classification

A classification has been made by ISO depending on the number of dimensions belonging in the nanoscale (1-100 nm). The Figure 2 shows the different dimensional based categories of nanomaterials.

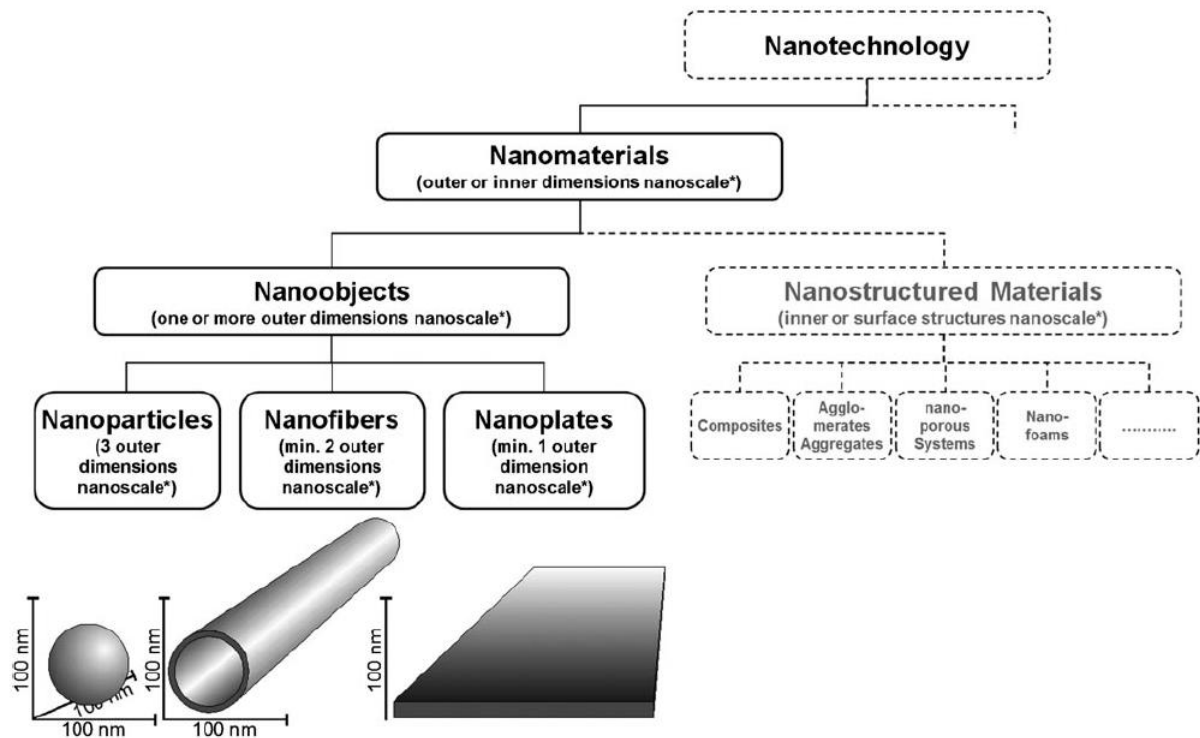


Figure 2 Classification of the nanomaterials based on their dimensions (from Krug *et al.*, 2011)

(Krug and Wick, 2011)

Saleh and co-workers propose another classification based on the same principle of the number of dimensions but with a different terminology, where the NMs are divided in four classes (Saleh, 2020). The zero dimensional (0D) nanomaterials have its 3 dimensions in the nanoscale. This category includes NPs, quantum dots and atoms clusters. The one dimensional (1D) nanomaterials possess two dimensions in the nanoscale and the two dimensional (2D) NMs

have only one dimension between 1 and 100 nm. The fourth category, the three dimensional nanomaterials (3D), include materials with no dimensions in the nanoscale but are constituted of nanocrystals which give them property belonging to the nanoscale (Saleh, 2020). The Figure 3 presents different examples of each category of NMs.

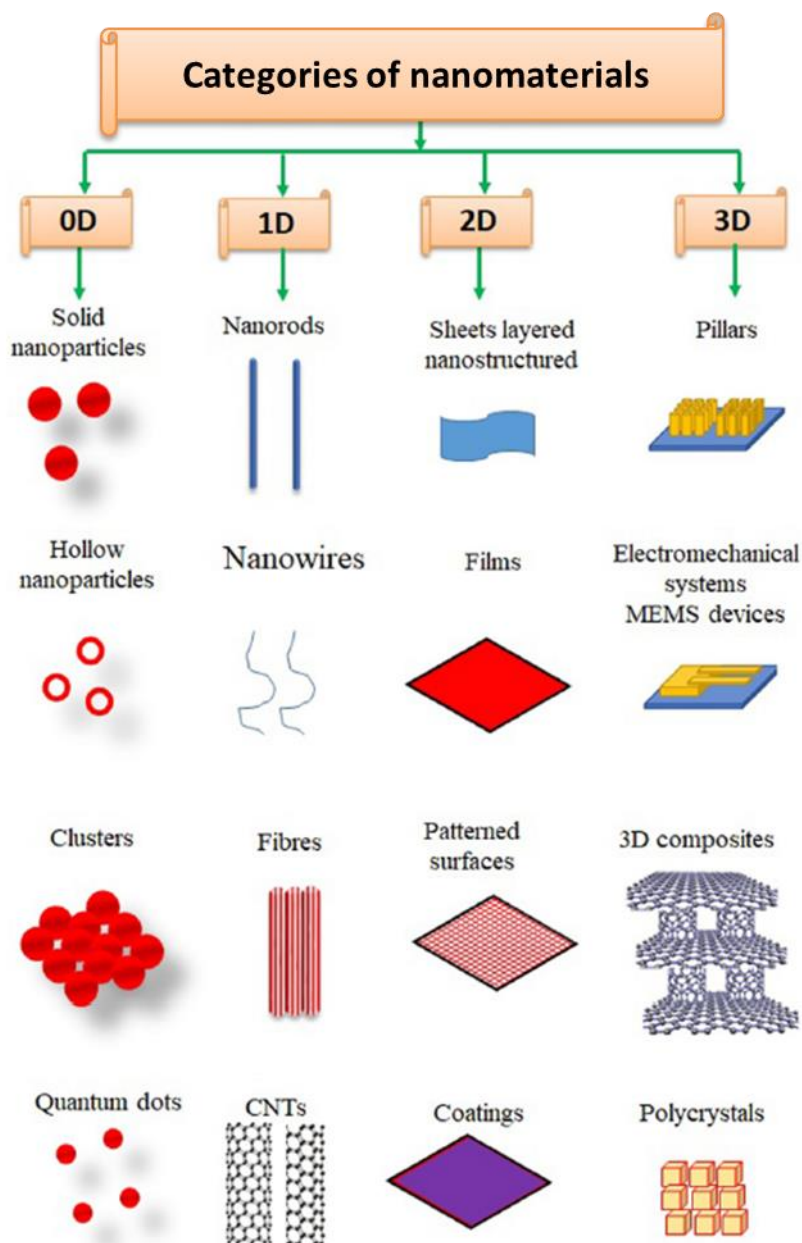


Figure 3 Examples of nanomaterials based on their dimensionality (Saleh, 2020)

1.3.2. Classification based on chemical composition and structure

Based on the chemical composition and the structure, the NMs can be divided in five categories (López-Serrano *et al.*, 2014):

- 1) Carbon based nanostructures: made up of carbon, this category is itself divided in two groups, which are the fullerenes, and the carbon nanotubes. The fullerene is an ensemble of 60 atoms of carbons at the minimum, which are assembled as a truncated icosahedron structure. Carbon based NMs have unique properties and are used in numerous fields. As an example, due to its good thermal and electrical conductivity the fullerene are applied in electronics and medicine (Sumi and Chitra, 2019).
- 2) Metal oxide NMs: this group include numerous transient metal oxides e.g. TiO₂, SiO₂, ZnO and CeO... Due to the decrease in size that influence the bandgap energy of materials, the metals oxide are applied can be applied as catalyst, chemical sensor or semiconductor(Saleh and Fadillah, 2019) .
- 3) Zero valent metal NMs: this group involves inorganic NMs composed of noble metal (Au, Ag) or transition metals (Fe, Zn). This category of nanomaterial is generally used as catalysers due to their reactivity (Kim and Lee, 2018)
- 4) Quantum dots: The quantum dots are semiconductor nanocrystal (CdSe, ZnS,PbS...)Their small size gives them unique optical and electronics properties. The electrical properties make them interesting in the construction of the solar panels while their optical properties are used in bioimaging (Bera *et al.*, 2010)
- 5) Polymeric NMs: they are usually organic based nanomaterial, manly nanosphere or nanocapsular shaped. The nanospheres are matrix particles where molecules are adsorbed at the outer boundary of the particle surface. On the contrary, for the nanocapsular the molecules are trapped inside the NPs. This capacity to encapsulate molecules is widely used for drugs delivery (Khan, Saeed and Khan, 2019).

1.3.3. Origin based classification

According to this classification, NMs can be first divided in two categories: natural or anthropogenic. The anthropogenic category can also be divided in two groups depending if the NMs are created intentionally (engineered NMs) or unintentionally. NPs that have an

involuntary or natural origin are generally called ultrafine particles(Dolez, 2015). Different emission sources of NMs have been classed in Table 1.

Table 1 Natural and anthropogenic sources of NMs

Natural	Anthropogenic	
	Unintentional	Intentional
volcano	Combustion engine	engineered NPs (TiO ₂ , carbon nanotubes; CdSe;ZnO...)
forest fires	power plant	
biogenic magnetite	incinerators	
	fumes (smelting, wedding)	

1.4.Fabrication methods

The different ways to synthesize NMs can be categorized into two types of processes: the top down and the bottom-up methods. Figure 4 shows the principle of these two processes (Ealias and Saravanakumar, 2017). The top-down method, also called destructive method, consists in reducing a bulk material to nanometric scale particles while the bottom-up or constructive methods consists to build NPs from the atoms.

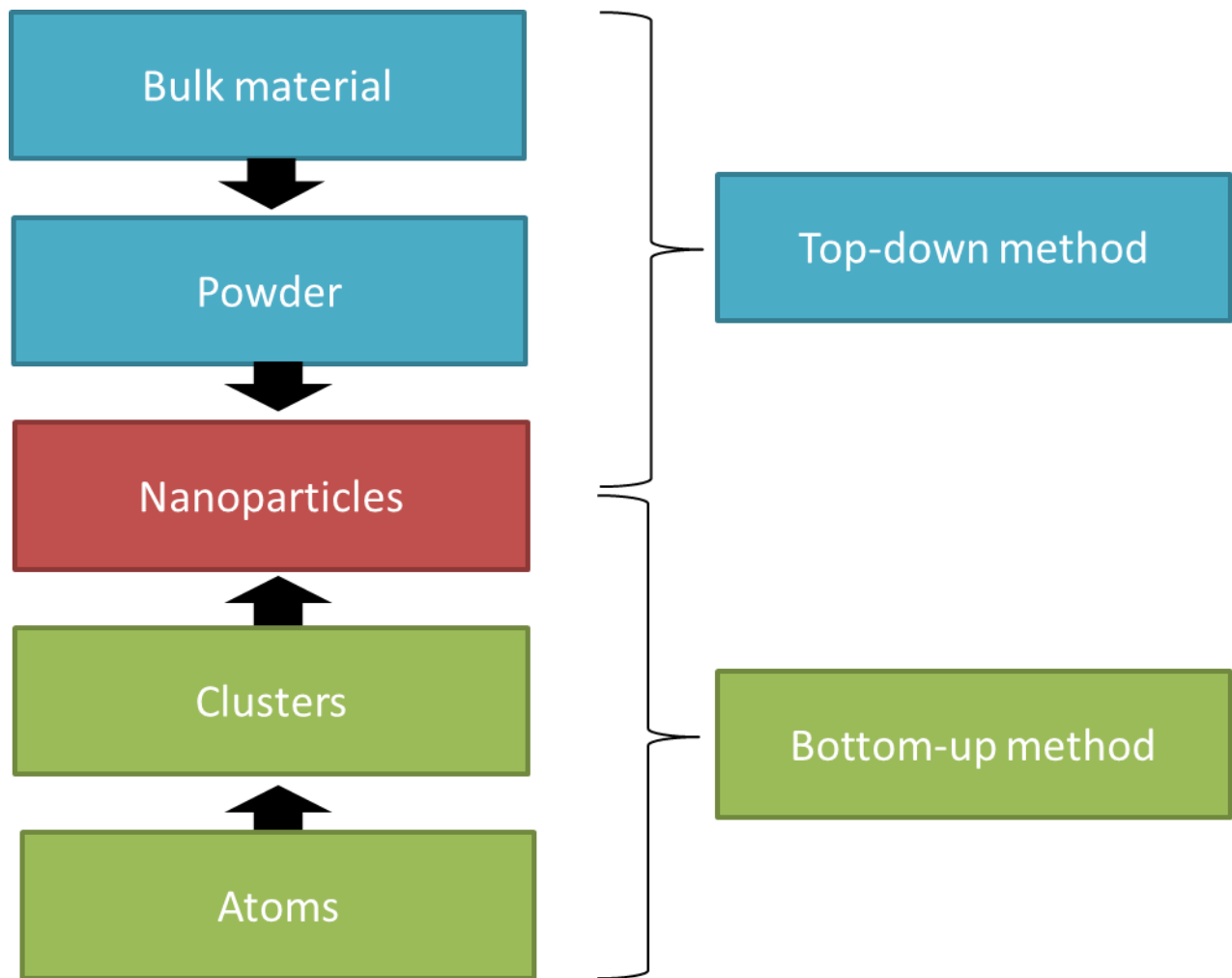


Figure 4 NPs fabrication processes

1.4.1. Top-down method

The most widely used synthesis methods belonging to this type of process are (Ealias and Saravanakumar, 2017):

- **Mechanical milling:** The bulk material is milled in an inert atmosphere down to the nanometric scale. Among the different types of milling, ball milling has been widely applied for the synthesis of various NMs. The principle consists to introduce a grinding material in a rotating chamber partially fill with balls. The process is easy to implement however the size distribution and morphology of the NMs produced can be very dispersed which orient the restrain the product application in fields where this polydispersity is not a problem (Ealias and Saravanakumar, 2017).
- **Laser ablation:** In laser ablation, a high-energy laser is used to vaporized material from a solid surface. The ionized particles ejected from the material combine each other to

form the intended NMs. Even if the process is generally performed under vacuum it can also be performed in liquid solvents (Ealias and Saravanakumar, 2017)

1.4.2. Bottom-up method

The principal methods using this approach are(Ealias and Saravanakumar, 2017):

- **Arc-discharge:** A plasma is generated by an arc discharge between two electrodes. The plasma will then condense and form nanomaterial. As the plasma is generated from the electrode, The type of nanomaterial produced depends of the nature of the electrode e.g Carbon nanotube can be produced by graphite electrode (Tantra, 2015)
- **Colloidal synthesis:** In this method, metal complexes are reduced in dilute solutions. The solution will become supersaturated with metal atoms, which will nucleate to form NPs. The agglomeration of NPs is prevented by ensuring that the concentration of NPs is low enough or by adding a surfactant.
- **Vapor vapour deposition:** The principle of this method consists in depositing material on a surface from a precursor in vapor phase. The vapor phase deposition can be classified in 2 types: the chemical vapor phase deposition (CVD) and physical vapor phase deposition (PVD). In PVD the precursor only physically deposits the material on the surface while in CVD the precursor will also react chemically with the surface (Tantra, 2015).
- **Flame synthesis:** A precursor is evaporated and taken into a stream of inert gas. Fuel and an oxidizing agent are then added in the gas stream and then injected into a flame. NMs are then produced within the flame(Tantra, 2015).

1.5.Properties of nanoparticles

The NPs have the particularity to display different properties compared to the bulk material moreover, these properties can change in function of their size. We will explain in the following paragraph how the size can affect the properties of a material at the nanoscale by presenting two majors properties of the NPs, the surface effect and the quantum confinement and how they influence the others properties of the NPs (Ju-Nam and Lead, 2008; Khan, Saeed and Khan, 2019)

1.5.1. Surface effect

When a particle is at the nanoscale, the proportion of surface atoms compared to the total number of atoms is much bigger than a macroscopic object (Figure 5). This high ratio surface

to volume increases the reactivity of NPs as they have more surface atoms available for a reaction, which makes them more sensitive to their environment than their bulk materials. This effect decreases significantly with the particle size. Figure 5 illustrates this tendency with a plot of the number of atoms at the surface of the particle in percent as a function of the particle size. The number of surface atom became non significant beyond 20 nm(Ju-Nam and Lead, 2008).

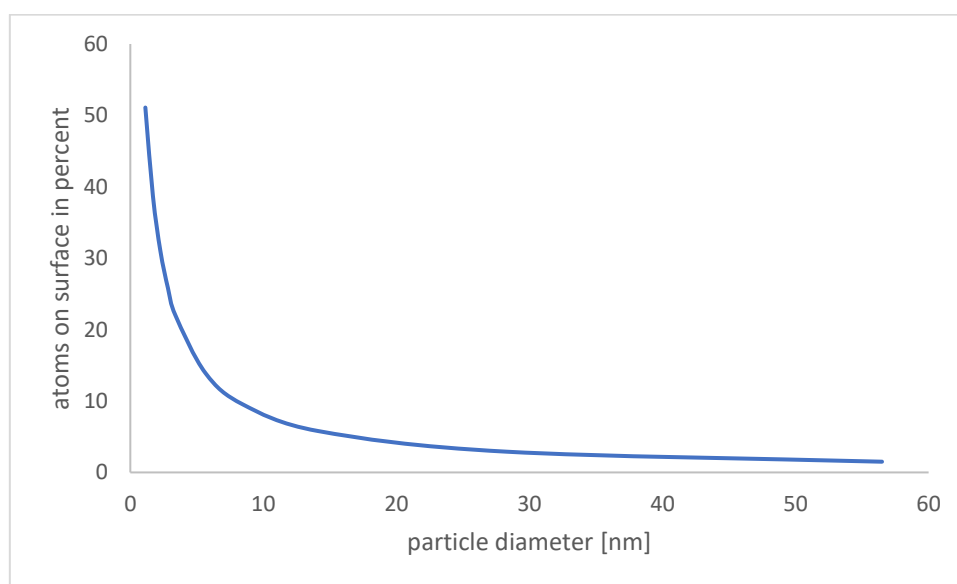


Figure 5. Percentage of atoms at the surface of different Gallium sulfide NPs. Adapted from(Ju-Nam and Lead, 2008)

Besides increasing the particle reactivity, the high surface atom ratio also affect the melting point of the particle. This effect is called the melting point depression. Indeed, as surface atoms tend to be unsaturated, a large energy is associated to the particle surface. Hence, a small particle will have, proportionally to its size, a surface energy bigger than large particle. As the energy state of a material is always lower in liquid phase than in solid phase. A small particle will be more incline to melt to reduce its energy state. The Figure 6 shows this property with the different melting point of gold NPs as a function of their diameter (Burda *et al.*, 2005). It is interesting to note that the melting point depression only affects the lower part of the nanoscale (1 – 10 nm) and that its effect increase significantly below 4 nm.

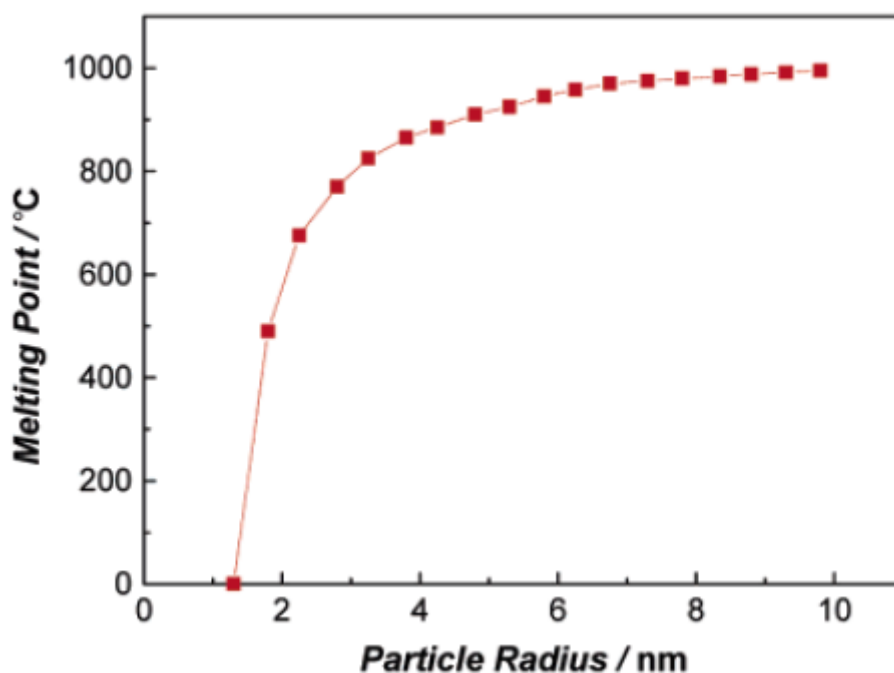


Figure 6 Melting point of gold NP as a function of its diameter (Burda *et al.*, 2005)

1.5.2. Quantum confinement effect

When the particle size decreases, the bandgap energy needed to move the electron between a valence band (VB) and a conduction band (CB) increases until the transition between them becomes discrete. This size dependent phenomenon changes the optical, electrical and magnetic properties of the NPs, which become different from bulk materials properties. This effect becomes important in the lower part of the nanoscale (below 10 nm). Good examples are quantum dots, which are semi-conductor nanocrystals of 2-10 nm. The Figure 7 illustrates an optical effect of the quantum confinement on a quantum dot where the decrease in size changes the color of the quantum dot.

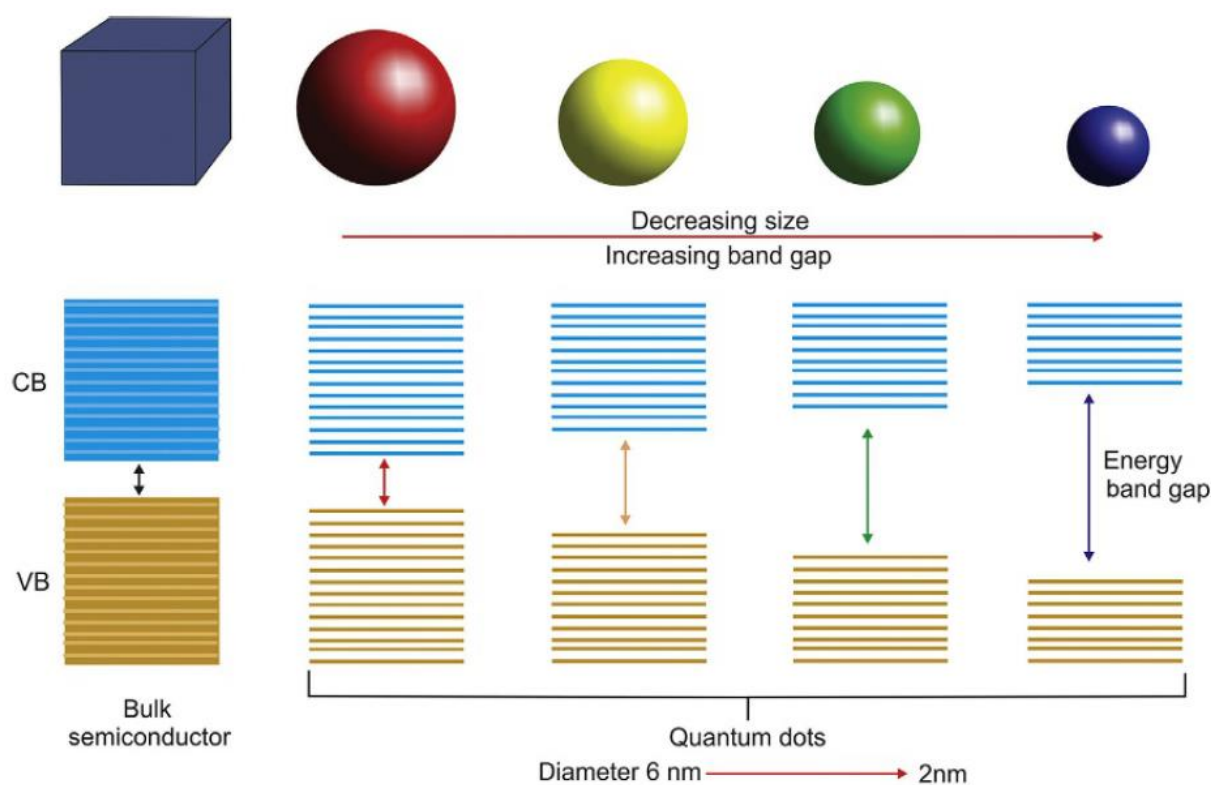


Figure 7. Modification of the optical property and the band gap energy due to the quantum confinement (from Bhagyaraj *et al.*, 2018 (Bhagyaraj *et al.*, 2018))

1.6.Applications

Due to their unique properties, the NPs have plenty of applications in numerous fields (Khan, Saeed and Khan, 2019). Some of the different fields of application involving NP are presented below.

1.6.1. Catalysis

The high surface to volume ratio of NPs give them a better reactivity than their bulk materials, which make them good catalyst for many applications. For example, the quantity of platinum used in the automotive catalytic converters has been reduced since platinum NPs, which have a better efficiency for the same quantity of matter, have been used (Ealias and Saravanakumar, 2017).

1.6.2. Environmental applications

Due to their properties, NPs have numerous applications in this sector. With their high surface to volume ratio, the NPs have a large adsorption capacity, which make them perfect candidate for bioremediation. For example, carbon nanotubes are used as nanosorbents to remove heavy metals, organic pollutants and biological impurities (2014 lopez serrano ref 47). Another domain of application is the acceleration of plant growth: indeed it has been shown that TiO_2

(rutile) facilitates the chlorophyll formation and increase the photosynthetic rate in spinach (López-Serrano *et al.*, 2014).

1.6.3. Medical applications

In medicine, NPs are synthesized in order to have affinity with a defined biological target, generally the cells that need to be cured or destroyed. Thanks to this characteristic they can be used as drug carriers to transport the medication in the target area, that enhances the drug efficacy and allows to reduce the dose administered (Drbohlavova *et al.*, 2013). The NPs can also be used during a treatment by hyperthermia where the cancer cells are destroyed by increasing the temperature at a given location. Magnetic NPs are placed in the designed area and are heated by the application of a magnetic field. This allows today a destruction of cancer cell more precise than before (Galvão *et al.*, 2016).

1.6.4. Optical applications

Inorganic pigments like TiO₂ are used in solar cream to absorb and scatter UV radiation. Larger particles were normally used, however they bring a white color on the surface protected. Since the scattered light intensity is a function of the wavelength of the incident light and the particle diameter, an optimal particle size was found to attenuate only UV and not the visible light. This size was found in the nanometric scale (Kruis, Fissan and Peled, 1998).

2. Characterization of nanomaterials

In 2012, both OECD ('Guidance on sample preparation and dosimetry for the safety testing of manufactured nanomaterials', 2012) and ISO ('ISO TR 13014 directives relative à la caractérisation physicochimiques des nano objets manufacturé soumis aux essais toxicologiques', no date) proposed a list of properties that need to be determined to characterize a nanomaterial. This list has been drawn up by answering following 3 questions:

“What does it look like?”, “What is it made of?” and “How does it interact with the surrounding environment/media?” ('ISO TR 13014 directives relative à la caractérisation physicochimiques des nano objets manufacturé soumis aux essais toxicologiques') The Table 2 lists these parameters and their measurand associated. Though all these parameters are important to have a complete characterization, the size characterization of a NM has a special importance as the size influences other properties of the NP like its surface to volume ratio, its quantum confinement effect or its toxic potential. Moreover, from the regulatory point of view, the size is the criterion, which classifies whether the analyte is a nano object. Consequently, a great

number of techniques have been developed to measure the particle size and have been reviewed in several articles (Hendrickson *et al.*, 2011; Meli *et al.*, 2012; López-Serrano *et al.*, 2014).

Lopez-Serrano et al. reviewed many of the analytical techniques that have been used in NP size characterization to elucidate the mechanisms of toxicity of NPs and to underpin the processes of their environmental fate and behavior (López-Serrano *et al.*, 2014). Hendricksson et al. compared several techniques on their capacity to characterize engineered NPs in environmental media (Hendrickson *et al.*, 2011). Meli et al. presented a size comparison between several techniques (AFM, SEM, DLS, SAXS) on the characterization of gold and polystyrene NPs (Meli *et al.*, 2012). The authors showed that, with the exception of the DLS, each technique finds the same diameter value for the gold NPs even if each technique analyzes the NPs in different medias (vacuum or liquid) and the samples were prepared in different ways depending on the technique used.

The most used analytical techniques for the size determination of nano-objects, NPs and NMs are summarized in the following paragraph.

Table 2. List proposed by ISO for the characterization of NMs. The measurand definition come from FD ISO/TR 13014

Parameter	Measurand [unit]
size	equivalent spherical diameter for particle with a regular geometry [m] ; the length of one or several specific aspect of the particle [m]
size distribution	number of particle, cumulative length area, volume of the particle or the signal intensity they produce in function size
aggregation/agglomeration state in relevant media	number of aggregate/agglomerate particles in comparison to the total number of primary particles
shape	size independent descriptor of shape, like aspect ratio or fractal dimension
surface area/ specific area	area of a substance divided by either it's mass or volume [m^2/g] or [m^2/cm^3]
composition	number and identity of elements alone or in molecules
purity	percentage of intended material
surface chemistry	elemental or molecular abundance unit [mol/mol], including thickness for fixed layer [number of molecules/surface area]
surface charge	number of charges per unit particles surface area [$\text{Coulomb}/\text{m}^2$]; zeta potential [V].
solubility	maximum mass or concentration of the solute that can be dissolved in a unit mass or volume of solvent at a specified temperature and pressure [kg/kg or kg/m^3 or mol/mol].
dispersibility	maximum mass or concentration of the dispersed phase present in a unit mass or volume of the dispersing medium at a specified temperature and pressure [kg/kg or kg/m^3 or mol/mol]

2.1.Size characterization techniques

One of the first simple criteria when choosing a size measurement technique might be the working range of the technique. We have summarized in Figure 8 the different working ranges of some size characterisation techniques. The extremity of the working range for almost all the techniques has been represented with a dashed line. This representation has been chosen to point at the fact that the limits cannot be easily defined since they depend on the properties of the material analysed (density, optical properties) and the medium in which the material is (environmental, biological...), consequently the end of the range is particularly sample dependent. Although, analytical ultracentrifugation (AUC) and asymmetrical flow-field-flow-fractionation (AF4) can be categorised as fractionation techniques, physical models describing the retention of fractionated objects exist for these two techniques and allow to determine their size.

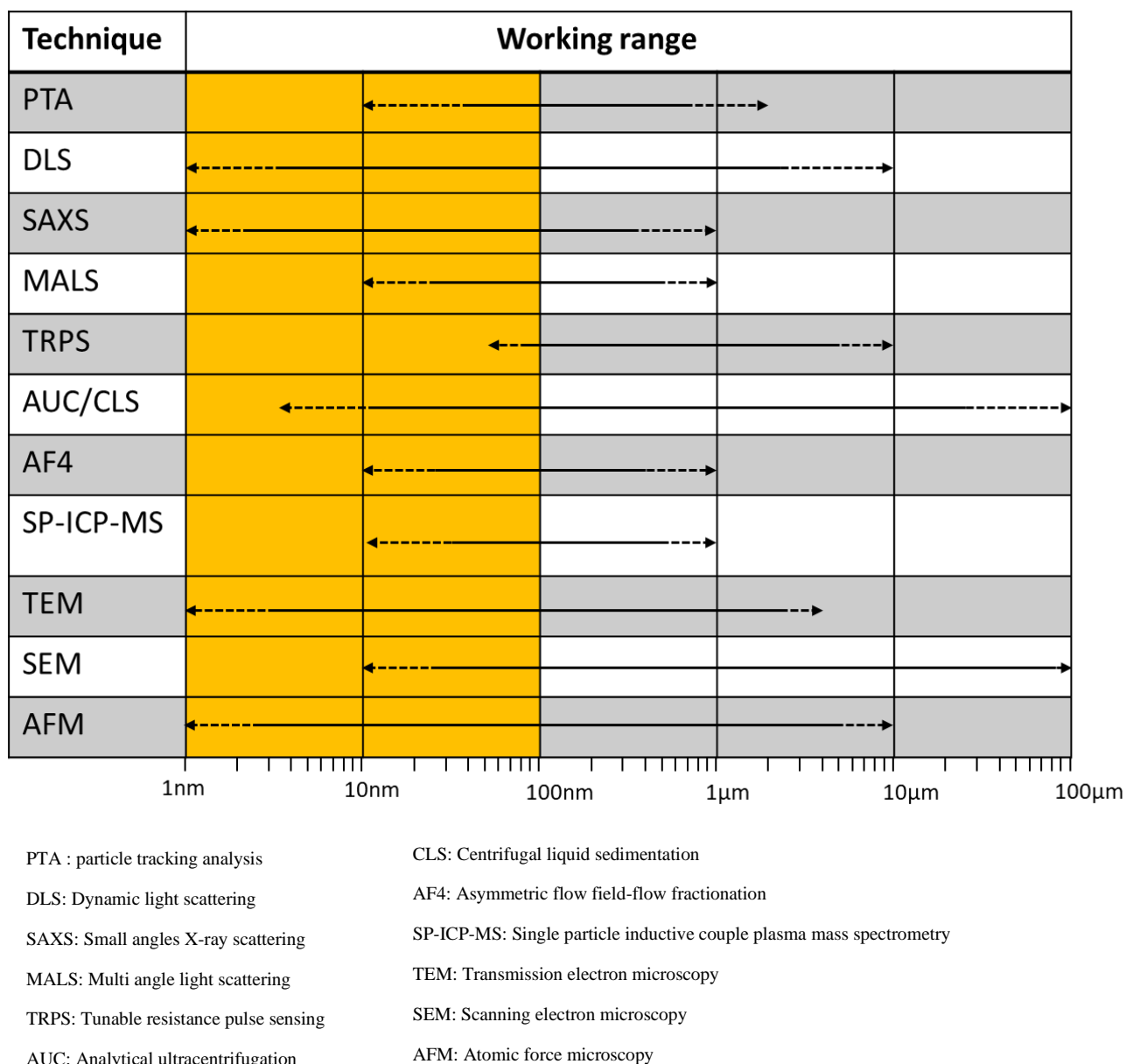


Figure 8. Working range of different size characterisation techniques.

2.1.1. Equivalent diameter

If the size is a concept simple to understand, in practice it is not easy task to attribute to a particle a representative size. Although the size of simple shaped particle like sphere can be described with one dimension, it is more complicate to do the same with particles that possess a more complex geometry. Moreover, most of the size characterization techniques are indirect techniques. These techniques measure a physical property of the particle (e.g. the diffusion

coefficient) and deduce the particle size by using equations linking this property to the particle size. Hence, the given size is expressed as an equivalent diameter, d_{eq} . The equivalent diameter implies that the particle has been assimilated to a sphere, which has, at least, one physical property identical to the sample (e.g. the diffusion coefficient for the hydrodynamic diameter or the particle area for the area equivalent diameter). The diameter of this sphere is used to represent the sample size (Figure 9) (DeCarlo *et al.*, 2004).

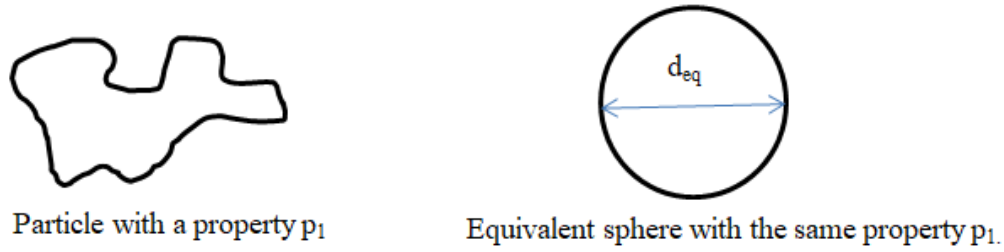


Figure 9. Representation of the equivalent diameter

A list of the principal size characterization techniques will be presented in next section. The different equivalent diameters used by these techniques are in Table 3 in the section 2.1.9.

2.1.2. Dynamic light scattering

Also called photon correlation spectroscopy or quasi-elastic light scattering, the dynamic light scattering (DLS) is one of the most used techniques by industrial laboratories because of the short analysis time and the little sample amount needed. This technique is based on the scattering of the light when it encounters an object. A laser is sent thorough a sample and a detector records the light intensity fluctuation in function of the time at a given angle (Figure 10). The diffusion coefficient of the particle, D , can be determined from the scattering signal. The hydrodynamic diameter, d_h , of the analyte is then determined using the Stokes-Einstein equation.

$$d_h = \frac{kT}{6\pi\eta D} \quad (I.1)$$

with k the Boltzmann constant, T the temperature and η the medium viscosity.

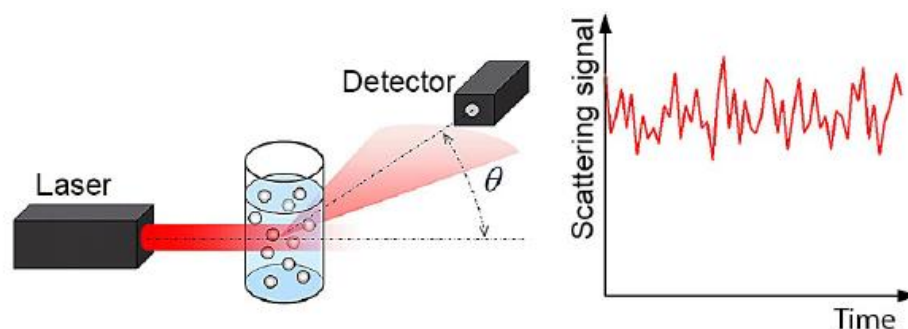


Figure 10. Principle of DLS, from Hodoroaba and al. (Hodoroaba, Unger and Shard, 2019)

The DLS can be used for all type of samples (organic or inorganic). If the sample concentration is high enough to give a good signal to noise ratio, DLS can measure sizes down to 1 nm. The principle of the DLS assumes that the Brownian motion is the only component that moves the particle. This assumption is verified up to the micrometer where the sedimentation forces are not negligible. Therefore, the working range upper limit (1-10 μm) depends on the particle density, which influences the sedimentation force. The DLS has the advantage to be simple to use and give fast results. However due to its measurement principle the DLS is not suitable for polydisperse samples. The intensity of the scattering signal is very sensible to the particle size. The presence of large particles and/or aggregates/agglomerates increases drastically the scattering signal, which will lead to an overestimation of the sample size (Hodoroaba, Unger and Shard, 2019) (ISO 22412).

2.1.3. Single particle inductive coupled plasma mass spectrometry SP-ICP-MS

Single particle ICPMS (SP-ICP-MS) is a technique able to determine the particle size as well as the number concentration of inorganic NPs in samples at ultra-trace concentration levels.

The principle of the SP-ICP-MS consists to reduce the time of the signal acquisition windows for a particular element in order to detect the peak corresponding of single particles passing through the detector. If the sample is diluted enough and the integration time used are short (dwell time < 10 ms), the signal will become discrete and will correspond to one NP which can be detected as a “single particle event” (SPE) (Figure 11)(Mitrano *et al.*, 2012).

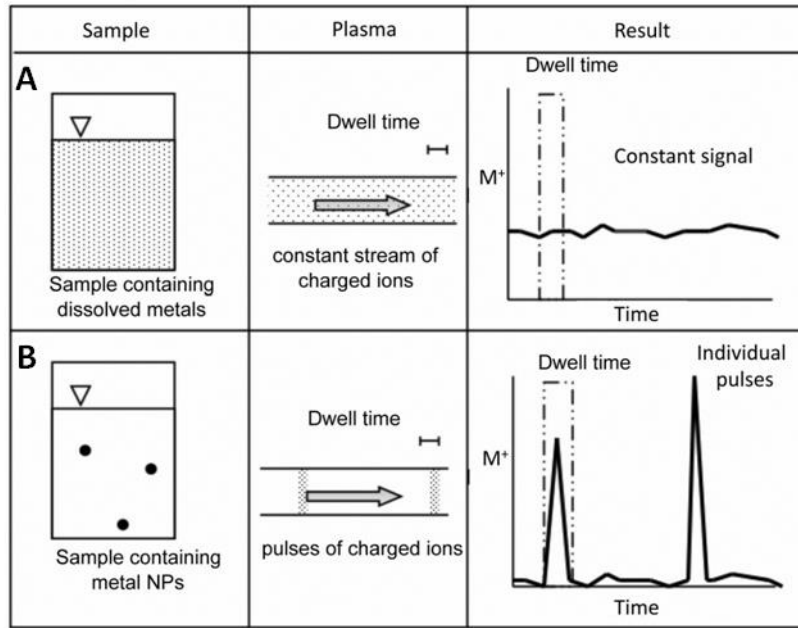


Figure 11 Behaviour of ICP-MS signal for a solution containing A) dissolved metals and B) metallic NPs(Mitrano *et al.*, 2012)

In these conditions, the frequency of the SPE is linked to the concentration of NPs in the solution and the intensity of each SPE is proportional to the mass of NP element detected. The mass equivalent diameter, d_m , of the NP is then calculated with Eq. (I.2).

$$d_m = \sqrt[3]{\frac{6m}{\pi\rho}} \quad (I.2)$$

Where m is the particle mass (kg) and ρ is the particle density (kg m^{-3}). The SP-ICP-MS can be applied on most types of metals and metalloids oxide particle from around 10 nm to 1 μm . The low limit depends on the particle composition (ISO/TS 19590:2017).

2.1.4. Multi angle light scattering

The multi angle light scattering (MALS) is a technique often used for polymer characterization and allow determining the molar mass and the size (gyration radius) of the analyte. It is often hyphenated with size fractionation techniques like AF4 or size exclusion chromatography (SEC) which allow to fractionate and characterize each population of analyte in one experiment.

A laser is sent on the sample and several detectors received the scattered light (Figure 12).

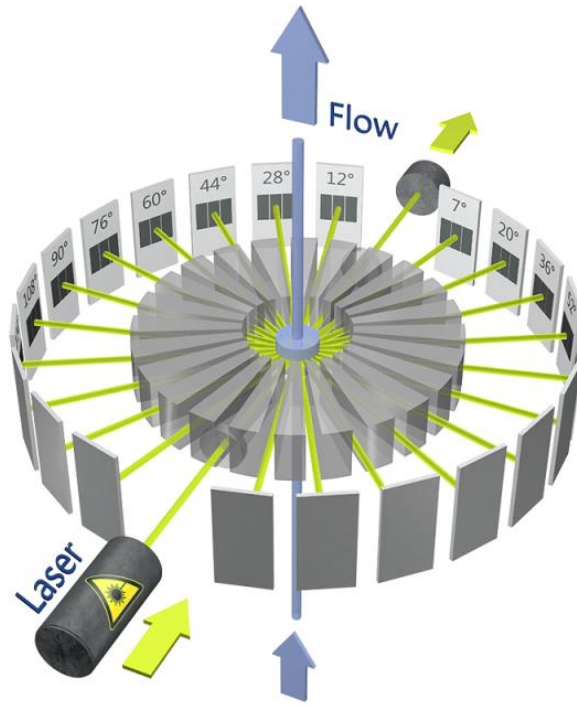


Figure 12. MALS principle from <https://www.azom.com/equipment-details.aspx?EquipID=4167>

The sample molar mass, M , and gyration radius, r_g , are determined according the two following equations (Andersson, Wittgren and Wahlund, 2003)

$$\frac{Kc}{R_\theta} = \frac{1}{P(\theta)M} + 2A_2c \quad (I.3)$$

$$P(\theta) = 1 - \frac{16\pi^2}{3\lambda_0^2} r_g^2 \sin^2\left(\frac{\theta}{2}\right) \quad (I.4)$$

where K is an instrumental constant that depends on the matrix refractive index, c is the sample concentration, R_θ is the excess Rayleigh ratio of the solution, A_2 is the second virial coefficient in the virial expansion of the osmotic pressure, $P(\theta)$ is a function which describes the regular dependence of the scattered light, with θ the angle between the incident light and the scattered light. λ_0 represents the laser wavelength. Others models exist to correctly determine the size of non spherical particle like rod or ellipsoid (Gigault *et al.*, 2011). The MALS can be applied to all types of analytes (organic and inorganic particles). However, some metal particles like gold that possess strong reflectance will hindrance the light scattering and give inaccurate diameter (Wyatt, 2018). The MALS can determine the size of particle from 10 nm to 1 μ m.

2.1.5. Electronic microscopy

Contrary to the traditional visible light microscopy, the electron microscopy uses an electron beam rather than a beam of visible light to visualize the sample, which increase the resolution of the analysis. With the scanning electron microscopy (SEM), the surface of sample is bombarded by an electron beam of low energy (<50 eV). These electrons, called primary electron, will generate secondary electrons (SE) when they hit the surface of the sample. The secondary electrons are collected by a system of lens. Once the image has been acquired the equivalent projected area diameter, d_{area} , of the particle can be determined (Hodoroaba, Unger and Shard, 2019).

In a transmission electron microscope (TEM) analysis the surface of sample is bombarded by an electron beam of high energy (around 100 000 eV). Contrary to the SEM, the primary electron will go through the sample and detected afterward. The image is constituted from the electron passing through the sample. The Figure 13 illustrates the differences in measurement between TEM and SEM. While both techniques can give the size and morphology of the sample only the TEM can give information on the sample crystalline structure (Hodoroaba, Unger and Shard, 2019). All the types of particles can be imaged by electronic microscopy, though the sample need to be dried before the analysis as the measurement is performed in high vacuum. The TEM and SEM have the advantage to give a visual image of the sample, which allows to distinguish primary particle from aggregate and agglomerate. However, collect enough data in order to have a representative measure of the sample population take a long time (Hodoroaba, Unger and Shard, 2019).

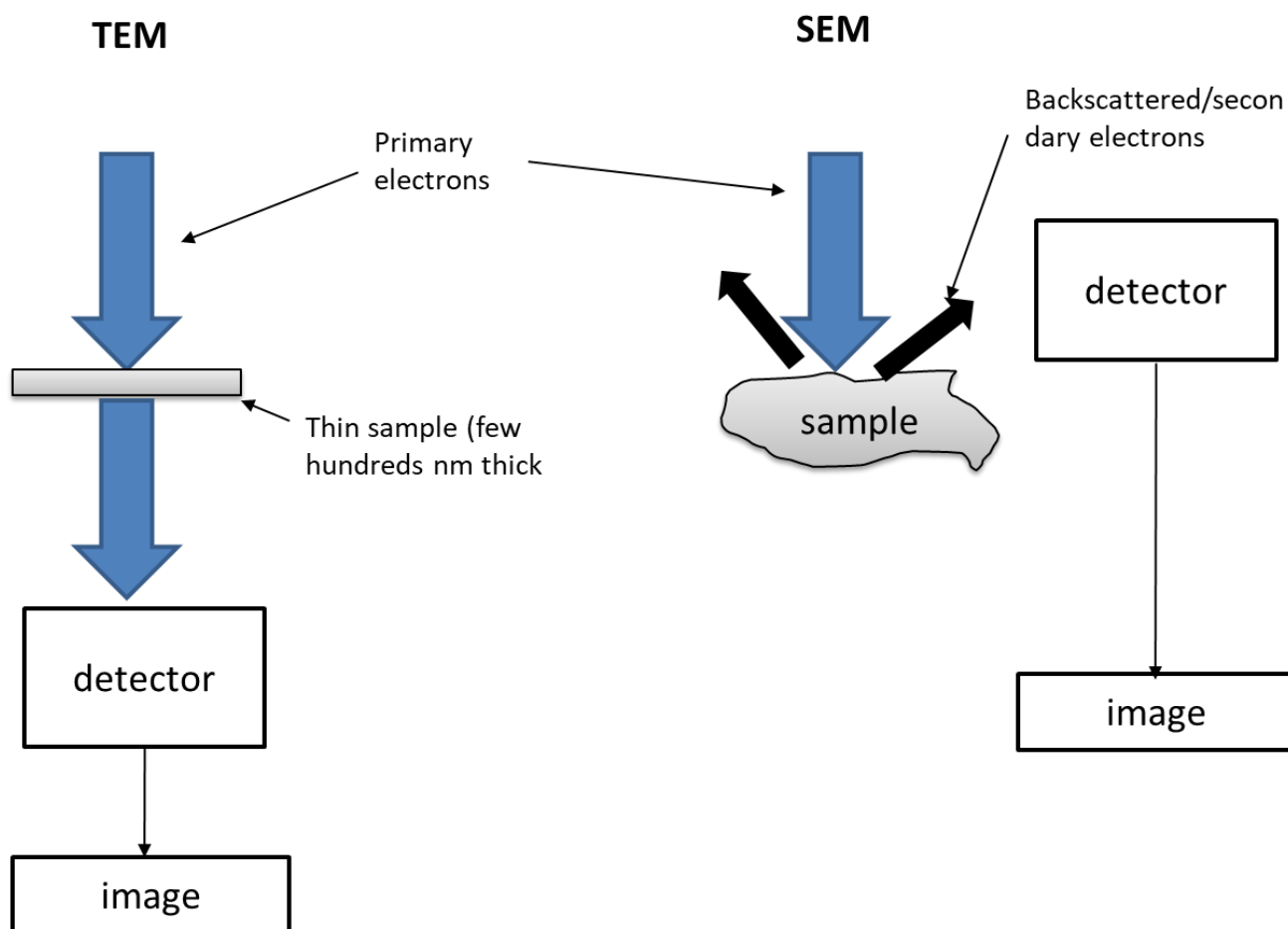


Figure 13. Difference in measurement principle between TEM and SEM

2.1.6. Atomic force microscopy

The atomic force microscopy (AFM) is based on the detection and the measurement of forces, which appears at the approach of a tip near the sample. When the tip goes near the sample, a field strength is created between the tip and the atoms below. These forces depend of the distance between the tip and the sample. Once the tip scanned all the analysis area, the measurement of these forces gives the topography of the sample (Figure 14). The AFM can be used for both organic and inorganic particle and has a working range going from 1 nm to 10 μm . While the TEM and SEM are interesting to have a precise measurement on the analyte width, the AFM can measure with more accuracy the particle height. Like the electronic microscopy a long time is necessary to measure enough particles to have a representative measurement (ASTM E2859 - 11(2017)).

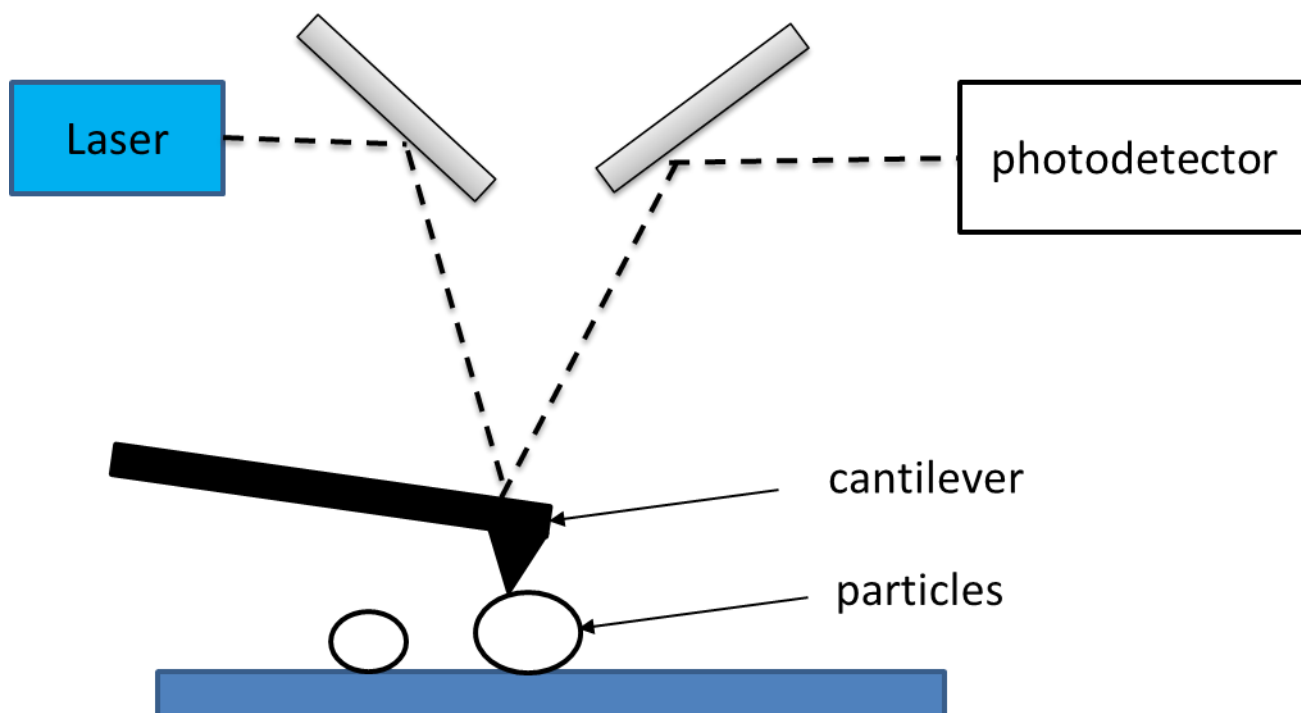


Figure 14. Measurement principle of AFM

2.1.7. Particle tracking analysis

The particle tracking analysis (PTA), also called NP tracking analysis (NTA), is a relatively new technique (< 20 years) which uses the property of light scattering and Brownian motion to determine the particle size in liquid suspensions. A laser goes through a suspension of particles: the scattered light from particles is collected through an objective lens and focused onto a camera (Figure 15). A video of the particles is recorded and the particles are identified by image analysis. It is important to note that the camera does not record the particles itself but the light scattered, which means that no particles structural information can be deduced from the video. An algorithm will then track each particle and determine its hydrodynamic diameter from the particle motion (Kestens *et al.*, 2017). The sample size distribution, in number, is then determined. The PTA can be used for both organic and inorganic particles in suspensions and has a working range going from 10 nm to 1 μm . The lower limit strongly depends on the particle refractive index. The limit of 10 nm refers to particles with high refractive index like gold or silver. The upper size limit depends on the particle density, which affects the sedimentation rate. A sedimentation rate too important will skew the measurement (Hodoroaba, Unger and Shard, 2019).

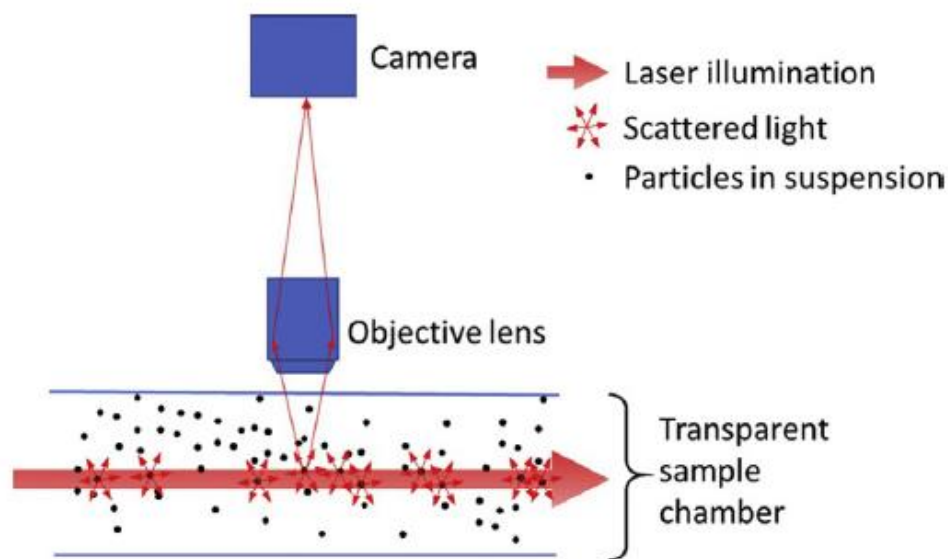


Figure 15 Principle of PTA (Hodoroaba, Unger and Shard, 2019)

2.1.8. Small-angle X-ray scattering

In a Small-angle X-ray scattering (SAXS) experiment, a beam of monochromatic X-rays is sent through the sample. An X-ray detector records the intensity of the scattered X-rays. The scattering pattern of the solvent is also collected. Its signal is then subtracted from the sample solution signal in order to only keep the particles signal. After this, the scattering curve (scattering intensity versus scattering angle) is traced. The gyration radius of the particle can be determined from this curve (Kikhney and Svergun, 2015). The SAXS can be used for both organic and inorganic particle in suspensions and has a working range going from 1 nm to 100 nm.

2.1.9. Tunable resistive pulse sensing (TRPS)

Tunable resistive pulse sensing (TRPS) is a technique that allows particle-by-particle detection from a range of 40 nm to 10 μm approximatively. The detection principle is based on the resistive pulse sensing. The system consists of a porous membrane equipped with a pair of electrodes. The sample goes through the membrane and the electrodes monitor the current during the passage of the solution through the membrane. If there is no particle in the solution a stable current is measured. However, when a particle goes through the membrane pore, a drop in current is registered. This drop is called “resistive pulse” (ΔR). The height, width and frequency of these resistive pulses allow determining the size, surface, zeta potential and

numbering concentration of the particles. The low limit of its working range of this technique (40 nm) is linked to the minimal pore size commercially available. The value of ΔR depends on the diameter of the sphere passing through the membrane pore so the TRPS give a sphere diameter with a volume equivalent to the particle volume (DeBlois et al., 1977).

One advantage of the TRPS is that the sample size distribution and the measurement of the zeta potential are realized simultaneously. On the other hand, an electrolyte with a high ionic strength is required for the analysis. This requirement makes this technic unsuitable for metal or semiconductor with a weak electrostatic stabilization for which the ionic strength might lead to agglomeration and/or aggregation.

2.1.10. Numerous techniques and numerous mesurands

In the previous paragraphs, we have described a part of the many existing size characterizing techniques reported in the literature (Hassellöv *et al.*, 2008; Sayes and Warheit, 2009; Hendrickson *et al.*, 2011). As one can expect, each technique have its own performances like accuracy, limit of detection, the time of the analysis, etc. Many studies have compared the performance of each technique and described their strength and weakness for a type of sample (Baalousha and Lead, 2012; Teulon *et al.*, 2019; Al-Khafaji *et al.*, 2020). Baalousha and Lead (Baalousha and Lead, 2012) compare the results find by AFM, DLS and FI-FFF and explained the different source responsible for the dispersion of the results. Teulon et al. (Teulon *et al.*, 2019) perform an intercomparaison between size techniques on nanoparticles of toxicological interest like TiO₂ and Ag NPs to find the most adequate technique for nanotoxicological study. While Al-Khafaji et al. (Al-Khafaji *et al.*, 2020) compare the ability of several technique to characterize a sample with a bimodal size population. However, the issue of the results comparability is rarely discussed. Indeed to compare two measurements they need to refer to the same mesurand. However, most of the techniques determine a size by an indirect way and give an equivalent spherical diameter based on different physical principles. Table 3 shows different types of equivalent diameters with their definition and the technics associated to these mesurand.

Table 3. Different types of equivalent diameters

Symbol	Equivalent diameter	Definition	Techniques associated
d_h	Hydrodynamic diameter	size of a hard sphere that diffuses in the same fashion as the particle being measured	DLS, AF4, PTA, AUC
r_g	Gyration radius	Average square distance of each point of the sample from its center of mass	MALS, SAXS
d_v	Volume equivalent diameter	diameter of a sphere with a volume equal to the sample volume	TRPS
d_d	Mass equivalent diameter	diameter of a sphere with the same mass and density as the sample	SP-ICP-MS
d_{area}	Equivalent projected area diameter	diameter of a circle with the same area as the sample	TEM, SEM
d_h	Equivalent height diameter		AFM

From this observation, the following question arises: can two different types of equivalent diameter be compared? In addition, for a given sample, does two equivalent diameters have the same value.

Jennings and Parslow (Jennings and Parslow, 1988) answered the questions by demonstrating that some equivalent diameter like d_{area} and d_v would give identical values if the sample is a sphere. Otherwise, a deep understanding of how the diameters are calculated might be necessary to compare the results of two techniques. One possibility is to use an equation to convert one equivalent diameter to the one desired. As an example it is possible to convert an hydrodynamic

diameter to gyration diameter by using the shape factor equation (Haydukivska, Blavatska and Paturej, 2020). However there is might not be a conversion equations adapted for all the equivalent diameter existing (Bau, 2008).

3. Fractionations techniques

Andersson et al. (Anderson *et al.*, 2013) highlighted that most routine analysis technique like PTA or DLS can characterize the particle size distribution of monomodal distribution, but shows difficulties for polydisperse samples. In this case, it is interesting to use a fractionation method in order to facilitate the measurement of the different populations present in the sample.

3.1. Field Flow Fractionation

Field flow fractionation (FFF) is a family of separation techniques like chromatography. The technique consists in the application of a field force perpendicularly to a laminar elution flow rate, allowing the particles to be separated in function of one characteristic depending on the nature of the force applied. The main difference between chromatography and FFF is that the separation is not based on the affinity between the analytes and the stationary phase but on the interactions between the analytes and the force applied perpendicularly to the elution flow (Figure 16).

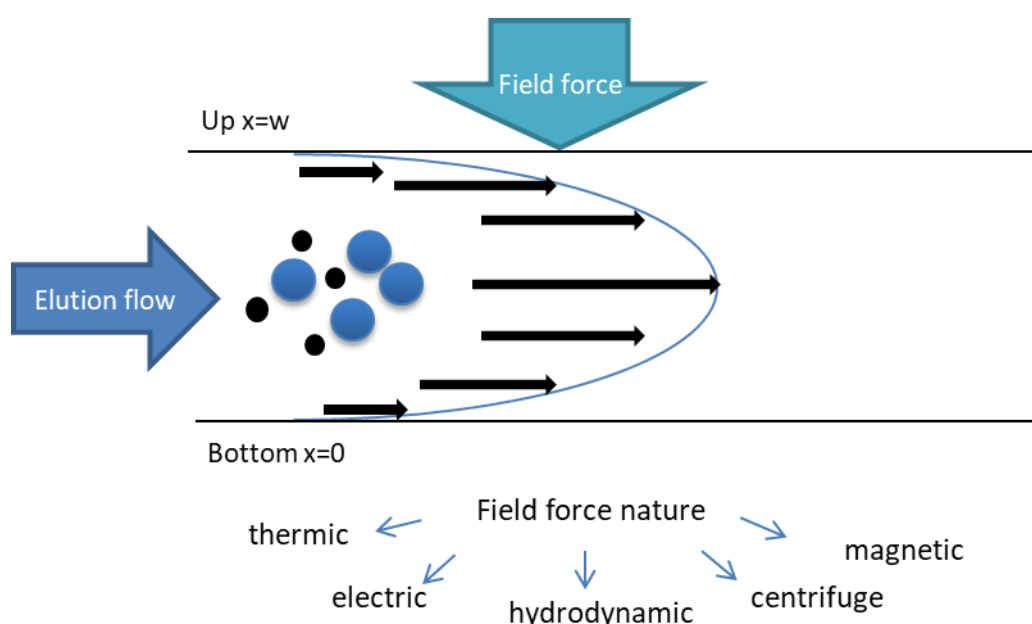


Figure 16. Separation principle of FFF

FFF techniques are suitable for micro and nano sized analytes. It is generally coupled with size detectors (MALS, DLS, TEM...)(Loosli *et al.*, 2019). This family of techniques is more detailed in chapter 2. The particle hydrodynamic diameter can be determined from its retention time inside the channel by Applying a mathematical model developed by *Giddings et al.* (Giddings, 1973).

3.2. Size exclusion chromatography

Size exclusion chromatography (SEC), also called gel chromatography or gel permeation chromatography, is a separation technique where the particles or the molecules in solution are separated via size exclusion. The column is packed with a stationary phase composed of small porous beads. Beads retain particles depending on their size and shape. A relation between the hydrodynamic size and the retention time can be observed. Hence, the size of the particle can also be determined by external calibration. One disadvantage of SEC is the possible interactions between the analytes and the stationary phase (Sun *et al.*, 2004).

3.3. Analytical ultracentrifugation and centrifugal liquid sedimentation

In analytical ultracentrifugation (AUC), the sample is subjected to a high centrifugal field. As large particles sediment faster than small particles, the different population present will be fractionated depending on their mass. Contrary of the other fractionation techniques, the samples are fractionated in solution. Therefore, there should be less problem due to adsorption on stationary phase or membrane. The AUC can also be used to determine the hydrodynamic size of samples by doing a sedimentation velocity (SV) experiment. This method consists to measure the rate at which particles move as a function of the centrifugal force applied. The hydrodynamic diameter is calculated from the particle sedimentation velocity and density (Planken, Kuipers and Philipse, 2008). The centrifugal liquid sedimentation (CLS) uses the same physical principles as the AUC to separate and determine the particles size. The main difference between the two techniques is that AUC uses a rotational speed higher than CLS. If the particles have a high density, The AUC can separate size from 5 nm to 100 μm (Planken, Kuipers and Philipse, 2008)(ISO 13318-1).

4. Metrology

Metrology is the science of measurement. It includes the theoretical aspects as well as the practical aspects for the experimental realization (Simpson, 1981). Metrology is not only a

scientific discipline but it is the foundation of our daily activities. Accessing specific knowledge often implies a number and the measurement providing this number cannot be conceived without units, standards or measuring instruments.

Requirements related to global trade, the control of industrial or agricultural production, safety, health and environmental concerns, the requirement to provide evidence in legal cases, etc., exert permanent pressure to provide reliable analytical results. Getting reliable and acceptable results is only possible through the implementation in laboratories of rigorous metrology practices.

The metrology is divided in three categories, which have their own specificities (Simpson, 1981). The **scientific metrology** aims to establish the definition of measurement units and develops new measurement methods as well as new measurement standards. It also ensures the transfer of these standards to the users. The **industrial metrology** deals with the measurement instruments used in industry, in production and testing processes, ensuring the suitability of the measurement instruments, their calibration and quality control, linking the results to international agreed references, when possible to the units of the international system (SI).

The **legal metrology** regroups the different governmental regulations set up to assure the quality of the instruments and the methods used particularly where these influence the transparency of economic transactions, particularly where there is a requirement for legal verification of the measuring instrument (Redgrave and Howarth, 2008).

4.1. International system of units

The International system of units (SI) is a consistent system of units for use in all aspects of life, including international trade, manufacturing, security, health and safety, protection of the environment, and in the basic science that underpins all of these. The system of units for the measures does not stop to evolve from the beginning of humankind. At the year 20, the Roman emperor August unified the mass and length units in the Roman Empire and, by doing so, abolished the standards used by the local populations. During French revolution a new system of units, the metric system, was set up with the intention to disseminate it thorough the world. This system was accepted at an international scale with a scientific treaty, “la convention du mètre” in 1875. Since then, the metric evolved and other units have integrated thorough time.

In 1960 at the eleventh “conférence générale des poids et mesures” (CGPM), the name of the metric system was replaced by the “international system of units” (Gumuchian *et al.*, 2019).

This system is composed of seven basic units:

- the meter (m), unit of length
- the kilogram (kg), unit of mass
- the second (s), unit of time
- the ampere(A) , unit of the intensity of an electric current
- The kelvin (K), unit of temperature
- the candela (cd), unit of light intensity in a given direction
- the mole (mol), unit of quantity of matter

as well as other units derived from the seven basic units.

Since their creation, the definition of these seven units has been redefined thorough time in parallel of the science development. Their latest definitions date from 2018 when the CGPM chose to define the different units from seven nature constants.

In this approach, the numerical value of the constants is considered exact and their uncertainty set equal to zero. The value of the unit is defined as a fraction of the constant associated. shows the constant associated to the determination of each unit.

Table 4. Natural constant associated with the basic units of the SI

Unit	Constant associated
m	speed of the light in the void: c
kg	Planck constant: h
s	frequency of the hyperfine transition at the fundamental state of the non-disturbed Cs ¹³³ : $\Delta\nu_{Cs}$
A	elementary charge: e
K	Boltzmann constant: k
cd	luminosity efficiency of a monochromatic radiation with a frequency of $540 \cdot 10^{12}$ Hz: K_{cd}
mol	Avogadro number: N_A

4.2. Metrological Traceability

One of the main goals of metrology is to produce comparable measurement results. In order to be comparable, the measurement results need to be linked to a common reference. According to the International Vocabulary of Metrology (VIM), the traceability is a “property of a measurement result whereby the result can be related to a reference through a documented unbroken chain of calibrations, each contributing to the measurement uncertainty” (*Vocabulaire international de métrologie-concepts fondamentaux et généraux et termes associés (VIM)*, 2012). A good example of this definition in the nanoscience is the traceability chain for an electronic microscopy technique (Figure 17) where the definition of the meter is passed down to the nanoscale with a metrological AFM. To this end, the metrological AFM is equipped with four interferometer which measure the position of the cantilever tip compared to the sample position. Each interferometer laser has their wavelength calibrated and traceable to the SI. This metrological AFM is used to produce transfer standards to calibrate other microscopes (Feltin *et al.*, 2013).

In chemistry, the establishment of the metrological traceability is more complex than in physics. Primary standards for each analyte can be made but they are only used to calibrate measuring

devices. This is not enough to guarantee the link between the measurement in a real sample and the SI. However, in real samples, the environment around the analyte, i.e. the matrix, may influence the measurement. Consequently, standards certified in the same matrix as the samples would be needed. However, this would require an infinite number of standards to cover all the applications. Therefore, primary measurement procedures are implemented. They are defined as “reference measurement procedure used to obtain a measurement result without relation to a measurement standard for a quantity of the same kind”. Results of a primary measurement method, which should directly be linked with the SI system, have the smallest uncertainty possible compared to this reference. Primary methods are usually developed by national metrology laboratories and are rarely applied to tests or to routine calibrations.

Matrix certified reference materials (CRMs) are metrological tools to validate the methods. A CRM is defined as a “material sufficiently homogenous and stable with reference to specified properties, which has been established to be fit for its intended use in measurement or in examination of nominal properties”. A certificate providing its property values with the associated uncertainties and traceability accompanies it.

A specific difficulty for the NP case when it comes to the elaboration of CRMs certified in size is that the techniques that can potentially be used to characterize the size, in reality do not measure the same measurand (cf. section numerous techniques and numerous measurands for more details). Therefore, a CRM needs to be characterized with the different methods that the users have in order to be correctly applied. Moreover, linking the measurement results to SI is not a trivial task. Indeed normally, to assign the reference value to a CRM, a primary method is applied. However, in this case the measurands are method dependent so if the method is not primary the CRM is not traceable to the SI for the given measurand. If a user calibrates its method by using this kind of CRM it will be traceable only to this CRM (Roebben *et al.*, 2013).

Another important step to provide reliable and comparable results is the demonstration of the method validation. According to the ISO standard 17025 the method validation can include, among others, calibration using reference standards or reference materials, systematic assessment of the factors influencing the result, comparison of results achieved with other validated methods, interlaboratory comparisons and evaluation of measurement uncertainty of the results based on an understanding of both theoretical and practical aspects of the method.

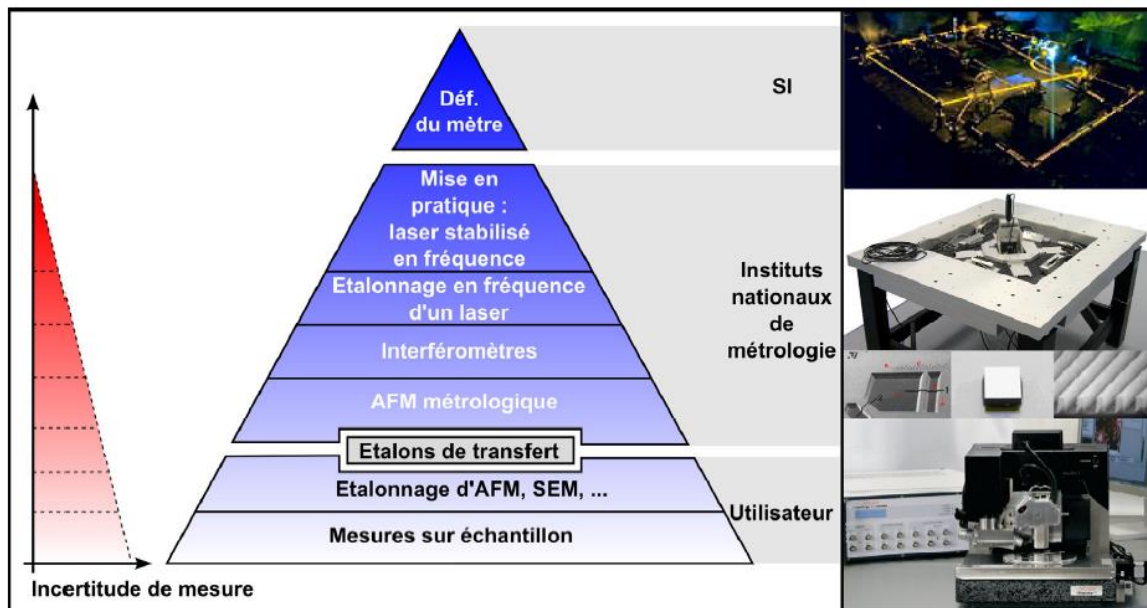


Figure 17 traceability to the SI for microscopy technique(Feltin *et al.*, 2013)

4.3. Measurement uncertainties

To compare different measurements it is necessary to associate to the result a quantitative evaluation of its quality. This quantity is called an uncertainty. The guide to uncertainty in measurement (GUM) proposed a method in four steps to evaluate and report a measurement result and its expanded uncertainty associated.

Step 1: Modeling the measurement

The goal of a measurement is to obtain an estimate y of a measurand Y and its associated uncertainty $u(y)$. Generally the measurand is not measured directly but determined with a relation f involving other quantities X_1, \dots, X_n .

Step 2: Evaluating the input quantities

After modeling the measurement it is necessary, in order to calculate y , to determine the values x_i of X_i . The standard uncertainties $u(x_i)$ as well as their covariance $u(x_i, x_j)$ also need to be estimate to determine $u(y)$.

Step 3: Evaluating the measurand and its standard uncertainty

The value y of Y is calculated with the model established in step 1: $y = f(x_1, \dots, x_n)$

The standard uncertainty $u(y)$ is determined with the law of propagation of uncertainty:

$$u^2(y) = \sum_{i=1}^N \left(\frac{\delta f}{\delta x_i} \right)^2 u^2(x_i) + 2 \sum_{i=1}^{N-1} \sum_{j=i+1}^N \left(\frac{\delta f}{\delta x_i} \right) \left(\frac{\delta f}{\delta x_j} \right) u(x_i, x_j) \quad \#(1)$$

Step 4: Determining a coverage interval

To express the result $u(y)$ need to be multiplied with a coverage factor, k_p , to give the expanded uncertainty U . The values of the k_p represents the level of confidence that the users accord to its measurement. U represents an interval about the result of the measurement that covered most of the values that could be attributed to the measurand.

References

- Al-Khafaji, M. A. *et al.* (2020) ‘Particle size distribution of bimodal silica nanoparticles: A comparison of different measurement techniques’, *Materials*, 13(14). doi: 10.3390/ma13143101.
- Anderson, W. *et al.* (2013) ‘A comparative study of submicron particle sizing platforms: Accuracy, precision and resolution analysis of polydisperse particle size distributions’, *Journal of Colloid and Interface Science*, 405, pp. 322–330. doi: 10.1016/j.jcis.2013.02.030.
- Andersson, M., Wittgren, B. and Wahlund, K. G. (2003) ‘Accuracy in multiangle light scattering measurements for molar mass and radius estimations. Model calculations and experiments’, *Analytical Chemistry*, 75(16), pp. 4279–4291. doi: 10.1021/ac030128+.
- Baalousha, M. and Lead, J. R. (2012) ‘Rationalizing nanomaterial sizes measured by atomic force microscopy, flow field-flow fractionation, and dynamic light scattering: Sample preparation, polydispersity, and particle structure’, *Environmental Science and Technology*, 46(11), pp. 6134–6142. doi: 10.1021/es301167x.
- Bau, S. (2008) *Etude des moyens de mesure de la surface des aerosols ultrafins pour l'évaluation de l'exposition professionnelle*. Institut National Polytechnique de Lorraine.
- Bayda, S. *et al.* (2020) ‘The history of nanoscience and nanotechnology: From chemical-physical applications to nanomedicine’, *Molecules*, 25(1). doi: 10.3390/molecules25010112.
- Bera, D. *et al.* (2010) ‘Quantum Dots and Their Multimodal Applications: A Review’, *materials*, pp. 2260–2345. doi: 10.3390/ma3042260.
- Bhagyaraj, S. M. *et al.* (eds) (2018) *Synthesis of inorganic nanomaterials*. Elsevier. Elsevier.

Boverhof, D. R. *et al.* (2015) ‘Comparative assessment of nanomaterial definitions and safety evaluation considerations’, *Regulatory Toxicology and Pharmacology*, 73(1), pp. 137–150. doi: 10.1016/j.yrtph.2015.06.001.

Burda, C. *et al.* (2005) *Chemistry and properties of nanocrystals of different shapes*, *Chemical Reviews*. doi: 10.1021/cr030063a.

DeBlois, R. W., Bean, C. P. and Wesley, R. K. A. (1977) ‘Electrokinetic measurements with submicron particles and pores by the resistive pulse technique’, *Journal of Colloid And Interface Science*, 61(2), pp. 323–335. doi: 10.1016/0021-9797(77)90395-2.

DeCarlo, P. F. *et al.* (2004) ‘Particle morphology and density characterization by combined mobility and aerodynamic diameter measurements. Part 1: Theory’, *Aerosol Science and Technology*, 38(12), pp. 1185–1205. doi: 10.1080/027868290903907.

Dolez, patricia I. (ed.) (2015) *Nanoengineering global approaches to health and safety issues*. Elsevier B.V. doi: 10.1016/b978-0-444-62747-6.01001-0.

Drbohlavova, J. *et al.* (2013) ‘Nanocarriers for Anticancer Drugs - New Trends in Nanomedicine’, *Current Drug Metabolism*, 14(5), pp. 547–564. doi: 10.2174/1389200211314050005.

Ealias, A. M. and Saravanakumar, M. P. (2017) ‘A review on the classification, characterisation, synthesis of nanoparticles and their application’, *IOP Conference Series: Materials Science and Engineering*, 263(3). doi: 10.1088/1757-899X/263/3/032019.

Feltin, N. *et al.* (2013) ‘CARMEN : une plateforme de caractérisation métrologique dédiée aux nanomatériaux’, *Revue française de métrologie*, (31), pp. 41–54. doi: 10.1051/rfm/2012009.

Galvão, W. S. *et al.* (2016) ‘Super-paramagnetic nanoparticles with spinel structure: A review of synthesis and biomedical applications’, *Solid State Phenomena*, 241, pp. 139–176. doi: 10.4028/www.scientific.net/SSP.241.139.

Giddings, J. C. (1966) ‘A New Separation Concept Based on a Coupling of Concentration and Flow Nonuniformities’, *Separation Science*, 1(1), pp. 123–125. doi: 10.1080/01496396608049439.

Giddings, J. C. (1973) ‘The Conceptual basis of field flow fractionation’, *journal of chemical education*, 50(10), pp. 667–669.

Gigault, J. *et al.* (2011) ‘Accurate determination of the length of carbon nanotubes using multi-angle light scattering’, *Microchimica Acta*, 175(3–4), pp. 265–271. doi: 10.1007/s00604-011-0687-z.

Glezer, A. M. (2011) ‘Structural Classification of Nanomaterials’, *Russian Metallurgy (Metally)*, 2011(4), pp. 263–269. doi: 10.1134/S0036029511040057.

‘Guidance on sample preparation and dosimetry for the safety testing of manufactured nanomaterials’ (2012).

Gumuchian, D. *et al.* (2019) *Le SI et la métrologie en France*. edp scienc.

Hansen, M. E. and Giddings, J. C. (1989) ‘Retention Perturbations Due to Particle–Wall Interactions in Sedimentation Field-Flow Fractionation’, *Analytical Chemistry*, 61(8), pp. 811–819. doi: 10.1021/ac00183a006.

Hassellöv, M. *et al.* (2008) ‘Nanoparticle analysis and characterization methodologies in environmental risk assessment of engineered nanoparticles’, *Ecotoxicology*, 17(5), pp. 344–361. doi: 10.1007/s10646-008-0225-x.

Haydukivska, K., Blavatska, V. and Paturej, J. (2020) ‘Universal size ratios of Gaussian polymers with complex architecture: radius of gyration vs hydrodynamic radius’, *Scientific Reports*, 10(1), pp. 1–11. doi: 10.1038/s41598-020-70649-z.

Hendrickson, O. D. *et al.* (2011) ‘Methods of detection and identification of manufactured nanoparticles’, *Biophysics*, 56(6), pp. 961–986. doi: 10.1134/S0006350911060066.

Hodoroaba, V. dan, Unger, W. E. and Shard, A. G. (2019) *characterization of nanoparticles measurement process for nanoparticles, micro and nano technologies*. Elsevier, Elsevier. Edited by V. dan Hodoroaba, W. E. Unger, and A. G. Shard. doi: 10.1016/b978-0-12-814182-3.09991-0.

Hovingh, M. E., Thompson, G. H. and Giddings, J. C. (1970) ‘Column Parameters in Thermal Field-Flow Fractionation’, *Analytical Chemistry*, 42(2), pp. 195–203. doi: 10.1021/ac60284a003.

‘ISO TR 13014 directives relative à la caractérisation physicochimiques des nano objets manufacturé soumis aux essais toxicologiques’ (no date).

Jennings, B. . and Parslow, K. (1988) ‘Particle size measurement: the equivalent spherical

diameter', *Proceeding of the royal society A*, 149, pp. 137–149. Available at: <http://rspa.royalsocietypublishing.org/content/royprsa/419/1856/137.full.pdf>.

Ju-Nam, Y. and Lead, J. R. (2008) 'Manufactured nanoparticles: An overview of their chemistry, interactions and potential environmental implications', *Science of the Total Environment*, 400(1–3), pp. 396–414. doi: 10.1016/j.scitotenv.2008.06.042.

Kestens, V. *et al.* (2017) 'Validation of a particle tracking analysis method for the size determination of nano- and microparticles', *Journal of Nanoparticle Research*, 19(8). doi: 10.1007/s11051-017-3966-8.

Khan, Ibrahim, Saeed, K. and Khan, Idrees (2019) 'Nanoparticles: Properties, applications and toxicities', *Arabian Journal of Chemistry*, 12(7), pp. 908–931. doi: 10.1016/j.arabjc.2017.05.011.

Kikhney, A. G. and Svergun, D. I. (2015) 'A practical guide to small angle X-ray scattering (SAXS) of flexible and intrinsically disordered proteins', *FEBS Letters*, 589(19), pp. 2570–2577. doi: 10.1016/j.febslet.2015.08.027.

Kim, C. and Lee, H. (2018) 'Light-assisted surface reactions on metal nanoparticles', *Catalysis Science and Technology*, 8(15), pp. 3718–3727. doi: 10.1039/c8cy00674a.

Krug, H. F. and Wick, P. (2011) 'Nanotoxicology: An interdisciplinary challenge', *Angewandte Chemie - International Edition*, 50(6), pp. 1260–1278. doi: 10.1002/anie.201001037.

Kruis, F. E., Fissan, H. and Peled, A. (1998) 'Synthesis of nanoparticles in the gas phase for electronic, optical and magnetic applications - A review', *Journal of Aerosol Science*, 29(5–6), pp. 511–535. doi: 10.1016/S0021-8502(97)10032-5.

Loosli, F. *et al.* (2019) 'Improved extraction efficiency of natural nanomaterials in soils to facilitate their characterization using a multimethod approach', *Science of the Total Environment*, 677, pp. 34–46. doi: 10.1016/j.scitotenv.2019.04.301.

López-Serrano, A. *et al.* (2014) 'Nanoparticles: A global vision. Characterization, separation, and quantification methods. Potential environmental and health impact', *Analytical Methods*, 6(1), pp. 38–56. doi: 10.1039/c3ay40517f.

Maynard, A. D. (2011) 'Don't define nanomaterials', *Nature*, p. 2011.

Meli, F. *et al.* (2012) 'Traceable size determination of nanoparticles, a comparison among

European metrology institutes', *Measurement Science and Technology*, 23(12). doi: 10.1088/0957-0233/23/12/125005.

Mitrano, D. M. *et al.* (2012) 'Silver nanoparticle characterization using single particle ICP-MS (SP-ICP-MS) and asymmetrical flow field flow fractionation ICP-MS (AF4-ICP-MS)', *Journal of Analytical Atomic Spectrometry*, 27(7), pp. 1131–1142. doi: 10.1039/c2ja30021d.

Mourdikoudis, S., Pallares, R. M. and Thanh, N. T. K. (2018) 'Characterization techniques for nanoparticles: Comparison and complementarity upon studying nanoparticle properties', *Nanoscale*, 10(27), pp. 12871–12934. doi: 10.1039/c8nr02278j.

Planken, K. L., Kuipers, B. W. M. and Philipse, A. P. (2008) 'Model independent determination of colloidal silica size distributions via analytical ultracentrifugation', *Analytical Chemistry*, 80(23), pp. 8871–8879. doi: 10.1021/ac801556t.

Rauscher, H *et al.* (2019) *Identification of nanomaterials through measurements*. doi: 10.2760/7644.

Redgrave, F. and Howarth, P. (2008) *Metrology – In Short 3rd Edition*.

Roebben, G. *et al.* (2013) 'Reference materials and representative test materials: The nanotechnology case', *Journal of Nanoparticle Research*, 15(3), pp. 1–13. doi: 10.1007/s11051-013-1455-2.

Saleh, T. A. (2020) 'Nanomaterials: Classification, properties, and environmental toxicities', *Environmental Technology and Innovation*, 20. doi: 10.1016/j.eti.2020.101067.

Saleh, T. A. and Fadillah, G. (2019) 'Recent trends in the design of chemical sensors based on graphene–metal oxide nanocomposites for the analysis of toxic species and biomolecules', *TrAC - Trends in Analytical Chemistry*, 120. doi: 10.1016/j.trac.2019.115660.

Sayes, C. M. and Warheit, D. B. (2009) 'Characterization of nanomaterials for toxicity assessment', *Wiley Interdisciplinary Reviews: Nanomedicine and Nanobiotechnology*, 1(6), pp. 660–670. doi: 10.1002/wnan.58.

Simpson, J. A. (1981) 'Foundations of Metrology.', *Journal of Research of the National Bureau of Standards (United States)*, 86(3), pp. 281–292. doi: 10.6028/jres.086.010.

Stone, V. *et al.* (2010) 'Nanomaterials for environmental studies: Classification, reference material issues, and strategies for physico-chemical characterisation', *Science of the Total*

Environment, 408(7), pp. 1745–1754. doi: 10.1016/j.scitotenv.2009.10.035.

Sumi, N. and Chitra, K. C. (2019) ‘Fullerene C60 nanomaterial induced oxidative imbalance in gonads of the freshwater fish, *Anabas testudineus* (Bloch, 1792)’, *Aquatic Toxicology*, 210(January), pp. 196–206. doi: 10.1016/j.aquatox.2019.03.003.

Sun, T. *et al.* (2004) ‘A study of the separation principle in size exclusion chromatography’, *Macromolecules*, 37(11), pp. 4304–4312. doi: 10.1021/ma030586k.

Taniguchi, N. (1974) ‘On the Basic Concept of Nanotechnology’, in *Proceedings of the International Conference on Production Engineering*.

Tantra, R. (2015) *Nanomaterial characterization An introduction*. Wiley, *Acta Universitatis Agriculturae et Silviculturae Mendelianae Brunensis*. Wiley. Edited by R. Tantra.

Tervonen, T. *et al.* (2009) ‘Risk-based classification system of nanomaterials’, *Journal of Nanoparticle Research*, 11(4), pp. 757–766. doi: 10.1007/s11051-008-9546-1.

Teulon, J. M. *et al.* (2019) ‘On the operational aspects of measuring nanoparticle sizes’, *Nanomaterials*, 9(1). doi: 10.3390/nano9010018.

Vocabulaire international de métrologie-concepts fondamentaux et généraux et termes associés (VIM) (2012).

Williams, P. S. *et al.* (1997) ‘Colloid Characterization by Sedimentation Field-Flow Fractionation: Correction for Particle–Wall Interaction’, *Analytical Chemistry*, 69(3), pp. 349–360. doi: 10.1021/ac9606012.

Wyatt, P. J. (2018) ‘Measuring nanoparticles in the size range to 2000 nm’, *Journal of Nanoparticle Research*, 20(12). doi: 10.1007/s11051-018-4397-x.

Chapter II.

Field-Flow Fractionation techniques: state of the art

Chapter II. Field-Flow Fractionation

techniques: state of the art

Symbols and Abbreviations

A_{123} : Hamaker constant (J)

D : diffusion coefficient ($\text{m}^2 \text{s}^{-1}$)

D_T : Thermal diffusion coefficient ($\text{m}^2 \text{s}^{-1}$)

d_h : analyte hydrodynamic diameter (m)

E : Electrical field strength (V m^{-1})

F : field strength applied on the analyte (N)

F_{AF4} : force applied on the analyte in AF4 (N)

F_2 : force that represents the sum of the interaction applied on the particle (N)

H_m : intensity of the magnetic field ($\text{N s C}^{-1} \text{m}^{-1}$)

k : Boltzmann constant ($\text{kg m}^2 \text{s}^{-2} \text{K}^{-1}$)

M : molecular mass (kg mol^{-1})

Q_c : cross flow ($\text{m}^3 \text{s}^{-1}$)

R : retention ratio (without unit)

R_1 : perfect gas constant ($\text{kg m}^2 \text{K}^{-1} \text{mol}^{-1} \text{s}^{-2}$)

T : temperature (K)

t_0 : void time (s)

t_r : retention time (s)

v_{analyte} : analyte velocity (m s^{-1})

v_{carrier} : carrier velocity (m s^{-1})

$v(x)$: fluid velocity in function of the x axis (m s^{-1})

$\langle v(x) \rangle$: fluid average velocity in function of the x axis (m s^{-1})

V^0 : void volume (m^3)

$W(x)$: potential energy of the particle (J)

$W_F(x)$: potential energy due to the field (J)

$W_{p-p}(x)$: potential energy due to the interactions between particles (J)

$W_{p-w}(x)$: potential energy due to the interaction between the particle and the wall (J)

$W_{p-w(el)}(x)$: potential energy due to the electrostatics interactions between the particle and the wall (J)

$W_{p-w(vdw)}(x)$: potential energy due to the van der Waals forces between the particle and the wall (J)

$W_{tot}(x)$: total potential energy of the particle (J)

Greek letters

α : ratio of the particle radius to the channel thickness (without unit)

ΔH_m : gradient of intensity of the magnetic field (N s C⁻¹ m⁻¹)

ΔT : temperature gradient (T)

λ : retention parameter (without unit)

η : carrier viscosity (kg m⁻¹ s⁻¹)

ϵ_0 : permittivity of the void (A² s⁴ kg⁻¹ m⁻³)

ϵ : dielectric constant of the carrier (without unit)

μ : electrophoretic mobility (cm² V⁻¹ s⁻¹)

$\omega^2 r$: centrifugal acceleration (m⁵ s⁻²)

χ_m : molar magnetic susceptibility m³ mol⁻¹

κ : inverse of the Debye length (m⁻¹)

ψ_p : surface charge of the particle (V)

ψ_w : surface charge of the accumulation wall (V)

ρ : solvent density (kg m⁻³)

ρ_s : particle density (kg m⁻³)

Abstract

The term “field flow fractionation” (FFF) represents a family of separation techniques applicable to many types of samples: macromolecules, colloids, polymer and particles. In this chapter, the principle and the equations that describe the sample retention inside an FFF channel will be presented. The work hypotheses associated to the equations and mismatches between theory and analytical practice will be discussed. Finally, the technique of flow-FFF (FI-FFF) will be presented, with a special focus on the asymmetrical flow-FFF (AF4) which is the technique studied in this work.

1. FFF principle

The concept of field flow fractionation (FFF) was invented by Giddings in 1966 (Giddings, 1966). FFF represents a large family of techniques which separation principle is based on the application of an external field perpendicularly to the axial flow (Figure 16). A carrier liquid is pumped through a narrow ribbon-like channel, where the sample is injected. Inside the channel, the flow adopts a laminar profile: the streamlines velocity depends on their height in the channel, varying from zero at the walls to a maximum in the centre of the channel. During the sample travelling through the channel, an external field is applied perpendicularly to the elution flow. Sample components are then subjected to two forces in opposite direction, the field force driving them to the channel bottom, called accumulation wall, and the Brownian diffusion. The difference in diffusion coefficient of particles of different size controls their equilibrium position in different layers of the parabolic velocity profile and an exponential concentration profile is established. Due to the laminar profile the sample components migrate thorough the longitudinal axis at different speed. Components closer to the accumulation wall elute later than components travelling in the layers at higher velocity, generating the sample fractionation.

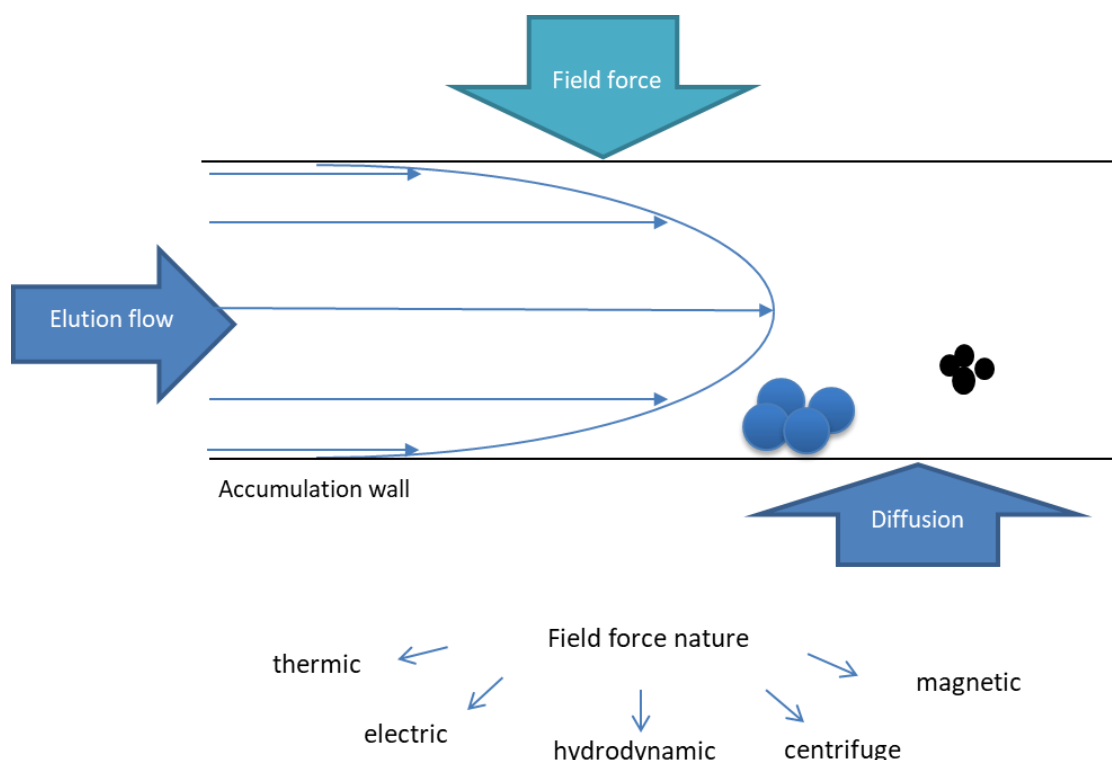


Figure 18. Separation principle of FFF

The field strength can be hydrodynamic, electric, thermic, centrifuge or magnetic. The different type of FFF are classified in function of the nature of the field strength applied. The field force in FFF is classically applied downward but, depending on the force nature, it can also be applied cyclically which mean the force is periodically reversed. This new application of the force is referred as cyclical FFF (Cy-FFF) (Giddings, 1986). This kind of practice is principally used when an electrical or magnetic field is applied (Gale and Srinivas, 2005; Tasci, Johnson and Gale, 2012).

The particularity of FFF, compared to liquid chromatography, is the absence of the stationary phase of the column. Initially, the FFF was also called “single-phase chromatography”, “one-phase chromatography” or even “polarization chromatography”, to illustrate the fact that the samples are solely separated in the mobile phase thanks to the interaction with the field force.

1.1. Elution modes

The analytes can be eluted according to different modes of elution that represents the transport/displacement of the analytes thorough the channel. In the case of a field strength applied downward there are three different elution modes (Messaud *et al.*, 2009) detailed hereafter.

Brownian mode. Also called normal mode (Wahlund, 2013), this mode governs the elution of most submicrometer analytes. In Brownian mode the field drives the analytes toward the accumulation wall. The analytes diffusion opposes the field strength and drives the analytes away from the wall, creating a concentration gradient until a steady state is reached. The diffusion is inversely proportional to the analyte size so the small analytes migrate farther from the accumulation wall than the big ones and elute first (Figure 19).

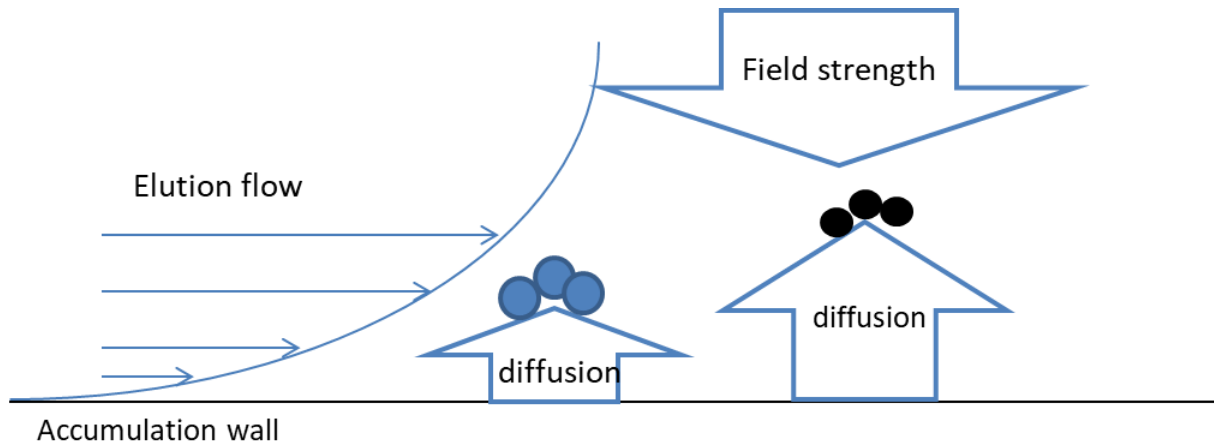


Figure 19. Elution in Brownian mode

Steric mode. When the analytes attain a certain size, generally in the micrometre range, the diffusion become negligible. Therefore, the analytes will reach the accumulation wall. The position of the analyte in the channel (i.e. their centre of gravity) will then depend on their size. The biggest analytes will have a higher position than the small ones and hence will be the first to elute (Figure 20)(Giddings, 1978).

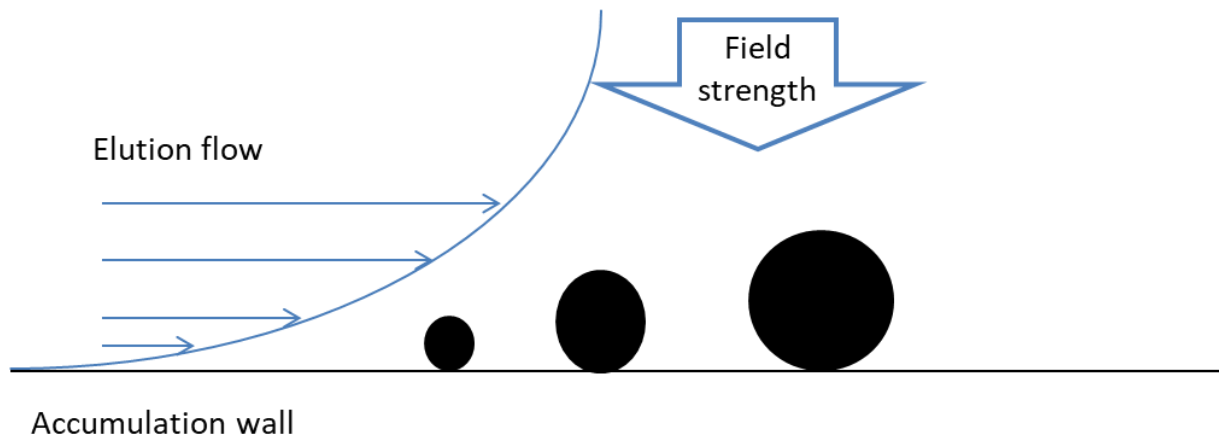


Figure 20. Elution in steric mode

Lift hyperlayer mode. Depending on the elution flow conditions, the lift forces acting on analytes of large size, generally in the micrometer range, can be sufficiently strong to drive the analytes away from the wall. The elution order is the same as for steric mode (Figure 21): when the particle is at a distance from the wall at least comparable to two times its radius, (Schimpf, 2000) the particle leaves the steric mode and enters the lift hyperlayer mode.

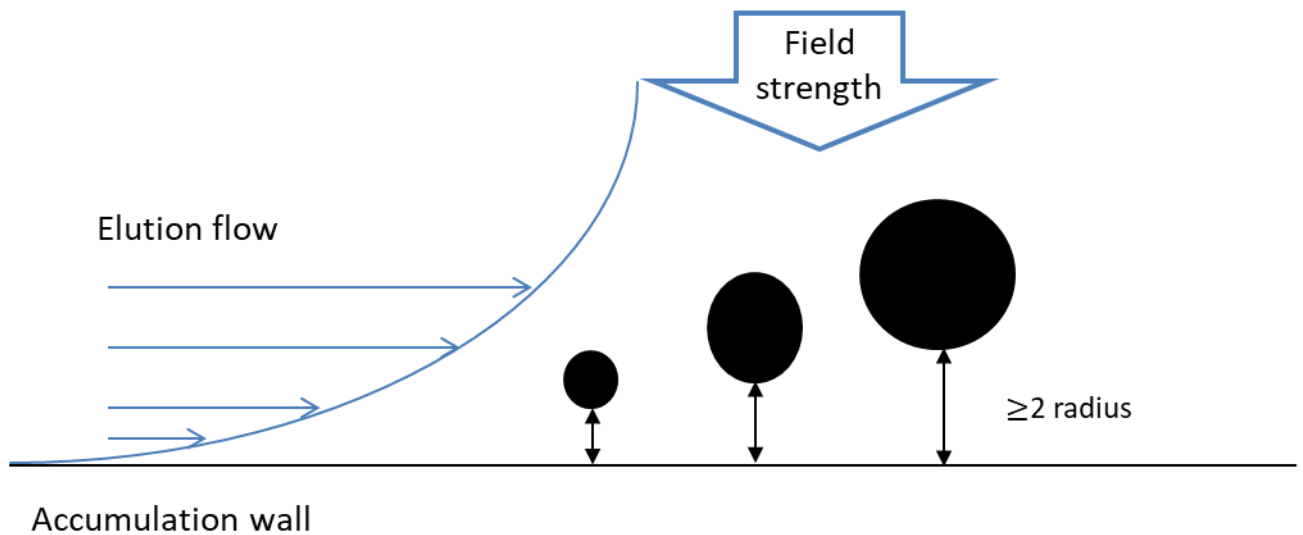


Figure 21. Separation of the analytes in the lift hyperlayer mode

When the field direction is periodically reversed (electrical/magnetic field forces), the analytes can elute in three different ways (Giddings, 1986) detailed hereafter (Figure 22).

Mode 1. The analyte oscillates near the accumulation wall under the effect of the field applied cyclically.

Mode 2. From the accumulation wall, the analyte travels across the channel, reaches the upper wall and then goes back to the accumulation wall when the field is inverted.

Mode 3: From the accumulation wall, the analyte travels across the channel, reaches the upper wall where it stays until the field is inverted.

The elution mode occurring depends on how long the field is reversed and the time needed by the analyte to reach the other wall. The mode 2 is just the formalization of a specific elution behaviour from the mode 1. Hence, the equations expressing the particles retention behaviour are the same for the model 1 and model 2 while the mode 3 depends of a different equation (Gale and Srinivas, 2005)

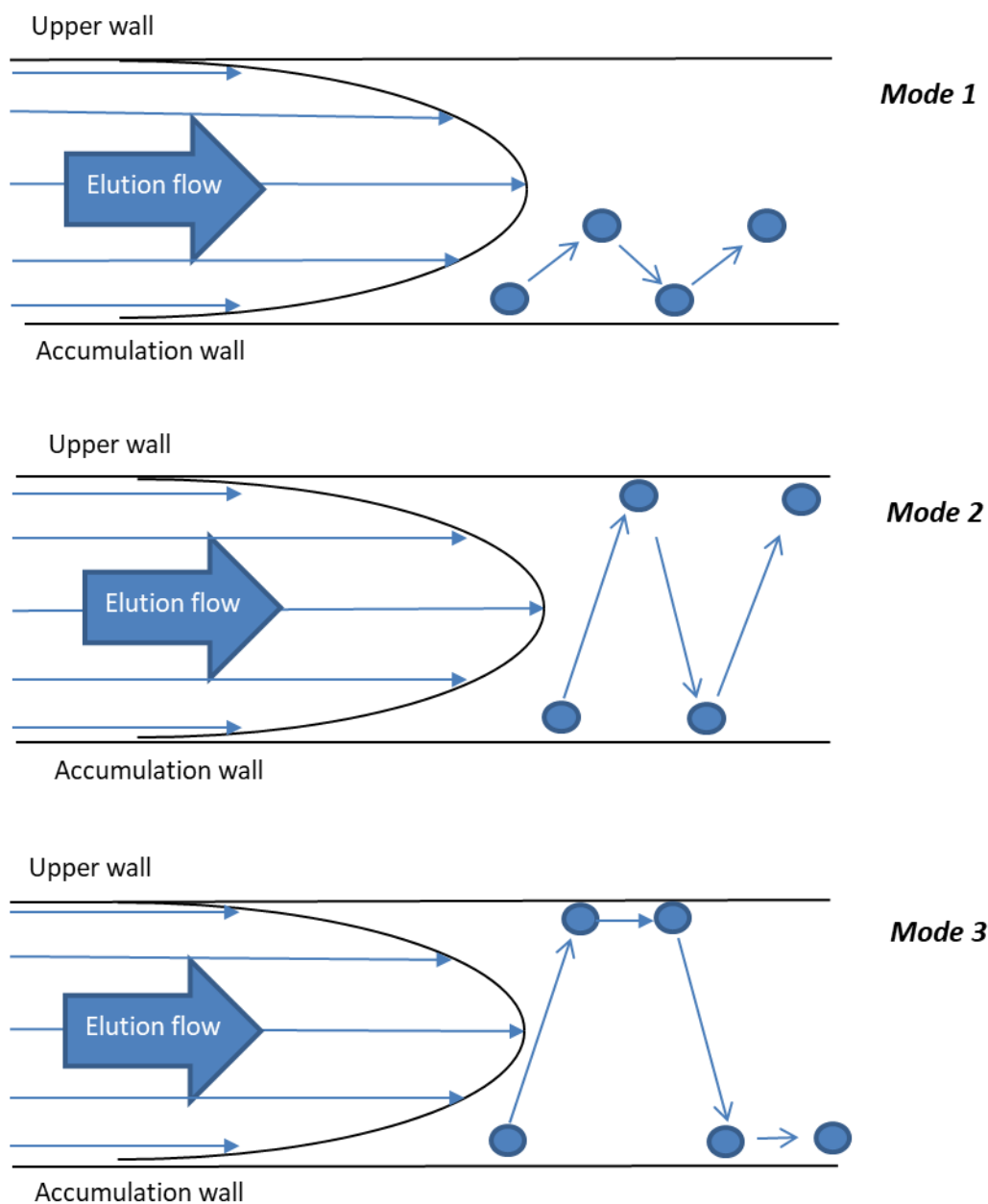


Figure 22. Different possible elution behaviour of the analyte submitted at a cyclical force.

1.2. Theoretical formalization

A theoretical model was developed in 1960s by Giddings (Giddings, 1966) to predict the behaviour of an analyte in a FFF channel eluting in the Brownian mode. If the geometry of the FFF channel is known exactly and the flow profile in the channel can be assumed as parabolic, it is possible to rely the retention time of the eluting peak to the particle diffusion coefficient

and by consequence, to the hydrodynamic diameter of the particle, thanks to the Stokes-Einstein equation.

In this section, the general theoretical expressions universally applicable to all FFF techniques operating in the Brownian mode are provided. The theory has been described in detail elsewhere (Giddings, 1973), therefore only the most important equations will be defined below.

In theory, a retention ratio, R , is defined which corresponds to the ratio of the mean velocity of the analyte zone and the mean velocity of the carrier fluid in the FFF channel. R can be expressed as the ratio of the retention time of an unretained analyte, also called void time (t_0) to the retention time of a retained analyte (Giddings, 1973):

$$R = \frac{v_{analyte}}{v_{carrier}} = \frac{t_0}{t_r} \quad (II.1)$$

Due to the large ratio width/thickness (y/x) of the channel, generally larger than 40 (Giddings and Schure, 1987), the channel can be assimilated to two parallel plates so that the velocity ratio can be expressed only in function of the transversal axis coordinate, x (Hovingh, Thompson and Giddings, 1970):

$$\frac{v_{analyte}}{v_{carrier}} = \frac{\int_0^w c(x)v(x)dx}{\langle v(x) \rangle \int_0^w c(x)dx} \quad (II.2)$$

where w is the thickness of the channel, $c(x)$ and $v(x)$ are respectively the velocity of the concentration profile and the velocity of the flow in function of the x -coordinate, and $\langle v \rangle$ is the average flow velocity. In the case of a laminar flow, a parabolic velocity distribution is assumed (Martin and Feuillebois, 2003):

$$v(x) = 6\langle v(x) \rangle \left(\frac{x}{w} - \frac{x^2}{w^2} \right) \quad (II.3)$$

The expression of $c(x)$ is based on the assumption of an analyte cloud in a steady state regime where only two opposite forces are applied on the analyte: the field and the diffusion forces. This leads to Eq. (II.4)(Schimpf, 2000):

$$c(x) = c_0 \exp \left(-\frac{Fx}{kT} \right) \quad (II.4)$$

where c_0 is the analyte concentration at the accumulation wall, F is the field strength applied on the analyte, k the Boltzmann constant and T the temperature. Eqs. (II.3) and (II.4) are then introduced in Eq. (II.2), which gives

$$R = 6\lambda \coth\left(\frac{1}{2\lambda}\right) - 12\lambda^2 \quad \textbf{Classical model (II.5)}$$

where λ is a dimensionless retention parameter equal to kT/Fw . Eq. (II.5) will be called in this work “classical model”.

Depending on λ value, Eq. (5) can be approximate by one of the two following expressions (Schimpf, 2000):

$$R = 6\lambda - 12\lambda^2 \quad (II.6)$$

$$R = 6\lambda \quad (II.7)$$

The first approximation (Eq. (II.6)) is accurate within 2% when $\lambda < 0.2$. The second approximation (Eq. (II.7)) can be used when $\lambda < 0.02$ and is accurate within 5%. Eq. (II.7) can be applied when $0.12 t_r > t_0$, condition which ensure the separation of the fractogram from the void peak and is easy to obtain. Eq. (II.7) is the most applied approximation in literature (e.g.(Perez-Rea, Zielke and Nilsson, 2017; Guo, Wang, *et al.*, 2019; Moens *et al.*, 2019; Maknun, Sumranjit and Siripinyanond, 2020; Tadjiki, Chittleborough and Beckett, 2020)). The parameter λ can be related to physicochemical quantities of the solute depending on the nature of the applied physical field. For the various FFF techniques, these relationships can be found in Table 5.

Table 5. Analyte physicochemical parameters that influence the fractionation in the different types of FFF (Schimpf, 2000).

FFF technique	λ	Physicochemical parameters of the analyte
Sedimentation-FFF	$\lambda = \frac{6kT}{d_h^3 \omega^2 r w (\rho_s - \rho)}$	d_h, ρ_s
Thermal-FFF	$\lambda = \frac{D}{D_T \Delta T}$	D, D_T
Electrical-FFF	$\lambda = \frac{D}{\mu E w}$	D, μ
Magnetic-FFF	$\lambda = \frac{RT}{M w \chi_m H_m \Delta H_m}$	M, χ_m
Flow-FFF	$\lambda = \frac{DV^0}{Q_c w^2}$	D

D : diffusion coefficient

D_T : thermal diffusion coefficient

d_h : hydrodynamic diameter

E : electrical field strength

Q_c : cross flow rate

H_m : intensity of the magnetic field

M : molecular mass

R : gas constant

V^0 : void volume

ρ : solvent density

ρ_s : particle density

ΔH_m : gradient of intensity of the magnetic field

ΔT : temperature gradient

μ : electrophoretic mobility

$\omega^2 r$: centrifugal acceleration

χ_m : molar magnetic susceptibility

1.3. Working hypotheses of the FFF retention theory

The classical model is based on several hypotheses. These hypotheses can be classified in four categories:

- 1) **Assumptions linked to the operating mode and the channel geometry:** the model assumes that the particles move under Brownian motion. The channel must be rectilinear. The channel volume can be considered as the space between two infinite uniform parallel plates. Hence, the edges effect is considered negligible (Martin, 1999).
- 2) **Assumptions linked to the stationarity of the migration process:** the model is developed for isocratic elution which mean that the force applied on the analyte, the cross flow in the case of FI-FFF, must be constant thorough the channel. The particle

migration is assumed to begin only once a steady state is reached by the particles (Martin, 1999).

- 3) **Assumption linked to the cross sectional concentration distribution:** the concentration profile is supposed to decrease exponentially. To this end, the analytes have been assimilated to material points, which means the steric effects are not considered in the equation. The electrostatic and van der Waals interactions particle-particle and particle-wall are considered negligible compared to the field induced strength. The hydrodynamic lift forces do not affect the particle motion (Martin, 1999).
- 4) **Assumptions linked to the cross sectional velocity distribution:** the elution flow is laminar. This implies that there is not a temperature gradient in the channel. Due to the point like particle assumption, the particle speed is the same as the flow line where the particle is positioned (no Faxén slip velocity)(Martin, 1999).

These assumptions are usually fulfilled by the different FFF techniques in common experimental conditions, but strong attention should be paid to check them because their fail may generate significant artefacts. Some of these hypotheses have been already verified experimentally. Concerning **hypothesis n°1**, the parallel plate assumption is considered to be just due to the large width to thickness ratio of FFF channels. *Giddings et al.* confirmed that edge effect could be neglected if the channel width is far superior to the channel thickness (Giddings and Schure, 1987).

Litzen et al. verified **hypothesis n°2** by showing that the cross flow is uniform thorough the channel. They modified the channel by adding four injection ports equally distributed through the channel length and they injected a sample by these different injection ports. After the elution, they found that the sample retention ratio was the same regardless of the location of the injection inlet, which would only have been possible if the cross flow was constant (Litzén, 1993).

The verification of the **third hypothesis** strongly depends on the experimental conditions. Indeed, the particles injected need to be sufficiently small to avoid the perturbations due to steric effects and hydrodynamic lift (Martin, 1999). Moreover, several articles showed the **effect of electrostatic interactions** by varying their carrier ionic strength (Litzén and Wahlund, 1991a; Mori, 1994; Neubauer, V.d. Kammer and Hofmann, 2011; Kato *et al.*, 2018; Kowalkowski, Sugajski and Buszewski, 2018; Nickel *et al.*, 2021). It was observed that, at low

ionic strength, the particle retention is greatly reduced due to the importance of electrostatics repulsion between the particles and the wall (Figure 23).

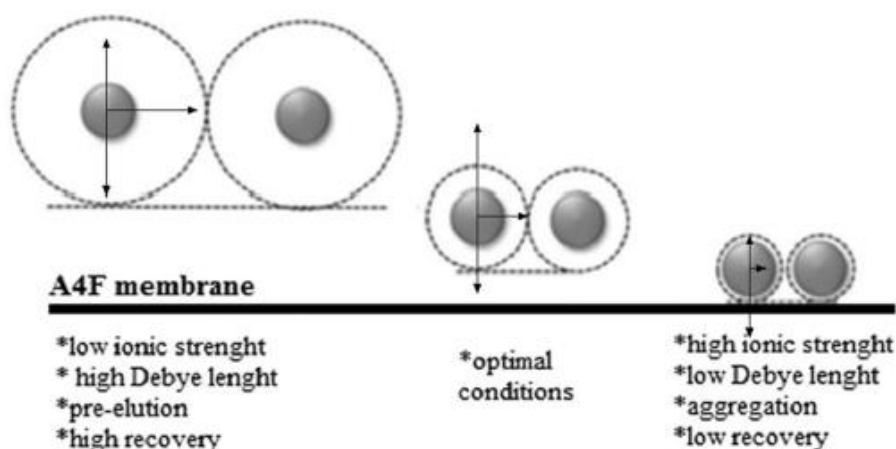


Figure 23. Changes of electric double layer depending on the ionic strength. From (Gigault, Pettibone, *et al.*, 2014; Kowalkowski, Sugajski and Buszewski, 2018)

The impact of liquid carrier composition on latex NPs separation has been observed comparing water and $10^{-3} \text{ mol L}^{-1} \text{ NH}_4\text{NO}_3$ carriers (Figure 24)(Kowalkowski, Sugajski and Buszewski, 2018). Using $10^{-3} \text{ mol L}^{-1} \text{ NH}_4\text{NO}_3$ as the carrier liquid, two peaks were obtained corresponding to particles of size 60 nm and 122 nm, respectively. Despite attempts to extend the separation time to 220 min, no peak has been achieved for particles of 356 nm in diameter. These experimental conditions corresponds to high ionic strength conditions, as shown in Figure 23.

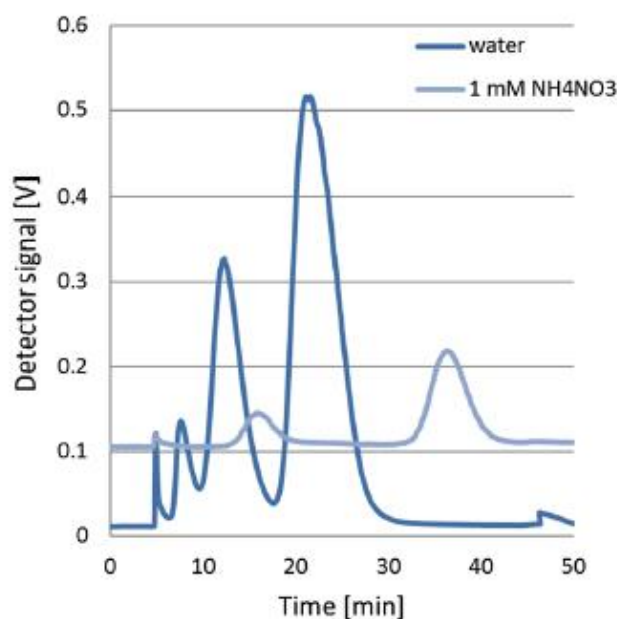


Figure 24. Impact of the carrier ionic strength on the retention of a mixture constituted by polystyrene particles with a diameter of 60, 121 and 356 nm. From Kowalkowski et al. (Kowalkowski, Sugajski and Buszewski, 2018).

On the other side, the carrier has to be enough concentrated in ions in order to keep the electrostatic interactions to a minimum (Figure 23). *Mori et al.* showed, using the sedimentation FFF (SdFFF), that these effects could be minimized when the carrier ionic strength is above $10^{-3} \text{ mol L}^{-1}$ and the mass injected is below $4 \mu\text{g}$ (Mori, Kimura and Tanigaki, 1990). In fact, the injected mass also needs to be controlled in order to avoid interferences on the retention behaviour. The **effect of particle-particle interaction** was investigated in literature and several authors stated that changing the injected sample mass influences its retention behaviour (Hansen, Giddings and Beckett, 1989; Martin and Feuillebois, 2003; Neubauer, V.d. Kammer and Hofmann, 2011). *Martin et al.* reported that two mechanisms affect the sample retention behaviour when the injected mass is increased. The first mechanism is related to the mean distance between the particles and the wall: the increase of particle concentration expand the particle cloud because particles hindrance each other. The mean distance between the particle cloud and the wall becomes greater than for a smaller sample load, making the particles eluting earlier. The second mechanism is due to a viscosity local change: as the mass of particles increases, the viscosity of the suspension increases, which increases the viscosity near the wall where the sample is carried. This difference in viscosity distorts the flow velocity profile and reduces the streamline velocity in correspondence with the area in which the viscosity increased. This effect produces an increase in the retention time (Martin and Feuillebois, 2003). This set of effects has been regrouped over the term “overloading”. The overloading effects can

either increase or decrease the particle retention time. It has been observed that the increase or decrease depends principally on the sample: increase for macromolecules suspension (Marioli and Kok, 2019) and decrease for colloidal suspension (Hansen, Giddings and Beckett, 1989) respectively.

Concerning the **hypothesis n°4**, the carrier temperature in FFF channel is generally uniform with the exception of the thermal FFF where a temperature gradient is voluntarily created. In this case, a model taking this deformation into account has been developed (Geisler and Lederer, 2020).

1.4. Practice *versus* classical theory

Even when the major hypothesis of the retention model are satisfied, several authors reported cases where the classical model could not explain the particle elution behaviour. *Gigault et al.* (Gigault and Hackley, 2013) reported size-independent retention effects, where particles with different chemical nature, but identical size, eluted at different times. These differences of behaviour were first attributed to the particle density. The authors developed a retention model that consider the gravity force and remarked that the impact of particle density on the retention time is not sufficient to explain the particle behaviour (Figure 25).

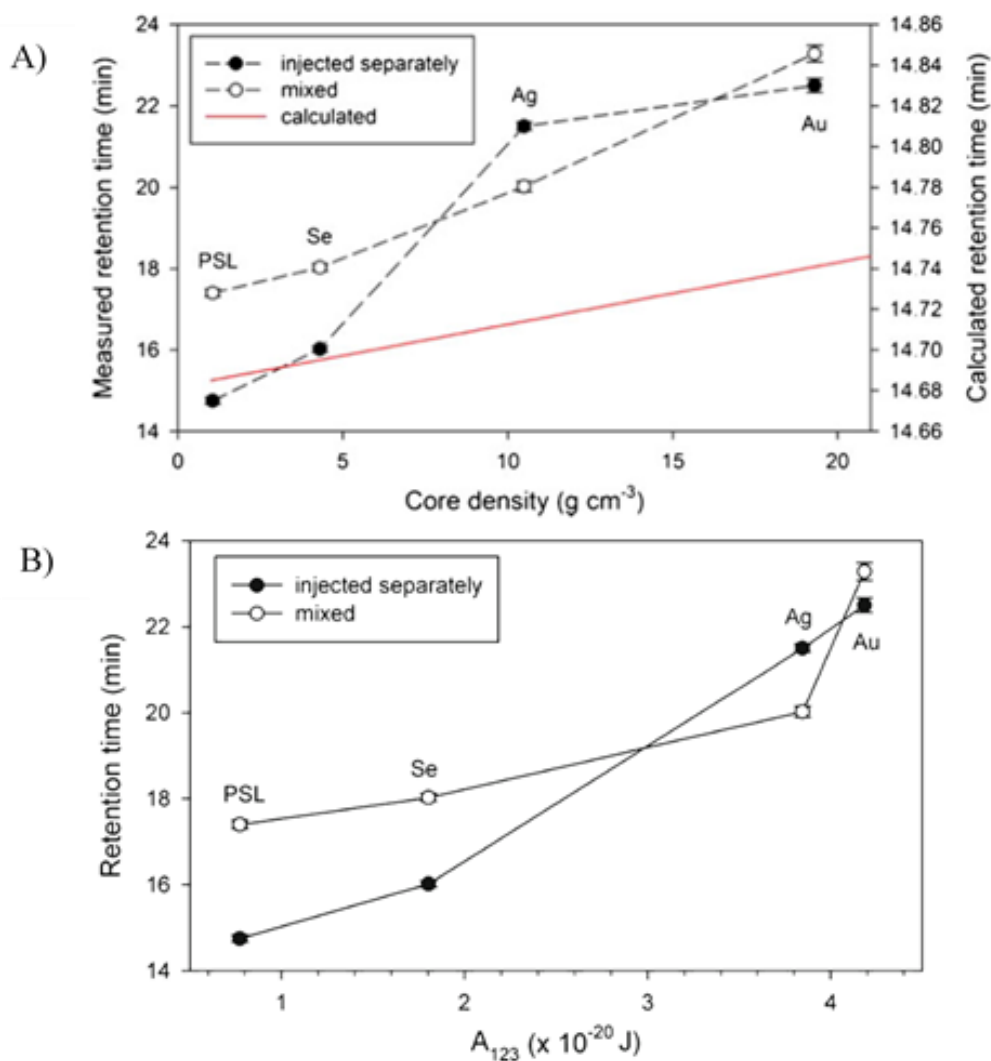


Figure 25. A) Retention time of 100 nm particles in function of their density. B) Retention time of 100 nm particles in function of their Hamaker constant. From (Gigault and Hackley, 2013).

Qu et al. also showed that gold particles have different retention time depending on their coating nature (*Qu et al.*, 2016). Furthermore, it has been reported that also the membrane nature, cut-off and zeta potential may affect the retention and the recovery rate of the sample. The difference in zeta potential or the different hydrophilic character of the membranes were mentioned to explain these differences in behaviour (Figure 26) (*Losert et al.*, 2013; *Bendixen et al.*, 2014). In another register, *Phelan et al.* showed that rod-like particles behave differently from sphere-like particles, particularly during steric transition (*Phelan and Bauer*, 2009).

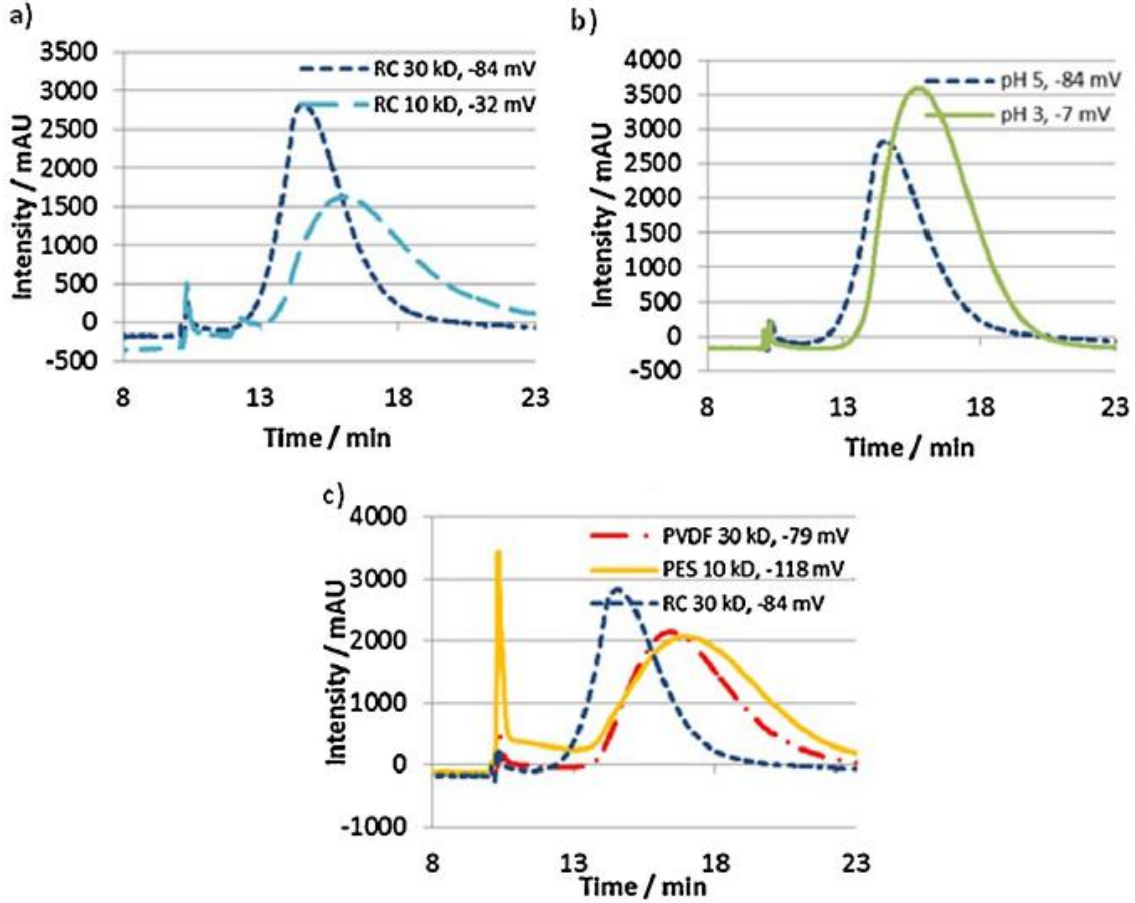


Figure 26. Modification of the retention time of titanium dioxide NPs. a) Effect of membrane cut-off. b) Effect of pH. c) Effect of membrane materials. From (Bendixen *et al.*, 2014).

1.5.Variants of the classical retention model

In order to represent more accurately the different phenomena in the channel and consequently to give a better estimation of the particle size and to allow a larger range of applications of the FFF theory, several authors proposed improvements of the classical model or defined substitutive models. Some examples are given thereafter.

1.5.1. Steric model

When particles surpass a certain size, the point-like approximation is not adapted anymore and the steric effect needs to be taken into consideration as the particle centre of gravity cannot approach the wall of the channel nearer than its radius. To this end, *Hovingh and Giddings* (Hovingh, Thompson and Giddings, 1970) changed the born of the integral in Eq. (II.2) from $x=0$ and $x=w$ to $x=r_h$ and $x=w-r_h$. After integration, Eq. (II.2) becomes

$$R = 6\alpha(1 - \alpha) + 6\lambda \left[(1 - 2\alpha) \coth \left(\frac{1 - 2\alpha}{2\lambda} \right) - 2\lambda \right] \quad \textbf{Steric model (II. 8)}$$

with α the ratio of the particle radius to the channel thickness. Eq. (II.8), that will be called thereafter “steric model”, gives a more accurate size result for particles with a diameter superior to 60 (Håkansson *et al.*, 2012). The inversion diameter from which the particle will elute in steric mode can also be determined by assuming that steric effect become important when $\alpha > \lambda$.

1.5.2. Model tacking into account the interaction particle-wall

The interactions between the particles and the accumulation wall are one of the deviations from the ideal behaviour that mostly limit the application range of the classical, or steric, models. Hansen *et al.* (Hansen and Giddings, 1989) proposed a model that include the two principal types of particle-wall interactions, the van der Waals and the electrostatics interactions, in the expression of the concentration profile. This approach has been used in SdFFF to determine the size and the Hamaker constant of the particle.

When all forces applied on the analyte derive from a potential energy function $W(x)$, the concentration profile can be expressed by the Boltzmann expression (Hansen and Giddings, 1989):

$$c(x) = c_0 \exp \left(\frac{-W_{tot}(x)}{kT} \right) \quad (II. 9)$$

where $W_{tot}(x)$ is the sum of the potential energies of a particle whose centre of mass is at the position x and c_0 is the concentration at the position where $W_{tot}(x)=0$. $W_{tot}(x)$ is the combination of the potential energy due to the field strength, $W_F(x)$, the sum of potential energies due to the interactions between the particles and the wall, $W_{p-w}(x)$ and the sum of potential energies due to the interaction between particles, $W_{p-p}(x)$:

$$W_{tot}(x) = W_F(x) + W_{p-w}(x) + W_{p-p}(x) \quad (10)$$

As the term $W_{p-p}(x)$ depends on the sample concentration, the authors considered it as an overloading effect and did not add it in the equation (Hansen and Giddings, 1989). By consequence, this retention model is valid only in dilute conditions.

According to the DeJarguin-Landau-Verwey-Overbeek (DLVO) theory, the two principal types of interactions between two solids are the **electrostatic interactions** and the **van deer Waals forces** (Grasso *et al.*, 2002). Eq. (10) can be expressed as

$$W_{tot}(x) = W_F(x) + W_{el(p-w)}(x) + W_{vdW(p-w)}(x) \quad (II.11)$$

where $W_{el(p-w)}(x)$ and $W_{vdW(p-w)}(x)$ are respectively the potential energy of the electrostatic interactions and van der Waals forces. The electrostatic interaction is expressed as (Hansen and Giddings, 1989):

$$W_{el(p-w)}(x) = 64\pi\epsilon_0\epsilon_r a \left(\frac{kT}{e}\right)^2 \tanh\left(\frac{e\psi_p}{4kT}\right) \tanh\left(\frac{e\psi_w}{4kT}\right) \exp(-\kappa(x-a)) \quad (II.12)$$

with ϵ_0 the permittivity of the void, ϵ_r the dielectric constant of the mobile phase, a the particle radius, e the electron charge, ψ_p and ψ_w respectively the surface charge of the particle and the wall and κ the inverse of the Debye length which is expressed as

$$\kappa = \sqrt{\frac{2e^2 N_a I}{\epsilon_0 \epsilon_r kT}} \quad (II.13)$$

where N_a is the Avogadro number and I is the ionic strength. Finally, the potential energy of the van der Waals forces is defined by (Hansen and Giddings, 1989):

$$W_{vdW(p-w)}(x) = -\frac{A_{123}}{6} \left(\frac{a}{x-a} + \frac{a}{x+a} + \ln \frac{x-a}{x+a} \right) \quad (II.14)$$

with A_{123} the Hamaker constant which represents the interactions between the particle 1 and the wall 3 in the medium 2. By adding this new expression of the concentration profile in Eq. (II.1) the retention ratio is now defined by

$$R = \frac{6 \int_{r_h}^{w-r_h} \exp\left(-\frac{W_{tot}(x)}{kT}\right) \left(\frac{x}{w} - \frac{x^2}{w^2}\right) dx}{\int_{r_h}^{w-r_h} \exp\left(-\frac{W_{tot}(x)}{kT}\right) dx} \quad \textbf{p - w model} \quad (II.15)$$

Eq. (15) will be called in this work “particle-wall model (p-w model)”.

1.5.3. Experimental correction for particle–wall interaction

Williams and co-workers (Williams *et al.*, 1997) proposed an original way to take the particles wall interactions into account by a semi experimental approach. They consider a force, F_2 , which represent the sum of the interactions between the analyte and the wall. F_2 depends on the distance between the surface of the analyte and the wall, δ , which is equal to $(x - a)$ with a , the analyte radius. If $F_2(\delta)$ is repulsive there will be an exclusion distance, δ_w , that the particle will not be able to access (Figure 27). If F_2 is attractive, δ_w will be negative and will mean that the analyte cloud is closer to the wall compared to the position predicted by the classical model.

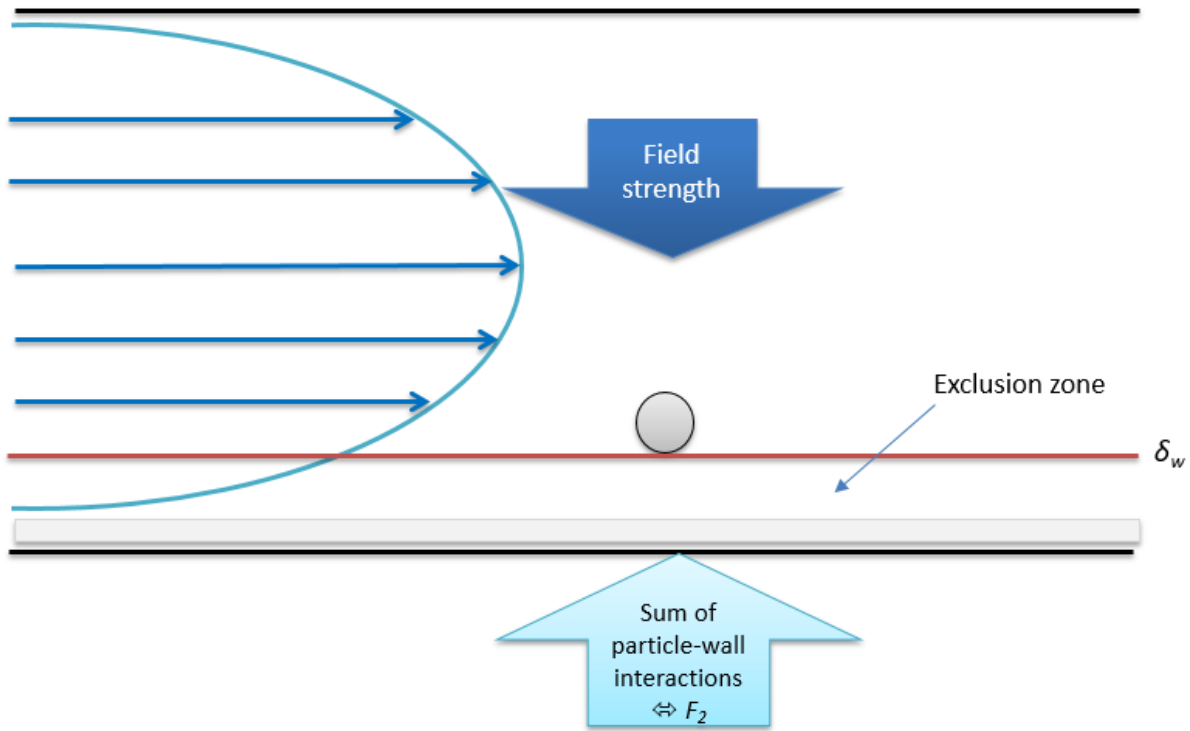


Figure 27. Illustration of the exclusion distance, δ_w

By considering $F_2(\delta)$, Eq. (8) becomes:

$$R = 6\alpha(1 - \alpha) + 6\lambda \left((1 - 2\alpha) \coth \frac{1 - 2\alpha}{2\lambda} - 2\lambda \right) \left(1 + \frac{\delta_w}{l} \right) \quad \text{sw model (II. 16)}$$

Where l is the thickness of the analyte cloud and is equal to λw . Eq. (II.16) will be called in this work “ δ_w model”. To determine δ_w Eq. (II.18) is rearranged as follows:

$$Y = \frac{R - 6\alpha(1 - \alpha)}{6\lambda \left((1 - 2\alpha) \coth \frac{1 - 2\alpha}{2\lambda} - 2\lambda \right)} = \left(1 + \frac{\delta_w}{l} \right) \quad \text{(II. 17)}$$

In this form δ_w is equal to the slope of $Y = f(l/l)$. The distance δ_w depends on the intensity of the particle-wall interactions so it depends on the analyte and wall composition and surface properties, and on the composition and concentration of the mobile phase. It can also depend on the particle size depending on the experimental conditions applied.

1.5.4. Models based on different assumptions

Variable field strength. All the models presented in the previous sections were based on the assumption that the field strength applied on the analytes was constant during the analysis. In practice, in some FFF techniques the users can program a gradient of strength during the analysis. This approach is often used in AF4 and, from a practical point of view, presents many advantages. Indeed, when a polydisperse sample is fractionated, the cross flow applied needs to be strong enough to retain the small analytes and separate them from the void peak, but this will also increase the residence time of big particles in the channel. As a result, the analysis time is long, the particle-wall and particle-particle interactions of larger particles are high and, in the worst case, the population of larger size do not elute from the channel. An example was given in Figure 24. Hence, the decrease of the cross flow during the elution step permits a reduction of the analysis time and can prevent the particle adsorption on the membrane.

Many authors developed different models to take into account the perturbation induced on the steady state due to the change of the applied strength (Giddings *et al.*, 1979; Williams and Giddings, 1994; Williams, 2017; Håkansson *et al.*, 2012). Due to the complexity of the topic, which is out of the scope of this work, these models will not be detailed here.

Slip-boundary model. A different approach to reduce particle-wall interactions and particle adsorption on the membrane is the addition of surfactants to the carrier. Several kind of surfactants have been used in literature, like Polysorbate 20 (also known as Tween 20) that is a polysorbate-type nonionic surfactant (Fraunhofer and Winter, 2004), sodium dodecyl sulfate (SDS) (Schwaferts *et al.*, 2020), and FL-70 that is an alkaline detergent (Schwaferts *et al.*, 2020) to cite just a few examples. However, the use of surfactants implies news types of interactions between the particles and the wall. Kim *et al.* developed a model in order to study the effect of surfactant concentration on the particles retention (Kim, Rah and Lee, 2012).

Non-spherical particles. Shape-based particle separation using FFF has gained attention due to increasing interest for applications using micro/nanorods such as metal- and polystyrene-

nanorods for drug delivery (Sharma, Park and Srinivasarao, 2009). To explain the behaviour of rod-like particles inside the FFF channel, *Beckett and Giddings* developed a model taking into account the entropic contribution specific to the particle shape in its retention behaviour (Beckett and Giddings, 1997). This model was then developed by *Park and co-authors* where the different mode of elution of rods are described (Alfi and Park, 2014; Park and Mittal, 2015; Monjezi *et al.*, 2019). The mathematical development of all these model is based on the idea that the rod particle behave as a pole that rotate on itself. Depending on its position, this rotation can be limited due to the accumulation wall, which result in a loss of entropy.

2. Flow-FFF and Asymmetrical Flow-FFF

Among the different techniques belonging to FFF family, which are distinguished by the nature of the force applied, we will focus in this work on the Flow-Field Flow Fractionation (Fl-FFF) technique, which fractionates the sample by applying a hydrodynamic force on the sample. This force is generated by a secondary flow, the cross flow, applied perpendicularly to the main flow of the solvent in the channel. The channel is constituted of two porous walls and a semi permeable membrane that covers one of them (Figure 28.A)(Giddings, Yang and Myers, 1976). Two pumping systems control the carrier flow for the axial and cross flows.

In 1986 another version of the Fl-FFF was developed by Granger *et al.* (Granger *et al.*, 1986) in which the channel had only one porous wall (Figure 28.A) and a single source of flow provided both the axial flow and the cross-flow. This model had the advantage to decrease the perturbation from the cross flow generated by the heterogeneous permeability of the two porous walls and was easier to make up. This version was called asymmetrical flow field flow fractionation (AF4)(Wahlund and Giddings, 1987) and the two-porous-wall version was then called “symmetrical flow FFF”. To ensure that the cross flow was constant thorough the channel, the channel was modified from a rectangular to a trapezoidal shape (Figure 28.B)(Litzén and Wahlund, 1991b).

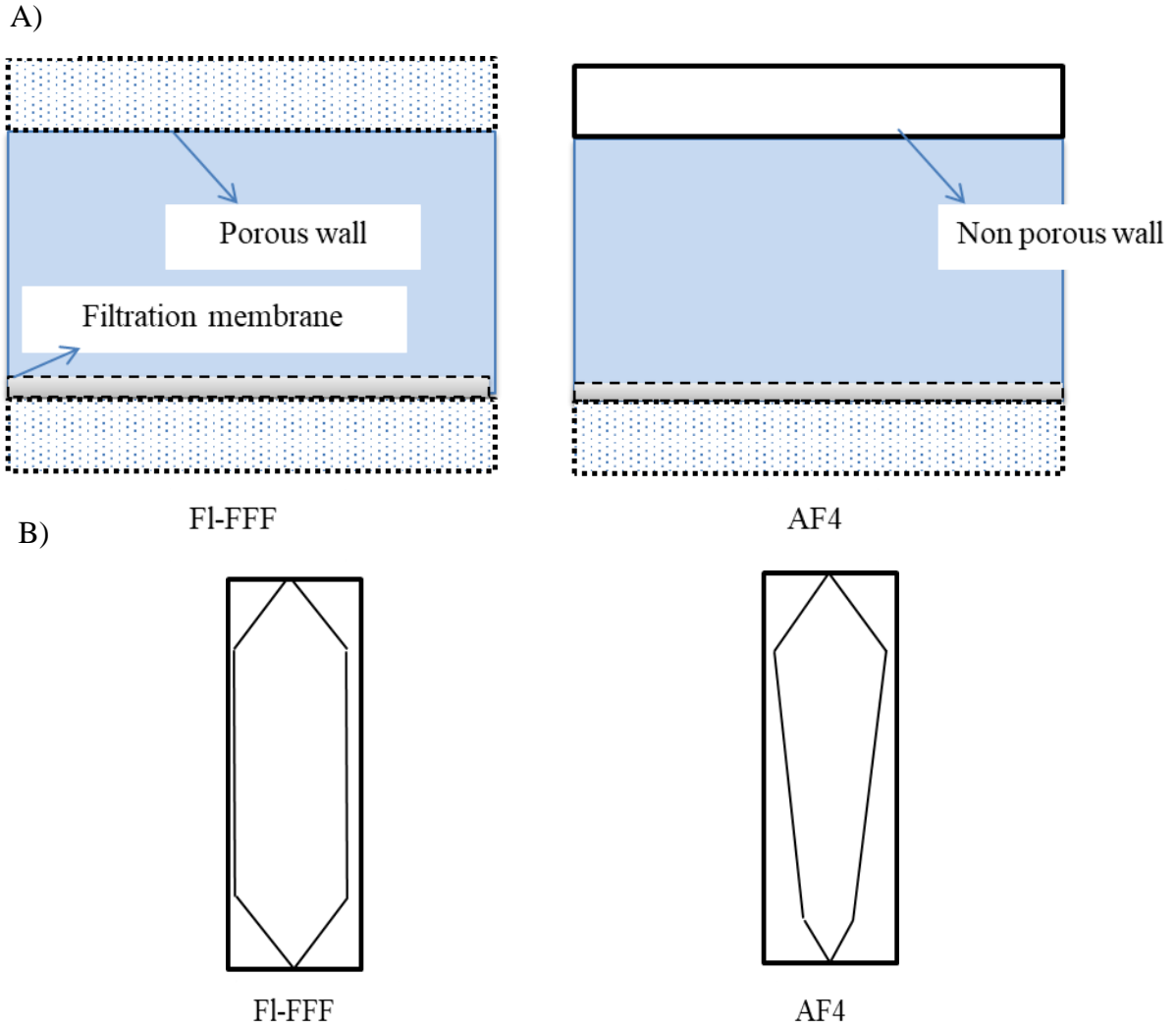


Figure 28. Difference between FI-FFF and AF4: A) side view; B) front view.

In FI-FFF the force applied on the channel can be approximated by (Schimpf, 2000):

$$F_{FI-FFF} = \frac{3\pi\eta d_h Q_c w}{V^0} \quad (II.20)$$

With η the carrier viscosity, d_h the hydrodynamic diameter of the particle, Q_c the cross flow rate and V^0 the channel volume.

By having only one permeable wall, the cross flow in AF4 is generated by a forced percolation of the elution flow through the wall, while in symmetrical FI-FFF the cross flow come from the upper permeable wall. This means the cross flow is not applied uniformly through the x-axis. Therefore the mathematical expression of the field strength in FI-FFF needed to be adapted to take this variation into account (Wahlund and Giddings, 1987):

$$F_{AF4} = \frac{Q_c w 3 \pi \eta d_h}{V^0} \left(1 - \frac{3x^2}{w^2} + \frac{2x^3}{w^3} \right) \quad (II.21)$$

It is worth noting that F_{AF4} decreases with the channel thickness. However, Wahlund and Giddings (Wahlund and Giddings, 1987) showed that this decrease is negligible near the accumulation wall where the majority of the sample is concentrated. In conclusion, the equations defined for the FI-FFF force do not need to be adapted for the AF4 case.

Combining Eq. (II.20) with the assumption that $R=6\lambda$ (Eq. (II.7)), an expression relying the retention time and the hydrodynamic diameter of the particle is obtained:

$$d_h = \frac{2kTV^0 t_r}{\pi \eta V_c w^2 t_0} \quad (II.22)$$

2.1. The different steps in AF4 analysis

An AF4 experiment is composed of three steps that are represented in Figure 29.

1) Sample injection: in a first time, the sample is injected in the channel.

2) Sample focusing: then the inlet flow (“Flow In” in Figure 29.1) and the focus flow, flowing in opposite directions, allow the sample to attain a steady state and to focalize at some intermediate position, between inject and focusing inlets. Meanwhile, sample components are subjected to the force generated in AF4 and to the Brownian diffusion: their difference in diffusion coefficient controls their equilibrium position in different layers of the parabolic velocity profile. At the end of the focusing procedure, sample components reach concentration profiles close to their quasi-equilibrium distributions before the elution step. The focusing procedure allows reducing the injection contribution to peak broadening.

3) Sample elution: once the steady state is attained, the focalization is stopped, the focusing flow is decreased to zero and the sample is fractionated and eluted.

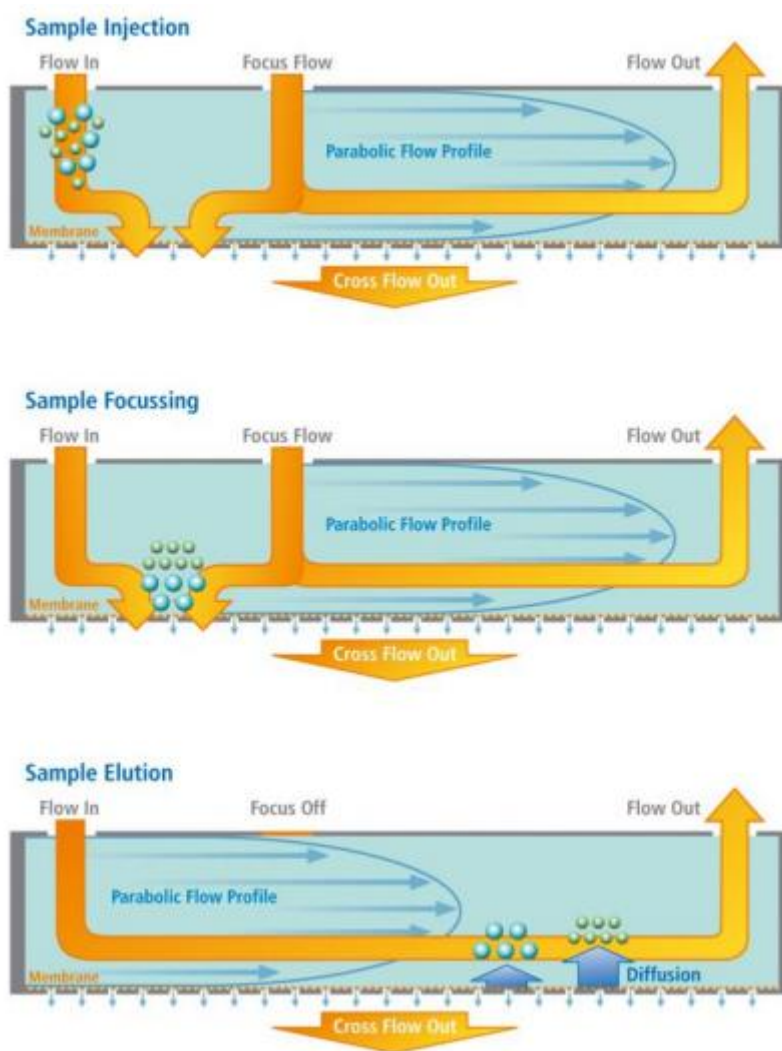


Figure 29. Different steps in AF4: (1) sample injection; (2) sample focussing; (3) sample elution. From Postnova Analytics website.

2.2. AF4 applications

The AF4 is an interesting technic for analytical strategies based on separation and characterization of micro or nano sized analytes (Williams, Runyon and Ashames, 2011; Correia and Loeschner, 2018; Yang *et al.*, 2020). Therefore, the AF4 is used in a large range of domains (material science, environmental science and life science) with analytes of various origins. Table 6 lists the principal applications found in the literature.

Table 6. Principal applications of AF4

Science field	Applications	References
Material sciences	- Metallic nanoparticles (Au, Ag, Pt...)	(Calzolari <i>et al.</i> , 2011; Gigault <i>et al.</i> , 2013; Sánchez-Cachero <i>et al.</i> , 2021)
	- Oxidized nanoparticles (TiO ₂ , ZnO, SiO ₂ ...)	(Heroult <i>et al.</i> , 2014; López-Heras, Madrid and Cámara, 2014; Hetzer <i>et al.</i> , 2017)
	- Polymers particles	(Kim <i>et al.</i> , 2018)
Life sciences	- Proteins	(Caputo <i>et al.</i> , 2019)
	- Microorganisms (viruses, bacteria...)	(Chuan <i>et al.</i> , 2008; Guo, Li, <i>et al.</i> , 2019)
	- Liposomes	(Hupfeld, Ausbacher and Brandl, 2009; Hupfeld <i>et al.</i> , 2010)
Environmental sciences	- Clay	(Tadjiki, Chittleborough and Beckett, 2020)
	- Colloids	(El Hadri <i>et al.</i> , 2014; Marassi <i>et al.</i> , 2021)
	- micro/nano plastics	(Gigault <i>et al.</i> , 2017; Caputo <i>et al.</i> , 2021)

2.3. Strength and weakness of AF4-multidetector

AF4-multidetector has many advantages as a size analysing technic. Firstly, AF4 separates the different components of the sample in a “gentle way” which does not harm the analytes (Messaud *et al.*, 2009). This allows the separation of fragile analytes like proteins aggregates or cells. AF4 may be coupled with a large variety detectors: dynamic light scattering (DLS), multi angle light scattering (MALS) and concentration detectors as UV/visible, fluorescence, differential refractometer, inductive coupled plasma mass spectrometry (ICP-MS), IR-Raman, giving access to the measurement of various parameters, as the average size, the size distribution, shape and elemental composition of the sample in one analysis (Bolea *et al.*, 2011a)(Schwaferts *et al.*, 2020). The sample can also be collected during the analysis by a fraction collector and be analysed by an off line detector (TEM, AFM, spICPMS among others). The retention model also gives a fast way to measure the sample size. However, due to the non-ideal behaviour of the sample depending on the fractionation conditions this method is underutilized (Figure 30). The Figure 30 compiles the different methods used by researchers to

characterize their sample size in more than one hundred papers using AF4 coupled online and offline to various size detectors, or using external calibration with standard of known size, or using a retention model¹. Papers have been selected from the last ten years and cover all the applications mentioned in the precedent section, in order to accurately represent the technic usage nowadays. The AF4 is most often coupled to a MALS detector to characterize the analyte size. Among the 42 papers where the MALS was not used, half of them is because the type of sample analysed in the publication cannot be correctly characterized by MALS, like for gold or silver nanoparticles.

¹ (Moon, Park and Kim, 1998; Kim *et al.*, 1999; Schure and Palkar, 2002; Kammer, Baborowski and Friese, 2005; Baalousha *et al.*, 2006; Dubascoux *et al.*, 2008; Tadjiki *et al.*, 2009; Zattoni *et al.*, 2009; Cho and Hackley, 2010; Calzolari *et al.*, 2011; Bolea *et al.*, 2011b; Kammer *et al.*, 2011; Reschiglian, Rambaldi and Zattoni, 2011; Hagendorfer *et al.*, 2011; Kato *et al.*, 2012; Baalousha and Lead, 2012; Mitrano *et al.*, 2012; Bae *et al.*, 2012; Geiss *et al.*, 2013; Loeschner, Navratilova, Købler, *et al.*, 2013; Loeschner, Navratilova, Legros, *et al.*, 2013; Gigault, Nguyen, *et al.*, 2014; Heroult *et al.*, 2014; John and Langer, 2014; López-Heras, Madrid and Cámara, 2014; Meisterjahn *et al.*, 2014; Grombe *et al.*, 2014; Chekli *et al.*, 2015; Artiaga *et al.*, 2015; Astefanei *et al.*, 2015; Zhou and Guo, 2015; Nguyen, Liu and Hackley, 2015; Saenmuangchin *et al.*, 2015; Sitar *et al.*, 2015; Barahona *et al.*, 2015; Tsai *et al.*, 2015; Vežočník *et al.*, 2015; Wagner *et al.*, 2015; Jang, Lee and Hwang, 2015; Omar *et al.*, 2016; Safenkova *et al.*, 2016; Sánchez-García *et al.*, 2016; Huynh *et al.*, 2016; Lee *et al.*, 2016; Gigault *et al.*, 2017; Hetzer *et al.*, 2017; Perez-Rea, Zielke and Nilsson, 2017; Sogne *et al.*, 2017; Kim *et al.*, 2018; Correia and Loeschner, 2018; Correia *et al.*, 2018; de la Calle *et al.*, 2018; Duthen *et al.*, 2018; Sikder *et al.*, 2019; Abbate *et al.*, 2019; Abdolapur Monikh *et al.*, 2019; Caputo *et al.*, 2019; Amde, Tan and Liu, 2019; Davranche *et al.*, 2019; Fuentes *et al.*, 2019; Guo, Li, *et al.*, 2019; Guo, Wang, *et al.*, 2019; Loosli, Zebang Yi, *et al.*, 2019; Loosli, Zebang Yi, *et al.*, 2019; López-Sanz *et al.*, 2019; Moens *et al.*, 2019; Motellier *et al.*, 2019; Nwoko *et al.*, 2019; Geiss *et al.*, 2019; Yu *et al.*, 2019; Zhang *et al.*, 2019; Sánchez-Cachero *et al.*, 2020; Bocca, Battistini and Petrucci, 2020; Ferreira *et al.*, 2020; Halabi *et al.*, 2020; Hu, Crist and Clogston, 2020; Itabashi *et al.*, 2020; Klein *et al.*, 2020; Maknun, Sumranjit and Siripinyanond, 2020; Ojeda *et al.*, 2020; Pascotto *et al.*, 2020; Bohsen *et al.*, 2020; Barber *et al.*, 2020; Tadjiki, Chittleborough and Beckett, 2020; Velimirovic, Wagner, Koeber, *et al.*, 2020; Velimirovic, Wagner, Monikh, *et al.*, 2020; Voss *et al.*, 2020; Yi *et al.*, 2020; Sánchez-Cachero *et al.*, 2021; Corps Ricardo *et al.*, 2021; Marassi *et al.*, 2021; Nabi *et al.*, 2021)

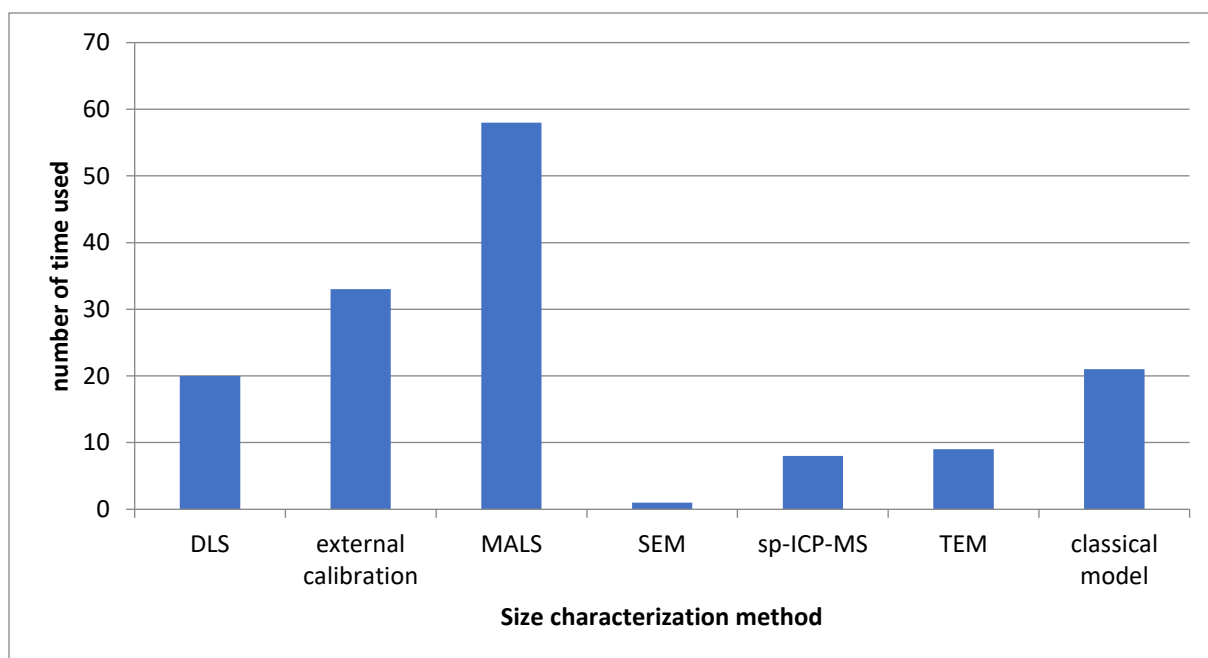


Figure 30. Size characterization methods used with the AF4

Scope of the work

Literature shows that the retention models existing today are not always adequate to describe the particle elution behaviour in the AF4 channel. The different chemical nature, the coating type, the membrane characteristics (material, cut-off and zeta potential) or the particle shape are examples of factors that may affect the retention and the recovery rate of the sample.

In order to represent more accurately the different phenomena in the channel and to give a precise estimation of the particle size, the classical model should be improved. This is the general idea of the thesis. The focus will be on the evaluation of the interactions between the particles and the accumulation wall following the footsteps of Williams and Hansen which firstly proposed to include the particle-wall interactions, using different approaches, empiric and theoretical. If the theoretical approach has been previously described by these authors, the applicability of the δ_w model and p-w model to the AF4 will be evaluated in this work. Best-developed model will be then validated through the evaluation of the method performances, including the assessment of the uncertainty and the metrological traceability of the results.

References

- Abbate, R. A. *et al.* (2019) 'Asymmetric flow field flow fractionation for the investigation of caseins cross-linked by microbial transglutaminase', *Food Hydrocolloids*, 92, pp. 117–124. doi: 10.1016/j.foodhyd.2019.01.043.
- Abdolahpur Monikh, F. *et al.* (2019) 'Development of methods for extraction and analytical characterization of carbon-based nanomaterials (nanoplastics and carbon nanotubes) in biological and environmental matrices by asymmetrical flow field-flow fractionation', *Environmental Pollution*, 255, p. 113304. doi: 10.1016/j.envpol.2019.113304.
- Alfi, M. and Park, J. (2014) 'Theoretical analysis of the local orientation effect and the lift-hyperlayer mode of rodlike particles in field-flow fractionation', *Journal of Separation Science*, 37(7), pp. 876–883. doi: 10.1002/jssc.201300902.
- Amde, M., Tan, Z. Q. and Liu, J. (2019) 'Separation and size characterization of zinc oxide nanoparticles in environmental waters using asymmetrical flow field-flow fractionation', *Talanta*, 200, pp. 357–365. doi: 10.1016/j.talanta.2019.03.074.
- Artiaga, G. *et al.* (2015) 'Migration and characterisation of nanosilver from food containers by AF4-ICP-MS', *Food Chemistry*, 166, pp. 76–85. doi: 10.1016/j.foodchem.2014.05.139.
- Astefanei, A. *et al.* (2015) 'Aggregation behavior of fullerenes in aqueous solutions: a capillary electrophoresis and asymmetric flow field-flow fractionation study', *Analytical and Bioanalytical Chemistry*, 407, pp. 8035–8045. doi: 10.1007/s00216-015-8976-8.
- Baalousha, M. *et al.* (2006) 'Size fractionation and characterization of natural colloids by flow-field flow fractionation coupled to multi-angle laser light scattering', *Journal of Chromatography A*, 1104, pp. 272–281. doi: 10.1016/j.chroma.2005.11.095.
- Baalousha, M. and Lead, J. R. (2012) 'Rationalizing nanomaterial sizes measured by atomic force microscopy, flow field-flow fractionation, and dynamic light scattering: Sample preparation, polydispersity, and particle structure', *Environmental Science and Technology*, 46(11), pp. 6134–6142. doi: 10.1021/es301167x.
- Bae, J. *et al.* (2012) 'Application of flow field-flow fractionation (FIFFF) for size characterization of carbon black particles in ink', *Microchemical Journal*, 104, pp. 44–48. doi:

10.1016/j.microc.2012.04.007.

Barahona, F. *et al.* (2015) ‘Simultaneous determination of size and quantification of silica nanoparticles by asymmetric flow field-flow fractionation coupled to ICPMS using silica nanoparticles standards’, *Analytical Chemistry*, 87(5), pp. 3039–3047. doi: 10.1021/ac504698j.

Barber, A. *et al.* (2020) ‘Coupling single particle ICP-MS with field-flow fractionation for characterizing metal nanoparticles contained in nanoplastic colloids’, *Environmental Science: Nano*, 7(2), pp. 514–524. doi: 10.1039/c9en00637k.

Beckett, R. and Giddings, J. C. (1997) ‘Entropic contribution to the retention of nonspherical particles in field-flow fractionation’, *Journal of Colloid and Interface Science*, 186(1), pp. 53–59. doi: 10.1006/jcis.1996.4612.

Bendixen, N. *et al.* (2014) ‘Membrane-particle interactions in an asymmetric flow field flow fractionation channel studied with titanium dioxide nanoparticles’, *Journal of Chromatography A*, 1334, pp. 92–100. doi: 10.1016/j.chroma.2014.01.066.

Bocca, B., Battistini, B. and Petrucci, F. (2020) ‘Talanta Silver and gold nanoparticles characterization by SP-ICP-MS and AF4-FFF-MALS-UV-ICP-MS in human samples used for biomonitoring’, *Talanta*, 220(May), p. 121404. doi: 10.1016/j.talanta.2020.121404.

Bohsen, M. S. *et al.* (2020) ‘(Sub)micron particles forming in aqueous dispersions of amorphous solid dispersions of the poorly soluble drug ABT-199: A combined particle optical counting and field-flow fractionation study’, *European Journal of Pharmaceutical Sciences*, 154(June), p. 105497. doi: 10.1016/j.ejps.2020.105497.

Bolea, E. *et al.* (2011a) ‘Size characterization and quantification of silver nanoparticles by asymmetric flow field-flow fractionation coupled with inductively coupled plasma mass spectrometry’, *Analytical and Bioanalytical Chemistry*, 401(9), pp. 2723–2732. doi: 10.1007/s00216-011-5201-2.

Bolea, E. *et al.* (2011b) ‘Size characterization and quantification of silver nanoparticles by asymmetric flow field-flow fractionation coupled with inductively coupled plasma mass spectrometry’, *Analytical and Bioanalytical Chemistry*, 401(9), pp. 2723–2732. doi: 10.1007/s00216-011-5201-2.

Calzolari, L. *et al.* (2011) 'Separation and characterization of gold nanoparticle mixtures by flow-field-flow fractionation', *Journal of Chromatography A*, 1218(27), pp. 4234–4239. doi: 10.1016/j.chroma.2011.01.017.

Caputo, F. *et al.* (2019) 'Measuring Particle Size Distribution by Asymmetric Flow Field Flow Fractionation: A Powerful Method for the Preclinical Characterization of Lipid-Based Nanoparticles', *Molecular Pharmaceutics*, 16(2), pp. 756–767. doi: 10.1021/acs.molpharmaceut.8b01033.

Caputo, F. *et al.* (2021) 'Measuring particle size distribution and mass concentration of nanoplastics and microplastics: addressing some analytical challenges in the sub-micron size range', *Journal of Colloid and Interface Science*, 588, pp. 401–417. doi: 10.1016/j.jcis.2020.12.039.

Chekli, L. *et al.* (2015) 'Agglomeration behaviour of titanium dioxide nanoparticles in river waters: A multi-method approach combining light scattering and field-flow fractionation techniques', *Journal of Environmental Management*, 159, pp. 135–142. doi: 10.1016/j.jenvman.2015.05.011.

Cho, T. J. and Hackley, V. A. (2010) 'Fractionation and characterization of gold nanoparticles in aqueous solution: Asymmetric-flow field flow fractionation with MALS, DLS, and UV-Vis detection', *Analytical and Bioanalytical Chemistry*, 398(5), pp. 2003–2018. doi: 10.1007/s00216-010-4133-6.

Chuan, Y. P. *et al.* (2008) 'Quantitative analysis of virus-like particle size and distribution by field-flow fractionation', *Biotechnology and Bioengineering*, 99(6), pp. 1425–1433. doi: 10.1002/bit.21710.

Corps Ricardo, A. I. *et al.* (2021) 'Screening-confirmation strategy for nanomaterials involving spectroscopic analytical techniques and its application to the control of silver nanoparticles in pastry samples', *Spectrochimica Acta - Part A: Molecular and Biomolecular Spectroscopy*, 246. doi: 10.1016/j.saa.2020.119015.

Correia, M. *et al.* (2018) 'Challenges in determining the size distribution of nanoparticles in consumer products by asymmetric flow field-flow fractionation coupled to inductively coupled plasma-mass spectrometry: The example of Al_2O_3 , TiO_2 , and SiO_2 nanoparticles in toothpaste', *Separations*, 5(4). doi: 10.3390/separations5040056.

- Correia, M. and Loeschner, K. (2018) 'Detection of nanoplastics in food by asymmetric flow field-flow fractionation coupled to multi-angle light scattering: possibilities, challenges and analytical limitations', *Analytical and Bioanalytical Chemistry*, 410(22), pp. 5603–5615. doi: 10.1007/s00216-018-0919-8.
- Davranche, M. *et al.* (2019) 'Are nanoplastics able to bind significant amount of metals? The lead example', *Environmental Pollution*, 249, pp. 940–948. doi: 10.1016/j.envpol.2019.03.087.
- Dubascoux, S. *et al.* (2008) 'Optimisation of asymmetrical flow field flow fractionation for environmental nanoparticles separation', *Journal of Chromatography A*, 1206(2), pp. 160–165. doi: 10.1016/j.chroma.2008.07.032.
- Duthen, S. *et al.* (2018) 'Physicochemical characterization and study of molar mass of industrial gelatins by AsFIFFFUV/ MALS and chemometric approach', *PLoS ONE*, 13(10), pp. 1–14. doi: 10.1371/journal.pone.0203595.
- Ferreira, H. S. *et al.* (2020) 'Capabilities of asymmetrical flow field – Flow fractionation on-line coupled to different detectors for characterization of water-stabilized quantum dots bioconjugated to biomolecules', *Talanta*, 206(July 2019), p. 120228. doi: 10.1016/j.talanta.2019.120228.
- Fraunhofer, W. and Winter, G. (2004) 'The use of asymmetrical flow field-flow fractionation in pharmaceutics and biopharmaceutics', *European Journal of Pharmaceutics and Biopharmaceutics*, 58(2), pp. 369–383. doi: 10.1016/j.ejpb.2004.03.034.
- Fuentes, C. *et al.* (2019) 'Characterization of molecular properties of wheat starch from three different types of breads using asymmetric flow field-flow fractionation (AF4)', *Food Chemistry*, 298(June). doi: 10.1016/j.foodchem.2019.125090.
- Gale, B. K. and Srinivas, M. (2005) 'Cyclical electrical field flow fractionation', *Electrophoresis*, 26(9), pp. 1623–1632. doi: 10.1002/elps.200410296.
- Geisler, M. and Lederer, A. (2020) 'Non-Parabolicity correction for fifty-nine solvents and a retention study for strongly distorted flow-profiles in thermal field-flow fractionation', *Journal of Chromatography A*, 1621. doi: 10.1016/j.chroma.2020.461082.
- Geiss, O. *et al.* (2013) 'Size and mass determination of silver nanoparticles in an aqueous matrix

using asymmetric flow field flow fractionation coupled to inductively coupled plasma mass spectrometer and ultraviolet-visible detectors', *Journal of Chromatography A*, 1321, pp. 100–108. doi: 10.1016/j.chroma.2013.10.060.

Geiss, O. *et al.* (2019) 'Challenges in isolating silica particles from organic food matrices with microwave-assisted acidic digestion', *Analytical and Bioanalytical Chemistry*, 411(22), pp. 5817–5831. doi: 10.1007/s00216-019-01964-2.

Giddings, J. C. (1966) 'A New Separation Concept Based on a Coupling of Concentration and Flow Nonuniformities', *Separation Science*, 1(1), pp. 123–125. doi: 10.1080/01496396608049439.

Giddings, J. C. (1973) 'The Conceptual basis of field flow fractionation', *journal of chemical education*, 50(10), pp. 667–669.

Giddings, J. C. (1978) 'Displacement and Dispersion of Particles of Finite Size in Flow Channels with Lateral Forces. Field-Flow Fractionation and Hydrodynamic Chromatography', *Separation Science and Technology*, 13(3), pp. 241–254. doi: 10.1080/01496397808060222.

Giddings, J. C. *et al.* (1979) 'Flow Programmed Field-Flow Fractionation', *Analytical Chemistry*, 51(1), pp. 30–33. doi: 10.1021/ac50037a015.

Giddings, J. C. (1986) 'Cyclical-Field Field-Flow Fractionation: A New Method Based on Transport Rates', *Analytical Chemistry*, 58(9), pp. 2052–2056. doi: 10.1021/ac00122a027.

Giddings, J. C. and Schure, M. R. (1987) 'Theoretical analysis of edge effects in field-flow fractionation', *Chemical Engineering Science*, 42(6), pp. 1471–1479. doi: 10.1016/0009-2509(87)85019-4.

Giddings, J. C., Yang, F. J. and Myers, M. N. (1976) 'Theoretical and Experimental Characterization of Flow Field-Flow Fractionation', *Analytical Chemistry*, 48(8), pp. 1126–1132. doi: 10.1021/ac50002a016.

Gigault, J. *et al.* (2013) 'Gold nanorod separation and characterization by asymmetric-flow field flow fractionation with UV-Vis detection', *Analytical and Bioanalytical Chemistry*, 405(4), pp. 1191–1202. doi: 10.1007/s00216-012-6547-9.

Gigault, J., Nguyen, T. M., *et al.* (2014) 'Accurate determination of the size distribution for

polydisperse, cationic metallic nanomaterials by asymmetric-flow field flow fractionation', *Journal of Nanoparticle Research*, 16(11). doi: 10.1007/s11051-014-2735-1.

Gigault, J., Pettibone, J. M., *et al.* (2014) 'Rational strategy for characterization of nanoscale particles by asymmetric-flow field flow fractionation: A tutorial', *Analytica Chimica Acta*, 809, pp. 9–24. doi: 10.1016/j.aca.2013.11.021.

Gigault, J. *et al.* (2017) 'Asymmetrical flow field flow fractionation methods to characterize submicron particles: application to carbon-based aggregates and nanoplastics', *Analytical and Bioanalytical Chemistry*, 409(29), pp. 6761–6769. doi: 10.1007/s00216-017-0629-7.

Gigault, J. and Hackley, V. A. (2013) 'Observation of size-independent effects in nanoparticle retention behavior during asymmetric-flow field-flow fractionation', *Analytical and Bioanalytical Chemistry*, 405(19), pp. 6251–6258. doi: 10.1007/s00216-013-7055-2.

Granger, J. *et al.* (1986) 'Flow and diffusion of particles in a channel with one porous wall: polarization chromatography', (1974).

Grasso, D. *et al.* (2002) 'A review of non DLVO interactions in environmental colloidal systems', *Reviews in Environmental Science & Biotechnology*, 97(1), pp. 17–38. doi: 10.1023/A.

Grombe, R. *et al.* (2014) 'Production of reference materials for the detection and size determination of silica nanoparticles in tomato soup Characterisation of Nanomaterials in Biological Samples', *Analytical and Bioanalytical Chemistry*, 406(16), pp. 3895–3907. doi: 10.1007/s00216-013-7554-1.

Guo, P., Li, Y., *et al.* (2019) 'Study on structure-function of starch by asymmetrical flow field-flow fractionation coupled with multiple detectors: A review', *Carbohydrate Polymers*, 226(August). doi: 10.1016/j.carbpol.2019.115330.

Guo, P., Wang, W., *et al.* (2019) 'Ultrasound-assisted dissolution and characterization of maize starch using asymmetrical flow field-flow fractionation coupled with multiple detectors', *Microchemical Journal*, 150(June), p. 104092. doi: 10.1016/j.microc.2019.104092.

El Hadri, H. *et al.* (2014) 'Optimization of flow field-flow fractionation for the characterization of natural colloids Field-Flow Fractionation', *Analytical and Bioanalytical Chemistry*, 406(6),

pp. 1639–1649. doi: 10.1007/s00216-013-7369-0.

Hagendorfer, H. *et al.* (2011) ‘Application of an asymmetric flow field flow fractionation multi-detector approach for metallic engineered nanoparticle characterization - Prospects and limitations demonstrated on Au nanoparticles’, *Analytica Chimica Acta*, 706(2), pp. 367–378. doi: 10.1016/j.aca.2011.08.014.

Håkansson, A. *et al.* (2012) ‘Hydrodynamic radius determination with asymmetrical flow field-flow fractionation using decaying cross-flows. Part I. A theoretical approach’, *Journal of Chromatography A*, 1253, pp. 120–126. doi: 10.1016/j.chroma.2012.07.029.

Halabi, A. *et al.* (2020) ‘Structural characterization of heat-induced protein aggregates in model infant milk formulas’, *Food Hydrocolloids*, 107(December 2019). doi: 10.1016/j.foodhyd.2020.105928.

Hansen, M. E. and Giddings, J. C. (1989) ‘Retention Perturbations Due to Particle–Wall Interactions in Sedimentation Field-Flow Fractionation’, *Analytical Chemistry*, 61(8), pp. 811–819. doi: 10.1021/ac00183a006.

Hansen, M. E., Giddings, J. C. and Beckett, R. (1989) ‘Colloid characterization by sedimentation field-flow fractionation. VI. Perturbations due to overloading and electrostatic repulsion’, *Journal of Colloid And Interface Science*, 132(2), pp. 300–312. doi: 10.1016/0021-9797(89)90245-2.

Heroult, J. *et al.* (2014) ‘The potential of asymmetric flow field-flow fractionation hyphenated to multiple detectors for the quantification and size estimation of silica nanoparticles in a food matrix Characterisation of Nanomaterials in Biological Samples’, *Analytical and Bioanalytical Chemistry*, 406(16), pp. 3919–3927. doi: 10.1007/s00216-014-7831-7.

Hetzer, B. *et al.* (2017) ‘Online-coupling of AF4 and single particle-ICP-MS as an analytical approach for the selective detection of nanosilver release from model food packaging films into food simulants’, *Food Control*, 80, pp. 113–124. doi: 10.1016/j.foodcont.2017.04.040.

Hovingh, M. E., Thompson, G. H. and Giddings, J. C. (1970) ‘Column Parameters in Thermal Field-Flow Fractionation’, *Analytical Chemistry*, 42(2), pp. 195–203. doi: 10.1021/ac60284a003.

Hu, Y., Crist, R. M. and Clogston, J. D. (2020) 'The utility of asymmetric flow field-flow fractionation for preclinical characterization of nanomedicines', *Analytical and Bioanalytical Chemistry*, 412(2), pp. 425–438. doi: 10.1007/s00216-019-02252-9.

Hupfeld, S. *et al.* (2010) 'Liposome fractionation and size analysis by asymmetrical flow field-flow fractionation/multi-angle light scattering: influence of ionic strength and osmotic pressure of the carrier liquid', *Chemistry and Physics of Lipids*, 163(2), pp. 141–147. doi: 10.1016/j.chemphyslip.2009.10.009.

Hupfeld, S., Ausbacher, D. and Brandl, M. (2009) 'Asymmetric flow field-flow fractionation of liposomes: Optimization of fractionation variables', *Journal of Separation Science*, 32(9), pp. 1465–1470. doi: 10.1002/jssc.200800626.

Huynh, K. A. *et al.* (2016) 'Detection and Quantification of Silver Nanoparticles at Environmentally Relevant Concentrations Using Asymmetric Flow Field-Flow Fractionation Online with Single Particle Inductively Coupled Plasma Mass Spectrometry', *Analytical Chemistry*, 88(9), pp. 4909–4916. doi: 10.1021/acs.analchem.6b00764.

Itabashi, D. *et al.* (2020) 'Determination of size distribution of nanoparticles using asymmetric flow field-flow fractionation (AF4)', *ISIJ International*, 60(5), pp. 979–987. doi: 10.2355/isijinternational.ISIJINT-2019-387.

Jang, M. H., Lee, S. and Hwang, Y. S. (2015) 'Characterization of silver nanoparticles under environmentally relevant conditions using asymmetrical flow field-flow fractionation (AF4)', *PLoS ONE*, 10(11). doi: 10.1371/journal.pone.0143149.

John, C. and Langer, K. (2014) 'Asymmetrical flow field-flow fractionation for human serum albumin based nanoparticle characterisation and a deeper insight into particle formation processes', *Journal of Chromatography A*, 1346, pp. 97–106. doi: 10.1016/j.chroma.2014.04.048.

Kammer, F. V.D., Baborowski, M. and Friese, K. (2005) 'Field-flow fractionation coupled to multi-angle laser light scattering detectors: Applicability and analytical benefits for the analysis of environmental colloids', *Analytica Chimica Acta*, 552(1–2), pp. 166–174. doi: 10.1016/j.aca.2005.07.049.

Kammer, F. von der *et al.* (2011) 'Separation and characterization of nanoparticles in complex

food and environmental samples by field-flow fractionation', *TrAC - Trends in Analytical Chemistry*, 30(3), pp. 425–436. doi: 10.1016/j.trac.2010.11.012.

Kato, H. *et al.* (2012) 'Accurate Size and Size-Distribution Determination of Polystyrene Latex Nanoparticles in Aqueous Medium Using Dynamic Light Scattering and Asymmetrical Flow Field Flow Fractionation with Multi-Angle Light Scattering', *Nanomaterials*, 2(1), pp. 15–30. doi: 10.3390/nano2010015.

Kato, H. *et al.* (2018) 'Separation of different-sized silica nanoparticles using asymmetric flow field-flow fractionation by control of the Debye length of the particles with the addition of electrolyte molecules', *Colloids and Surfaces A: Physicochemical and Engineering Aspects*, 538(October 2017), pp. 678–685. doi: 10.1016/j.colsurfa.2017.11.067.

Kim, S. T., Rah, K. and Lee, S. (2012) 'Effect of surfactant on retention behaviors of polystyrene latex particles in sedimentation field-flow fractionation: Effective boundary slip model approach', *Langmuir*, 28(29), pp. 10672–10681. doi: 10.1021/la301593b.

Kim, W. *et al.* (2018) 'Study on dispersibility of thermally stable carbon black particles in ink using asymmetric flow field-flow fractionation (AsFIFFF)', *Microchemical Journal*, 142(June), pp. 167–174. doi: 10.1016/j.microc.2018.06.035.

Kim, W. S. *et al.* (1999) 'Size determination of diesel soot particles using flow and sedimentation field-flow fractionation', *Analytical Chemistry*, 71(15), pp. 3265–3272. doi: 10.1021/ac990048z.

Klein, M. *et al.* (2020) 'Advanced nanomedicine characterization by DLS and AF4-UV-MALS: Application to a HIV nanovaccine', *Journal of Pharmaceutical and Biomedical Analysis*, 179. doi: 10.1016/j.jpba.2019.113017.

Kowalkowski, T., Sugajski, M. and Buszewski, B. (2018) 'Impact of Ionic Strength of Carrier Liquid on Recovery in Flow Field-Flow Fractionation', *Chromatographia*, 81(8), pp. 1213–1218. doi: 10.1007/s10337-018-3551-z.

de la Calle, I. *et al.* (2018) 'Study of the presence of micro- and nanoparticles in drinks and foods by multiple analytical techniques', *Food Chemistry*, 266(November 2017), pp. 133–145. doi: 10.1016/j.foodchem.2018.05.107.

- Lee, W. C. *et al.* (2016) 'Optimisation, evaluation and application of asymmetrical flow field-flow fractionation with single particle inductively coupled plasma mass spectrometry (SP-ICP-MS) to characterise silver nanoparticles in environmental media', *Microchemical Journal*, 129, pp. 219–230. doi: 10.1016/j.microc.2016.06.030.
- Litzén, A. (1993) 'Separation Speed, Retention, and Dispersion in Asymmetrical Flow Field-Flow Fractionation as Functions of Channel Dimensions and Flow Rates', *Analytical Chemistry*, 65(4), pp. 461–470. doi: 10.1021/ac00052a025.
- Litzén, A. and Wahlund, K. G. (1991a) 'Effects of temperature, carrier composition and sample load in asymmetrical flow field-flow fractionation', *Journal of Chromatography A*, 548(C), pp. 393–406. doi: 10.1016/S0021-9673(01)88622-2.
- Litzén, A. and Wahlund, K. G. (1991b) 'Zone Broadening and Dilution in Rectangular and Trapezoidal Asymmetrical Flow Field-Flow Fractionation Channels', *Analytical Chemistry*, 63(10), pp. 1001–1007. doi: 10.1021/ac00010a013.
- Loeschner, K., Navratilova, J., Købler, C., *et al.* (2013) 'Detection and characterization of silver nanoparticles in chicken meat by asymmetric flow field flow fractionation with detection by conventional or single particle ICP-MS', *Analytical and Bioanalytical Chemistry*, 405(25), pp. 8185–8195. doi: 10.1007/s00216-013-7228-z.
- Loeschner, K., Navratilova, J., Legros, S., *et al.* (2013) 'Optimization and evaluation of asymmetric flow field-flow fractionation of silver nanoparticles', *Journal of Chromatography A*, 1272, pp. 116–125. doi: 10.1016/j.chroma.2012.11.053.
- Loosli, F., Yi, Z. Y., *et al.* (2019) 'Dispersion of natural nanomaterials in surface waters for better characterization of their physicochemical properties by AF4-ICP-MS-TEM', *Science of the Total Environment*, 682, pp. 663–672. doi: 10.1016/j.scitotenv.2019.05.206.
- Loosli, F., Yi, Z. Y., *et al.* (2019) 'Improved extraction efficiency of natural nanomaterials in soils to facilitate their characterization using a multimethod approach', *Science of the Total Environment*, 677, pp. 34–46. doi: 10.1016/j.scitotenv.2019.04.301.
- López-Heras, I., Madrid, Y. and Cámara, C. (2014) 'Prospects and difficulties in TiO₂ nanoparticles analysis in cosmetic and food products using asymmetrical flow field-flow fractionation hyphenated to inductively coupled plasma mass spectrometry', *Talanta*, 124, pp.

71–78. doi: 10.1016/j.talanta.2014.02.029.

López-Sanz, S. *et al.* (2019) ‘Analytical strategy based on asymmetric flow field flow fractionation hyphenated to ICP-MS and complementary techniques to study gold nanoparticles transformations in cell culture medium’, *Analytica Chimica Acta*, 1053, pp. 178–185. doi: 10.1016/j.aca.2018.11.053.

Losert, S. *et al.* (2013) ‘Membrane-particle interactions in asymmetric flow field flow fractionation (A4F)-The influence of the zeta-potential’, 1, pp. 155–158.

Maknun, L., Sumranjit, J. and Siripinyanond, A. (2020) ‘Use of flow field-flow fractionation and single particle inductively coupled plasma mass spectrometry for size determination of selenium nanoparticles in a mixture’, *RSC Advances*, 10(11), pp. 6423–6435. doi: 10.1039/c9ra07120b.

Marassi, V. *et al.* (2021) ‘Characterization of red wine native colloids by asymmetrical flow field-flow fractionation with online multidetection’, *Food Hydrocolloids*, 110(July 2020), p. 106204. doi: 10.1016/j.foodhyd.2020.106204.

Marioli, M. and Kok, W. T. (2019) ‘Recovery, overloading, and protein interactions in asymmetrical flow field-flow fractionation’, *Analytical and Bioanalytical Chemistry*, 411(11), pp. 2327–2338. doi: 10.1007/s00216-019-01673-w.

Martin, M. (1999) ‘Deviations to classical retention theory of field-flow fractionation’, *Journal of Chromatography A*, 831(1), pp. 73–87. doi: 10.1016/S0021-9673(98)00901-7.

Martin, M. and Feuillebois, F. (2003) ‘Onset of sample concentration effects on retention in field-flow fractionation’, *Journal of Separation Science*, 26(6–7), pp. 471–479. doi: 10.1002/jssc.200390063.

Meisterjahn, B. *et al.* (2014) ‘Asymmetrical flow-field-flow fractionation coupled with inductively coupled plasma mass spectrometry for the analysis of gold nanoparticles in the presence of natural nanoparticles’, *Journal of Chromatography A*, 1372, pp. 204–211. doi: 10.1016/j.chroma.2014.10.093.

Messaud, F. A. *et al.* (2009) ‘An overview on field-flow fractionation techniques and their applications in the separation and characterization of polymers’, *Progress in Polymer Science*

(Oxford), 34(4), pp. 351–368. doi: 10.1016/j.progpolymsci.2008.11.001.

Mitrano, D. M. *et al.* (2012) ‘Silver nanoparticle characterization using single particle ICP-MS (SP-ICP-MS) and asymmetrical flow field flow fractionation ICP-MS (AF4-ICP-MS)’, *Journal of Analytical Atomic Spectrometry*, 27(7), pp. 1131–1142. doi: 10.1039/c2ja30021d.

Moens, C. *et al.* (2019) ‘A systematic evaluation of Flow Field Flow Fractionation and single-particle ICP-MS to obtain the size distribution of organo-mineral iron oxyhydroxide colloids’, *Journal of Chromatography A*, 1599, pp. 203–214. doi: 10.1016/j.chroma.2019.04.032.

Monjezi, S. *et al.* (2019) ‘The shape effect on the retention behaviors of ellipsoidal particles in field-flow fractionation: Theoretical model derivation considering the steric-entropic mode’, *Journal of Chromatography A*, 1587, pp. 189–196. doi: 10.1016/j.chroma.2018.12.019.

Moon, M. H., Park, I. and Kim, Y. (1998) ‘Size characterization of liposomes by flow field-flow fractionation and photon correlation spectroscopy: Effect of ionic strength and pH of carrier solutions’, *Journal of Chromatography A*, 813(1), pp. 91–100. doi: 10.1016/S0021-9673(98)00325-2.

Mori, Y. (1994) ‘Retention behavior of colloidal dispersions in sedimentation field-flow fractionation’, *Advances in Colloid and Interface Science*, 53(C), pp. 129–140. doi: 10.1016/0001-8686(94)00220-7.

Motellier, S. *et al.* (2019) ‘On the transformation mechanism of polyethylene glycol- and citrate-coated silver nanocolloids under sunlight exposure’, *Journal of Nanoparticle Research*, 21(7). doi: 10.1007/s11051-019-4584-4.

Nabi, M. M. *et al.* (2021) ‘Concentrations and size distribution of TiO₂ and Ag engineered particles in five wastewater treatment plants in the United States’, *Science of the Total Environment*, 753, p. 142017. doi: 10.1016/j.scitotenv.2020.142017.

Neubauer, E., V.d. Kammer, F. and Hofmann, T. (2011) ‘Influence of carrier solution ionic strength and injected sample load on retention and recovery of natural nanoparticles using Flow Field-Flow Fractionation’, *Journal of Chromatography A*, 1218(38), pp. 6763–6773. doi: 10.1016/j.chroma.2011.07.010.

Nguyen, T., Liu, J. and Hackley, V. (2015) ‘Fractionation and Characterization of High Aspect

Ratio Gold Nanorods Using Asymmetric-Flow Field Flow Fractionation and Single Particle Inductively Coupled Plasma Mass Spectrometry', *Chromatography*, 2(3), pp. 422–435. doi: 10.3390/chromatography2030422.

Nickel, C. *et al.* (2021) 'Observation of interaction forces by investigation of the influence of eluent additives on the retention behavior of aqueous nanoparticle dispersions in asymmetrical flow field-flow fractionation', *Journal of Chromatography A*, 1637, p. 461840. doi: 10.1016/j.chroma.2020.461840.

Nwoko, K. C. *et al.* (2019) 'Matrix-dependent size modifications of iron oxide nanoparticles (Ferumoxytol) spiked into rat blood cells and plasma: Characterisation with TEM, AF4-UV-MALS-ICP-MS/MS and spICP-MS', *Journal of Chromatography B: Analytical Technologies in the Biomedical and Life Sciences*, 1124(March), pp. 356–365. doi: 10.1016/j.jchromb.2019.06.029.

Ojeda, D. *et al.* (2020) 'Size characterization and quantification of titanium dioxide nano- and microparticles-based products by Asymmetrical Flow Field-Flow Fractionation coupled to Dynamic Light Scattering and Inductively Coupled Plasma Mass Spectrometry', *Analytica Chimica Acta*, 1122, pp. 20–30. doi: 10.1016/j.aca.2020.04.080.

Omar, J. *et al.* (2016) 'Optimisation of asymmetric flow field-flow fractionation for the characterisation of nanoparticles in coated polydisperse TiO₂ with applications in food and feed', *Food Additives and Contaminants - Part A Chemistry, Analysis, Control, Exposure and Risk Assessment*, 33(12), pp. 1775–1784. doi: 10.1080/19440049.2016.1239031.

Park, J. and Mittal, A. (2015) 'An Improved Model for the Steric-Entropic Effect on the Retention of Rod-like Particles in Field-Flow Fractionation: Discussion of Aspect Ratio-Based Separation', *Chromatography*, 2(3), pp. 472–487. doi: 10.3390/chromatography2030472.

Pascotto, K. *et al.* (2020) 'Fractionation and characterization of polyphenolic compounds and macromolecules in red wine by asymmetrical flow field-flow fractionation', *Journal of Chromatography A*, 1629. doi: 10.1016/j.chroma.2020.461464.

Perez-Rea, D., Zielke, C. and Nilsson, L. (2017) 'Co-elution effects can influence molar mass determination of large macromolecules with asymmetric flow field-flow fractionation coupled to multiangle light scattering', *Journal of Chromatography A*, 1506, pp. 138–141. doi: 10.1016/j.chroma.2017.05.029.

Phelan, F. R. and Bauer, B. J. (2009) ‘Comparison of steric effects in the modeling of spheres and rodlike particles in field-flow fractionation’, *Chemical Engineering Science*, 64(8), pp. 1747–1758. doi: 10.1016/j.ces.2008.10.006.

Qu, H. *et al.* (2016) ‘Importance of material matching in the calibration of asymmetric flow field-flow fractionation: material specificity and nanoparticle surface coating effects on retention time’, *Journal of Nanoparticle Research*, 18(10). doi: 10.1007/s11051-016-3601-0.

Reschiglian, P., Rambaldi, D. C. and Zattoni, A. (2011) ‘Flow field-flow fractionation with multiangle light scattering detection for the analysis and characterization of functional nanoparticles’, *Analytical and Bioanalytical Chemistry*, 399(1), pp. 197–203. doi: 10.1007/s00216-010-4197-3.

Saenmuangchin, R. *et al.* (2015) ‘Separation of silver nanoparticles by hollow fiber flow field-flow fractionation: Addition of tannic acid into carrier liquid as a modifier’, *Journal of Chromatography A*, 1415, pp. 115–122. doi: 10.1016/j.chroma.2015.08.047.

Safenkova, I. V. *et al.* (2016) ‘Complex analysis of concentrated antibody-gold nanoparticle conjugates’ mixtures using asymmetric flow field-flow fractionation’, *Journal of Chromatography A*, 1477, pp. 56–63. doi: 10.1016/j.chroma.2016.11.040.

Sánchez-Cachero, A. *et al.* (2020) ‘A method based on asymmetric flow field flow fractionation hyphenated to inductively coupled plasma mass spectrometry for the monitoring of platinum nanoparticles in water samples’, *Talanta*, 222(August 2020), p. 121513. doi: 10.1016/j.talanta.2020.121513.

Sánchez-Cachero, A. *et al.* (2021) ‘A method based on asymmetric flow field flow fractionation hyphenated to inductively coupled plasma mass spectrometry for the monitoring of platinum nanoparticles in water samples’, *Talanta*, 222(April 2020), pp. 1–8. doi: 10.1016/j.talanta.2020.121513.

Sánchez-García, L. *et al.* (2016) ‘Size determination and quantification of engineered cerium oxide nanoparticles by flow field-flow fractionation coupled to inductively coupled plasma mass spectrometry’, *Journal of Chromatography A*, 1438, pp. 205–215. doi: 10.1016/j.chroma.2016.02.036.

Schimpf, M. (2000) *Field flow fractionation handbook*. Wiley Inte. Edited by M. Schimpf, K.

Caldwell, and J. C. Giddings. Wiley Interscience.

Schure, M. R. and Palkar, S. A. (2002) 'Accuracy estimation of multiangle light scattering detectors utilized for polydisperse particle characterization with field-flow fractionation techniques: A simulation study', *Analytical Chemistry*, 74(3), pp. 684–695. doi: 10.1021/ac011006p.

Schwaferts, C. *et al.* (2020) 'Nanoplastic Analysis by Online Coupling of Raman Microscopy and Field-Flow Fractionation Enabled by Optical Tweezers', *Analytical Chemistry*, 92(8), pp. 5813–5820. doi: 10.1021/acs.analchem.9b05336.

Sharma, V., Park, K. and Srinivasarao, M. (2009) 'Colloidal dispersion of gold nanorods: Historical background, optical properties, seed-mediated synthesis, shape separation and self-assembly', *Materials Science and Engineering R: Reports*, 65(1–3), pp. 1–38. doi: 10.1016/j.mser.2009.02.002.

Sikder, M. *et al.* (2019) 'Synthesis, characterization, and environmental behaviors of monodispersed platinum nanoparticles', *Journal of Colloid and Interface Science*, 540, pp. 330–341. doi: 10.1016/j.jcis.2019.01.036.

Sitar, S. *et al.* (2015) 'Size Characterization and Quantification of Exosomes by Asymmetrical-Flow Field-Flow Fractionation', *Analytical Chemistry*, 87(18), pp. 9225–9233. doi: 10.1021/acs.analchem.5b01636.

Sogne, V. *et al.* (2017) 'Investigation of zinc oxide particles in cosmetic products by means of centrifugal and asymmetrical flow field-flow fractionation', *Journal of Chromatography A*, 1515, pp. 196–208. doi: 10.1016/j.chroma.2017.07.098.

Tadjiki, S. *et al.* (2009) 'Detection, separation, and quantification of unlabeled silica nanoparticles in biological media using sedimentation field-flow fractionation', *Journal of Nanoparticle Research*, 11(4), pp. 981–988. doi: 10.1007/s11051-008-9560-3.

Tadjiki, S., Chittleborough, D. J. and Beckett, R. (2020) 'Combining centrifugal and flow field-flow fractionation with ICPAES to characterize the size and elemental composition of soil clay minerals', *Applied Clay Science*, 195(June). doi: 10.1016/j.clay.2020.105705.

Tasci, T. O., Johnson, W. P. and Gale, B. K. (2012) 'Cyclical magnetic field flow fractionation',

Journal of Applied Physics, 111(7), pp. 1–5. doi: 10.1063/1.3679156.

Tsai, D. H. *et al.* (2015) ‘Orthogonal analysis of functional gold nanoparticles for biomedical applications’, *Analytical and Bioanalytical Chemistry*, 407(28). doi: 10.1007/s00216-015-9011-9.

Velimirovic, M., Wagner, S., Monikh, F. A., *et al.* (2020) ‘Accurate quantification of TiO₂ nanoparticles in commercial sunscreens using standard materials and orthogonal particle sizing methods for verification’, *Talanta*, 215(March), p. 120921. doi: 10.1016/j.talanta.2020.120921.

Velimirovic, M., Wagner, S., Koeber, R., *et al.* (2020) ‘Intra-laboratory assessment of a method for the detection of TiO₂ nanoparticles present in sunscreens based on multi-detector asymmetrical flow field-flow fractionation’, *NanoImpact*, 19(June). doi: 10.1016/j.impact.2020.100233.

Vezočnik, V. *et al.* (2015) ‘Size fractionation and size characterization of nanoemulsions of lipid droplets and large unilamellar lipid vesicles by asymmetric-flow field-flow fractionation/multi-angle light scattering and dynamic light scattering’, *Journal of Chromatography A*, 1418, pp. 185–191. doi: 10.1016/j.chroma.2015.09.048.

Voss, L. *et al.* (2020) ‘The presence of iron oxide nanoparticles in the food pigment E172’, *Food Chemistry*, 327(March), p. 127000. doi: 10.1016/j.foodchem.2020.127000.

Wagner, S. *et al.* (2015) ‘First steps towards a generic sample preparation scheme for inorganic engineered nanoparticles in a complex matrix for detection, characterization, and quantification by asymmetric flow-field flow fractionation coupled to multi-angle light scattering and ’, *Journal of Analytical Atomic Spectrometry*, 30(6), pp. 1286–1296. doi: 10.1039/c4ja00471j.

Wahlund, K.-G. and Giddings, J. C. (1987) ‘an Asymmetrical Flow Field-Flow Fractionation Channel Having One Permeable Wall’, *Society*, (6), pp. 1332–1339.

Wahlund, K. G. (2013) ‘Flow field-flow fractionation: Critical overview’, *Journal of Chromatography A*, 1287, pp. 97–112. doi: 10.1016/j.chroma.2013.02.028.

Williams, P. S. *et al.* (1997) ‘Colloid Characterization by Sedimentation Field-Flow Fractionation: Correction for Particle–Wall Interaction’, *Analytical Chemistry*, 69(3), pp. 349–360. doi: 10.1021/ac9606012.

Williams, P. S. (2017) 'Fractionating power and outlet stream polydispersity in asymmetrical flow field-flow fractionation. Part II: programmed operation', *Analytical and Bioanalytical Chemistry*, 409(1), pp. 317–334. doi: 10.1007/s00216-016-0007-x.

Williams, P. S. and Giddings, J. C. (1994) 'Theory of Field-Programmed Field-Flow Fractionation with Corrections for Steric Effects', *Analytical Chemistry*, 66(23), pp. 4215–4228. doi: 10.1021/ac00095a017.

Williams, S. K. R., Runyon, J. R. and Ashames, A. A. (2011) 'Field-flow fractionation: Addressing the nano challenge', *Analytical Chemistry*, 83(3), pp. 634–642. doi: 10.1021/ac101759z.

Yang, J. *et al.* (2020) 'Exploring the upper particle size limit for field flow fractionation online with ICP-MS to address the challenges of water samples from the Taihu Lake', *Analytica Chimica Acta*, 1093, pp. 16–27. doi: 10.1016/j.aca.2019.09.044.

Yi, Z. *et al.* (2020) 'How to distinguish natural versus engineered nanomaterials: insights from the analysis of TiO₂ and CeO₂ in soils', *Environmental Chemistry Letters*, 18(1), pp. 215–227. doi: 10.1007/s10311-019-00926-5.

Yu, K. *et al.* (2019) 'Size-dependent adsorption of antibiotics onto nanoparticles in a field-scale wastewater treatment plant', *Environmental Pollution*, 248, pp. 1079–1087. doi: 10.1016/j.envpol.2019.02.090.

Zattoni, A. *et al.* (2009) 'Asymmetrical flow field-flow fractionation with multi-angle light scattering detection for the analysis of structured nanoparticles', *Journal of Chromatography A*, 1216(52), pp. 9106–9112. doi: 10.1016/j.chroma.2009.06.037.

Zhang, W. *et al.* (2019) 'Study on the retrogradation behavior of starch by asymmetrical flow field-flow fractionation coupled with multiple detectors', *Food Chemistry*, 277(November 2018), pp. 674–681. doi: 10.1016/j.foodchem.2018.11.033.

Zhou, Z. and Guo, L. (2015) 'A critical evaluation of an asymmetrical flow field-flow fractionation system for colloidal size characterization of natural organic matter', *Journal of Chromatography A*, 1399, pp. 53–64. doi: 10.1016/j.chroma.2015.04.035.

Chapter III:

Materials and methods

Chapter III. Materials and methods

Abstract

In this chapter, the experimental set-up used in the work has been described: the AF4 platform, and its specificity (channel thickness, retention and void time, focusing position, recovery), the principle of the zeta potential measurements for NPs standards and for the membranes, as well as SEM equipment used for NPs standard size characterization. The NPs standards used throughout the work have been described and their characterisation in size was discussed. Finally, the experimental approach used in the thesis on which next chapters are based on, has been described.

1. AF4-multidetector instrumentation

The experiments were realized with an AF4 system (AF2000 Postnova Analytics, Landsberg Germany) coupled to a UV detector (Shimadzu, Kyoto Japan), a differential refractive index detector (DRI) (20A, Shimadzu) and a Multiangle Laser Light Scattering (MALS) detector (DAWN HELEOS II, Wyatt Technology) (Figure 31). The MALS detector use the information from the static light scattered by nano-objects at different angles to determine their molar mass and their size (radius of gyration). The theory of light scattering is well established in literature (Chu, 2007; Thielking et al., 1995; Boren 2007) and will not be described here. Indeed, the MALS detector was mainly used to verify the average size of the standard fractionated to check the quality of the analysis, but this information has not been reported in the manuscript. In this work, the UV detector was used to measure the retention time of the analytes.



Figure 31. AF4-UV-DRI-MALS system used in this work

The wavelength of the UV detector was adjusted in function of the chemical nature of the sample analysed, values are reported in Table 7.

Table 7. UV wavelength used in function of the nature of the sample

Sample	UV wavelength [nm]
polystyrene	254
silica dioxide	254
gold	520

An analytic AF4 channel (335 mm × 60 mm) metal-free (Postnova Analytics) has been used. The **geometrical parameters of the channel** were accurately measured in LNE previous research (Wang *et al.*, 2018) and they are summarized in Table 8. The parameters were measured manually using a ruler. The uncertainty associated with the experimental measurements takes in account the parallax error, as well as the operator effect and it was evaluated to be equal to 0.5 mm.

Table 8. Geometrical parameters of the analytic AF4 channel

Channel geometry	Measured value (cm)
z_1	3.3
b_1	2.0
z_2	26.8
b_2	0.5
L	27.7

When not otherwise specified, a spacer of 350 μm was used.

Two types of **carriers** were used: solutions of ammonium nitrate, NH_4NO_3 (Sigma Aldrich) and sodium chloride, NaCl (Sigma Aldrich), prepared in ASTM Type I ultrapure water (from a Milli-Q system Q-POD Element (Millipore, USA) at a concentration ranging from 10^{-5} to 10^{-3} mol L^{-1} and filtered through a 0.1 μm RC filter (Postnova Analytics). The ionic strength has been checked by conductivity measurements with a conductivity sensor (Hach, Lognes, France). The carrier pH was adjusted for the zeta potentials measurement with solutions of ammonia, NH_3 (Prolabo) and nitric acid, HNO_3 (Prolabo) at 0.05 mol L^{-1} .

Two types of **membranes** were used: regenerated cellulose (RC) membranes and polyether sulfone membranes (PES) both of 10-kDa cut-off (Postnova Analytics). The zeta potential of the membranes was measured at 20°C, at pH between 3 and 9, under ionic strengths of 0.1 and 1 mmol L^{-1} : the principle of the method and the protocol are described in section 2.2; results are presented in chapter V, section 4.1.

In this study the outlet flow rate (Q_{out}) was fixed at 0.5 mL min^{-1} .

The **focusing conditions** have been widely studied in previous research work at LNE (Wang *et al.*, 2018) and they were set for this work as follows: inlet flow rate of 0.2 mL min^{-1} , focusing

time of 5 min, and the crossflow rate was imposed equal to the crossflow rate used in the elution step.

The crossflow rate during **elution conditions** was constant and varied in the range 0.5 - 2 mL min⁻¹.

Injectons were performed by an automatic injection valve Rheodyne (IDEX Corporation, Oak Harbor, WA) equipped with a 500 µL sample loop. The **injection volume** was equal to 60 µL for all experiments.

1.1. Determination of the effective channel thickness

Unlike other FFF techniques (sedimentation, electrical, thermal...), the AF4 employs an ultrafiltration membrane posed at the bottom of the channel to prevent the loss of the sample. However, due to the pressure applied on it, the membrane is supposed to protrude into the channel (Wahlund, 2013) (Figure 32). This protrusion changes the value of channel thickness, which is then called effective channel thickness, w_{eff} .

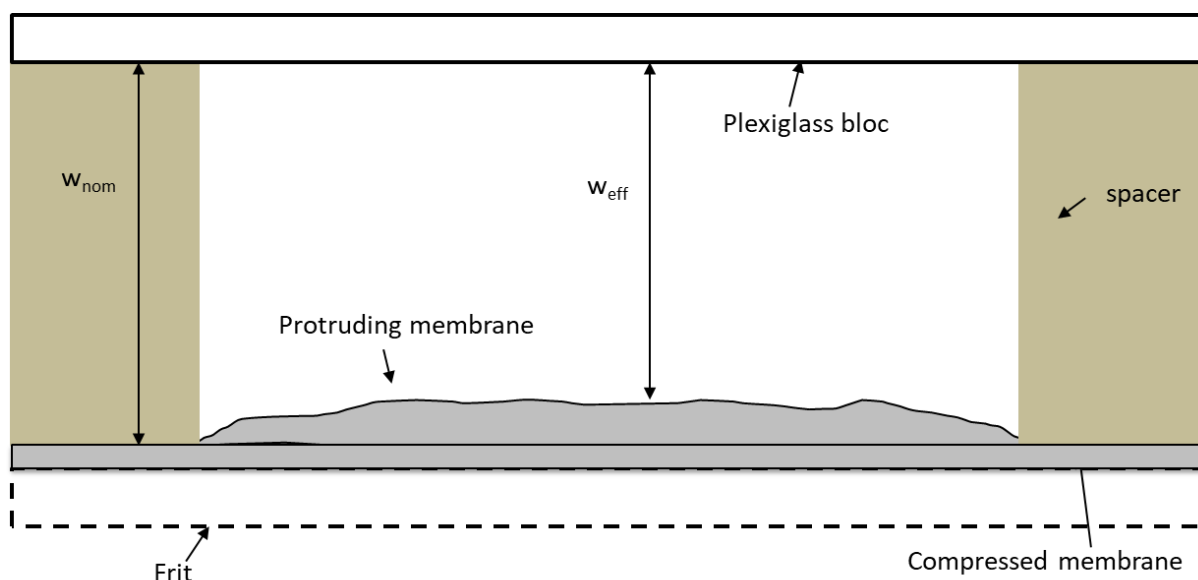


Figure 32. Effect of a protruding membrane on the channel thickness.

The effective channel thickness (w_{eff}) is a significant parameter occurring in the retention models with higher weight than the other parameters: the hydrodynamic diameter is inversely

proportional to the square of w_{eff} . Therefore, w_{eff} needs to be accurately determined when the retention models are applied for the measurement of the size.

Due to the importance of this issue for the work here performed, the accurate determination of the effective channel thickness was one of the objectives of this thesis:

- chapter VII is dedicated to the description of a new approach to experimentally determine the channel thickness;
- in chapter V (§ V.4.4) the use of calibration particle suspensions and the calculation of the thickness from the retention models have been widely discussed.

1.2. Determination of the retention time

By definition, the retention time is the mean time of the elution peak. In the case of a Gaussian peak, the retention time corresponds to the summit of the elution peak. However, the form of the fractogram in AF4 presents often a tailing, in function of the experimental conditions. Hence, it is important to determine the retention time by taking in account the real experimental form of the fractogram, using the following equation:

$$t_r = \frac{\sum s_i * t_i}{\sum s_i} \quad (III.1)$$

with s_i the intensity of the signal generated by a concentration detector at the time t_i . The concentration detector used in this study was the UV detector.

1.3. Determination of the void time

The void time correspond to the time needed for an unretained component to go through the channel (Wahlund and Giddings, 1987). The void time can be determined by two different methods. The first one consists to measure the elution of the void peak that elute just after the end of the focusing phase. The second determine the void time mathematically by using the Eq. (III.2) developed by Litzen and co-worker (Litzén and Wahlund, 1991):

$$t_0 = \frac{V^0}{Q_c} \ln \left(1 + \frac{Q_c}{Q_{out}} \left(1 - \frac{w \left(b_0 z_{foc} - \frac{b_0 - b_L}{2L} z_{foc}^2 - Y \right)}{V^0} \right) \right) \quad (III.2)$$

where b_0 and b_L are the maximum and minimum channel breadth, z_{foc} is the focus position, L is the channel length, Q_{out} the elution flow and Y the area reduction of the accumulation wall due to the tapered channel inlet (Litzén, 1993). The Figure 33 shows the different geometrical parameters used in the equation.

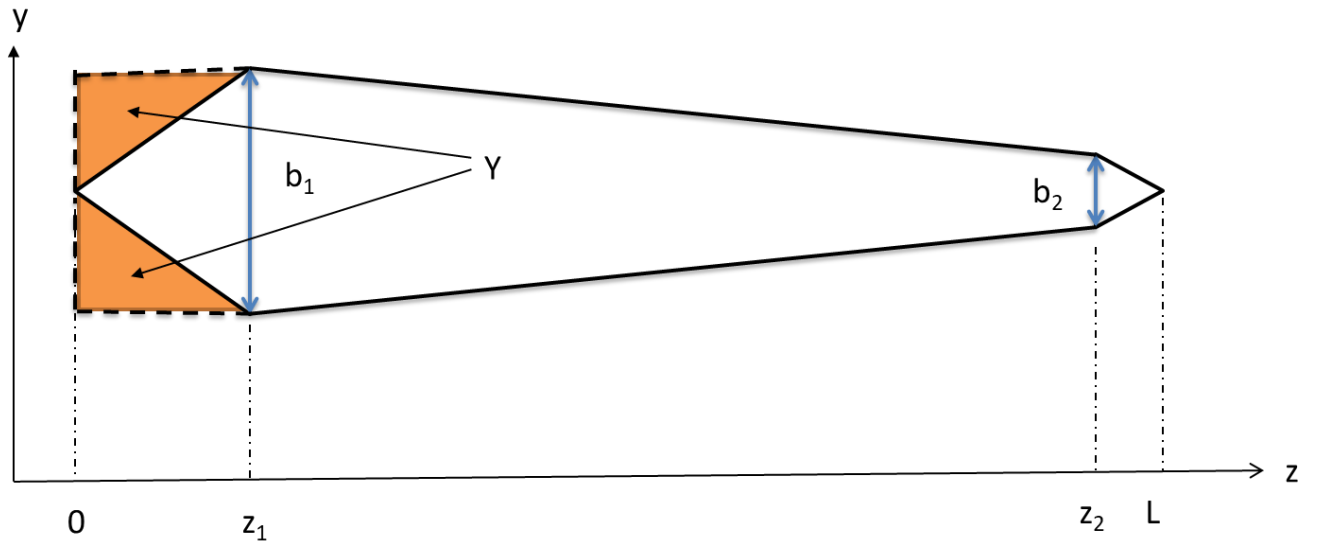


Figure 33. Geometric parameters of the AF4 channel

1.4. Determination of the focusing position

The focusing position designates the position where the particles are focused during the focusing phase. The focusing position being one of the input quantity to determine the void time, it is important to know where the particles are focused. In this work the focusing position was determined by applying Eq. (III.3) developed by Wang *et al.* in a previous work (Wang *et al.*, 2018).

$$z_{foc} = z_1 + \frac{b_1 - \sqrt{b_1^2 - 2 \left(\frac{b_1 - b_2}{z_2 - z_1} \right) \frac{Q_{in}}{Q_c} A_{tot} + b_1 z_1 \left(\frac{b_1 - b_2}{z_2 - z_1} \right)}}{\frac{b_1 - b_2}{z_2 - z_1}} \quad (III.3)$$

The validity of the equation was already demonstrated by *Wang et al.* by comparing the results given by the equation and the focusing position experimentally determined by injecting a colorant like dextran blue or ferritin in the channel and applying the focusing conditions (*Wang et al.*, 2018).

1.5. Determination of the recovery rate

The recovery rate of the analysis, $R\%$ was determined as the ratio of the sample peak area when the cross flow is applied, A_1 to the area of the sample peak obtained when no cross flow is applied, A_2 (Neubauer, V.d. Kammer and Hofmann, 2011):

$$R\% = \frac{A_1}{A_2} * 100\% \quad (III.4)$$

2. Zeta potential analyses

The zeta potential is one of the critical parameters in colloids science. Its measurement allows to predict the stability or the adsorption of particle on surfaces. The zeta potential corresponds to the electrical potential at the shear plane between the stationary layer also called Stern layer and diffuse layer of ions formed at the interface solid-liquid (*Kaszuba et al.*, 2010)(Figure 34).

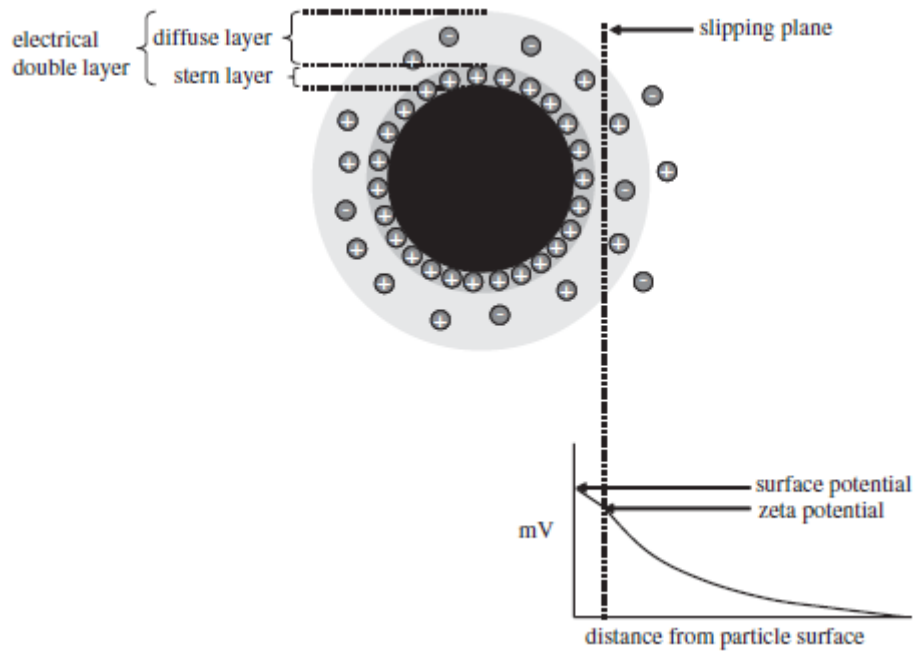


Figure 34. Model of the electric double layer at the solid-liquid interface (from Kaszuba et al. (Kaszuba *et al.*, 2010)).

The particle and membrane surface charge are two input parameters in the particle-wall model presented in chapter 2. Due to the difficulty to measure a solid surface charge, the particles and membranes surface charge needed to apply the model have been approximated by the zeta potential values determined here. This approximation was already made by Hansen et al. in their article (Hansen and Giddings, 1989) and by others authors in the literature (Martinez *et al.*, 2008).

2.1. Measurement of the zeta potential of particle suspensions

The measurement of particles zeta potential was carried out using a Zetasizer Wallis (Corduan technologies, Pessac, France): particles zeta potential is determined by using the principle of Doppler Laser electrophoresis also known as electrophoresis light scattering (ELS). The ELS is an indirect method to determine the zeta potential from the measurement of the Doppler frequency shift in scattered light (Varenne *et al.*, 2015). In ELS experiments, an electrical field is generated in the sample solution by an electrode. Particles present in the solution start moving toward the anode or the cathode depending on their charge. At the same time, a laser beam illuminate the measurement cell. Due to the presence and the movement of the particles, the frequency of the light scattered by the particles is shifted because of the Doppler effect. This frequency, called the Doppler frequency shift, f_D , is linked to the particle electrophoretic mobility, μ_e , by the following equation:

$$\mu_e = \frac{\lambda_l}{E \sin \theta_d} f_D \quad (III.5)$$

with E the electric field applied in the solution, λ the wavelength of the laser and θ_d , the angle from which the frequency shift is measured. The zeta potential, ζ , is then calculated via the electrophoretic mobility value (Varenne *et al.*, 2015) :

$$\zeta = \mu_e \frac{\eta}{\varepsilon_0 \varepsilon_r} f(\kappa, a) \quad (III.6)$$

where η is the medium viscosity, ε_0 is the vacuum permittivity, ε_r is the relative dielectric constant of the liquid and $f(\kappa, a)$ is the Henry's function which represents the force of the counter ion cloud around the particle which moves in the opposite direction compared to the particle. This phenomenon is called the electrophoretic retardation effect (Ohshima, 1996; Strubbe *et al.*, 2013). The Henry function depends on the particle radius, a , and the inverse of Debye length, κ and it varies between 1 and 1.5 depending on κ and a value.

Measurement protocol. The samples were prepared within the carrier solutions used for the AF4 experiments. The samples concentration was adjusted in order to obtain a detectable signal in the measurement cell: this adjustment was sample and medium dependent. The measurements were realized at a constant temperature of 20°C. The value of the Henry function value has been calculated by the Smoluchowski approximation which assumes that κ is smaller than a . This assumption fits well for aqueous solutions. The results of the measurement of standard NPs zeta potential are summarized in section 4.

2.2. Measurement of the zeta potential of membranes

The measurements of the membrane zeta potential were performed with a SurPASS electrokinetic analyzer (Anton Paar GmbH, Graz, Austria). This technique allows determining the zeta potential of macroscopic solids through the measurement of the streaming potential or the streaming current. When an aqueous solution streams through a capillary system, an electrical response due to the movement of the charge at the liquid-solid interface is generated. This response can be detected as a streaming potential (or as a streaming current). The device is made up of two pumps, one measurement cell, an electrical detector and a pressure detector (Figure 35). The pumps push the electrolyte through the measurement cell at a constant flow

rate and the appropriate detector, ammeter or voltmeter, measures the current or the difference of potential generated by the displacement of the interface ions (Bukšek, Luxbacher and Petrinić, 2010).

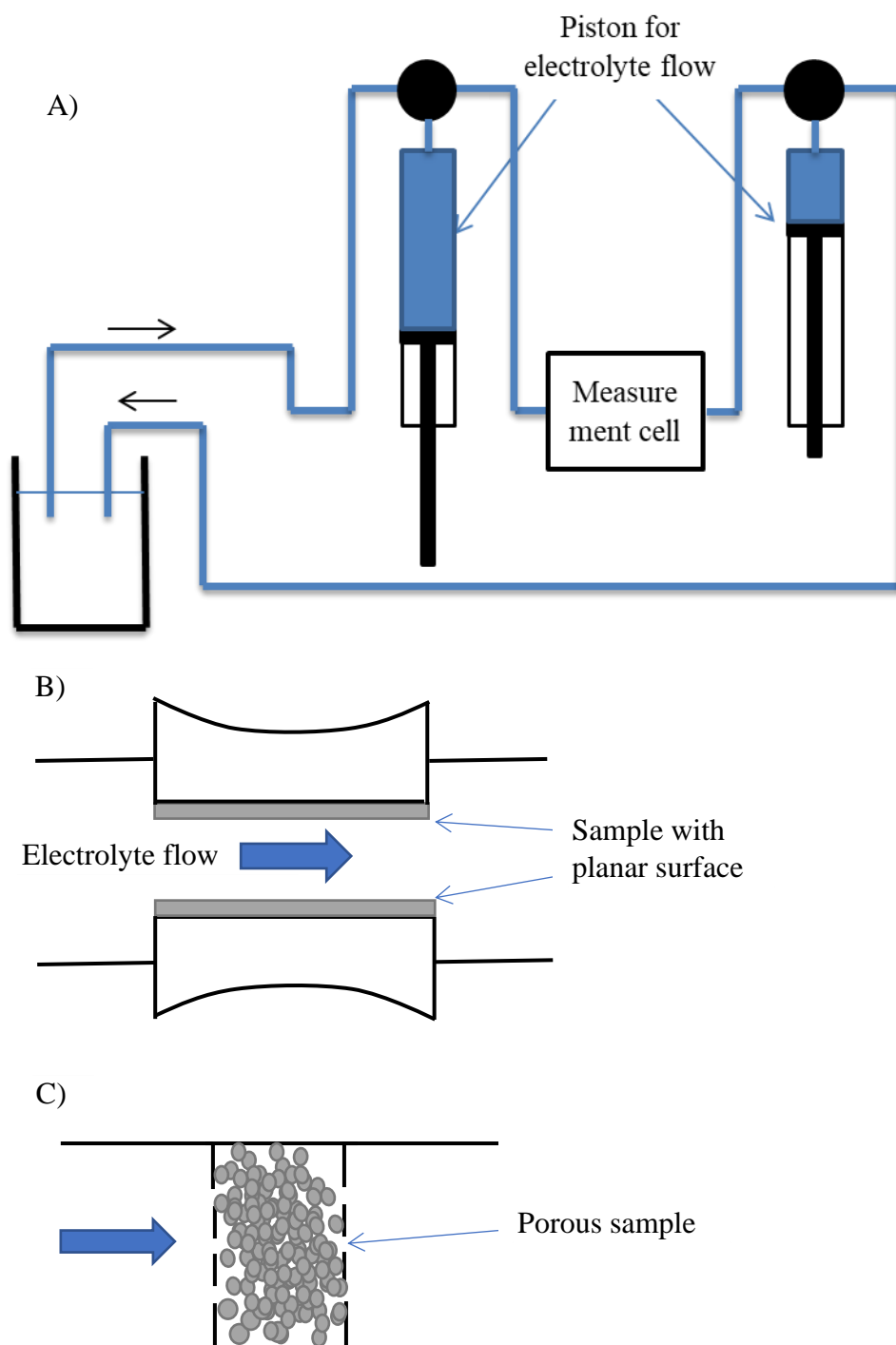


Figure 35. Scheme of the A) electrokinetic analyser and its measurement cells adapted for B) planar samples and C) samples with irregular shape (i.e. powder)

In the case of a solid sample with a planar surface (

Figure 35), the zeta potential can be determined by the two following equation (Werner *et al.*, 1999).

$$\zeta = \frac{dI_{str}}{d\Delta p} \frac{\eta}{\varepsilon_r \varepsilon_0} \frac{L}{A} \quad (III. 7)$$

with I_{str} the streaming current, Δp the difference of pressure applied, η the carrier viscosity, ε_0 the vacuum permittivity and ε_r the relative dielectric constant of the liquid. L is the length of the sample and A is the product of the sample width and the distance between the two samples pieces.

By using Ohm's law ($U = RI$) the zeta potential can be determined in function of the streaming potential:

$$\zeta = \frac{dU_{str}}{d\Delta p} \frac{\eta}{\varepsilon_r \varepsilon_0} \frac{L}{A} \frac{1}{R} \quad (III. 8)$$

where R is here the resistance inside the measurement cell.

If the dimension of the sample cannot be determined, for example in the case of a powder, the expression L/AR can be replaced by the electrolyte conductivity κ (Ribitsch *et al.*, 2001).

Measurement protocol. Two squares of membranes of 1×1cm were cut out and placed in the measurement cell. The measurements were performed with the same carriers used for AF4 experiments. The zeta potential has been measured as a function of the pH and the ionic strength. The pH of the carrier was adjusted by adding appropriate quantities of ammonia, NH_3 (0.04 mol L⁻¹) or nitric acid, HNO_3 (0.06 mol L⁻¹).

The results of the measurement of membranes and NPs zeta potential are summarized hereafter in Table 9. All the measurements were performed in a solution at pH 8.5 and 293 K. The measurement were performed for each carrier ionic strength in which the sample was exposed. Hence, only the PS and the membranes zeta potential were measured in different ionic strength. The electrokinetic analyser used to measure the membrane zeta potential required an ionic strength minimum of 0.1 mmol L⁻¹ to function therefore the membrane zeta potential when $I =$

0.01 mmol L⁻¹ was extrapolated from the measurement performed at 0.1 mmol L⁻¹ when necessary.

Table 9. Zeta potential of membranes and particles used in this work. All the measurement were performed at pH 8.5 and in a solution at 293K

Particle	Zeta potential [mV]		
	I=0.01 mmol L ⁻¹	I=0.1 mmol L ⁻¹	I=1 mmol L ⁻¹
PS20	-35±5	-30±5	-25±5
PS60	-69±3	-62±2	-59±5
PS100	-62±5	-55±2	-49±3
PS200	-55±3	-55±1	-55±2
Au20	-26±5	N/A	
Au40	-50±10		
Au60	-30±5		
Au80	-57±12		
Si80	-50±10		
Si140	-50±10		
Si200	-50±10		
Membrane			
RC 10 kDa	N/A	-51±4	-36±3
PES 10kDa		-76±2	-64±2

3. Scanning electron microscopy analyses

In order to have standards traceable to the SI for size values, the PS standards were characterised by Scanning electron microscopy (SEM) at the LNE CARMEN platform (department of material characterisation). SEM measurements were performed with a Zeiss Ultra-Plus scanning electron microscope equipped with two secondary electron detectors: SE2 and In-Lens. The SEM was calibrated by using the transfer standard P₉₀₀H₆₀ traceable to the meter unit. This standard is a plate where a succession of hole where lithographed at its surface. Each hole has a mean depth of 60nm. The holes are spaced from each other by 900 nm. A drop of suspension was slowly deposited on a silica substrate placed on a spin-coater. The drop was then dispersed on a silica substrate by making the substrate rotate on itself slowly. Three replicates

were performed. For each replicate 200 particles were measured automatically by the Platypus software (Pollen Metrology, Morians France). The mode value of the 200 measurements was then determined. The size values obtain by SEM for the PS are reported in Table 10. These value were used rather the one given by the provider.

Table 10. PS standards diameter determined by SEM

Name	diameter
PS20	$23 \pm 5 (k=1)$
PS60	$60 \pm 2 (k=1)$
PS100	$99 \pm 4 (k=1)$
PS200	$186 \pm 3 (k=1)$

4. Particle standards

The AF4 experiments were realised with polystyrene latex (PS), gold (Au) and silica dioxide (SiO₂) size standards particles. The Table 11 lists the characteristics (size and technique used by the provider to characterise the standard) and the provider of each standard, as well as the abbreviation used to name each sample thorough this work.

Table 11. Characteristics and origins of each size standard used

Name	Diameter	Technique used by the provider to characterise the sample	Provider
PS20	23±1 (k=1)	DLS	Sigma-Aldrich, Buch, Switzerland
PS60	60±2 (k=1)	TEM	
PS100	107±3 (k=1)	DCS	Thermo-Scientific, Freemont, USA
PS200	186±3 (k=1)	DCS	
Au20	19.6±1.6 (k=1)	Not given by the providers	BBI solution, Crumlin, UK
Au40	42.4±3.4 (k=1)		
Au60	60.8± 4.9 (k=1)		
Au80	80±6.4 (k=1)		
Si80	81±6 (k=1)	TEM	Nano-composix, San Diego, USA
Si140	142±16 (k=1)		
Si200	194±16 (k=1)		

Before sample injection, samples vials were shaken several times during 30 s to ensure the homogeneity of the suspension and re-suspension of any settled particles. No filtration, no US

The working solutions were prepared by diluting the stock solution in the carrier to obtain a mass concentration of 13 µg g⁻¹. All the samples were diluted in the carrier. The dilution and the injection volume were adjusted in order to have a particle mass injected lower than 1 µg. This threshold has been chosen in order to limit the interaction between particles in the channel. Samples have been stored at room temperature, protected from light, until measurements.

5. Experimental approach and method validation of AF4 method

The method performances have been evaluated in this work thorough the establishment of the repeatability, reproducibility, trueness and the uncertainty.

Several tests have been performed in order to evaluate the repeatability and reproducibility of the retention time measurement. The aim was (i) to have a first rough estimation of the uncertainty associated to this measurand to interpret the results of the study and (ii) to establish laboratory best practices taking in account the degradation of the “good-working conditions” occurring over the analyses time. Indeed, the filtration membrane in AF4 is known to age through the experiments (Hungerbühler *et al.*, 2012; Losert *et al.*, 2013). The aging is due to physical phenomena, like the analyte and salt adsorption on the membrane or the friction of the carrier on the membrane changing the membrane roughness, which results in the membrane surface alteration. In extreme cases, this alteration can modify in a non-negligible way the analyte retention time. Figure 36 illustrates this phenomenon by showing the repeatability of the elution time of a 60 nm polystyrene standard (PS60) on a new RC membrane, for a cross flow rate of 0.5 mL min^{-1} and a $10^{-4} \text{ mol L}^{-1}$ NaCl carrier. All the analyses were realized in the same sequence, in order to perform the analyses in the shortest time. It can be noticed that the PS60 retention times steadily increases as the number of analysis increase. The adsorption of Na^+ on the cellulose surface could explained this tendency as this adsorption would increase the local ionic strength which would decrease repulsion interactions occurring between the membrane and the particles and hence, increase the particle retention. The Na^+ may also reduce the membrane surface charge which allows the PS particles to come nearer the accumulation wall and consequently elute slower.

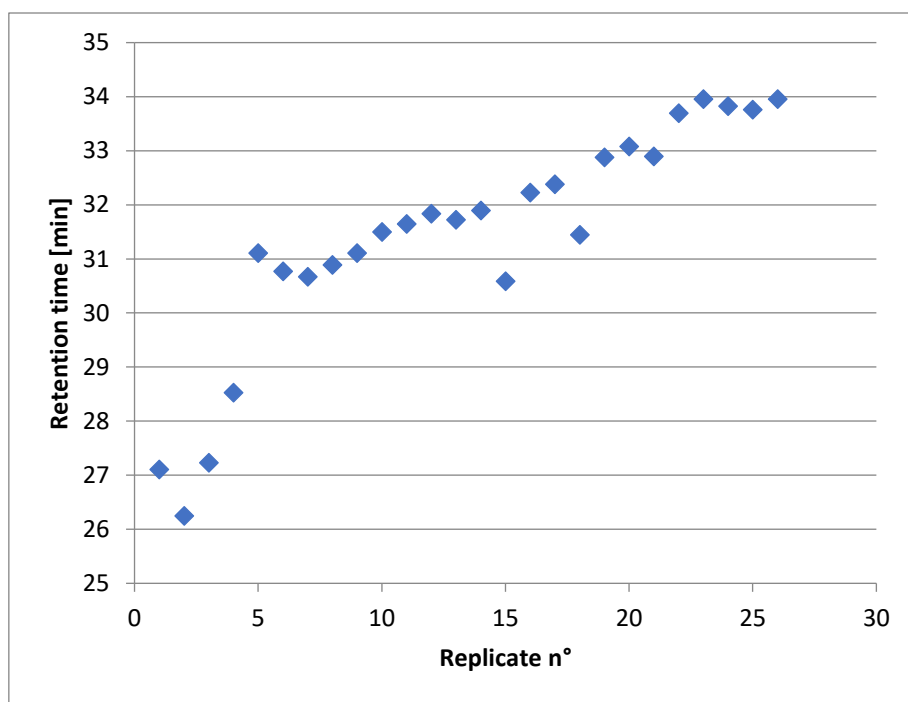



Figure 36. Retention time of the PS60 in function of the number of replicates. Carrier: NaCl 10-4mol/L; membrane: RC 10 kDa; cross flow rate and elution flow rate: 0.5mL min⁻¹.

To evaluate the **measurement repeatability** every analysis was replicated three times. However, when the membrane surface alteration is significant (Figure 36), experiments performed at the beginning of the membrane life and at the end are not reproducible. This can generate result's misinterpretation. To overcome this problem the injection sequence has been designed in order to include the membrane aging effect in the repeatability. An example is given to explain the sequence approach (Table 12). When three different cross flow rates (Q_{c1} , Q_{c2} , Q_{c3}) are tested, instead of injecting 3 times the sample using the same experimental conditions (Q_{c1}), then testing 3 times the following experimental conditions (Q_{c2}) and so on, it was preferred to test 3 times one series of experimental conditions (Q_{c1} , Q_{c2} , Q_{c3}) (Table 12). This experimental plan, by increasing the uncertainty associated to the retention time allows the comparison between two set of data acquired at different ages of the membrane. The repeatability showed in Figure 36 is an extreme case, which occurred only once on the 70 membranes used during this work. The experimental plan presented in Table 12 was used for all the analysis to prevent such cases. The typical repeatability obtained was of 0.7 min.

Table 12. Experiment planning for testing the influence of three different values of cross flow rate (Q_c) on the retention time (3 replicates): example of injection sequence used.

Analysis n°	Typical sequence		Sequence applied in this study
1	replicate 1 Q_{c1}		replicate 1 Q_{c1}
2	replicate 2 Q_{c1}		replicate 1 Q_{c2}
3	replicate 3 Q_{c1}		replicate 1 Q_{c3}
4	replicate 1 Q_{c2}		replicate 2 Q_{c1}
5	replicate 2 Q_{c2}		replicate 2 Q_{c2}
6	replicate 3 Q_{c2}		replicate 2 Q_{c3}
7	replicate 1 Q_{c3}		replicate 3 Q_{c1}
8	replicate 2 Q_{c3}		replicate 3 Q_{c2}
9	replicate 3 Q_{c3}		replicate 3 Q_{c3}
Standard deviation obtained	$u(t_r) \approx 0.2 \text{ min}$		$u(t_r) \approx 0.7 \text{ min}$

The **reproducibility** of the analyses was estimated by repeating three analyses on three new membranes and using a new suspension for each membrane. The reproducibility was determined as the standard deviation of the nine analyses. The typical reproducibility obtained was around 1.7 min.

The **trueness** of the retention models has been evaluated by comparing the diameter calculated to the reference diameter of the standards analysed. The assessment of the uncertainty was determined following the recommendation of Guide for uncertainty determination (GUM)

References

- Bukšek, H., Luxbacher, T. and Petrinič, I. (2010) 'Zeta potential determination of polymeric materials using two differently designed measuring cells of an electrokinetic analyzer', *Acta Chimica Slovenica*, 57(3), pp. 700–706.
- Hansen, M. E. and Giddings, J. C. (1989) 'Retention Perturbations Due to Particle–Wall Interactions in Sedimentation Field-Flow Fractionation', *Analytical Chemistry*, 61(8), pp. 811–819. doi: 10.1021/ac00183a006.
- Hungerbühler, K. *et al.* (2012) 'Critical aspects of sample handling for direct nanoparticle analysis and analytical challenges using asymmetric field flow fractionation in a multi-detector approach', *Journal of Analytical Atomic Spectrometry*, 27(7), p. 1120. doi: 10.1039/c2ja30024a.
- Kaszuba, M. *et al.* (2010) 'High-concentration zeta potential measurements using light-scattering techniques', *Philosophical Transactions of the Royal Society A: Mathematical, Physical and Engineering Sciences*, 368(1927), pp. 4439–4451. doi: 10.1098/rsta.2010.0175.
- Litzén, A. (1993) 'Separation Speed, Retention, and Dispersion in Asymmetrical Flow Field-Flow Fractionation as Functions of Channel Dimensions and Flow Rates', *Analytical Chemistry*, 65(4), pp. 461–470. doi: 10.1021/ac00052a025.
- Litzén, A. and Wahlund, K. G. (1991) 'Effects of temperature, carrier composition and sample load in asymmetrical flow field-flow fractionation', *Journal of Chromatography A*, 548(C), pp. 393–406. doi: 10.1016/S0021-9673(01)88622-2.
- Losert, S. *et al.* (2013) 'Membrane-particle interactions in assymetric flow field flow fractionation (A4F)-The influence of the zeta-potential', 1, pp. 155–158.
- Martinez, R. E. *et al.* (2008) 'Surface charge and zeta-potential of metabolically active and dead cyanobacteria', *Journal of Colloid and Interface Science*, 323(2), pp. 317–325. doi: 10.1016/j.jcis.2008.04.041.
- Ohshima, H. (1996) 'Henry's function for electrophoresis of a cylindrical colloidal particle', *Journal of Colloid and Interface Science*, 180(1), pp. 299–301. doi: 10.1006/jcis.1996.0305.
- Ribitsch, V. *et al.* (2001) 'The significance of surface charge and structure on the accessibility

of cellulose fibres', *Macromolecular Materials and Engineering*, 286(10), pp. 648–654. doi: 10.1002/1439-2054(20011001)286:10<648::AID-MAME648>3.0.CO;2-6.

Strubbe, F. *et al.* (2013) 'Electrophoretic retardation of colloidal particles in nonpolar liquids', *Physical Review X*, 3(2), pp. 1–9. doi: 10.1103/PhysRevX.3.021001.

Varenne, F. *et al.* (2015) 'Standardization and validation of a protocol of zeta potential measurements by electrophoretic light scattering for nanomaterial characterization', *Colloids and Surfaces A: Physicochemical and Engineering Aspects*, 486, pp. 218–231. doi: 10.1016/j.colsurfa.2015.08.044.

Wahlund, K.-G. and Giddings, J. C. (1987) 'an Asymmetrical Flow Field-Flow Fractionation Channel Having One Permeable Wall', *Society*, (6), pp. 1332–1339.

Wang, J. L. *et al.* (2018) 'Theoretical and experimental investigation of the focusing position in asymmetrical flow field-flow fractionation (AF4)', *Journal of Chromatography A*, 1561, pp. 67–75. doi: 10.1016/j.chroma.2018.04.056.

Werner, C. *et al.* (1999) 'Electrokinetic surface characterization of biomedical polymers - A survey', *Colloids and Surfaces A: Physicochemical and Engineering Aspects*, 159(2–3), pp. 519–529. doi: 10.1016/S0927-7757(99)00290-3.

Chapter IV:
**Study of the mechanism governing the
retention inside the AF4 channel and
application of the δ_w model for the
characterisation of nanoparticle
hydrodynamic diameter**

Chapter IV: Study of the mechanisms governing the retention inside the AF4 channel and application of the δ_w model for the characterisation of nanoparticle hydrodynamic diameter

Abstract:

In this first chapter about experimental results, the elution behaviour of standard particles has been studied as a function of the following parameters:

- The cross flow rate
- The channel thickness
- The standard particle size and chemical composition
- The chemical nature of the ultrafiltration membrane
- The carrier ionic strength

This study allowed to confirm that the particle chemical nature influences their retention. The carrier ionic strength was also identified as an important parameter which influence greatly the particle retention. This conclusion showed that the interactions particle-wall cannot be neglected in most experimental conditions. Therefore, conditions where the assumption concerning the non-interaction between particle and membrane may be difficult to obtain.

This study also generated a large dataset to evaluate the applicability range of the δ_w model, presented in the chapter II, that takes into account the particle-wall interactions governing the particle behaviour inside the AF4 channel. The behaviour of the semi-empirical parameter that takes into account the particles-wall interactions, δ_w , has been studied to verify if the observation made by *Williams et al.* on sub micrometric particles is also valid on nanoparticles. The model was then applied on size standard particles to test its validity as a size characterization method. This study shows that, in the experimental domain tested, the value of δ_w is independent of the standard size used to calibrate it. The δ_w model gives results close to the reference value the number of analyses required to obtain result with a small uncertainty is too important to choose as a first choice this model as a size determination technique.

1. Study of the retention behaviour of spherical nanoparticles in AF4 channel using the classical model

The first step of the work has consisted in the study of the mechanisms governing particles retention in the AF4 channel. For this purpose, the chosen approach was to use well-known standards of size of spherical shape between 20 and 200 nm in diameter to check typical experimental conditions used in AF4 and to verify if behaviours not consistent with the retention theory predictions can be observed.

In this preliminary phase the classical model (Eq. (II.9) in Chapter II) using the approximation $R=6\lambda$ was used as reference to compare the particle behaviour observed and predicted. The equation of the classical model expresses the retention time, t_r , as a function of the following parameters: the temperature of the carrier, T , the carrier viscosity, η , the particle hydrodynamic diameter, d_h , the cross flow rate and the elution flow rate, Q_c and Q_{out} , the focusing position, z_{foc} and the channel geometry. The geometry of the channel includes various parameters describing the shape of the channel (b_0 and b_L which are the maximum and minimum channel breadth, the channel length, L , the channel thickness, w , and the area reduction of the accumulation wall due to the tapered channel inlet, Y) and the channel thickness.

$$t_r = \frac{\pi\eta w^2 d_h \ln \left(1 + \frac{Q_c}{Q_{out}} \left(1 - \frac{(b_1 z_{foc} - z_{foc}^2 \frac{b_1 - b_2}{2L} - Y)}{0.5(b_1 z_2 + b_2(L - z_1))} \right) \right)}{2kT} \quad (IV.1)$$

This study was performed in aqueous carrier for a temperature of 20°C with three different kind of spacers. Therefore, the parameters that are expected to have the higher impact on the sample behaviour in the AF4 channel and, by consequence, on the retention time and recovery rate were selected. A range of variation covering commonly used experimental conditions, was attributed to each chosen parameter (Table 13). The most important parameters in Eq. (IV.1) are the **crossflow rate**, which is the field force, and the **channel thickness**. The cross flow rate was varied in the range 0.5-2 mL min⁻¹. The channel thickness is of utmost importance since (i)

it presents a higher weight than the other parameters because its square is inversely proportional to the hydrodynamic diameter; (ii) due to the membrane protrusion issue it is calculated by different indirect methods, which can induce large estimation errors. For these reasons, the strategy in this work has been to develop firstly a direct method to measure this parameter (chapter VII) and to have a value that only represents the effective channel thickness. Only after this estimation, it would be possible to study the effect of the channel thickness on the retention time in different separation conditions. The direct method not being finalised, for the sake of this preliminary work, the channel thickness has been varied to see if any deviation from the predicted behaviour by Eq. (IV.1) can be observed.

The **elution flow rate** is usually optimized with the cross flow rate to optimise the fractogram resolution and the time of the analysis. Hence this parameter is defined according to specific analytical needs (nature, size, polydispersity of the sample) and according to the system configuration (detectors coupled, backpressure in the channel), then is usually maintained constant during experiments. From a theoretical point of view, the elution flow rate influences the importance of the lift forces acting on the particles (Martin, 1999). An elution flow rate value of 0.5 mL min^{-1} was chosen as elution flow rate and kept constant for all the analyses.

The **focusing position** is a well-controlled parameter: in this work, the Eq. (III.3) has been used, validated in a previous work (Wang et al., 2018) with a managed uncertainty. During the focusing step, the inlet flow rate and the focusing time were fixed at optimized conditions; the study of their influence on the elution step was out of the scope of this work. The crossflow rate during the focusing step was imposed to be equal to the crossflow rate used in the elution step, to not perturb the concentration distribution obtained at the end of the relaxation, when the elution starts.

Geometric parameters, excluding the channel thickness, are proper to the channel rigid system and are not supposed to change over the time. Although errors can be committed in the measurement of these parameters, these systematic errors are taken in account in the uncertainty calculation.

The effect of the **temperature** was not studied since AF4 analysis need to be performed with a carrier with no temperature gradient in order to fulfil the assumption of a parabolic profile. A system to maintain the AF4 carrier temperature at the same temperature thorough the analysis would have been necessary but was not available. The laboratory room temperature is maintained in the range 19°C to 22°C throughout the year.

The working hypothesis of the FFF retention theory, described in Chapter II.2.3, were assumed as fulfilled. This can be summarized as follow: the channel is placed between two infinite parallel plates, the cross flow force is uniform in the channel, the flow profile is parabolic, the concentration profile of the sample is in steady state, and steric effects, electrostatic and van der Waals interactions are considered negligible compared to the field induced strength. Although these last effects and forces are supposed to be negligible, it is common knowledge that the carrier **ionic strength** and the **chemical nature** of the **membrane** play an important role in fractionation optimization (Ulrich *et al.*, 2012; Gigault *et al.*, 2014). Furthermore, the **chemical nature of the particle** seems also to play a role (Gigault and Hackley, 2013). Therefore, two types of membranes, the polyethersulfone (PES) and regenerated cellulose (RC) membrane have been tested, the ionic strength has been studied in the range from 10^{-7} to 10^{-3} mol L⁻¹ and different types of particles were used (Table 13). In order to reduce the particle adsorption, it is common practice to add surfactants like FL-70, tween 20, SDS or triton X in the carrier (Ulrich *et al.*, 2012). However, if their effects on the particle adsorption is clearly observed by many authors (Fraunhofer and Winter, 2004; Kim, Rah and Lee, 2012), their mechanisms is not perfectly understood. Consequently, the surfactants were not used in this work in order to simplify the system studied. All the analyses in this study were realized at the same temperature in aqueous carriers, no surfactants were added to the carrier and the maximum salt concentration used was small enough to not impact the viscosity. Hence, the influence of **the carrier viscosity** on the particle retention was not studied and the carrier viscosity was assumed to be constant for all the analyses.

Table 13. List of the parameters studied. For each parameter, the range of study or the types are given

	Parameter	Range/type
From retention model	cross flow, Q_c	0.5-2 mL min ⁻¹
	channel thickness, w	190-500 μm (nominal)
	particle size, d_h	20-200 nm
From experimental optimization	ionic strength	deionised water ($\sim 10^{-7}$)- 10^{-3} mol L ⁻¹
	membrane nature	RC, PES
	particle chemical composition	polystyrene, gold and silica dioxide

To evaluate the influence of these parameters, the variation of the retention time of particle standards has been monitored, as well as their recovery rate. The results that show an influence of the studied parameters are presented thereafter (sections 1.2, 1.3, 1.4). The channel thickness was varied in the range 190-500 μm : no relevant deviations from the behaviour expected from Eq. (1) have been highlighted.

1.1. Influence of the carrier ionic strength on the particle retention

The carrier is one of the first parameters that needs to be choose in order to perform an analysis. The salt concentration present in the carrier determines the ionic strength value, I . As I influences the magnitude of the electrostatic interactions, these interactions might have a significant impact on the particle retention time and recovery.

To evaluate the influence of the carrier ionic strength on the particle retention, polystyrene particle standards of 60 nm (PS60) have been analysed using four different carriers at different ionic strength in the range 10^{-7} - 10^{-3} mol L⁻¹ and keeping constant all the other parameters.

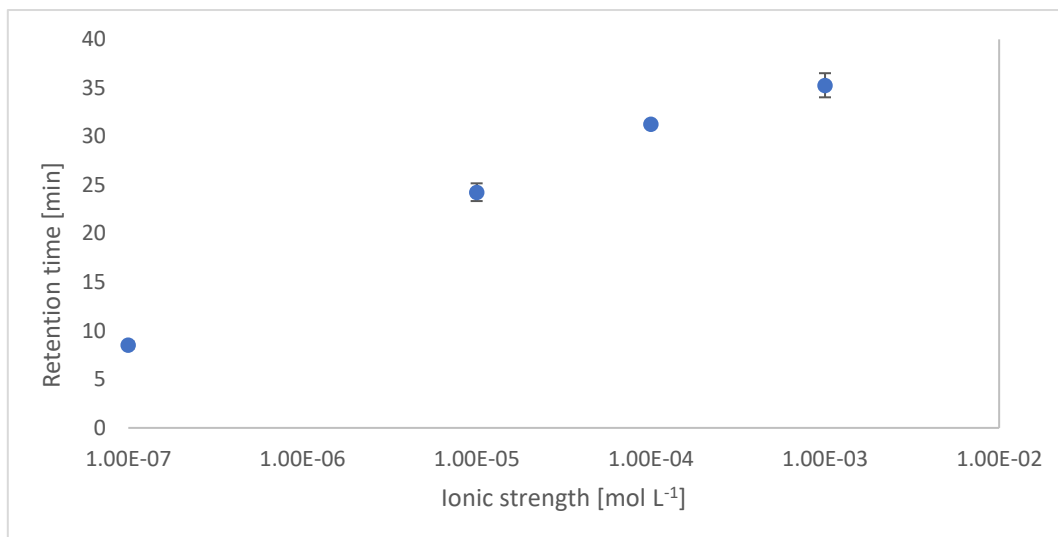


Figure 37. Influence of the carrier ionic strength on PS60 retention time. $Q_c = 1 \text{ mL min}^{-1}$; $w=350 \text{ }\mu\text{m}$; membrane: RC 10 kDa.

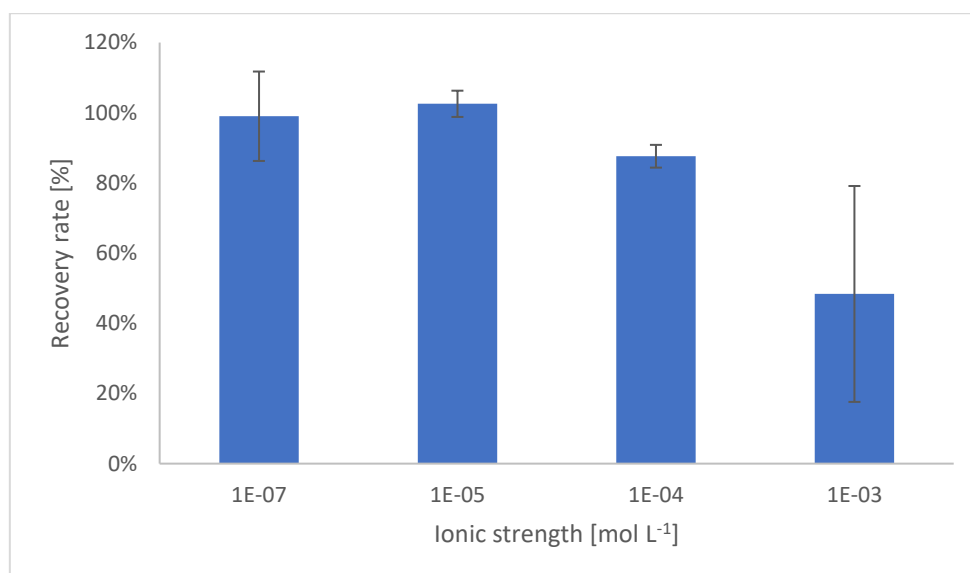


Figure 38. Influence of the carrier ionic strength on PS60 recovery rate. $Q_c = 1 \text{ mL min}^{-1}$; $w=350 \text{ }\mu\text{m}$; membrane: RC 10 kDa.

Figure 37 shows a net increase in the particle retention time when the ionic strength increases whereas a decrease on the recovery rate can be observed in Figure 38. These two effects can be explained by the decrease of the electrostatic repulsion, which allows the particle to nearer the accumulation wall. Consequently, the particle will be slower and will have more chance to be adsorbed on the membrane. These experiments show that working at weak ionic strength might be useful to prevent adsorption when the use of surfactant is not an option.

1.2. Influence of the membrane nature on the particle retention and recovery rate

The influence on the membrane nature on the particles retention and recovery rate was evaluated by analysing four polystyrene standards (PS20, PS60, PS100, PS185) on a PES 10 kDa and RC 10 kDa membrane with a spacer 350 μ m thick. The carrier was NH_4NO_3 at 10^{-4}mol L^{-1} . The cross flow rate was fixed at 0.5 mL min^{-1} .

The influence of the membrane zeta potential and Hamaker constant on the particle retention and recovery rate was evaluated. The retention time and recovery rate of each standard is presented in Figure 39 and Figure 40. In this figure, it can be observed that all the polystyrene standards have a higher retention time and recovery rate when they are analysed with the PES membrane. If these effects are analysed with the DLVO theory the only interactions between the particles and the membrane are the van der Waals and electrostatics interactions. The properties of the membranes that influence these interactions are its zeta potential and its Hamaker constants. The membrane zeta potentials were measured with an electrokinetic analyser and the Hamaker constants representing the system polystyrene-water-membrane were found in the literature (Qu *et al.*, 2016a)(Table 14). It can be noted that the PES membrane has a zeta potential and a Hamaker constant higher than the RC membrane.

The sum of the electrostatic and van der Waals interactions for the system with the PES membranes should repulses the particles either more or less than the RC membrane. If the interactions are less repulsive, the particles will be nearer the membrane which will result in a longer retention, as the streamlines which transport the particles are slower near the channel bottom. The odds of particles adsorption on the membrane should also increases as the particles get closer of the membranes and therefore, decrease the recovery rate. However, a better recovery but also a longer retention time is observed in the analyses with the PES which is contradictory. The explanation for this difference was the different compressibility of the PES and RC membrane. Kavurt *and al.* reported that the PES membrane is stiffer than the RC membrane (Kavurt *et al.*, 2015). This signify that the PES membrane protrudes less in the channel space than the RC. Therefore, a channel with a PES membrane has a bigger effective thickness than a channel with a RC membrane. This difference in thickness can explain why the particles have a larger retention time while also having a high recovery rate.

Table 14 . Zeta potential and Hamaker constant of the PES and RC 10 kDa membrane. The zeta potentials measurement were performed in NH_4NO_3 $10^{-4} \text{ mol L}^{-1}$ at pH 8.5 and $T= 293 \text{ K}$.

	zeta potential [mV]	Hamaker constant (PS-water-membrane) [J]
PES	-76 ± 2	$31.8 \cdot 10^{-20}$
RC	-51 ± 4	$4.26 \cdot 10^{-20}$

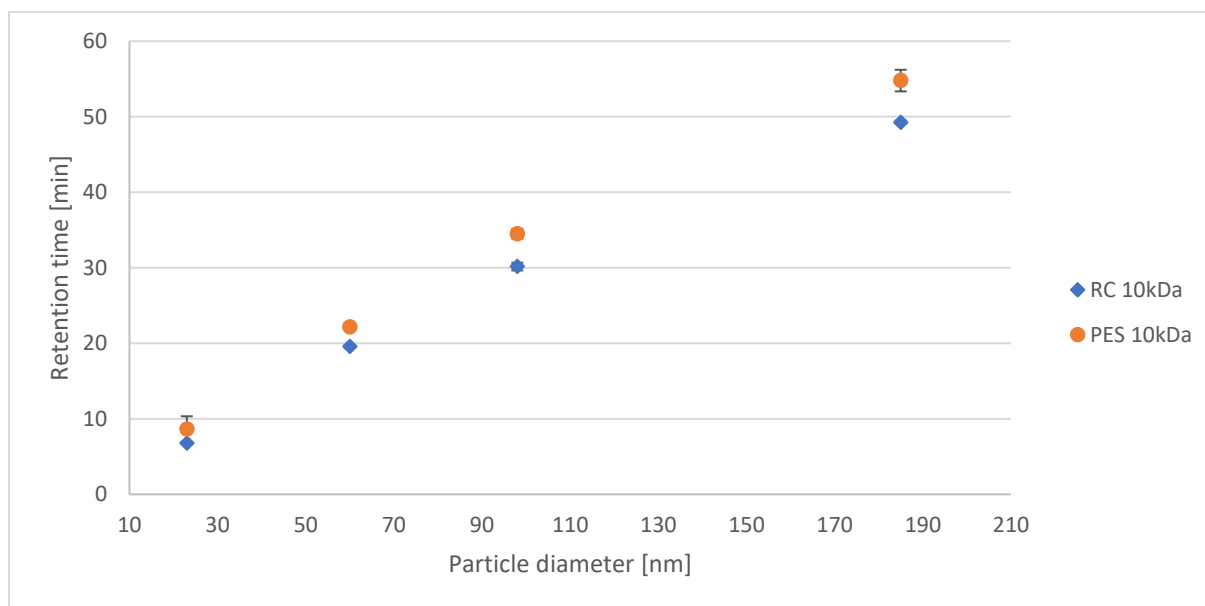


Figure 39. Influence of the membrane nature on the retention time of polystyrene standards. $I= 10^{-4} \text{ mol L}^{-1}$, $Q_c= 0.5 \text{ mL min}^{-1}$; $w=350 \text{ }\mu\text{m}$; membrane: RC 10 kDa.

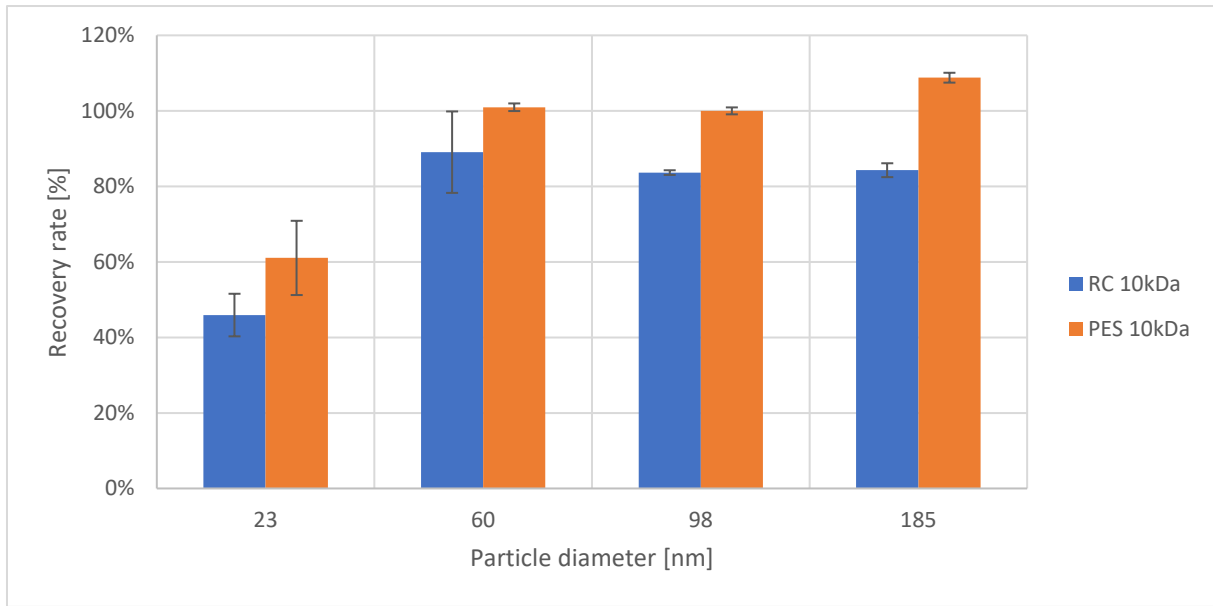


Figure 40. Influence of the membrane nature on polystyrene standards recovery rate. $I = 10^{-4}$ mol L⁻¹ $Q_c = 0.5$ mL min⁻¹; $w = 350$ μ m; membrane: RC 10kDa.

Due to the difference in effective thickness, the influence of the membrane zeta potential and the Hamaker constant on the retention could not be estimated. Nonetheless the difference in the recovery rate indicates that the zeta potential has a biggest influence on the particles recovery than the Hamaker constant.

1.3. Influence of the particle size on the particle retention

As presented in chapter 2, particle retention in the AF4 channel under strong conditions of retention can be described by Eq. (IV.1):

where it can be seen that t_r varies linearly with d_h . To verify the linearity of Eq. (IV.1), four polystyrene standards of different size (PS20, PS60, PS100, PS185) have been measured keeping constant all the experimental parameters. The cross flow rate was constant and fixed at 0.8 mL min⁻¹ for the experiments: the chosen value was the best compromise to sufficiently retain the small particles and not retain too long the large particles. The experiment was repeated at three different ionic strengths: 10^{-5} , 10^{-4} and 10^{-3} mol L⁻¹. Figure 41 shows the influence of the ionic strength on the relationship between t_r and d_h as predicted by Eq. (IV.1). It can be observed that the relationship between the t_r and the d_h becomes less linear at 10^{-4} mol L⁻¹ compared to 10^{-3} mol L⁻¹, and even asymptotic at very low ionic strength. This tendency can be explained by the increase of repulsion interactions inside the channel. At low ionic strength, the particle-wall interactions may influence the particle retention and change the relationship

$t_r=f(d_h)$ as the particle size is one of the input quantities entering the electrostatics and van der Waals interactions Eq (II.12 and (II.14).

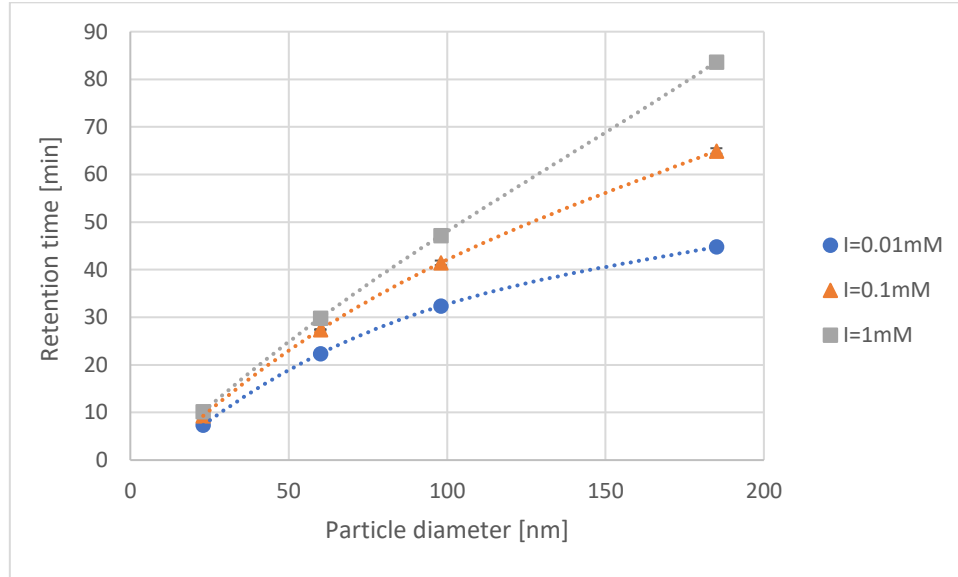


Figure 41. Influence of the ionic strength on the relationship between the retention time and the particle size (PS20, PS60, PS100, PS185). $Q_c=0.8 \text{ mL min}^{-1}$; $w=350 \text{ }\mu\text{m}$; membrane: RC 10 kDa.

1.4. Influence of the particle nature on the particle retention

It has already been showed in the literature that the particle chemical composition influences the elution (Gigault and Hackley, 2013): particles of the same expected size elute at different retention times. The different behaviour in the channel may be attributed to the difference in particle density or in their Hamaker constant. In order to verify the influence of the density on the retention time, gold and polystyrene standards of 60 nm were used with a density of 18 and 1.01 g cm^{-3} respectively (Gigault and Hackley, 2013). The Hamaker constant, A_{123} , for each system: particle-water-cellulose was equal to $4.26 \times 10^{-20} \text{ J}$ for the polystyrene and $26.8 \times 10^{-20} \text{ J}$ for the gold (Qu *et al.*, 2016b). Both particles were analysed using the same fractionation conditions (Figure 42). The experiment has been reproduced at different cross flow rates in the range $0.5\text{--}2 \text{ mL min}^{-1}$. Unlike *Gigault and Hackley* (Gigault and Hackley, 2013) in this work the AF4 channel was positioned vertically and not horizontally. In this position the gravity force, if operating on the particles, would drive the particles toward the direction of the channel flow and not downward to the channel accumulation wall. Consequently, the gravity force in this case should not influence the particle retention. Even excluding the influence of the particle

density, it can be observed that the retention times of gold is significantly higher than the PS standards (Figure 42). The high A_{123} of the gold compared to the polystyrene could explain this difference, indeed if the van der Waals forces impact the retention, a high A_{123} will attract the particle nearer the accumulation wall and consequently slow down the particle motion. Increasing the cross flow rate did not change the gap in retention time.

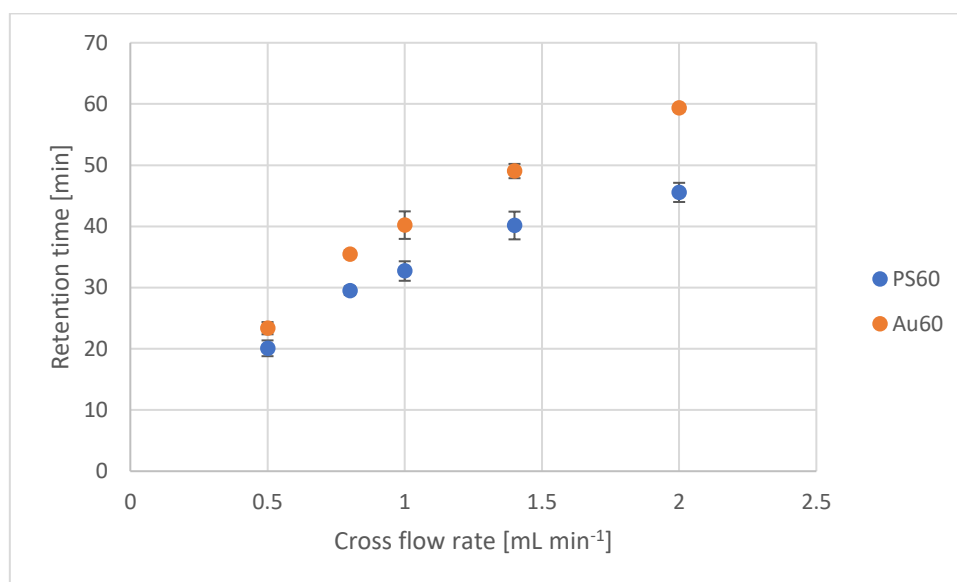


Figure 42. Effect of particle chemical composition on the retention time. $w=350\text{ }\mu\text{m}$; membrane: RC 10 kDa, $I=10^{-5}\text{ mol L}^{-1}$.

1.5. Lessons retained from preliminary tests on retention behaviour of spherical nanoparticles in AF4 channel

This study showed the influence of particle wall interactions on the particles retention behaviour and recovery rate by varying the carrier ionic strength, and chemical nature of the membrane and particles. The ionic strength shows a large influence on the particle retention and recovery. *Mori et al.* once proposed for the SdFFF to do analyses at $I=10^{-3}\text{ mol L}^{-1}$ in order to have a behaviour conform to the classical model (Mori et al, 1990). However, the analysis performed at $I=10^{-3}\text{ mol L}^{-1}$ exhibit low recovery rate which make them not interesting as experimental conditions. Moreover, the difference in retention time between polystyrene and gold particles would not be taken into account by the classical model and lead to systematic error for at least one of this two kind of particles. Consequently, a retention model tacking theses interactions into account is mandatory if the model is used as a characterisation method.

2. Application of the δ_w model to AF4 for the size characterization of nanoparticles

The aim of this study was to apply the δ_w model in the case of the AF4 at the nanoscale range and to evaluate if the model is a good candidate to represent more accurately the different phenomena that may occur in the channel, namely the electrostatic interactions between the particles and the membrane.

The δ_w model (Williams, Xu, Pierluigi Reschiglian, *et al.*, 1997), presented in Chapter II, section 1.5.3, can be summarized as follows: the sum of all the interactions applied on the particle, either repulse or attract the particle from/to the wall and may be represented by an distance, δ_w . In principle, if two particles present in the channel have the same interactions, the δ_w associated to the particles should be the same. In the theory section of their paper, *Williams et al.* assumes that δ_w may vary as a function of the carrier composition, the wall and the particles composition, their surface properties and the particles size. However, the experiments done with polystyrene particles in the size range between 197 and 742 nm did not change the δ_w value (Williams, Xu, Pierluigi Reschiglian, *et al.*, 1997). The authors concluded that in this range of size δ_w value is independent from the size of the standard used to calibrate it.

Du and Schimpf applied δ_w model in AF4 on a size range between 64 and 1000 nm. The authors observed a difference in the δ_w determined by the 64 nm standard compared to the other size standards (Schimpf and Du, 2002).

In this work, to evaluate the Williams model for AF4 applications, standards of polystyrene of size in the range of 23 to 185 nm have been used. Three carriers at different ionic strengths have been employed. The effect of (i) the ionic strength and of (ii) the particle size on δ_w have been monitored. An uncertainty assessment has been performed.

As detailed in Chapter II, Eq. (17), δ_w is equal to the slope of the linear equation $Y = f(I/l)$:

$$Y = \frac{\frac{t_0}{t_r} - 6\alpha(1 - \alpha)}{6\lambda \left((1 - 2\alpha) \coth \frac{1 - 2\alpha}{2\lambda} - 2\lambda \right)} = \left(1 + \frac{\delta_w}{l} \right) \quad (3)$$

For each condition tested δ_w was calibrated by performing five analysis using five different cross flow rates from 0.5 to 2 mL min⁻¹.

2.1. Determination of the channel thickness in the case of the δ_w model

It exists different indirect methods to determine w_{eff} and they will be detailed in Chapter VII. One of the most common approach is to use a standard particle of well-known diffusion coefficient or size (Wahlund, 2013): the particle is analysed in optimised conditions, then a retention model is applied using the experimental retention time measured, the nominal thickness value and the nominal particle size. The model equation is then resolved for the channel thickness, which is considered as the “effective thickness”. However, contrarily to the other retention models, the δ_w model has two unknown parameters that need to be determined for given conditions: w_{eff} and δ_w . Therefore, in this particular case, the common approach to calculate w_{eff} here explained cannot be applied. It has been decided for this work to use the nominal thickness for the calculations. The consequence of this choice is illustrated in Figure 43. In realistic conditions, the membrane protrusion takes place and the value of δ_{w1} is only due to repulsive interactions. When assuming the width of the channel equal to the nominal value (Figure 43B), the difference between w_{nom} and w_{eff} will be considered by the model as a repulsive interaction: the particle will elute earlier than predicted for the given nominal thickness, and this will be taken into account in the value of δ_{w2} .

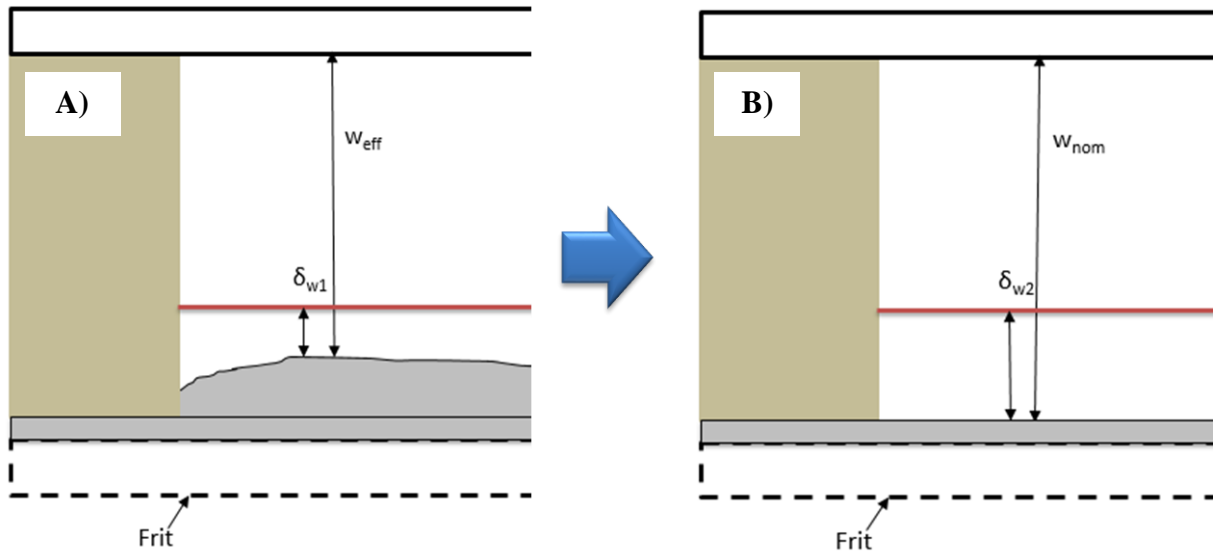


Figure 43. Consequences of choosing w_{nom} as the channel thickness on the calibration of δ_w : A) realistic condition, with membrane protrusion; B) assumption that the channel thickness is not modified.

2.2. Effect of the ionic strength and of the particle size on δ_w

The retention time of four polystyrene standards of 23; 60; 98 and 185 nm diameter, was measured using ammonium nitrate carriers at three different ionic strengths: 10^{-5} , 10^{-4} and 10^{-3} mol L⁻¹. For each tested carrier, the retention time of each particle was measured at five different cross flow rates: 0.5; 0.8, 1, 1.4 and 2 mL min⁻¹. Figure 44 shows the linear regression lines obtained for Eq. (3) using a polystyrene of 60 nm.

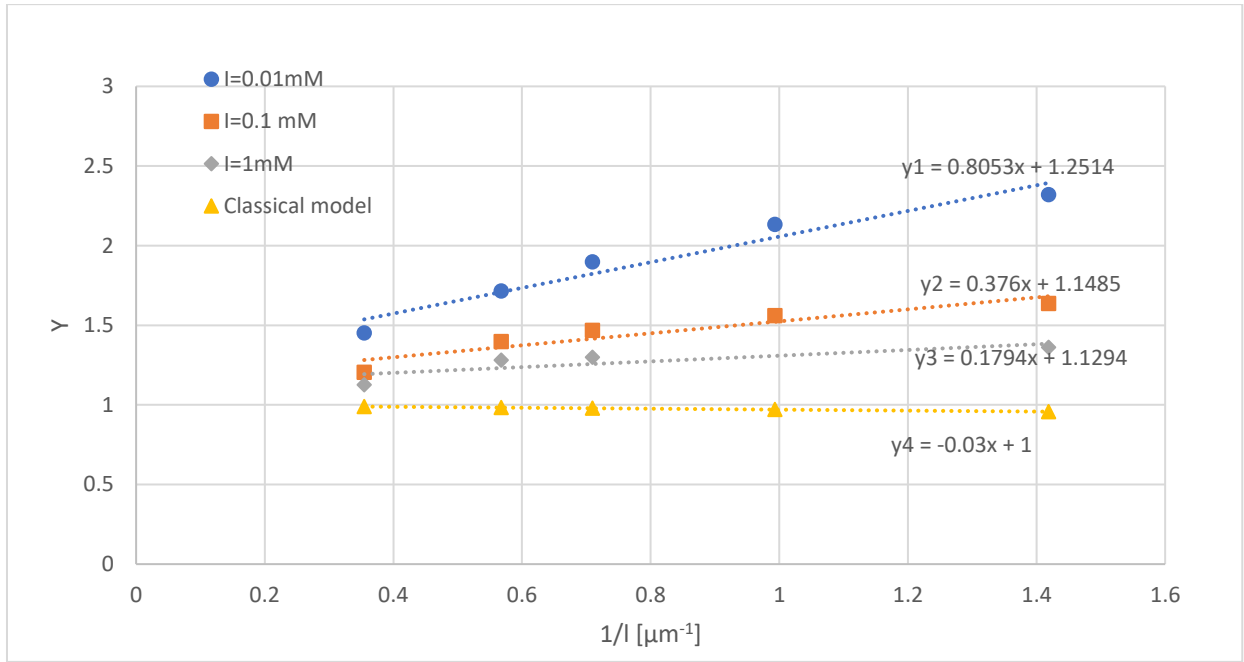


Figure 44. Calibration of δ_w in three carriers with different ionic strength. PS60; $w=350 \mu\text{m}$; membrane: RC 10 kDa.

The retention in the different experimental conditions has been calculated using the classical model and has been plotted as a quality control (Figure 44, yellow triangles). Data from the classical model show the correlation $Y=f(1/l)$ for a sample that does not get affected by any kind of interaction; this should result in a slope of the line close to zero, which is the case here.

It can be observed that the slope of linear regression lines, i.e. δ_w value, decreases when the ionic strength increase. This tendency was expected as the ionic strength influences the electrostatic repulsion between the particle and the membrane and this repulsion become weaker as the ionic strength increases.

Williams showed for SdFFF and for a size range going from 197 to 742 nm, that the δ_w parameter is independent from the size of the standard used for the calibration (Williams et al., 1997). Du and Shimpf tested for AF4 in the range going from 64 to 1000 nm: they observed a

different trend for the regression realized using a standard of 64 nm compared to the rest of the standards (Schimpf and Du, 2002).

To evaluate the effect of the size of the standards used for the calibration on δ_w , the retention time of four polystyrene standards of 20, 60, 100 and 200 nm was measured using NH_4NO_3 at 10^{-5}mol L^{-1} as carrier and varying the cross flow rate in the range of 0.5 to 2 mL min^{-1} . Figure 45.A) shows the different calibration curve obtained with the four size standards. The δ_w value obtained with each standard are reported in Figure 45.B).

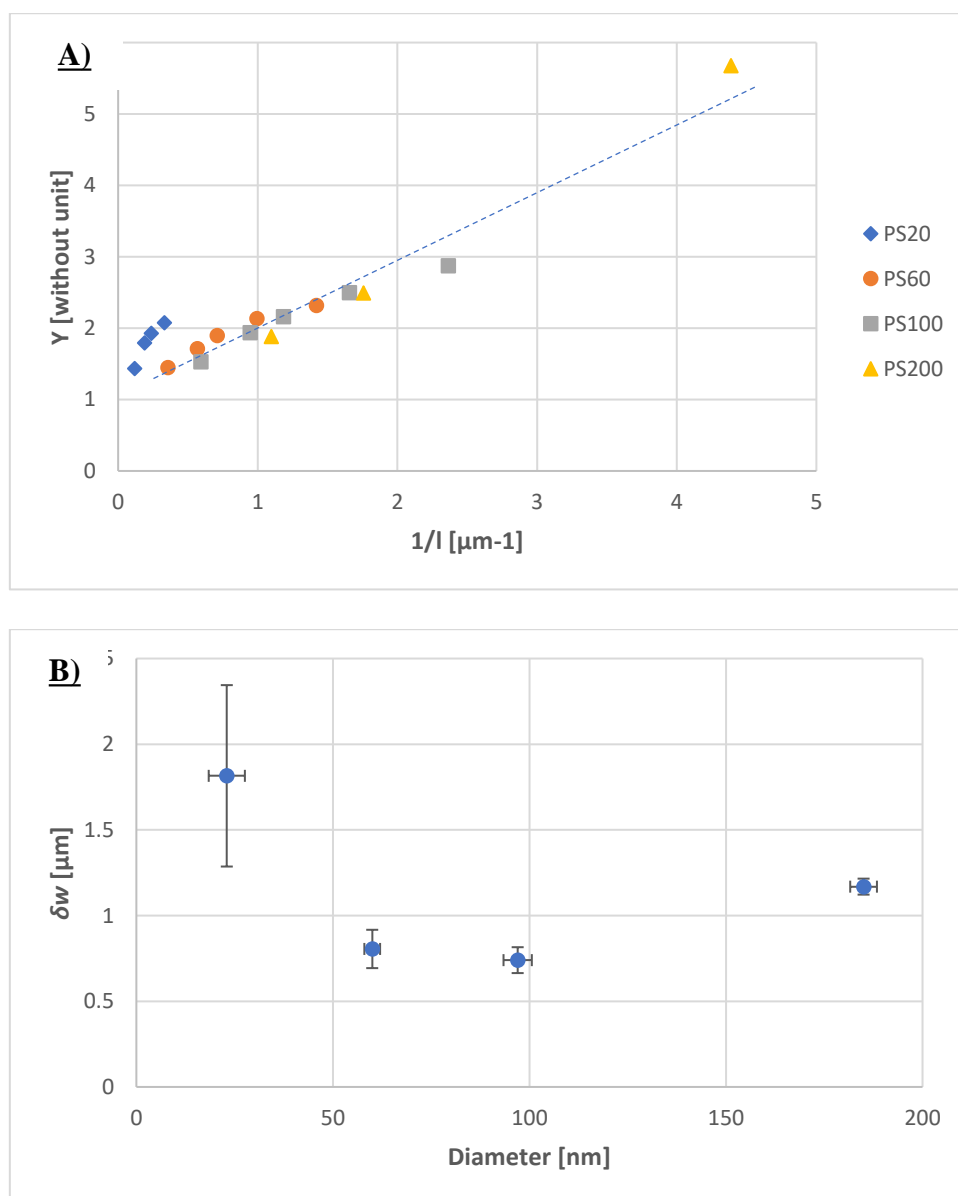


Figure 45. Effect of the standard size on δ_w . A) Calibration curves realised with four PSL standards. B) Values of δ_w determined from the calibration curves. The experiments were realized with: $w=350\text{ }\mu\text{m}$; membrane: RC 10 kDa; $[\text{NH}_4\text{NO}_3] = 10^{-5}\text{ mol L}^{-1}$.

Standards of 60, 100 and 200 nm show a very similar calibration curve. In particular, PS60 and PS100 have comparable values of δ_w (Figure 45.B). These results are close to the results presented in *Du and Schimpf* (Schimpf and Du, 2002).

On the other hand, the calibration curve performed with the PS20 shows a different trend compared to the three other curves. According to *Williams et al.* (Williams, Xu, Pierluigi Reschiglian, *et al.*, 1997) this means that the PS20 has a different behaviour compared to the other polystyrene standards.

The two main types of interactions experienced by the particles are the van der Waals interactions and the electrostatics forces. The intensity of van der Waals interactions depends on the Hamaker constant value, A_{123} . However, A_{123} depends on the chemical composition of the particle and PS20 has, *a priori*, the same composition as the others polystyrene standards.

Concerning the electrostatics forces, the particle zeta potential, ζ_p , is the only parameter that can be responsible of a different behaviour for PS20. To confirm this hypothesis, particles zeta potential has been measured. Measurements have been performed in AF4 carrier (NH_4NO_3 at $10^{-5} \text{ mol L}^{-1}$ and pH 8.5) with a zetameter Wallis (Corduan, Pessac, France) (Table 15).

Table 15. Zeta potential of polystyrene particle standards

Particle	Zeta potential [mV]
PS20	-35±5
PS60	-69±3
PS100	-62±5
PS200	-55±3

The ζ_p of the PS20 is indeed different from the other standards. However, its value is smaller than the others are. This means that the repulsion induced from the electrostatics forces is smaller and consequently, the δ_w representing the exclusion distance should be smaller in the case of the PS20 which is not the case.

To see if the difference in δ_w between the PS20 and the other particles is specific to the standard PS20 or may be related to the size range, the calibration of δ_w was performed with gold

standards of 20 and 60 nm. The calibration was performed in ultrapure water and the cross flow rate varied in the same range previously specified.

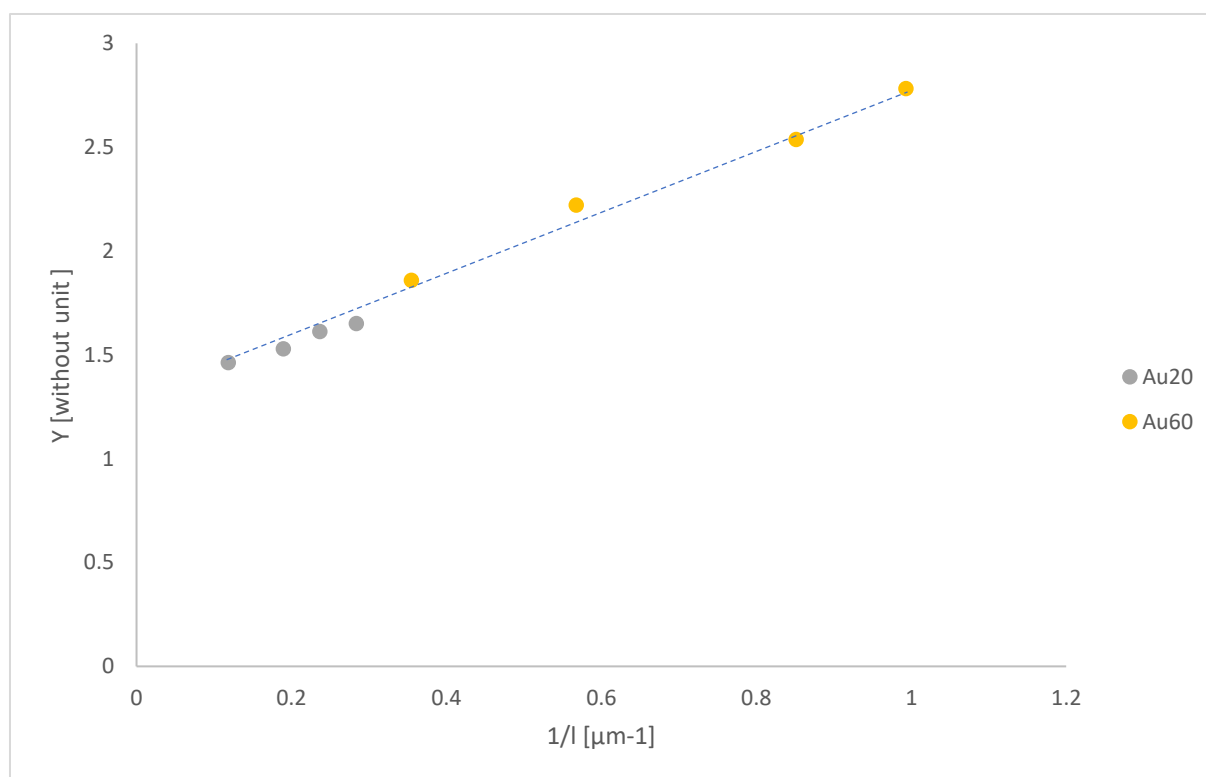


Figure 46. Effect of the standard size on δ_w using golds standards in ultrapure water. $w = 350$ μm , membrane: RC 10 kDa.

The calibrations points of the Au20 and Au60 follow a very similar trend (Figure 46). The slope of Au20 ($\delta_w = 1.2 \pm 0.1$ μm) is not significantly different from one of Au60 ($\delta_w = 1.4 \pm 0.1$) contrary to what was observed for PS20 and the others polystyrenes standards. Consequently, the size does not seem to be the origin of the issue presented by the PS20. A possible explanation comes from the presence of surfactants in the stock solution. Indeed, the supplier indicates in the certificate that the 20 nm suspensions contain large amounts of surfactants. Although the standard is diluted before injection and even though the focalisation step "wash" the sample matrix out of the channel, is it possible that residual surfactant increases the repulsion interaction between the PS20 and the wall more importantly than for the others polystyrene standards..

2.3. Validation of the model

The trueness of the model has been tested by comparing the size of polystyrene standards calculated using the δ_w determined previously and the expected nominal size. Furthermore, an uncertainty assessment has been performed.

To assess the uncertainty on d_h , the first step consists to arrange the Eq. (IV.4) in order to have an explicit equation with the form: $d_h = f(t_r, \dots, V_c)$. Due to the complexity Eq. (IV.4), an algorithm was elaborated in order to solve the equation for d_h with a numerical approach.

$$\frac{t_0}{t_r} = 3 \frac{d_h}{w} \left(1 - \frac{d_h}{2w}\right) + 6 \frac{kTA_{tot}}{3\pi\eta Q_c w d_h} \left(1 - \frac{d_h}{w} - 2 \frac{kTA_{tot}}{3\pi\eta Q_c w d_h}\right) \left(1 + \frac{\delta_{eq}}{\frac{kTA_{tot}}{3\pi\eta Q_c d_h}}\right) \quad (IV.4)$$

As this solution does not provide an analytical expression of $d_h = f(t_r, \dots, w)$, the uncertainty propagation was performed using the Monte Carlo method (MCM). The principle of the MCM consists to obtain the measurand distribution by calculating a large number of times the measurand value by picking input quantities generated from the PDF of each input quantity. Firstly, a PDF is attributed to each input parameter. The choice of PDF depends on the knowledge either experimental or in the literature available for the parameter. Supplement 1 of the GUM (Joint Committee For Guides In Metrology, 2008) shows how to choose the appropriate PDF. Secondly, a random number generator is used to generate numbers from the PDF of input parameters to calculate the measurand PDF. Here, the simulation was run 300 000 times in order to have a good compromise between the representativeness of the results and the calculation time.

Table 16 lists all the input values used to calculate the hydrodynamic diameter of the PS100. The blue boxes in Table 16 represent the parameters that did not change regardless of the experiment whereas the yellow boxes show the parameters that varied as function of the sample analysed. The input quantities were classified as type A or type B parameters depending on how their values were determined. The type A indicates that the parameters were determined with a direct measurement, whereas type B values were found in the literature. In this case only the viscosity and the channel thickness values were taken from the literature. All the other input quantities were measured and by consequent are type A. Each type A quantities were measured three times. The mean and standard deviation from these three measurements were taken as input values. The carrier viscosity value and its uncertainty have been taken from the literature for a temperature of 192.98 K (Berstad *et al.*, 1988). The temperature was measured with a

temperature sensor. The input quantities associated to the channel geometry (L , b_1 , b_2 , z_1 , z_2) were measured with a ruler. In this special case, the uncertainty was taken as half of the ruler graduation, i.e. 0.5 mm. The channel thickness value was taken from the data sheet given by Postnova Analytics. Its uncertainty was fixed at 1 μm . The different flow rates (Q_{out} , Q_{in} , Q_c) were determined by gravimetry. A PS100 retention time was used for the calculation. The δ_w presented in Table 16 has been calibrated by the PS60 with NH_4NO_3 at $10^{-5} \text{ mol L}^{-1}$ as a carrier. Its uncertainty was taken as the slope uncertainty of the calibration function $Y=f(1/I)$ determined using the Excel function *droite reg*. In order to obtain a small uncertainty for δ_w the PS60 was analysed with five different cross flow rates and each condition was replicated 3 times. The distribution law case indicates how the parameter value is expected to vary: a parameter with a normal law has a high probability to have its mean value generated, whereas a parameter with a uniform law has an equivalent probability to have any number within the range indicated to be generated. The uniform law has been affected to δ_w to maximize the uncertainty associated because the behaviour of δ_w is not known. The δ_w presented in Table 16 has been calibrated by the PS60 with NH_4NO_3 at $10^{-5} \text{ mol L}^{-1}$ as a carrier.

Table 16. Range value of the parameter used for the simulation.

Parameter	Symbol	Type	Mean value	$u(x)$	Distribution law	Unit
Boltzmann constant	k	B	$1.38065 \cdot 10^{-23}$	0	normal	J.K ⁻¹
viscosity	η	B	$1.00103 \cdot 10^{-3}$	$1.3 \cdot 10^{-7}$	normal	kg m ⁻¹ s ⁻¹
temperature	T	A	293.15	0.5	normal	K
maximum channel breadth	b_1	A	2	0.05	normal	cm
minimum channel breadth	b_2	A	5	0.05	normal	cm
distance from channel tip to b_1	z_1	A	3.3	0.05	normal	cm
distance from channel tip to b_2	z_2	A	26.8	0.05	normal	cm
channel length	L	A	27.7	0.05	normal	cm
elution flow rate	Q_{out}	A	0.55	$1.5 \cdot 10^{-4}$	normal	mL min ⁻¹
inlet flow rate during the focusing phase	Q_{in}	A	0.21	$2.1 \cdot 10^{-4}$	normal	mL min ⁻¹
channel thickness	w	B	350	3.5	normal	μm
exclusion distance	δ_w	A	0.8	0.07	uniform	μm
cross flow rate	Q_c	A	1.01	$2.2 \cdot 10^{-3}$	normal	mL min ⁻¹
retention time	tr	A	34.8	0.7	normal	min

Figure 47 represents the probability distribution function (PDF) obtained by the algorithm.

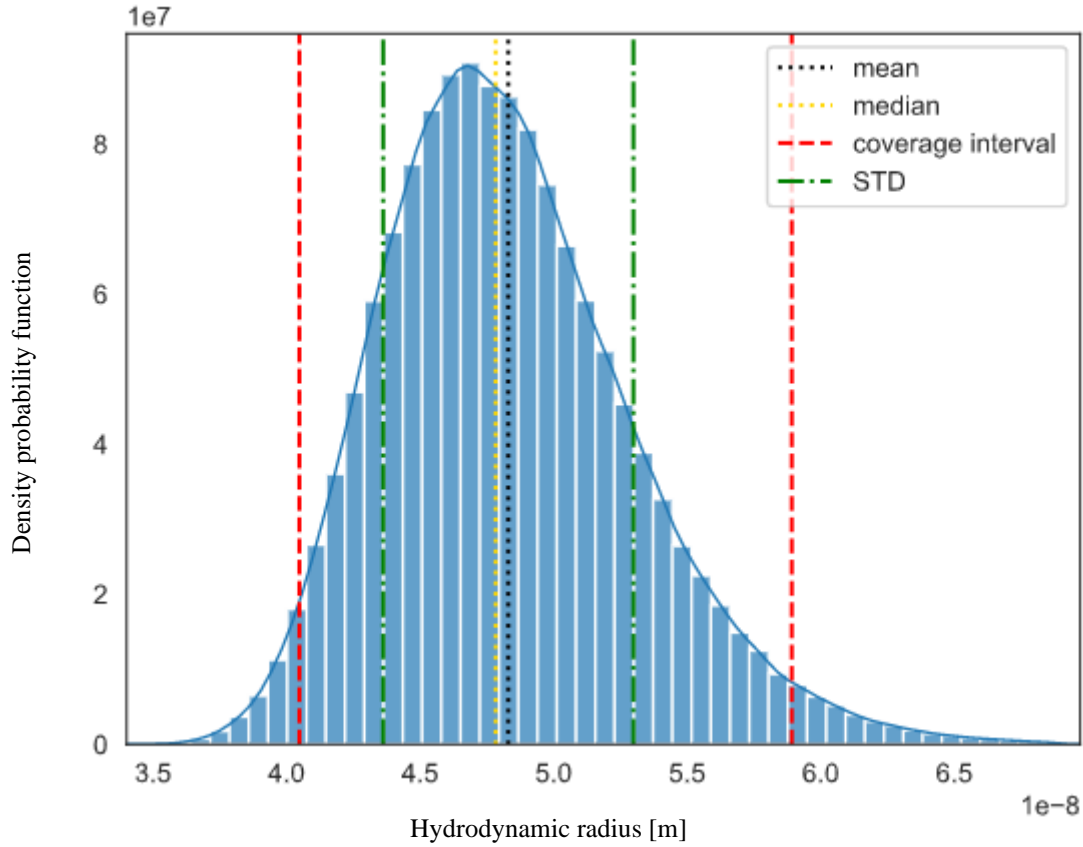


Figure 47. Distribution of the r_h calculated from the values presented in Table 16.

A distribution with a mean r_h value of 48.3 nm, a median value of 47.8 nm, and a standard deviation of 5 nm has been calculated. The PDF showed in Figure 47 is asymmetric. Hence, the expanded uncertainty cannot be expressed as 2 times the standard deviation. In this case the expanded uncertainty is expressed as an interval covering 95% of the distribution values presented as $[y_{\min}; y_{\max}]$. The coverage interval of Figure 47 is $[r_{h\min} = 41.5 \text{ nm}; r_{h\max} = 56.66 \text{ nm}]$.

This coverage interval is too large to use the model as a size determination method. A sensibility analysis was therefore conducted in order to know which input quantity has the most important contribution to the uncertainty and see if the input uncertainty can be reduced. Figure 48 represents the relative contribution of each input quantity on the r_h uncertainty. Each contribution was determined by calculating the rank correlation coefficient of Spearman (Allard and Fischer, 2018). It can be seen that the majority of r_h uncertainty depends of δ_w which represents 46% of the uncertainty. A solution to decrease δ_w would be to increase the number of point on the calibration curve.

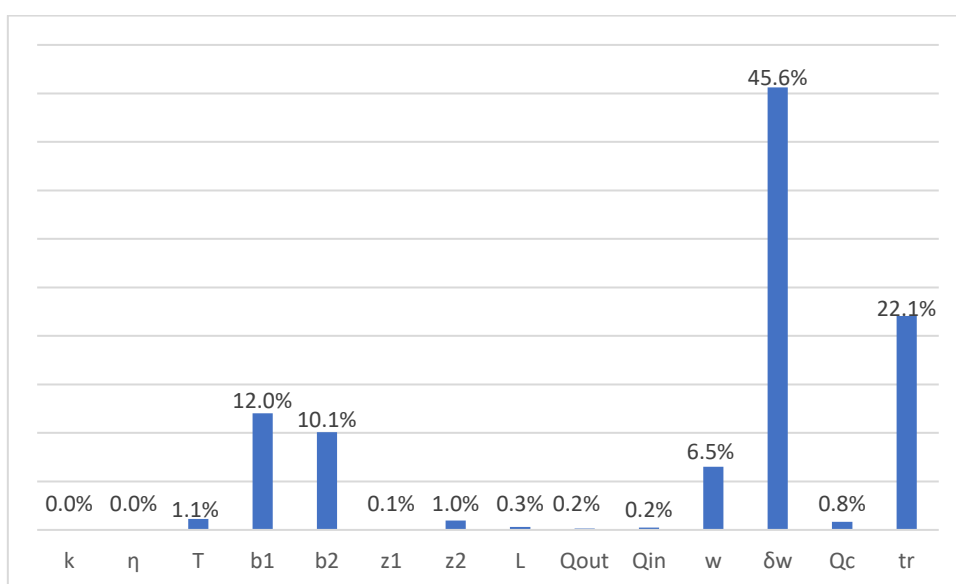


Figure 48. Relative contribution to each input quantity on r_h uncertainty.

The trueness of the δ_w model was evaluated qualitatively on the four polystyrene standards. The standards values was compared with the coverage interval obtained by the MCM. The results were considered true when the reference value is included in the coverage interval (Table 17). The results shows that the references diameter are all included in the coverage intervals calculated. The covering interval obtained for the PS20 is almost did not recoup with the reference value. However, this result is understandable since the PS20 calibration exhibited a different behaviour from the other polystyrene standards as discussed before. Therefore, the δ_w used for the calculation was not adapted for the PS20. It can be noticed than contrary to the MEB where the expanded uncertainty is practically the same regardless of the particle measured, the δ_w model gives coverage interval which increase with the size of the particle analysed while the uncertainty of each standards retention time is similarly i.e. (0.7-1min). This phenomenon can be explained with the principle of the model. Since the δ_w represents an exclusion distance that the particles cannot access, the particle should from a certain size elute with the same streamlines. The relation between the particle hydrodynamic diameter and the retention tends to becomes asymptotic and lead to a broad size distribution when the Monte Carlo method is applied.

Table 17. Evaluation of the δ_w model trueness on polystyrene standards. The analysis were performed in NH_4NO_3 at $10^{-5} \text{ mol L}^{-1}$; $w = 350 \text{ }\mu\text{m}$; membrane: RC 10 kDa; $Q_c = 0.8 \text{ mL min}^{-1}$.

Standard	standard diameter $\pm U$ ($k=2$)[nm]	d_h min - d_h max [nm]		d_h median [nm]	Results significantly different
PS20	23 \pm 10	12.2	13.8	13.1	No
PS60	60 \pm 8	49.3	59.8	53.8	No
PS100	99 \pm 8	86.8	114.3	99.0	No
PS200	186 \pm 6	172.3	328.7	224.1	No

Conclusion

The aim of this first study was to evaluate how the different parameters of the AF4 system may influence the particle retention. This study paid a special attention on parameters influencing particles-wall interactions, like the ionic strength or membrane chemical nature, since their effects need to be negligible compared to the field strength, to use the classical retention model.

The results highlighted the influence of particle wall interactions on the particle retention behaviour. It has been showed that the carrier ionic strength greatly influences the particle retention. Even if their effect is smaller than the ionic strength, the chemical composition of particles also influence significantly the particles retention time. Therefore, the interactions particle-walls cannot be neglected in retention models that purports to accurate describe the retentions mechanisms. These findings suggested a study on the applicability for AF4 of a retention model developed by *Williams et al.* tacking the particle-wall interactions into account, the δ_w model, initially applied for the SdFFF. The results confirmed that, in the experimental domain tested and when the standard size belongs to the nanoscale, δ_w value is independent from the size of the standard used to calibrate it. The results showed that the δ_w model allows to quantitatively estimate the sum of particle-membrane interactions present in the channel. The δ_w model provided results close to the reference values. However, the δ_w model require a large number of experiment in order to determine a δ_w value with a small uncertainty. Consequently, another retention model tacking the particles wall interactions into account was studied as potential size determination method (chapter V).

References

- Allard, A. and Fischer, N. (2018) 'Sensitivity analysis in practice: Providing an uncertainty budget when applying supplement 1 to the GUM', *Metrologia*, 55(3), pp. 414–426. doi: 10.1088/1681-7575/aabd55.
- Berstad, D. A. *et al.* (1988) 'Accurate measurements of the viscosity of water in the temperature range 19.5-25.5°C', *Physica A: Statistical Mechanics and its Applications*, 151(2–3), pp. 246–280. doi: 10.1016/0378-4371(88)90015-5.
- Dubascoux, S. *et al.* (2008) 'Optimisation of asymmetrical flow field flow fractionation for environmental nanoparticles separation', *Journal of Chromatography A*, 1206(2), pp. 160–165. doi: 10.1016/j.chroma.2008.07.032.
- Fraunhofer, W. and Winter, G. (2004) 'The use of asymmetrical flow field-flow fractionation in pharmaceuticals and biopharmaceuticals', *European Journal of Pharmaceutics and Biopharmaceutics*, 58(2), pp. 369–383. doi: 10.1016/j.ejpb.2004.03.034.
- Gigault, J. *et al.* (2014) 'Rational strategy for characterization of nanoscale particles by asymmetric-flow field flow fractionation: A tutorial', *Analytica Chimica Acta*, 809, pp. 9–24. doi: 10.1016/j.aca.2013.11.021.
- Gigault, J. and Hackley, V. A. (2013) 'Observation of size-independent effects in nanoparticle retention behavior during asymmetric-flow field-flow fractionation', *Analytical and Bioanalytical Chemistry*, 405(19), pp. 6251–6258. doi: 10.1007/s00216-013-7055-2.
- El Hadri, H. *et al.* (2014) 'Optimization of flow field-flow fractionation for the characterization of natural colloids Field-Flow Fractionation', *Analytical and Bioanalytical Chemistry*, 406(6), pp. 1639–1649. doi: 10.1007/s00216-013-7369-0.
- Joint Committee For Guides In Metrology (2008) *Evaluation of measurement data — Guide to the expression of uncertainty in measurement*, International Organization for Standardization Geneva ISBN. Available at: <http://www.bipm.org/en/publications/guides/gum.html>.
- Kavurt, U. B. *et al.* (2015) 'Membranes for separation of biomacromolecules and bioparticles via flow field-flow fractionation', *Journal of Chemical Technology and Biotechnology*, 90(1), pp. 11–18. doi: 10.1002/jctb.4473.
- Kim, S. T., Rah, K. and Lee, S. (2012) 'Effect of surfactant on retention behaviors of polystyrene latex particles in sedimentation field-flow fractionation: Effective boundary slip

model approach', *Langmuir*, 28(29), pp. 10672–10681. doi: 10.1021/la301593b.

Loeschner, K. *et al.* (2013) 'Optimization and evaluation of asymmetric flow field-flow fractionation of silver nanoparticles', *Journal of Chromatography A*, 1272, pp. 116–125. doi: 10.1016/j.chroma.2012.11.053.

Martin, M. (1999) 'Deviations to classical retention theory of field-flow fractionation', *Journal of Chromatography A*, 831(1), pp. 73–87. doi: 10.1016/S0021-9673(98)00901-7.

Mori, Y., Kimura, K. and Tanigaki, M. (1990) 'Influence of Particle-Wall and Particle-Particle Interactions on Retention Behavior in Sedimentation Field-Flow Fractionation', *Analytical Chemistry*, 62(24), pp. 2668–2672. doi: 10.1021/ac00223a004.

Omar, J. *et al.* (2016) 'Optimisation of asymmetric flow field-flow fractionation for the characterisation of nanoparticles in coated polydisperse TiO₂ with applications in food and feed', *Food Additives and Contaminants - Part A Chemistry, Analysis, Control, Exposure and Risk Assessment*, 33(12), pp. 1775–1784. doi: 10.1080/19440049.2016.1239031.

Qu, H. *et al.* (2016a) 'Importance of material matching in the calibration of asymmetric flow field-flow fractionation: material specificity and nanoparticle surface coating effects on retention time', *Journal of Nanoparticle Research*, 18(10). doi: 10.1007/s11051-016-3601-0.

Qu, H. *et al.* (2016b) 'Importance of material matching in the calibration of asymmetric flow field-flow fractionation: material specificity and nanoparticle surface coating effects on retention time', *Journal of Nanoparticle Research*, 18(10). doi: 10.1007/s11051-016-3601-0.

Schimpf, M. E. and Du, Q. (2002) 'Correction for Particle–Wall Interactions in the Separation of Colloids by Flow Field-Flow Fractionation', *Analytical Chemistry*, 74(11), pp. 2478–2485. doi: 10.1021/ac0200318.

Ulrich, A. *et al.* (2012) 'Critical aspects of sample handling for direct nanoparticle analysis and analytical challenges using asymmetric field flow fractionation in a multi-detector approach', *Journal of Analytical Atomic Spectrometry*, 27(7), p. 1120. doi: 10.1039/c2ja30024a.

Wahlund, K. G. (2013) 'Flow field-flow fractionation: Critical overview', *Journal of Chromatography A*, 1287, pp. 97–112. doi: 10.1016/j.chroma.2013.02.028.

Williams, P. S., Xu, Y., Reschiglian, Pieriugi, *et al.* (1997) 'Colloid Characterization by Sedimentation Field-Flow Fractionation: Correction for Particle - Wall Interaction', *Analytical Chemistry*, 69(3), pp. 349–360. doi: 10.1021/ac9606012.

Williams, P. S., Xu, Y., Reschiglian, Pierluigi, *et al.* (1997) 'Colloid Characterization by Sedimentation Field-Flow Fractionation: Correction for Particle–Wall Interaction', *Analytical Chemistry*, 69(3), pp. 349–360. doi: 10.1021/ac9606012.

**Chapter V. Implementation and evaluation
of a retention model taking into account
particle-wall interactions for the
measurement of nanoparticle
hydrodynamic diameter by asymmetrical
flow field-flow fractionation**

Chapter V. Implementation and evaluation of a retention model taking into account particle-wall interactions for the measurement of nanoparticle hydrodynamic diameter by asymmetrical flow field-flow fractionation

*Valentin de Carsalade du pont*¹, *Enrica Alasonati*^{1*}, *Sophie Vaslin-Reimann*¹, *Mauricio Hoyos*², *Michel Martin*^{2*}, *Clément Guibert*³ and *Paola Fisticaro*¹

¹ Department of Biomedical and Inorganic Chemistry, Laboratoire National de Métrologie et d'Essai (LNE), 1 rue Gaston Boissier, Paris, 75015, France

² Laboratoire de Physique et Mécanique des Milieux Hétérogènes (PMMH), ESPCI Paris, CNRS, 10 rue Vauquelin, 75231, Paris Cedex 05, France

³ Sorbonne Université, CNRS, Laboratoire de Réactivité de Surface, F-75005 Paris, France

*Corresponding authors

Email: martin@pmmh.espci.fr (M. Martin)

Phone number: +33 140794707

Email: enrica.alasonati@lne.fr (E. Alasonati)

Phone number: +33 140433971

Abstract

According to the field-flow fractionation (FFF) theory, the hydrodynamic diameter can be determined from its retention time by using a retention model. The classical retention model describing the retention mechanisms in FFF is based on the assumption of an exponential

transversal distribution of the particles. This assumption supposes that the interactions between particles as well as between particles and the accumulation wall are negligible compared to the field strength. However, several articles show that, depending on the experimental conditions, this assumption is not fulfilled. Therefore, the applicability of the classical equation is restrained. In this paper, a model taking the particles-wall interactions into account (p-w model), developed and tested by *Hansen et al.* for sedimentation FFF (SdFFF), is applied to asymmetrical flow FFF (AF4). The p-w model was applied to the measurement of polystyrene standards using carrier with three different ionic strengths. Experimental results were compared to p-w model predictions to evaluate the model applicability. Then results have been compared with those obtained by models generally used in literature. The three models compared predicted different retention behaviour especially for large particles in weak ionic strength media, where the particle-wall model was found to be more accurate and robust than the other models tested. Finally, part of the work focused on the determination of a key parameter, the channel thickness, and on its consequences on the results obtained by the different models.

1. Introduction

Field-flow fractionation (FFF) is a family of separation methods which separates the analytes by applying a field strength perpendicularly to the elution flow (Giddings, 1973). The physical nature of the field strength (electric, thermic, gravitational...) induces a fractionation depending on different physico-chemical properties. In asymmetrical flow field-flow fractionation (AF4), the fractionation is realized by a hydrodynamic force, the cross-flow, that fractionate in function of the analyte hydrodynamic diameter (Wahlund and Giddings, 1987). An equation describing the retention behaviour of an analyte in a FFF channel has been described for the first time by *Hovingh et al* (Hovingh, Thompson and Giddings, 1970). In the case of AF4, this equation can be used to determine the hydrodynamic diameter of an analyte from its retention time. However, this equation has been developed by making several assumptions: (a) the particles are like point mass; (b) these point mass do not interact with each other; (c) the transversal force experienced by the particles is constant thorough the channel; (d) the channel can be approximate as the space between two infinite parallel plate; (e) the flow between the planar wall is parabolic (Martin, 1999). Hypothesis (c) implies that non uniform forces (like van der Waal and

electrostatics interaction) between the particles and the channel can be considered as negligible. However, the literature showed that depending on the conditions, the interactions between the particles and the accumulation wall cannot be neglected and lead to a deviation from the behaviour predicted by the model. *Hansen et al.* reported a difference in the elution behaviour of polystyrene latex bead due to the variation of mass injected and the carrier ionic strength (Hansen, Giddings and Beckett, 1989). *Lang et al.* showed that the ion nature of the carrier could induce a difference in the retention time (Lang, Eslahian and Maskos, 2012). *Gigault et al.* noticed retention behaviours independent of the particle size (Gigault and Hackley, 2013). *Qu et al.* reported that particles with the same chemical nature but different coating do not have the same behaviour in the channel and elute at different time, which can induce difficulties when using external calibration (Qu *et al.*, 2016). Moreover, several authors reported that the carrier ionic strength played an important role in the particle retention (Litzén and Wahlund, 1991; Neubauer, V.d. Kammer and Hofmann, 2011; Schachermeyer *et al.*, 2012; Johann *et al.*, 2016; Mudalige, Qu and Linder, 2017; Boll *et al.*, 2018; Kato *et al.*, 2018; Kowalkowski, Sugajski and Buszewski, 2018).

To describe more precisely the analyte behaviour several other models have been proposed (Hansen and Giddings, 1989; Williams *et al.*, 1997; Gigault and Hackley, 2013). *Williams et al.* (Williams *et al.*, 1997) took into account the particle-wall interaction in sedimentation FFF (SdFFF) by adding a semi-empirical parameter, δ_w , representing the distance not accessible to the analyte due to sum of repulsive and attractive interactions. The value of δ_w is determined by calibration and allows to evaluate the intensity of the interactions between the particle and the wall and if they are attractive or repulsive (Jeon, Schimpf and Nyborg, 1997). In order to understand the different behaviours display by particle with the same size but different chemical nature *Gigault et al.* (Gigault and Hackley, 2013) included the gravity force in the retention model to see if the particle density could explained the difference in their retention time. Unfortunately, this force was not the origin of the difference in retention time. *Hansen et al.* (Hansen and Giddings, 1989) proposed another approach by adding the two principal types of particle-wall interactions, the van der Waals and the electrostatic interactions, in the expression of the concentration profile, as outlined in the theory section, to have a better understanding of particle elution behaviour. This approach has been used in SdFFF to determine the size or the Hamaker constant of the particle (Farmakis *et al.*, 2006). This kind of approach has been called *potential barrier FFF* (Koliadima and Karaiskakis, 1990; Karaiskakis *et al.*, 2002). Up to our knowledge, the *potential FFF* has not been yet applied to the AF4. In this work, the reliability

of the model proposed by *Hansen et al.* has been tested in AF4 for size characterization of polystyrene particles from 20 to 200 nm in diameter dispersed in carriers with different ionic strengths. These results have been compared with those obtained with two models generally applied in literature (Moens *et al.*, 2019), called in this work *classical* and *steric* models, that assume these interactions as negligible. Before comparing these three different models, the issue on the determination of key parameters, the void time and the channel thickness was briefly presented. In AF4 the determination of the effective channel thickness is necessary to apply the retention models (Wahlund, 2013). How to determine this parameter and the influence of the chosen approach on the comparison of the different models will be discussed in detail.

2. Theory

The theory has been described in detail elsewhere (Hansen and Giddings, 1989), hence only the most important equations will be defined below. The equation of the retention taking into account particle-wall interaction will be here formalised.

The retention ratio, R , is defined as the ratio of the average velocity of the analyte zone to the average velocity of the carrier liquid in the FFF channel. If we assume a parallel-plate channel, R can be expressed in function of only the transversal axis coordinate, x (Hovingh, Thompson and Giddings, 1970):

$$R = \frac{\int_0^w c(x)v(x)dx}{\langle v \rangle \int_0^w c(x) dx} = \frac{t_0}{t_r} \quad (1)$$

Where w is the thickness of the channel, $\langle v \rangle$ is the cross-sectional average flow velocity, $c(x)$ and $v(x)$ are respectively the concentration profile and the flow velocity in function of the x -coordinate. This equation is equal to the ratio of the void time, t_0 to the retention time, t_r .

In the case of a parabolic flow, the flow velocity is expressed as

$$v(x) = 6\langle v \rangle \left(\frac{x}{w} - \frac{x^2}{w^2} \right) \quad (2)$$

If all the forces applied on the particle derive from a potential energy function $W(x)$, $c(x)$ can be expressed with the Boltzmann expression (Williams *et al.*, 1997)

$$c(x) = c_0 \exp\left(\frac{-W_{tot}(x)}{kT}\right) \quad (3)$$

where $W_{tot}(x)$ is the sum of the potential energies of a particle whose center of mass is at the position x , c_0 is the concentration at the position where $W_{tot}(x) = 0$, k is the Boltzmann constant and T the temperature.

In dilute conditions, the forces applied on the analyte are the cross-flow, the van der Waals forces and the electrostatic interactions between the particle and the wall. The potential energy of the cross-flow force, W_{vc} , is equal to (Wahlund and Giddings, 1987)

$$W_{Qc} = \frac{Q_c w 6 \pi \eta r_h}{V^0} \left(x - \frac{x^3}{w^2} + \frac{x^4}{2w^3} \right) \quad (4)$$

where Q_c is the cross-flow rate, η the carrier viscosity, r_h the hydrodynamic radius of the particle and V^0 the geometric void volume. The potential energy of the van der Waals forces, $W_{vdW(p-w)}$, can be expressed as (Hoek and Agarwal, 2006)

$$W_{vdW(p-w)} = -\frac{A_{123}}{6} \left(\frac{r_h}{x - r_h} + \frac{r_h}{x + r_h} + \ln \frac{x - r_h}{x + r_h} \right) \quad (5)$$

where A_{123} is the Hamaker constant which represents the interactions between the particle 1 and the wall 3 in the medium 2. Finally, the potential energy of the electrostatics interactions, $W_{el(p-w)}$, is defined by (Hansen and Giddings, 1989)

$$W_{el(p-w)} = 64 \pi \varepsilon_0 \varepsilon_r r_h \left(\frac{kT}{e} \right)^2 \tanh\left(\frac{e\psi_p}{4kT}\right) \tanh\left(\frac{e\psi_w}{4kT}\right) \exp(-\kappa(x - r_h))$$

where ε_0 and ε_r are the dielectric constants of the void and the medium respectively, e is the elementary charge, ψ_p and ψ_w are the surface charges of the particle and the wall respectively. The constant κ is the inverse of the Debye length and can be expressed as (Hansen and Giddings, 1989)

$$\kappa = \sqrt{\frac{2e^2 N_a I}{\varepsilon_0 \varepsilon_r kT}} \quad (7)$$

in which N_a is the Avogadro constant and I , the carrier ionic strength.

In the case where the particle size cannot be neglected, eq.1 needs to take into account that the center of gravity of a particle cannot approach the wall closer than a particle radius by changing the integral bound to $x = r_h$ and $x = w - r_h$. Eq. 1 becomes

$$R = \frac{6 \int_{r_h}^{w-r_h} \exp\left(-\frac{W_{tot}(x)}{kT}\right) \left(\frac{x}{w} - \frac{x^2}{w^2}\right) dx}{\int_{r_h}^{w-r_h} \exp\left(-\frac{W_{tot}(x)}{kT}\right) dx} \quad \textbf{p - w model (8)}$$

where

$$W_{tot}(x) = W_{Qc}(x) + W_{vdW(p-w)}(x) + W_{el(p-w)}(x) \quad (9)$$

Eq. 8 will be called thereafter **particle-wall model**. The equation has been resolved numerically by using Simpson method: the channel thickness coordinate, along the x axis, was divided into 20 000 intervals with finer spacing (below 50 μm) where the deviations from normal behaviours were the most important.

Let us assume that, at the bottom of the channel where the sample should be, and where $\left(x - \frac{x^3}{w^2} + \frac{x^4}{2w^3}\right)$ can be considered equal to 1 (Wahlund and Giddings, 1987), the applied cross-flow is constant and uniform across the channel and the other forces are negligible compared to it. In this case, Eq. 8 can be resolved analytically and we obtain the well-known equation (Giddings, 1978):

$$R = 6\alpha(1 - \alpha) + 6\lambda(1 - 2\alpha) \left(\coth\left(\frac{1 - 2\alpha}{2\lambda}\right) - \frac{2\lambda}{1 - 2\alpha} \right) \quad \textbf{steric model (10)}$$

where α is the ratio of the particle radius to the channel thickness and λ is the retention parameter expressed as:

$$\lambda = \frac{kTV^0}{6\pi\eta Q_c r_h w^2} \quad (11)$$

In the case of point-like particles, this equation becomes

$$R = 6\lambda \left(\coth\left(\frac{1}{2\lambda}\right) - 2\lambda \right) \quad \textbf{classical model (12)}$$

Eq.12 and 10 will be called thereafter classical and steric model respectively.

3. Materials and methods

3.1. Instrumentation

Experiments were carried out in this study using an AF4 system (AF2000 Postnova Analytics, Landsberg Germany) coupled to a UV detector (Shimadzu, Kyoto Japan) set at 254 nm. A 350 μm thick spacer was used; channel dimensions were 27.7 cm in length and from 2.0 to 0.5 cm in width. Regenerated cellulose (RC) membrane of 10 kDa cut-off (Postnova Analytics, Landsberg Germany) was used for the experiments. In this study the outlet flow rate (Q_{out}), the cross-flow rate and the focus flow rate were fixed at 0.5 mL/min. Injections were performed by an automatic injection valve Rheodyne (IDEX Corporation, Oak Harbor, WA) equipped with a 500 μL sample loop. The injection volume was set at 60 μL for all experiments.

A Zetasizer Wallis (Corduan technologies, Pessac France) was used to determine the particle zeta potential of the carrier solutions with the laser Doppler electrophoresis (ELS) method. The zeta potential of the RC membrane was measured with a SurPASS electrokinetic analyser (Anton Paar GmbH, Graz Austria) using the streaming current approach (Bukšek, Luxbacher and Petrinić, 2010). The zeta potential is determined by using the measure of the streaming current between the extremities of the membrane resulted after ions displacement at the membrane-liquid interface, when applying a flow along the membrane for various pressure gradients.

The zeta potential measurements of the standards were carried out in a cell maintained at 20°C. The standards were diluted in NH_4NO_3 at 0.1 mmol L^{-1} to obtain a concentration of 13 $\mu\text{g g}^{-1}$. For the RC membrane, a square of 1 cm^2 was cut and placed in the flow through cell of the electrokinetic analyser. The device was then filled with NH_4NO_3 at different concentrations before measuring the zeta potential of the membrane.

To characterise the particle standards diameter, SEM measurements were conducted with a Zeiss Ultra-Plus scanning electron microscope equipped with two secondary electron detectors: SE2 and In-Lens. A drop of suspension was slowly deposited on a silica substrate placed on a spin-coater. The drop was then dispersed on a silica substrate by making the substrate slowly rotate on itself.

3.2.Reagents and Samples

Polystyrene latex nanosphere (PS) size standards used to study the effect of the particle size on the retention time had the following sizes: 23 ± 2 nm ($k=2$) measured by Photo Correlation Spectroscopy (PCS); 60 ± 10 nm ($k=1$) measured by Transmission Electron Microscopy (TEM), mean diameters traceable to NIST (Thermo Scientific, Freemont, USA); 107 ± 6 nm ($k=2$) measured by Disk Centrifuge Sedimentation (DCS), traceable to NIST (Sigma-Aldrich, Buch, Switzerland) and 200 nm (Sigma Aldrich) in diameter, (Thermo-Scientific, Freemont, USA); 190 ± 6 nm ($k=2$) measured by Disk Centrifuge Sedimentation (DCS), traceable to NIST (Sigma-Aldrich, Buch, Switzerland). They are called thereafter PS20, PS60, PS100 and PS200. The working solutions were prepared by diluting the stock solution in the carrier to obtain a mass concentration of $13 \mu\text{g g}^{-1}$. The carrier was a solution of ammonium nitrate, NH_4NO_3 (Sigma Aldrich), prepared in ultrapure water at a concentration ranging from 10^{-5} to 10^{-3} mol L^{-1} and filtered through a $0.1 \mu\text{m}$ RC filter (Postnova Analytics). The carrier pH was adjusted for the zeta potentials measurement with solutions of NH_3 and HNO_3 (Sigma-Aldrich, Buch, Switzerland), at 0.05 mol L^{-1} .

4. Results and discussion

The particle-wall model described by Eq. 8 has been tested for AF4 using polystyrene particles of increasing size from 20 to 200 nm. In order to test the model, it was necessary to first define all the parameters entering Eq. 8 and to overcome two fundamental questions concerning the determination of the void time and of the channel thickness. These two main issues have been discussed in section 4.1 and 4.4. The measurement of the zeta potential of the membrane (§4.2) and the particles (§4.3) is also presented.

4.1.Zeta potential of the membrane

Among parameters involved in Eq. 8, it was imperative to determine the zeta potential of the membrane to check whether its real impact on the retention time is in conformity with model predictions. The zeta potential of the membrane was measured at 20°C , at pH between 3 and 9 under ionic strengths of 0.1 and 1 mmol L^{-1} (Figure 49).

The instrument required a minimum ionic strength of 0.1 mmol L^{-1} to give a reliable result so the determination of the zeta potential at 0.01 mmol L^{-1} could not be realized. The ionic strength

affects the zeta potential value due to its influence on the Debye length. Therefore the magnitude of the zeta potential decreases when increasing ionic strength (Salgin, Salgin and Soyer, 2013). The calculated value of t_r did not increase significantly when the zeta potential value was below -50mV (data not shown). Hence, to model experiments operated at ionic strength of 0.01mmol L^{-1} , a value of -50mV was assumed as the membrane zeta potential.

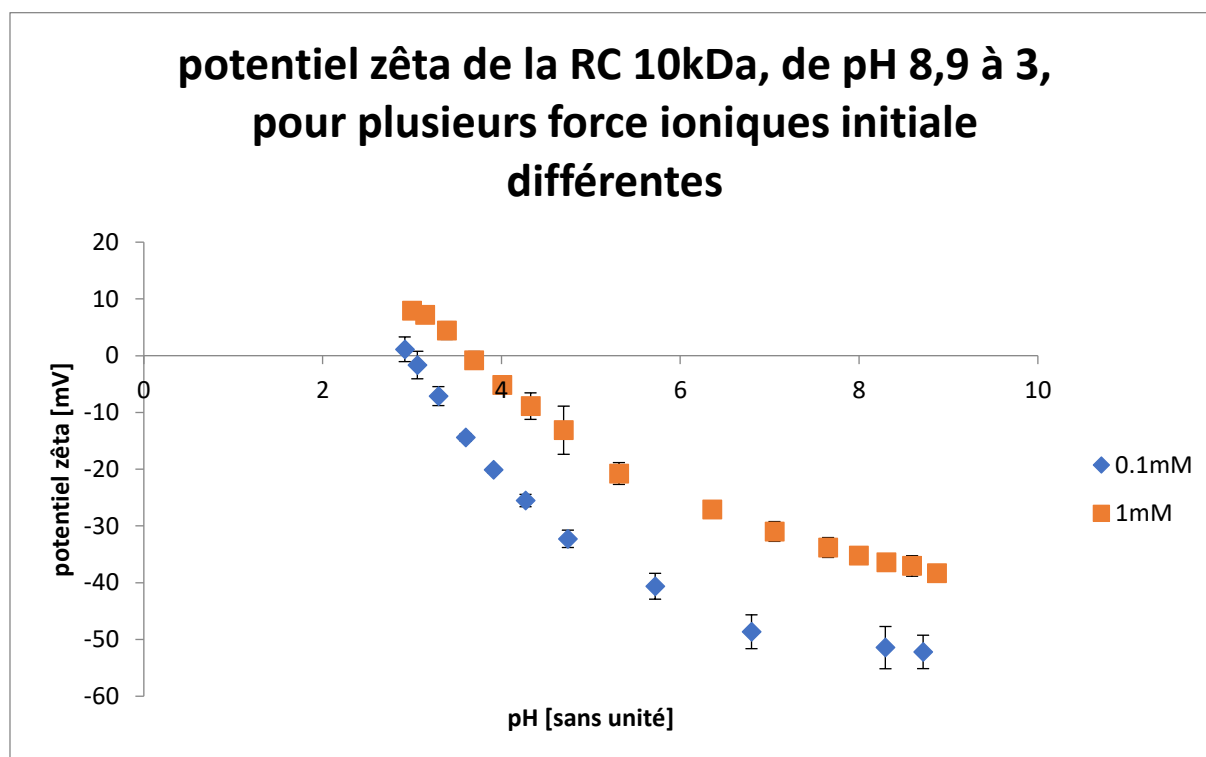


Figure 49. Zeta potential of a RC membrane as a function of pH at two different ionic strengths.

4.2.Characterization of the particles standard

The zeta potential of the polystyrene standards was measured at 20°C and pH 8.5 for ionic strengths of 0.01, 0.1 and 1 mmol L^{-1} . The measured values have been reported in Figure 50.

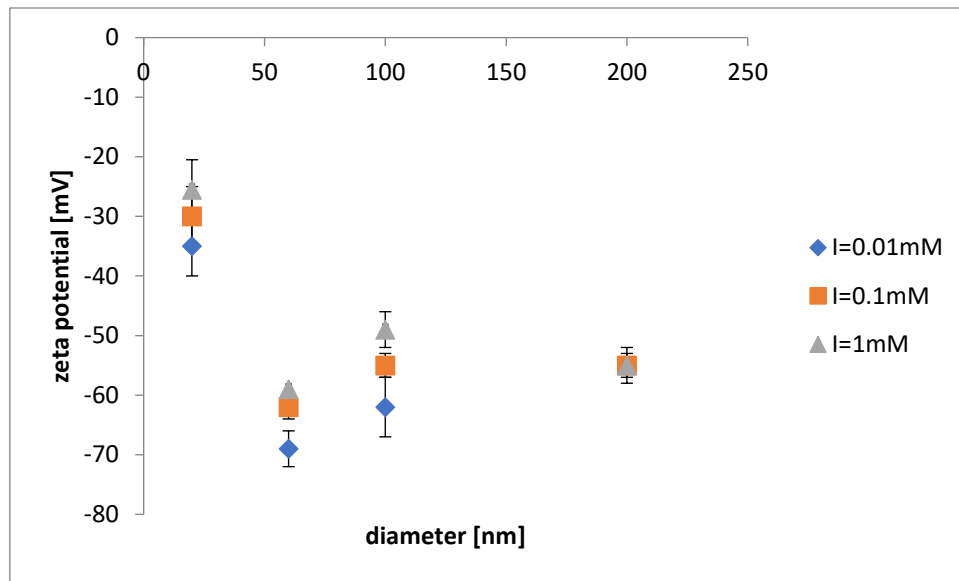


Figure 50. Zeta potentials of polystyrene standards at different ionic strengths

The standards diameter were characterised by SEM. Each standard suspension was analysed three times. In each analysis the diameter of 200 particles were measured automatically by the Platypus software (Pollen Metrology, Morians France). The mode value and standard deviation of each standard are reported in Table 18.

Table 18. Polystyrene standards diameter determined by SEM

Name	diameter [nm]
PS20	23±5(k=1)
PS60	60±2 (k=1)
PS100	99±4 (k=1)
PS200	186±3 (k=1)

4.3.Determination of the void time

The void time is the time that it would take for an “unretained” component to travel through the channel (Giddings, Williams and Benincasa, 1992). In every retention model, the void time needs to be determined or measured. Two approaches are reported in the literature. The first

way to determinet₀ is to use the equation elaborated by *Litzen and co-workers* (Litzén and Wahlund, 1991)

$$t_0 = \frac{V^0}{Q_c} \ln \left(1 + \frac{Q_c}{Q_{out}} \left(1 - \frac{w \left(b_0 z_{foc} - \frac{b_0 - b_L}{2L} z_{foc}^2 - Y \right)}{V^0} \right) \right) \quad (13)$$

where b_0 and b_L are the maximum and minimum channel breadth, z_{foc} is the focus position, L is the channel length, Q_{out} the elution flow rate and Y the area reduction of the accumulation wall due to the tapered channel inlet (Litzén, 1993).

In the second approach t_0 is considered as the elution time corresponding to the first peak eluted (Wahlund and Giddings, 1987; Dou, Jung and Lee, 2015). This approach is discouraged by *Wahlund* (Wahlund, 2013) because the composition of this first peak is unknown. According to Eq. 13, t_0 should only depend on the channel geometry and on the flow rate applied.

In practice, our experiments have shown that the void peak position also depends on the size of the sample as illustrated in Figure 51. The four standards have been injected one by one in the channel with a cross-flow and outflow rates fixed at 0.5 mL min⁻¹ and the void time was assumed in each experience as the average elution time of the void peak. Compared to small particles of 20 nm, the retention time decreases of about 0.3 min for particles higher than 60 nm and it seems to stabilize for 100 and 200 nm. The reason of this size dependence has not been elucidated, thereby to determine t_0 in the rest of this work it was preferred to use the approach based on Eq. 13. In fact, this approach will ensure that, in case the t_0 value is not the real one and an error is thus generated, it would be a systematic error and not a random one.

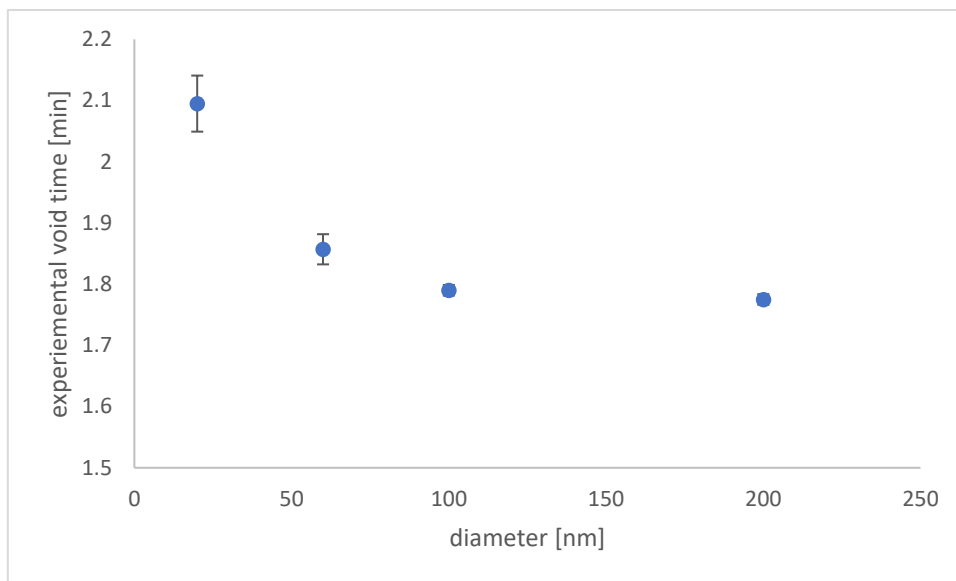


Figure 51. Experimental void time of different polystyrene latex standards of size; $Q_c = Q_{out} = 0.5 \text{ mL min}^{-1}$. The void time was assumed to be the average elution time of the void peak.

4.4.Channel thickness determination

The channel thickness is an important parameter that needs to be determined in order to apply the different retention models. Different methods have been proposed to determine the channel thickness (Giddings, Williams and Benincasa, 1992; Litzén, 1993; Bolinsson *et al.*, 2018). Among these methods, one implies the use of a calibration particle suspension and the calculation of the thickness from the retention model (Dou, Jung and Lee, 2015; Bolinsson *et al.*, 2018; Marioli *et al.*, 2019). This method has the advantage of determining the thickness when the cross-flow is applied, that is using the same experimental conditions for sample fractionation, which is an important factor to get a reliable value (Dou, Jung and Lee, 2015). In this study, three models have been mentioned in the theory part. Therefore, the three models have been also used to determine the effective thickness. In order to investigate the effect of the model on the effective thickness, the retention time of a series of polystyrene latex bead (PS20; PS60; PS100; PS200) was measured while the cross-flow and the outlet flow rates were kept constant at 0.5 mL min^{-1} in an AF4 channel with a nominal thickness of $350 \mu\text{m}$ equipped with a RC membrane. The carrier was a 1 mmol L^{-1} solution of NH_4NO_3 . The NH_4NO_3 concentration was fixed at 1 mmol L^{-1} to minimize the electrostatic interaction and to be in experimental conditions where the classical model can be used (Mori, Kimura and Tanigaki, 1990). The effective thickness has been determined from measured t_r using Eq. 8, 10 and 12, where t_r has been calculated as the mean retention time of the analyte peak.

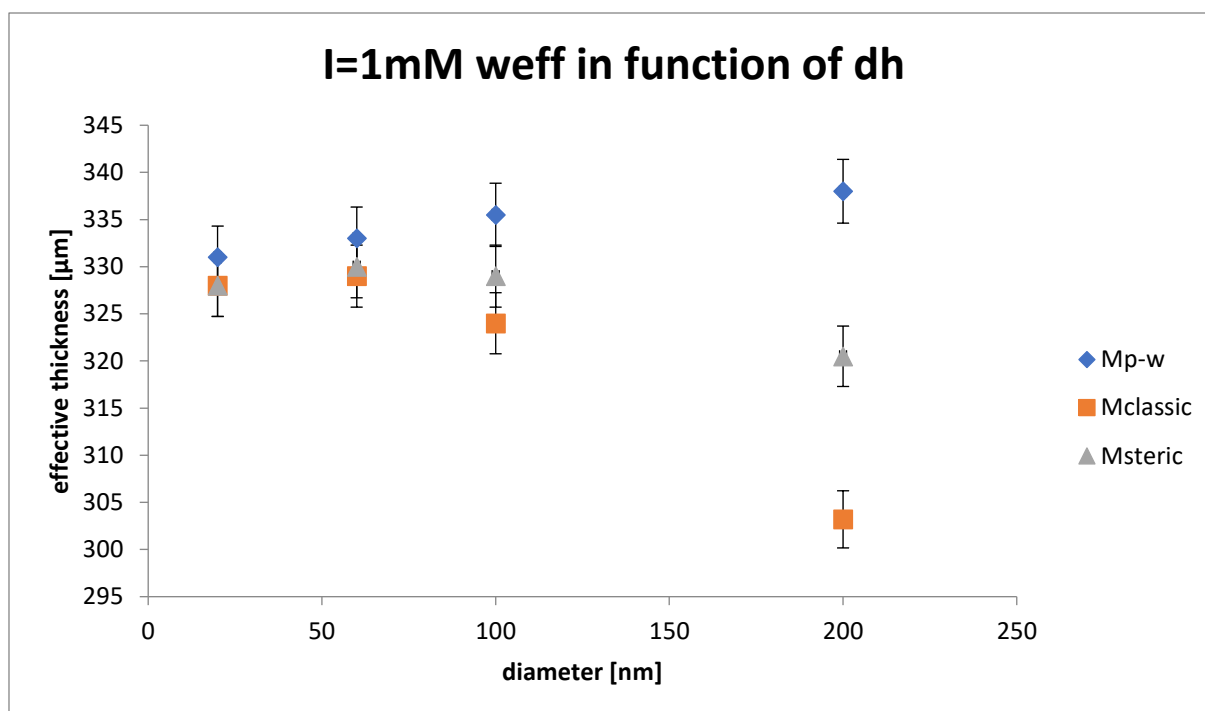
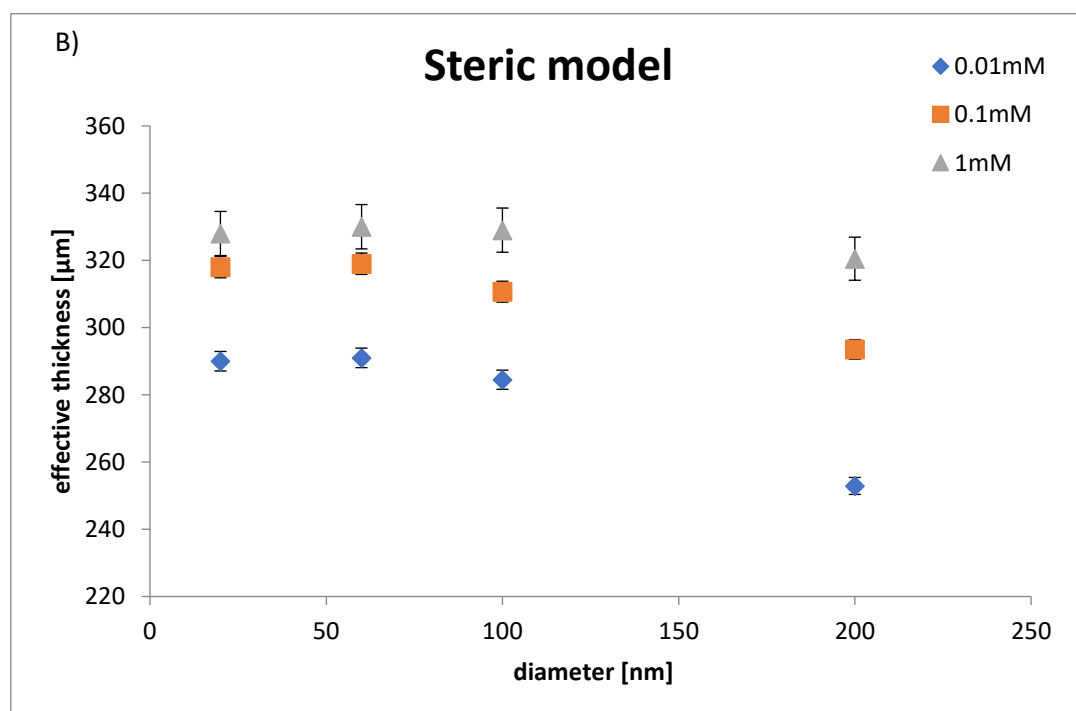
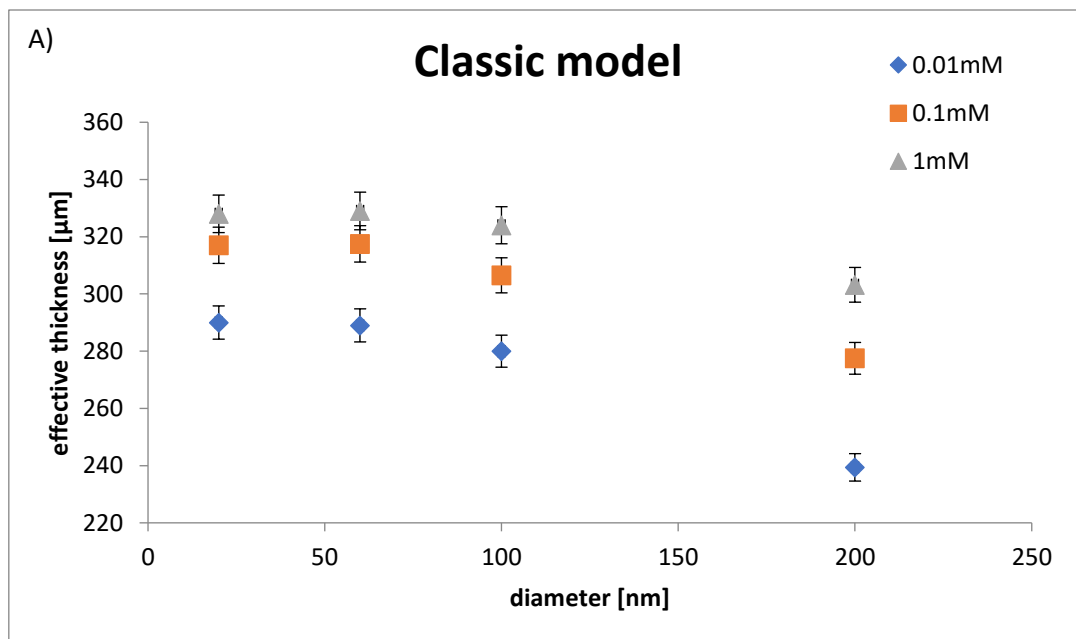


Figure 52. Effective thickness deduced for a nominal thickness of 350 μm , using PS of different size and applying the p-w model (blue circle), the classical model (red square) and the steric model (green triangle). $Q_c = Q_{out} = 0.5 \text{ mL min}^{-1}$. The carrier is a 1 mmol L^{-1} solution of NH_4NO_3 .

We can note in Figure 52 that with a hydrodynamic diameter below 100 nm the three models give consistent results, but for larger particles of 100 nm the results start to differ, and for 200 nm they significantly differ. The difference between the three models could be explained by a combination of the steric effect and the particle-wall interaction. As expected, the steric model compared to the classic one takes in account the steric effect, which is significant for particles with a diameter larger than 100 nm. In the same way, the p-w model corrects for the particle-wall interactions that apparently have a non-negligible impact on the retention of the 200 nm standard whereas their effect does not affect the retention of the smaller particles. This can be explained by the fact that big particles are closer to the wall than small particles during the elution. Indeed, the particle-wall interactions have the biggest impact on their retention behaviour. The same experiments have been performed for two other ionic strengths and the results are shown for each model in Figure 53.



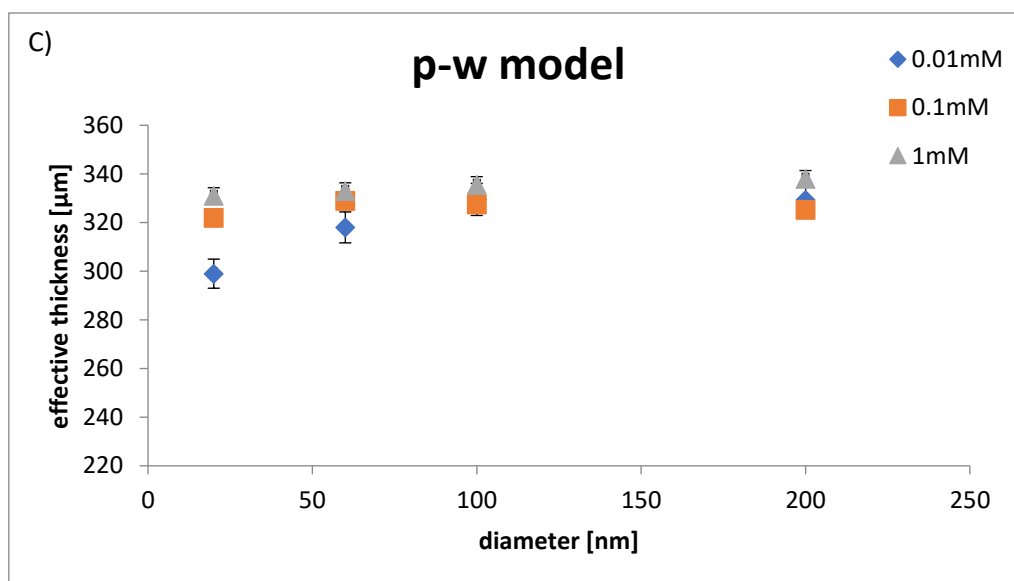


Figure 53. Determination of the channel effective thickness for different ionic strengths, with a) classical model, b) steric model, c) particle-wall model.

The classical and steric models have the same trends: the effective thickness decreases when the size of standard increases regardless of the ionic strength of the carrier. For both classical and steric models, the mean effective thickness increases when the ionic strength increases. This can be explained by the decrease of the electrostatic repulsion, which allowed the particles to remain longer in the channel and so artificially increase the channel effective thickness. By taking it into account, the particle-wall model allows to derive a constant value of w_{eff} regardless of the operating conditions, except for PSL20 at 0.01 mmol L⁻¹. One explication could be that the cross-flow rate applied is not strong enough to retain the PS20 in this condition. However, the cross-flow value was chosen as the best compromise for the elution of the four standards in the three different media and thus could not be changed.

To compare the three models for the calculation of the hydrodynamic diameter there are two possibilities: I) one may consider that, as w_{eff} is a physical parameter with only one true value in defined working conditions, based on the presented results one value of w_{eff} is selected and used for the model comparisons that follows. This value will be calculated as the average of the twelve w_{eff} determined by the particle-wall model that we have shown to be more accurate to find a constant value regardless of the operating conditions. II) The second possibility consists to admit that the effective thickness determined by the model is a kind of correction factor that includes the variation of the channel thickness from the nominal value but also other undefined

factors. In this case, the w_{eff} is proper to each model and each set of conditions. These two approaches have been evaluated in the following section.

4.4.1. Effective channel thickness as a physical parameter

Figure 54 shows the particle size found by each model as a function of the retention time of polystyrene standards for an applied cross-flow rate of 0.5 mL min^{-1} and different ionic strengths from 0.01 to 1 mmol L^{-1} . The blue, red and green curves represent the particle-wall model predictions for ionic strengths of 0.01 , 0.1 and 1 mmol L^{-1} respectively. The experimental points determined for each ionic strength were added in the figure in the same colour to compare the theory to the practice. A w_{eff} average value of $327 \text{ }\mu\text{m}$ was used, calculated with all the values found by the particle-wall model that we have shown to be more accurate to find a constant value regardless of the operating conditions. In fact, this model has provided the lowest standard deviation, $10 \text{ }\mu\text{m}$, on w_{eff} out of the three models regardless of the standard and the carrier ionic strength used. A w_{eff} of $327 \mu\text{m}$ is in agreement with previous studies reporting that RC membranes generally display a $20 \text{ }\mu\text{m}$ difference between the compressed and uncompressed part (Litzén, 1993; Wahlund, 2013). The parameters used for the models calculations are reported in Table 19.

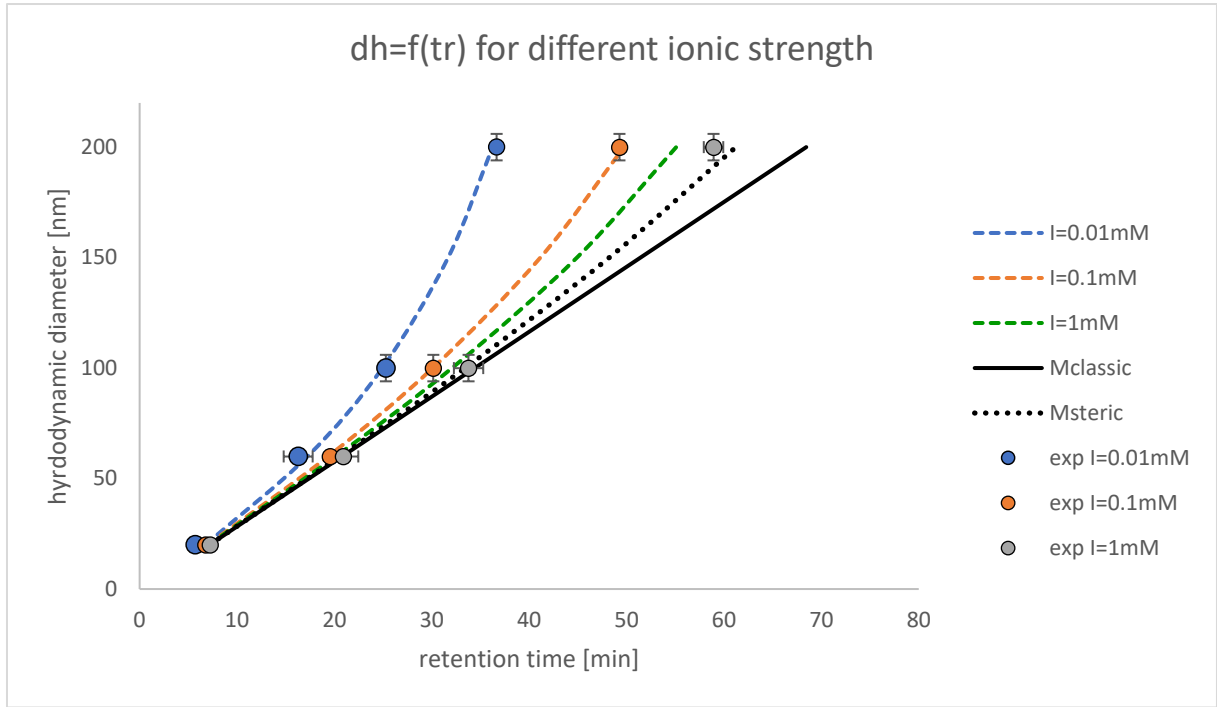


Figure 54. Hydrodynamic diameter predicted by the classic model (black line), the steric model (black dotted line) and the p-w model at different ionic strengths in the range 0.01-1 mmol L⁻¹.

$$Q_{out} = 0.5 \text{ mL min}^{-1}, Q_c = 0.8 \text{ mL min}^{-1}, w = 350 \text{ }\mu\text{m}.$$

The Hamaker constant necessary for the application of the particle-wall model was taken from the literature (Qu *et al.*, 2016) and the geometric void volume has been calculated as the product of w_{eff} by the channel total area. The zeta potentials of the AF4 membrane and of the particles have been measured for a pH value of 8.5 for the corresponding ionic strengths (Figures 49 and 50).

Table 19. List of the parameters used for models calculations

parameters	Values	Unit
A_{123}	$4.26 \cdot 10^{-20}$	J
A_{tot}	32.9 ± 0.1	cm^2
T	293 ± 1	K
Qc	0.5 ± 0.05	mL min^{-1}
$w_{eff-classic}$	327 ± 10	μm
$w_{eff-steric}$	310 ± 12	μm
$w_{eff-p-w}$	326 ± 3	μm
η	$0.01 \pm 2.5 \cdot 10^{-5}$	$\text{g cm}^{-1} \text{s}^{-1}$

The three models predicted different retention behaviour with larger gaps for big particles in weak ionic strength media (Figure 54, blue curve vs steric and classic models). All the experimental points fit with the particle-wall model, apart for the PS200 that is slightly shifted from the prediction curve for an ionic strength of 1mmol L^{-1} . It is worth noting that even if the retention time changes with the ionic strength, a linear relation between the retention time and the particle is still observed for the small particles regardless of the carrier ionic strength (cf. Figure 54). Yet, the ionic strength influences the coefficient of this relationship and the upper size value below which this correlation can be observed. The fact that this linear relation is observed means that the classical model can be used for the size determination as long as the model has the same slope as the experimental trend. This can be achieved by introducing a correction factor to adjust the slope of the model with the experimental points. This factor may be the effective thickness.

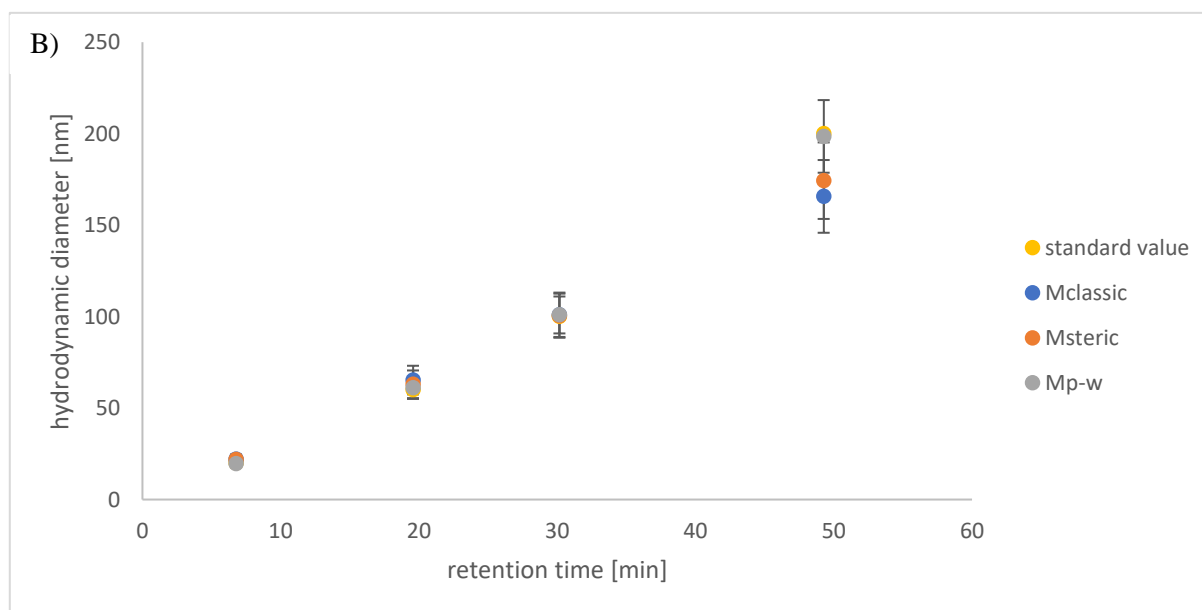
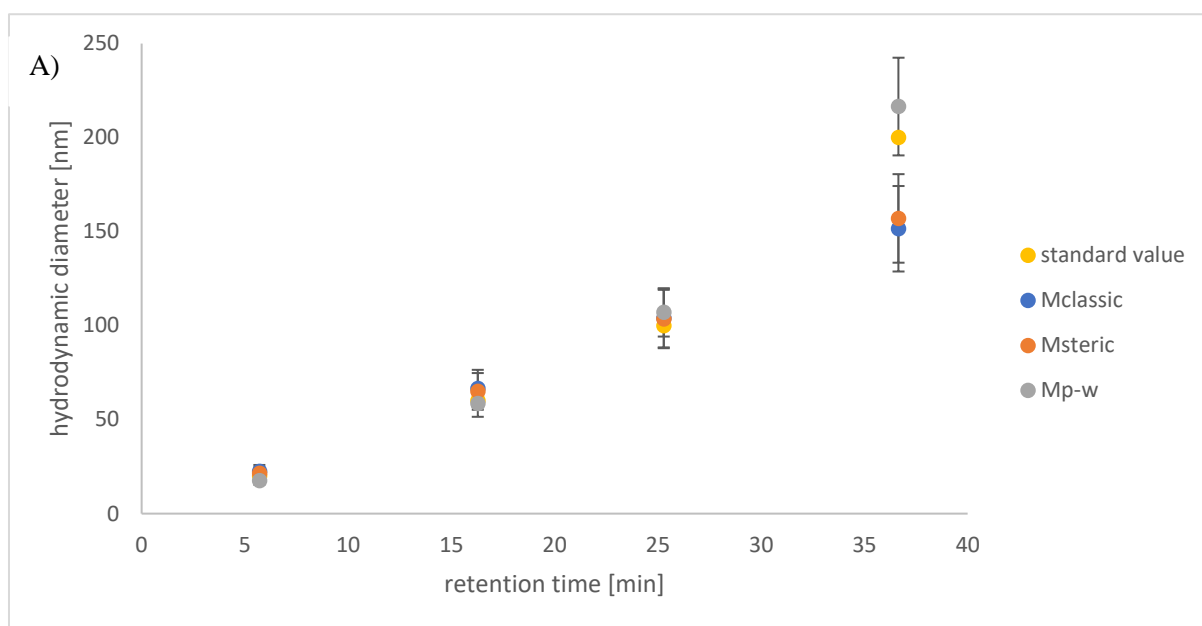
4.4.2. Effective thickness as a correction factor

When using the second approach, the thickness needs to be determined for each carrier and cross flow rate used as the behaviour of the particle depends on the interaction magnitude as shown by *Dou et al.* (Dou, Jung and Lee, 2015). The effective thickness used for each carrier has been determined as the average thickness found by using the four standards. Values are reported in Table 20 with the uncertainty associated ($k=1$) calculated as the standard deviation of the three replicates.

Table 20. Effective thickness value [μm] used for each model for ammonium nitrate carrier at different ionic strength

	[NH ₄ NO ₃] 0.01mM	[NH ₄ NO ₃] 0.1mM	[NH ₄ NO ₃] 1mM
M _{classic}	275±24	304±18	321±12
M _{steric}	279±18	310±12	327±4
M _{p-w}	319±13	326±3	336±4

By applying this approach, each model allows to determine hydrodynamic diameters close to the reference values from 20 nm to 100 nm, for each carrier ionic strength. For the 200 nm particles, the classical and steric models give values that differ significantly from the reference. That difference decreases with the ionic strength increase and became non-significant at 0.1 mmol L⁻¹ (Figure 55). This trend can be explained as follows. The goal of this approach is to use a channel thickness value calibrated with a size standard so that the models fit with practice and can be used regardless of the conditions. However, it is limited by the calibration conditions, if the standards used for the calibration do not exhibit the same elution behaviour as the analytes, some of the corresponding values of the sample will not be reproduced by the models fit. In the case studied here, the behaviour of the PS200 at ionic strength below 1 mmol L⁻¹ was different enough from the other standards so that average w_{eff} could not give a result that fit with the experimental value. This implies that, in order to use this approach, the user needs to calibrate the thickness with standards behaving similarly as the whole sample, which can be really challenging when dealing with polydisperse samples. A solution would be to calibrate the channel with several standards like here but the interest of using a model is less significant if it needs as many experiments as a regular external calibration to calculate a sample size.



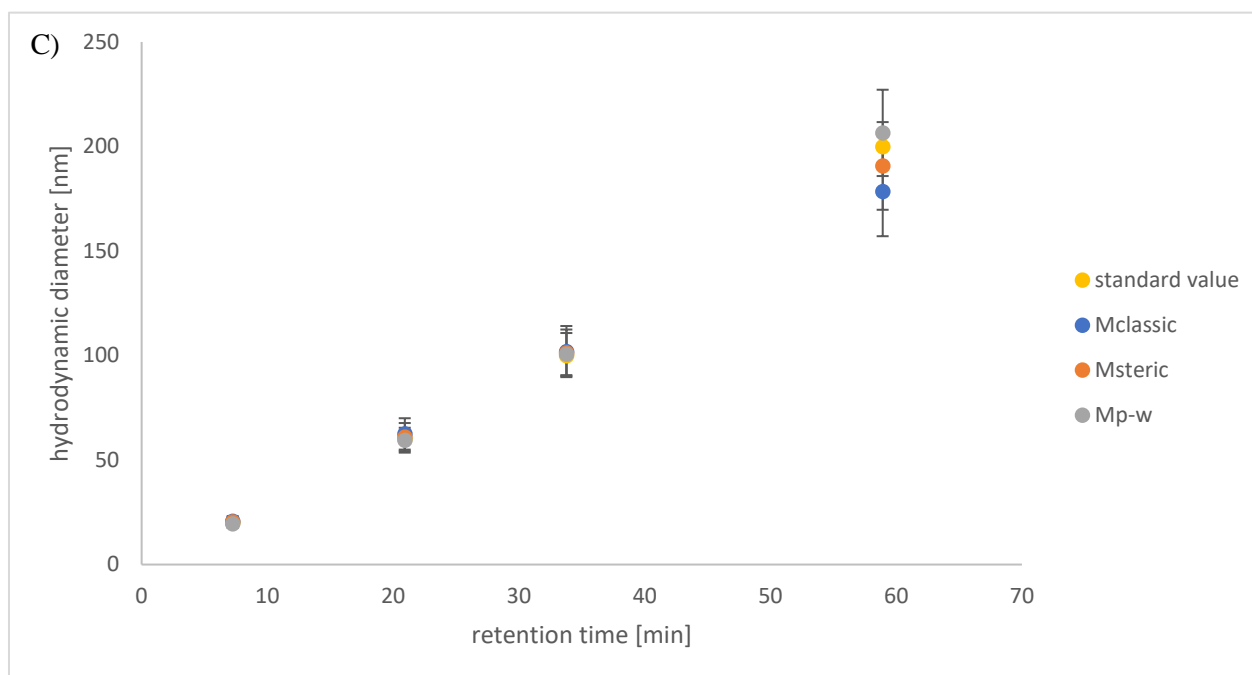


Figure 55. Hydrodynamic diameters determined through the 3 models for different ionic strengths: A) 0.01 mmol L⁻¹; B) 0.1 mmol L⁻¹; C) 1 mmol L⁻¹ by using a calibrated w_{eff} . $Q_c = Q_{out} = 0.5 \text{ mL min}^{-1}$.

By taking into account the electrostatic and van der Waals interactions, the particle wall model is able to give a better description of the retention behaviour in medium with low ionic strengths compared to the classic and steric model. One major advantage of this model is that the thickness determined by calibration is the same regardless of the ionic strength of the medium and would allow using the model without the need of a calibration when a direct measure of the thickness will be possible.

Conclusion

In this work, the applicability of a retention model that takes into account particle-wall interactions in AF4 is presented and its results compared with two well-known retention models. The issue of the channel thickness determination in AF4 was addressed by applying two different approaches. The first approach considered the thickness as a physical quantity which should be the same for all the retention models, while the second approach considered the thickness as a correction factor. This correction factor, specific for each model, allows to calibrate each model to fit with the retention behaviour observed in the experimental conditions

chosen. In both approaches, the particle-wall model was found to be more accurate and robust than the classical and steric models, especially in small ionic strength (i.e. $I \leq 0.1 \text{ mmol L}^{-1}$), to determine the size of the particle standards. A study to validate the performance of the particle-wall model as a size determination method is ongoing.

Nomenclature

A_{123}	the Hamaker constant [J]
A_{tot}	the total area of the channel [m^2]
b_0	the maximum channel breadth [m]
b_L	the minimum channel breadth [m]
c_0	the concentration at the position x_0 where $W_{tot}(x_0) = 0$ [$\text{mol} \cdot \text{m}^3$]
$c(x)$	the concentration profile in function of the x axis [$\text{mol} \cdot \text{m}^3$]
I	the ionic strength [mol m^{-3}]
k	the Boltzmann constant [J K^{-1}]
L	the channel length [m]
N_a	the Avogadro constant [mol^{-1}]
Q_c	the cross-flow [$\text{m}^3 \text{s}^{-1}$]
Q_{out}	Elution flow [$\text{m}^3 \text{s}^{-1}$]
R	the retention ratio [without unit]
r_h	the hydrodynamic radius [m]
T	the temperature [K]
t_0	the void time [s]
t_r	the retention time [s]
$\langle v \rangle$	the carrier average velocity [m s^{-1}]
$v(x)$	the carrier velocity in function of the x axis [m s^{-1}]
V^0	the void volume [m^3]
w	the channel thickness [m]
w_{eff}	the channel effective thickness [m]
$W_{el(p-w)}$	the potential energy due to the electrostatics interactions between the particle and the wall [J]

W_{vc}	the potential energy due to the cross-flow [J]
$W_{vdw(p-w)}$	the potential energy due to the van der Waal interactions between the particle and the wall [J]
$W_{tot}(x)$	the sum of the potential energy of a particle whose centre of mass is at the position x [J]
Y	area reduction of the accumulation wall due to the tapered channel inlet [m ²]
z_{foc}	focusing position [m]

Greek letters

α	ratio between the particle radius and the channel thickness [without unit]
ε_0	dielectric constant of the void [F m ⁻¹]
ε_r	dielectric constant of the medium [without unit]
η	viscosity of the medium [kg m ⁻¹ s ⁻¹]
ζ_p	particle zeta potential [V]
ζ_w	membrane zeta potential [V]
λ	retention parameter [without unit]
κ	Inverse of the Debye length [m ⁻¹]

Acknowledgment

This work has been supported by Ile de France Region through the DIM Analytics program.

References

Bolinsson, H. *et al.* (2018) ‘An alternative method for calibration of flow field flow fractionation channels for hydrodynamic radius determination: The nanoemulsion method (featuring multi angle light scattering)’, *Journal of Chromatography A*, 1533, pp. 155–163. doi: 10.1016/j.chroma.2017.12.026.

Boll, B. *et al.* (2018) ‘Impact of non-ideal analyte behavior on the separation of protein

aggregates by asymmetric flow field-flow fractionation', *Journal of Separation Science*, 41(13), pp. 2854–2864. doi: 10.1002/jssc.201701457.

Bukšek, H., Luxbacher, T. and Petrinić, I. (2010) 'Zeta potential determination of polymeric materials using two differently designed measuring cells of an electrokinetic analyzer', *Acta Chimica Slovenica*, 57(3), pp. 700–706.

Dou, H., Jung, E. C. and Lee, S. (2015) 'Factors affecting measurement of channel thickness in asymmetrical flow field-flow fractionation', *Journal of Chromatography A*, 1393, pp. 115–121. doi: 10.1016/j.chroma.2015.03.025.

Farmakis, L. *et al.* (2006) 'Estimation of the Hamaker constants by sedimentation field-flow fractionation', *Journal of Chromatography A*, 1137(2), pp. 231–242. doi: 10.1016/j.chroma.2006.10.019.

Giddings, J. ., Williams, P. S. and Benincasa, M. A. (1992) 'Rapid breakthrough measurement of void volume for field-flow fractionation channels', *Journal of Chromatography A*, 627(1–2), pp. 23–35. doi: 10.1016/0021-9673(92)87183-9.

Giddings, J. C. (1973) 'The Conceptual basis of field flow fractionation', *journal of chemical education*, 50(10), pp. 667–669.

Giddings, J. C. (1978) 'Displacement and Dispersion of Particles of Finite Size in Flow Channels with Lateral Forces. Field-Flow Fractionation and Hydrodynamic Chromatography', *Separation Science and Technology*, 13(3), pp. 241–254. doi: 10.1080/01496397808060222.

Gigault, J. and Hackley, V. A. (2013) 'Observation of size-independent effects in nanoparticle retention behavior during asymmetric-flow field-flow fractionation', *Analytical and Bioanalytical Chemistry*, 405(19), pp. 6251–6258. doi: 10.1007/s00216-013-7055-2.

Hansen, M. E. and Giddings, J. C. (1989) 'Retention Perturbations Due to Particle–Wall

Interactions in Sedimentation Field-Flow Fractionation', *Analytical Chemistry*, 61(8), pp. 811–819. doi: 10.1021/ac00183a006.

Hansen, M. E., Giddings, J. C. and Beckett, R. (1989) 'Colloid characterization by sedimentation field-flow fractionation. VI. Perturbations due to overloading and electrostatic repulsion', *Journal of Colloid And Interface Science*, 132(2), pp. 300–312. doi: 10.1016/0021-9797(89)90245-2.

Hoek, E. M. V. and Agarwal, G. K. (2006) 'Extended DLVO interactions between spherical particles and rough surfaces', *Journal of Colloid and Interface Science*, 298(1), pp. 50–58. doi: 10.1016/j.jcis.2005.12.031.

Hovingh, M. E., Thompson, G. H. and Giddings, J. C. (1970) 'Column Parameters in Thermal Field-Flow Fractionation', *Analytical Chemistry*, 42(2), pp. 195–203. doi: 10.1021/ac60284a003.

Jeon, S. J., Schimpf, M. E. and Nyborg, A. (1997) 'Compositional Effects in the Retention of Colloids by Thermal Field-Flow Fractionation', *Analytical Chemistry*, 69(17), pp. 3442–3450. doi: 10.1021/ac9613040.

Johann, C. *et al.* (2016) 'Colloidal Mechanisms of Gold Nanoparticle Loss in Asymmetric Flow Field-Flow Fractionation', *Analytical Chemistry*, 88(20), pp. 10065–10073. doi: 10.1021/acs.analchem.6b02397.

Karaiskakis, G. *et al.* (2002) 'Potential-barrier field-flow fractionation: Potential curves and interactive forces', *Journal of Liquid Chromatography and Related Technologies*, 25(13–15), pp. 2153–2172. doi: 10.1081/JLC-120013999.

Kato, H. *et al.* (2018) 'Separation of different-sized silica nanoparticles using asymmetric flow field-flow fractionation by control of the Debye length of the particles with the addition of

electrolyte molecules’, *Colloids and Surfaces A: Physicochemical and Engineering Aspects*, 538(October 2017), pp. 678–685. doi: 10.1016/j.colsurfa.2017.11.067.

Koliadima, A. and Karaiskakis, G. (1990) ‘Potential-barrier field-flow fractionation, a versatile new separation method’, *Journal of Chromatography A*, 517(C), pp. 345–359. doi: 10.1016/S0021-9673(01)95733-4.

Kowalkowski, T., Sugajski, M. and Buszewski, B. (2018) ‘Impact of Ionic Strength of Carrier Liquid on Recovery in Flow Field-Flow Fractionation’, *Chromatographia*, 81(8), pp. 1213–1218. doi: 10.1007/s10337-018-3551-z.

Lang, T., Eslahian, K. A. and Maskos, M. (2012) ‘Ion effects in field-flow fractionation of aqueous colloidal polystyrene’, *Macromolecular Chemistry and Physics*, 213(22), pp. 2353–2361. doi: 10.1002/macp.201200132.

Litzén, A. (1993) ‘Separation Speed, Retention, and Dispersion in Asymmetrical Flow Field-Flow Fractionation as Functions of Channel Dimensions and Flow Rates’, *Analytical Chemistry*, 65(4), pp. 461–470. doi: 10.1021/ac00052a025.

Litzén, A. and Wahlund, K. G. (1991) ‘Effects of temperature, carrier composition and sample load in asymmetrical flow field-flow fractionation’, *Journal of Chromatography A*, 548(C), pp. 393–406. doi: 10.1016/S0021-9673(01)88622-2.

Marioli, M. *et al.* (2019) ‘Application of microstructured membranes for increasing retention, selectivity and resolution in asymmetrical flow field-flow fractionation’, *Journal of Chromatography A*, 1605, p. 360347. doi: 10.1016/j.chroma.2019.07.001.

Martin, M. (1999) ‘Deviations to classical retention theory of field-flow fractionation’, *Journal of Chromatography A*, 831(1), pp. 73–87. doi: 10.1016/S0021-9673(98)00901-7.

Moens, C. *et al.* (2019) ‘A systematic evaluation of Flow Field Flow Fractionation and single-

particle ICP-MS to obtain the size distribution of organo-mineral iron oxyhydroxide colloids', *Journal of Chromatography A*, 1599, pp. 203–214. doi: 10.1016/j.chroma.2019.04.032.

Mori, Y., Kimura, K. and Tanigaki, M. (1990) 'Influence of Particle-Wall and Particle-Particle Interactions on Retention Behavior in Sedimentation Field-Flow Fractionation', *Analytical Chemistry*, 62(24), pp. 2668–2672. doi: 10.1021/ac00223a004.

Mudalige, T. K., Qu, H. and Linder, S. W. (2017) 'Rejection of Commonly Used Electrolytes in Asymmetric Flow Field Flow Fractionation: Effects of Membrane Molecular Weight Cutoff Size, Fluid Dynamics, and Valence of Electrolytes', *Langmuir*, 33(6), pp. 1442–1450. doi: 10.1021/acs.langmuir.6b03749.

Neubauer, E., V.d. Kammer, F. and Hofmann, T. (2011) 'Influence of carrier solution ionic strength and injected sample load on retention and recovery of natural nanoparticles using Flow Field-Flow Fractionation', *Journal of Chromatography A*, 1218(38), pp. 6763–6773. doi: 10.1016/j.chroma.2011.07.010.

Qu, H. *et al.* (2016) 'Importance of material matching in the calibration of asymmetric flow field-flow fractionation: material specificity and nanoparticle surface coating effects on retention time', *Journal of Nanoparticle Research*, 18(10). doi: 10.1007/s11051-016-3601-0.

Salgin, S., Salgin, U. and Soyer, N. (2013) 'Streaming potential measurements of polyethersulfone ultrafiltration membranes to determine salt effects on membrane zeta potential', *International Journal of Electrochemical Science*, 8(3), pp. 4073–4084.

Schachermeyer, S. *et al.* (2012) 'Impact of carrier fluid composition on recovery of nanoparticles and proteins in flow field flow fractionation', *Journal of Chromatography A*, 1264, pp. 72–79. doi: 10.1016/j.chroma.2012.09.050.

Wahlund, K.-G. and Giddings, J. C. (1987) 'an Asymmetrical Flow Field-Flow Fractionation

Channel Having One Permeable Wall', *Society*, (6), pp. 1332–1339.

Wahlund, K. G. (2013) 'Flow field-flow fractionation: Critical overview', *Journal of Chromatography A*, 1287, pp. 97–112. doi: 10.1016/j.chroma.2013.02.028.

Williams, P. S. *et al.* (1997) 'Colloid Characterization by Sedimentation Field-Flow Fractionation: Correction for Particle–Wall Interaction', *Analytical Chemistry*, 69(3), pp. 349–360. doi: 10.1021/ac9606012.

**Chapter VI: Metrological validation of a
retention model taking in account particle-wall
interactions for the measurement of
nanoparticle hydrodynamic diameter by
asymmetrical flow field-flow fractionation**

Chapter VI. Metrological validation of a retention model taking in account particle-wall interactions for the measurement of nanoparticle hydrodynamic diameter by asymmetrical flow field-flow fractionation

*Valentin de Carsalade du pont*¹, *Jabran Zaouali*² *Enrica Alasonati*^{1*}, *Nicolas Fischer*², *Mauricio Hoyos*³, *Michel Martin*³ and *Paola Fisicaro*¹

¹ Department of Biomedical and Inorganic Chemistry, Laboratoire National de Métrologie et d'Essai (LNE), 1 rue Gaston Boissier, Paris, 75015, France

² Mathematics and Statistics Department, Laboratoire National de Métrologie et d'Essais (LNE), 29 avenue Roger Hennequin, 78197 Trappes Cedex, France

³ Laboratoire de Physique et Mécanique des Milieux Hétérogènes (PMMH), ESPCI Paris, CNRS, 10 rue Vauquelin, 75231, Paris Cedex 05, France

*Corresponding authors

Email: enrica.alasonati@lne.fr (E. Alasonati)

Phone number: +33 140433971

Abstract:

Asymmetrical Flow Field-Flow Fractionation (AF4) is a fractionation technique that is widely used for analysing polydisperse particle and macromolecules samples. A retention model relying the particle retention time and its hydrodynamic radius has been validated as a method for particle size characterisation. The analytical performances of the method namely, the reproducibility, trueness and robustness of the method were evaluated. An uncertainty propagation by a Monte Carlo Method and a sensibility analysis were also performed in order to see which input quantities contribute the most to the radius uncertainty. This sensibility analysis showed that the channel thickness and the particle retention time contribute up to 81 % of the hydrodynamic radius uncertainty. The traceability of the most influential inputs parameters to the international system (SI) of unit were established.

Keywords: AF4, Method validation, Metrological traceability, Uncertainty propagation, Monte Carlo simulations

1. Introduction

Field flow fractionation (FFF) is a family of elution based techniques where the sample is injected in a flat channel through which a liquid flow elute in laminar regime transporting the sample thorough the channel. The sample components are fractionated during the elution by an external field applied perpendicularly to the elution flow (Giddings, 1966). The field push the sample components toward the channel bottom, called accumulation wall. Then the components migrate at different height in the channel according to their physico-chemical parameters (diffusion coefficient, electrophoretic mobility, thermal diffusion...) depending on the nature of the external field applied (hydrodynamic, electric, thermic...) (Schimpf, 2000; Gale and Srinivas, 2005; Geisler *et al.*, 2019). Due to the laminar regime the components equilibrated at different height will move at different speed and elute at different time. The FFF techniques have been increasingly used in recent years to fractionate several kind of macromolecules (Nilsson, 2013; Kavurt *et al.*, 2015; Abbate *et al.*, 2019; Fuentes *et al.*, 2019; Halabi *et al.*, 2020; Pascotto *et al.*, 2020; Marassi *et al.*, 2021), polymer (Noskov, Scherer and Schupp, 2010; Noskov, Scherer and Maskos, 2013) and nanoparticles (Abdolapur Monikh *et al.*, 2019; Amde, Tan and Liu, 2019; Loosli *et al.*, 2019; López-Sanz *et al.*, 2019; Nwoko *et al.*, 2019; Sikder *et al.*, 2019; Barber *et al.*, 2020; Klein *et al.*, 2020; Caputo *et al.*, 2021). An important FFF sub-technique, called asymmetric flow FFF (AF4), applies a hydrodynamic field on the sample components, called thereafter particles, by using a cross flow created by aspiring or pushing a part of the elution flow through the accumulation wall. In this case the particles are fractionated as a function of their diffusion coefficient (Wahlund and Giddings, 1987) (Figure 56). A retention model describing the particles behaviour inside a FFF channel has been developed by Giddings *et al.* (Giddings, 1973). This model allows determining the particle hydrodynamic radius from its retention time (Bae *et al.*, 2012; Astefanei *et al.*, 2015). This model depends of the following assumptions: a) the channel volume can be approximated as the space between infinite uniform parallel plates; b) the elution flow is parabolic; c) the interactions between particles and between the particles and the wall are considered as negligible compared to the field strength; d) steric effects are considered as negligible; e) the transverse concentration distribution of particles is close to equilibrium; f) the field strength is applied uniformly thorough the channel. However, several authors showed that the particles-wall interactions could not be neglected when the carrier salt concentration is low (Ulrich *et al.*, 2012; Losert *et al.*, 2013; Bendixen *et al.*, 2014; Kowalkowski, Sugajski and Buszewski, 2018). Hansen *et al.* proposed a retention model for the sedimentation FFF which takes the particle-

membrane interactions into account (Hansen and Giddings, 1989). The applicability of the model to the AF4 has been recently demonstrated (cf. Chapter V).

To provide reliable and comparable results, method validation and metrological traceability have to be demonstrated. According to the ISO standard 17025 the method validation can include, among others, calibration using reference standards or reference materials, systematic assessment of the factors influencing the result, comparison of results achieved with other validated methods, interlaboratory comparisons and evaluation of measurement uncertainty of the results based on an understanding of both theoretical and practical aspects of the method (ISO/IEC 17025:2017)

In this paper the validation of the model applied to AF4 taking the particle-membrane interactions into account is presented. According to the ISO/IEC 17025:2017, the following approach has been applied: use of reference standards to evaluate the method trueness by the normalised error, establishment of a complete uncertainty budget based on a Monte Carlo method (MCM)(Ceria *et al.*, 2017) including the evaluation of all the input quantities and a sensitivity analysis using the Spearman correlation coefficient to identify the variables that influence more the measurand uncertainty (Allard and Fischer, 2018). Finally, the metrological traceability of the method is discussed.

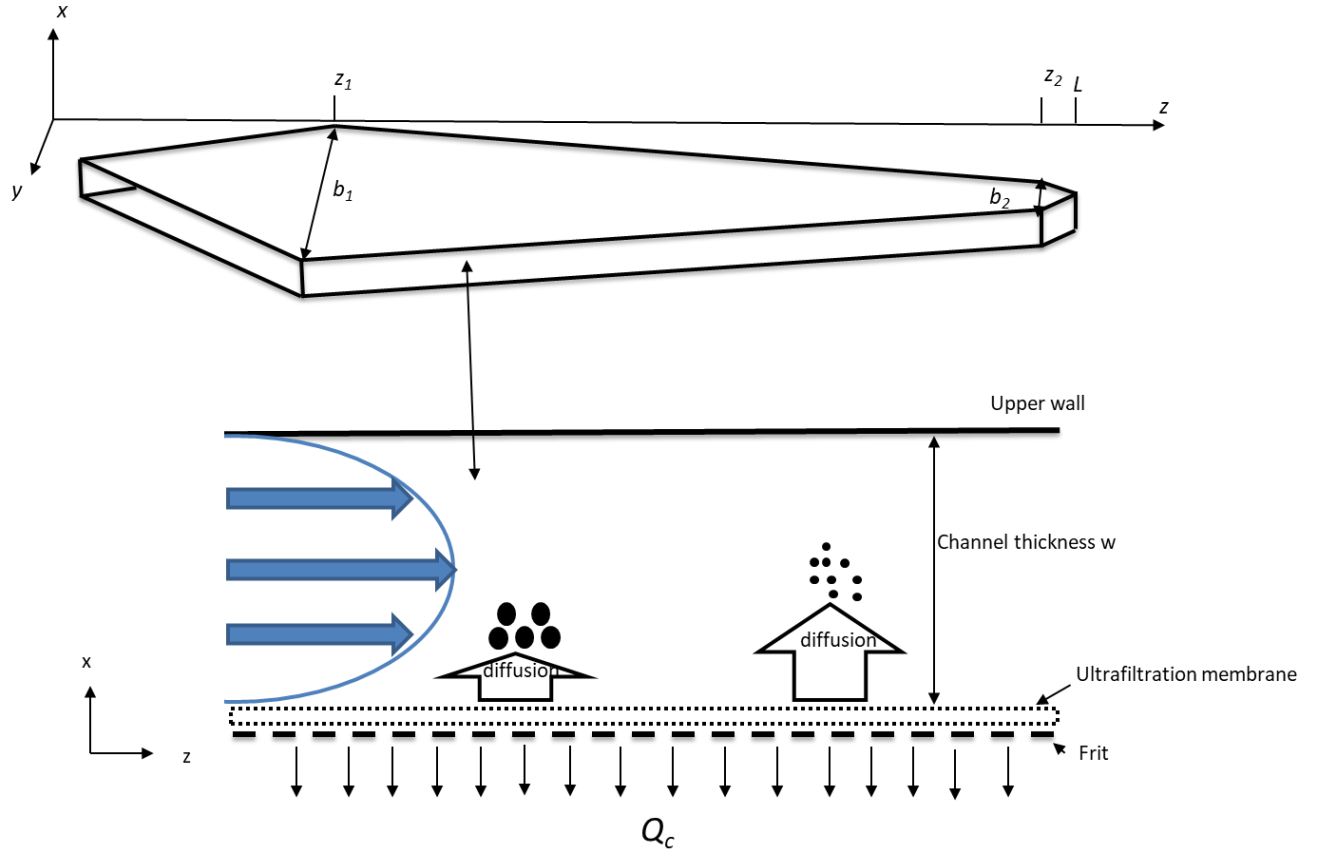


Figure 56. AF4 principle and channel geometry

2. Theory

2.1 FFF theory

The FFF theory describing the particle retention behaviour in the channel and the relationship relying the hydrodynamic diameter to the particle retention time has been described in detail elsewhere (Giddings, 1966; Hovingh, Thompson and Giddings, 1970) The present work focus on the retention model taking into account particle-wall interaction which mathematic formalisation has been fully described in (Hansen and Giddings, 1989): only the most important equations will be defined below.

The particle retention time, t_r , can be determined by (Hansen and Giddings, 1989)

$$t_r = \frac{t_0 \int_{r_h}^{w-r_h} \exp\left(-\frac{W_{tot}(x)}{kT}\right) dx}{6 \int_{r_h}^{w-r_h} \exp\left(-\frac{W_{tot}(x)}{kT}\right) \left(\frac{x}{w} - \frac{x^2}{w^2}\right) dx} \quad (1)$$

Where t_0 is the void time, w is the thickness of the channel, r_h is the particle hydrodynamic radius, $W_{tot}(x)$ is the sum of the potential energies of a particle whose centre of mass is at the position x , k is the Boltzmann constant and T the temperature.

In dilute conditions, the forces applied on the analyte are the cross-flow, the van der Waals forces and the electrostatic interactions between the particle and the wall. The potential energy of the cross-flow force, W_{Qc} , can be expressed as (Wahlund and Giddings, 1987)

$$W_{Qc} = \frac{Q_c w 6 \pi \eta r_h}{V^0} \left(x - \frac{x^3}{w^2} + \frac{x^4}{2w^3} \right) \quad (2)$$

where Q_c is the cross-flow rate, η the carrier viscosity and V^0 the geometric void volume. The potential energy of the van der Waals forces, $W_{vdW(p-w)}$, is equal to (Hoek and Agarwal, 2006)

$$W_{vdW(p-w)} = -\frac{A_{123}}{6} \left(\frac{r_h}{x - r_h} + \frac{r_h}{x + r_h} + \ln \frac{x - r_h}{x + r_h} \right) \quad (3)$$

where A_{123} is the Hamaker constant which represents the interactions between the particle 1 and the wall 3 in the medium 2. Finally, the potential energy of the electrostatics interactions, $W_{el(p-w)}$, is defined by (Hansen and Giddings, 1989)

$$W_{el(p-w)} = 64 \pi \varepsilon_0 \varepsilon_r r_h \left(\frac{kT}{e} \right)^2 \tanh \left(\frac{e\psi_p}{4kT} \right) \tanh \left(\frac{e\psi_w}{4kT} \right) \exp(-\kappa(x - r_h)) \quad (4)$$

where ε_0 and ε_r are the dielectric constants of the void and the medium respectively, e is the elementary charge, ψ_p and ψ_w are the surface charges of the particle and the wall respectively. The constant κ is the inverse of the Debye length and can be expressed as (Hansen and Giddings, 1989)

$$\kappa = \sqrt{\frac{2e^2 N_a I}{\varepsilon_0 \varepsilon_r kT}} \quad (5)$$

in which N_a is the Avogadro constant and I , the carrier ionic strength. The t_0 has been determined using the equation developed by Litzen et al.

$$t_0 = \frac{V^0}{Q_c} \ln \left(1 + \frac{Q_c}{Q_{out}} \left(1 - \frac{w \left(b_0 z_{foc} - \frac{b_0 - b_L}{2L} z_{foc}^2 - Y \right)}{V^0} \right) \right) \quad (6)$$

where b_0 and b_L are the maximum and minimum channel breadth, z_{foc} is the focus position, L is the channel length, Q_{out} the elution flow rate and Y the area reduction of the accumulation wall due to the tapered channel inlet (Litzén, 1993). The focusing position was also determined by the equation presented by Wang et al. (Wang *et al.*, 2018):

$$z_{foc} = z_1 + \frac{b_1 - \sqrt{b_1^2 - 2 \left(\frac{b_1 - b_2}{z_2 - z_1} \right) \frac{Q_{in}}{Q_c} A_{tot} + b_1 z_1 \left(\frac{b_1 - b_2}{z_2 - z_1} \right)}}{\frac{b_1 - b_2}{z_2 - z_1}} \quad (7)$$

Where z_1 and z_2 correspond to the position of b_1 and b_2 on the z -axis. A_{tot} is the total surface area of the membrane and Q_{in} is the inlet flow rate.

When including Eq. (2), (3) and (4) in Eq. (1), we obtain the relationship relying the hydrodynamic radius to the particle retention time. Due to the complexity of this equation, it was not possible to give an explicit analytical expression of the hydrodynamic radius. A numerical expression was determined by using the Python function *scipy.optimize.fsolve* to resolve this inverse problem. In this case, the conventional approach of GUM could not be realised so the propagation of the uncertainty in Eq. (1) has been performed using the MCM.

3. Materiel and methods

3.1. Nanoparticles Standards for size values

The following nanoparticles have been used as size standards: polystyrene latex nanosphere of 20, 60, 100 and 200 nm (called thereafter PS20, PS60, PS100 and PS200), gold nanoparticles of 20, 40, 60 and 80 nm (called thereafter Au20, Au40, Au60 and Au80) and silicon dioxide nanoparticles of 80, 140 and 200 nm (called thereafter Si80, Si140 and Si200). The particles nominal diameter, the supplier and the technique used to characterise the standards are reported in Table 21. The working solutions were prepared by diluting the stock solution in the carrier to obtain a mass concentration of $13 \mu\text{g g}^{-1}$. The carrier was a solution of ammonium nitrate, NH_4NO_3 (Sigma Aldrich, Buch, Switzerland), prepared in ultrapure water at a concentration of $10^{-5} \text{ mol L}^{-1}$ and filtered through a $0.1 \mu\text{m}$ RC filter (AF2000 Postnova Analytics, Landsberg Germany). The carrier pH was adjusted for the zeta potential measurement with solutions of NH_3 and HNO_3 (Sigma Aldrich) at 0.05 mol L^{-1} .

Table 21. List of the standard nanoparticles diameter, supplier and technique used to characterise the size

Abbreviation	Diameter [nm]	Technique used to characterise the sample	Supplier
PS20	23 ± 5 (k=1)	SEM (characterized by LNE, Trappes, France)	Sigma-Aldrich, Buch, Switzerland
PS60	60 ± 2 (k=1)		
PS100	99 ± 4 (k=1)		Thermo-Scientific, Freemont, USA
PS200	186 ± 3 (k=1)		
Au20	19.6 ± 1.6 (k=1)	Not specified by the supplier	BBI solution, Crumlin, UK
Au40	42.4 ± 3.4 (k=1)		
Au60	60.8 ± 4.9 (k=1)		
Au80	80 ± 6.4 (k=1)		
Si80	81 ± 6 (k=1)	TEM	Nano-composix, San Diego, USA
Si140	142 ± 16 (k=1)		
Si200	194 ± 16 (k=1)		

3.2. Instrumentation

Experiments were carried out in this study using an AF4 system (AF2000 Postnova Analytics, Landsberg Germany) coupled to a UV detector (Shimadzu, Kyoto Japan) set at 254 nm. A 350 μm thick spacer was used; channel dimensions were 27.7 cm in length and from 2.0 to 0.5 cm in width. Regenerated cellulose (RC) membrane of 10 kDa cut-off (Postnova Analytics) was used for the experiments. In this study the outlet flow rate (Q_{out}), the cross-flow rate and the focus flow rate were fixed at 0.5 mL/min. The injection volume was set at 60 μL for all experiments.

A Zetasizer Wallis (Corduan technologies, Pessac France) was used to determine the particle zeta potential of the carrier solutions with the laser Doppler electrophoresis (ELS) method. The zeta potential of the RC membrane was measured with a SurPASS electrokinetic analyser (Anton Paar GmbH, Graz Austria) using the streaming current approach (Bukšek, Luxbacher and Petrinić, 2010).

The zeta potential measurements of the standards were carried out in a cell maintained at 20 °C. The standards were diluted in NH_4NO_3 at 0.1 mmol L^{-1} to obtain a concentration of 13 μg

g^{-1} . For the RC membrane, a square of 1 cm^2 was cut and placed in the flow through cell of the electrokinetic analyser. The device was then filled with NH_4NO_3 at different concentrations before measuring the zeta potential of the membrane.

SEM measurements were performed at LNE (LNE Nanotech Institute, Trappes, France) with a Zeiss Ultra-Plus scanning electron microscope equipped with two secondary electron detectors: SE2 and In-Lens were conducted to measure the nanoparticles standards diameter.

4. Results and discussion

4.1. Program operation and uncertainty propagation

The probability density function (PDF) of the measurand was obtained numerically, by using a MCM. The principle of the MCM consists to obtain the measurand distribution by calculating a large number of times the measurand value by picking input quantities generated from the PDF of each input quantity. In a first step, a PDF is attributed to each input parameter. The choice of PDF depends on the knowledge either experimental or in the literature available for the parameter. Supplement 1 of the GUM (Joint Committee For Guides In Metrology, 2008)) shows how to choose the appropriate PDF. Secondly, a random number generator is used to generate numbers from the PDF of input parameters to calculate the measurand PDF. Here, the simulation was run 10^6 times in order to have a distribution with a good representativeness.

Then it was necessary to develop a function working in two steps. Indeed, in AF4 the membrane placed at the channel bottom intrudes the channel space due to the compression exerted by the spacer: the channel effective thickness, w_{eff} , is then different from the spacer thickness (Fraunhofer and Winter, 2004). A classical method to determine the channel effective thickness is to use a particle with a known hydrodynamic diameter and measure its retention time in fixed experimental conditions. A retention model, in this case Eq. (1), is then used to determine w_{eff} (Wahlund, 2013; Dou, Jung and Lee, 2015; Bolinsson *et al.*, 2018). Consequently, initially, the program determines the w_{eff} PDF using the standard characteristics (r_h , A_{123et} and ζ_{pet}) by using the Monte Carlo method. The w_{eff} PDF is then used to determine the r_h PDF by repeating the same process. The others inputs parameters were not changed between the two steps.

4.2. Determination of the standard uncertainty of the inputs parameters

All the parameters used in the model have been listed in Table 22. The parameters have been divided in fourth categories. The first category groups all the **physical constants** used in the

model. Their values and uncertainties have been taken from the literature. The second category regroups all the **parameters constant for all the experiments** performed in this work, because they are characteristic of the system as, for example, the geometric parameters. The third category represent the **parameters associated to the size of the standard used to calibrate w_{eff}** as, for example its radius and its zeta potential. The last category groups the **parameter associated to the analysed sample**, like its retention time and zeta potential. Uncertainties resulting from statistical treatment of repeated measurement results are called type A whereas uncertainties resulting using some means other than statistical treatment of repeated measurement results are called type B. Values of the carrier viscosity, the Hamaker constants and the physical constants were taken from the literature and therefore are type B. All the others parameters values were measured experimentally.

Finally, a distribution law was attributed to each parameter. This distribution law represents the measure dispersion of the parameter. This distribution law is chosen in function on the knowledge on the parameter. In practice most of the measurement can be represent by a Gaussian distribution, also called normal law. The aim of this work was to represent accurately each parameter, therefore a normal law was applied on every parameter at the exception of the Hamaker constant which was represented with a rectangular distribution law also called uniform distribution law. This law increases the uncertainty compared to a normal law. It was chosen because, the Hamaker constant values were taken in the literature and no uncertainty was associated to the given value. Consequently, the parameter is presented with a range of its possible values rather than a mean and a standard deviation.

The parameters associated to the **channel geometry** (L, b_1, b_2, z_1, z_2) were measured with a ruler. Their uncertainty was taken as half of the ruler graduation, i.e. 0.5 mm. The different **flow rates** (Q_{out}, Q_{in}, Q_c) were determined by gravimetry. The mean and standard deviation of the flow rates were obtained by repeating three times the measurement. The **carrier viscosity** value and its uncertainty have been taken from the literature for a temperature of 192.98 K (Berstad *et al.*, 1988). The **carrier ionic strength** was calculated using the ion concentration determined by gravimetry. The mean and standard deviation were obtained by performing three times the measurement. The carrier **temperature** was measured with a temperature sensor. The mean and standard deviation were obtained by performing three times the measurement. Due to the difficulties to measure a **surface charge**, the membrane and particles surface charge entering in Eq. (1) have been approximated to their zeta potential. This approximation has already been used for similar cases when the surface charge was needed (Hansen and Giddings, 1989;

Martinez *et al.*, 2008). The **membrane zeta potential** was measured at 293 K, at pH 8.5 and for an ionic strength of 10^{-4} mol L⁻¹. The ionic strength used for the zeta potential measurement is higher than the one used during the AF4 analyses as the electrokinetic analyser used needed a minimum ionic strength of 10^{-4} mol L⁻¹ to function. It is known that the zeta potential decreases as the ionic strength increases (Salgin, Salgin and Soyer, 2013). However the calculation showed that there was no influence on the particle radius when the membrane zeta potential was over -50 mV. Which is the value measured with the ionic strength at 10^{-4} mol L⁻¹. Hence, the zeta potential of the membrane was taken as -50 mV. The mean value and standard deviation were determined from six measurements performed on 2 RC membranes coming from 2 distinct package.

The zeta potential of the standard and of the sample, ζ_{per} and ζ_p , were measured in the same conditions as the AF4 experiments (pH 8.5, T = 293 K and I = 0.01 mol L⁻¹). The mean values and standard deviations were determined from six measurements performed on 2 distinct suspensions. The PS standard radius was determined by SEM while the radius value of the other particles was taken from their data sheet given by the supplier. The size value of PS standards were taken as the mean value obtained from the 200 particles by SEM. The sample and standard retention time was determined as the mean time of the particle or standard retention peak. Special attention was paid to the estimate of the retention time, which is the experimental observed quantity of an AF4 analysis. The reproducibility of the analyses was taken into account by repeating the analysis nine times on three RC membranes with three different suspensions preparation. Moreover, the membrane aging was also considered by alternating the replicates of the sample and the standard (de Carsalade du pont *et al.*, 2019). The Hamaker constant values for the system particle-water-cellulose were taken from the literature (Leite *et al.*, 2012; Qu *et al.*, 2016). The w_{eff} in Table 22 was determined with the data of the PS60. The Au20 and Si200 were also used to calibrate w_{eff} when the model trueness is evaluated to verify if the choice of the standard used for the calibration has a significant impact on the results. These three particles were chosen as sufficiently representative of different size range and chemical natures.

Table 22. Input parameters used in Monte Carlo method

	parameter	type	mean value	uncertainty	distribution law	unit
Physical constants	k	B	$1.38065 \cdot 10^{-23}$	0	normal	J K ⁻¹
	ε_0	B	$8.85419 \cdot 10^{-12}$	0	normal	F m ⁻¹
	ε_r	B	78.5	0	normal	
	Na	B	$6.02214 \cdot 10^{23}$	0	normal	mol ⁻¹
	e	B	$1.60218 \cdot 10^{-19}$	0	normal	C
Parameters constant for all the experiments	η	B	$1.00103 \cdot 10^{-3}$	$1.3 \cdot 10^{-7}$	normal	kg m ⁻¹ s ⁻¹
	T	A	293.15	0.5	normal	K
	b_1	A	0.02	$5.0 \cdot 10^{-4}$	normal	m
	b_2	A	0.005	$5.0 \cdot 10^{-4}$	normal	m
	z_1	A	0.033	$5.0 \cdot 10^{-4}$	normal	m
	z_2	A	0.268	$5.0 \cdot 10^{-4}$	normal	m
	L	A	0.277	$5.0 \cdot 10^{-4}$	normal	m
	Q_{out}	A	0.55	$1.5 \cdot 10^{-4}$	normal	mL min ⁻¹
	Q_{in}	A	0.21	$2.1 \cdot 10^{-4}$	normal	mL min ⁻¹
	Q_c	A	0.5	0.02	normal	mL min ⁻¹
	ζ_w	A	-0.051	0.004	normal	V
	I	A	10^{-5}	$2.5 \cdot 10^{-8}$	normal	mol L ⁻¹
Parameters associated to the standard to determine w	A_{123et}	B	$4.26 \cdot 10^{-20} - 8 \cdot 10^{-20}$		uniform	J
	ζ_{pet}	A	-0.069	$5 \cdot 10^{-3}$	normal	V
	r_{het}	A	$3 \cdot 10^{-8}$	$1 \cdot 10^{-9}$	normal	m
	tr_{et}	A	976	48	normal	s
W_{eff} determined	W_{eff}	A	336	10	normal	μm
Parameters associated to the sample	A_{123}	B	$0.85 \cdot 10^{-20} - 0.95 \cdot 10^{-20}$		uniform	J
	ζ_p	A	-0.069	$5 \cdot 10^{-3}$	normal	V
	tr	A	28.05	1	normal	min

4.3.Result of the r_h probability density function

The probability density function of the hydrodynamic radius of the Si140, calculated with the experimental conditions listed in Table 22, is presented in Figure 57. In this configuration the MCM gives a mean value of 65.5 nm, a standard deviation representing 11.7% of the mean value and a 95% coverage interval with [r_{hmin} = 54.8 nm; r_{hmax} = 79.5 nm].

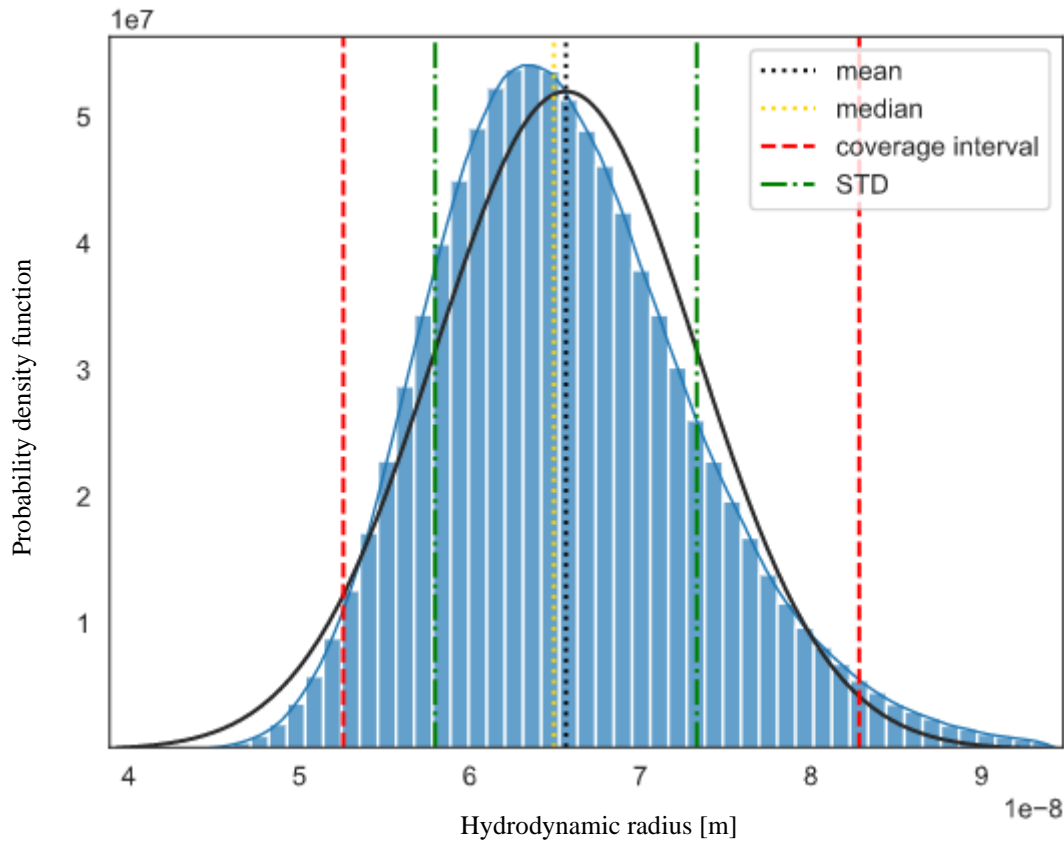


Figure 57. Probability density function of Si140 r_h

In order to optimize further measurements and understand the influence of the input quantities on the r_h calculation, the contribution of each input quantities to the r_h distribution have been evaluated. Such information can be obtained by calculating the sensibility coefficient of each parameter following the uncertainty propagation. The effect of each parameter was determined by using the rank correlation coefficient of Spearman(Allard and Fischer, 2018). Figure 58 represents the relative contribution of each input quantity to the r_h uncertainty.

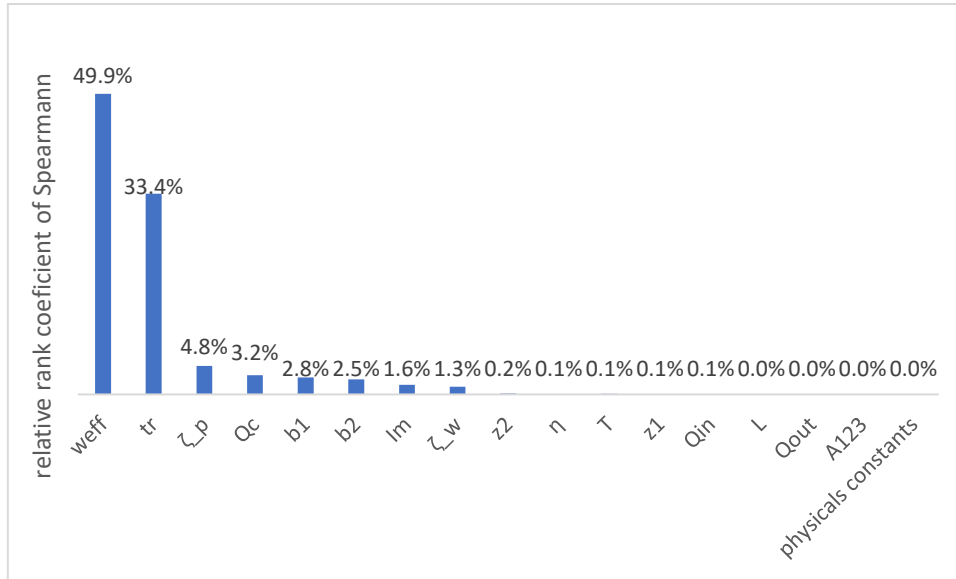


Figure 58. Relative contribution of each input quantity on the r_h uncertainty

It can be seen that w_{eff} has the largest contribution to r_h uncertainty by representing 49% of the total uncertainty. The second largest contributor is t_r followed by ζ_p , Q_c , b_1 and b_2 . The sum of the other parameters represents only 3.4% of the uncertainty and therefore can be considered as negligible. w_{eff} being the largest contributor, it will be important to reduce its uncertainty to improve r_h uncertainty. As w_{eff} is determined in the same way than r_h , the contribution of each input quantity was also determined using the rank correlation coefficient of Spearman (Figure 59).

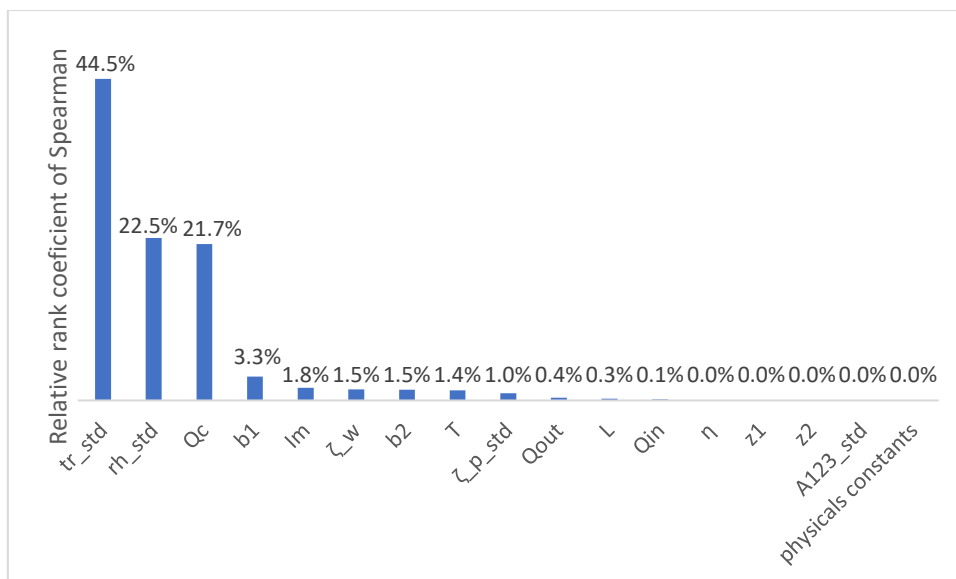


Figure 59. Relative contribution of each input quantity in the w uncertainty

The main contributor to w uncertainty are: The retention time and hydrodynamic radius of the standard followed by the cross flow rates. These three inputs contribute for 88%.

Based on the uncertainties obtained, the calculation of the normalized error (EN) has been applied to evaluate the trueness and the range of validity of the model. The EN corresponds to the difference between the radius calculated and the reference radius is divided by the sum of their variance (Eq.8). The calculated radius were considered to be not significantly different when $1 < EN < 1$ (Amarouche, 2015).

$$EN = \frac{r_1 - r_2}{\sqrt{U_1^2 + U_2^2}} \quad (8)$$

where r_{h1} is the calculated radius, r_{h2} is the reference radius and U_1 and U_2 their expanded uncertainty ($k=2$).

All the particles were analysed by using the same parameters presented in Table 22. The fractionation conditions used were the best compromise found to sufficiently retain the small particles and not retain too much the large particles in the channel. The particle radius was then calculated and an EN was determined for each particle. The effect of w_{eff} calibration was evaluated by using three different standards, Au20, PS60 and Si200 to calibrate w_{eff} . These standards were chosen in order to represents all the types of particles and different size. Figure 60 presents the normalised errors determined for each particle with a w_{eff} calibrated with three different standards. Among the 11 particles analysed, only one, the Au80, does not give a satisfying EN score. The Au80 was different from the other sample as the fractionation conditions applied for all sample resulted to a fractogram with a small UV signal compared to the other gold standard. A recovery rate showed that 85% of the Au80 injected was adsorbed during the analysis. It may be possible that the remaining part that attained the UV detector have been partially adsorbed on the membrane and then desorbed after a certain period which lead to an increase in retention time not taken into account by the model. Except for the Au80, the models provide good results regardless of the standard chosen or w_{eff} calibration.

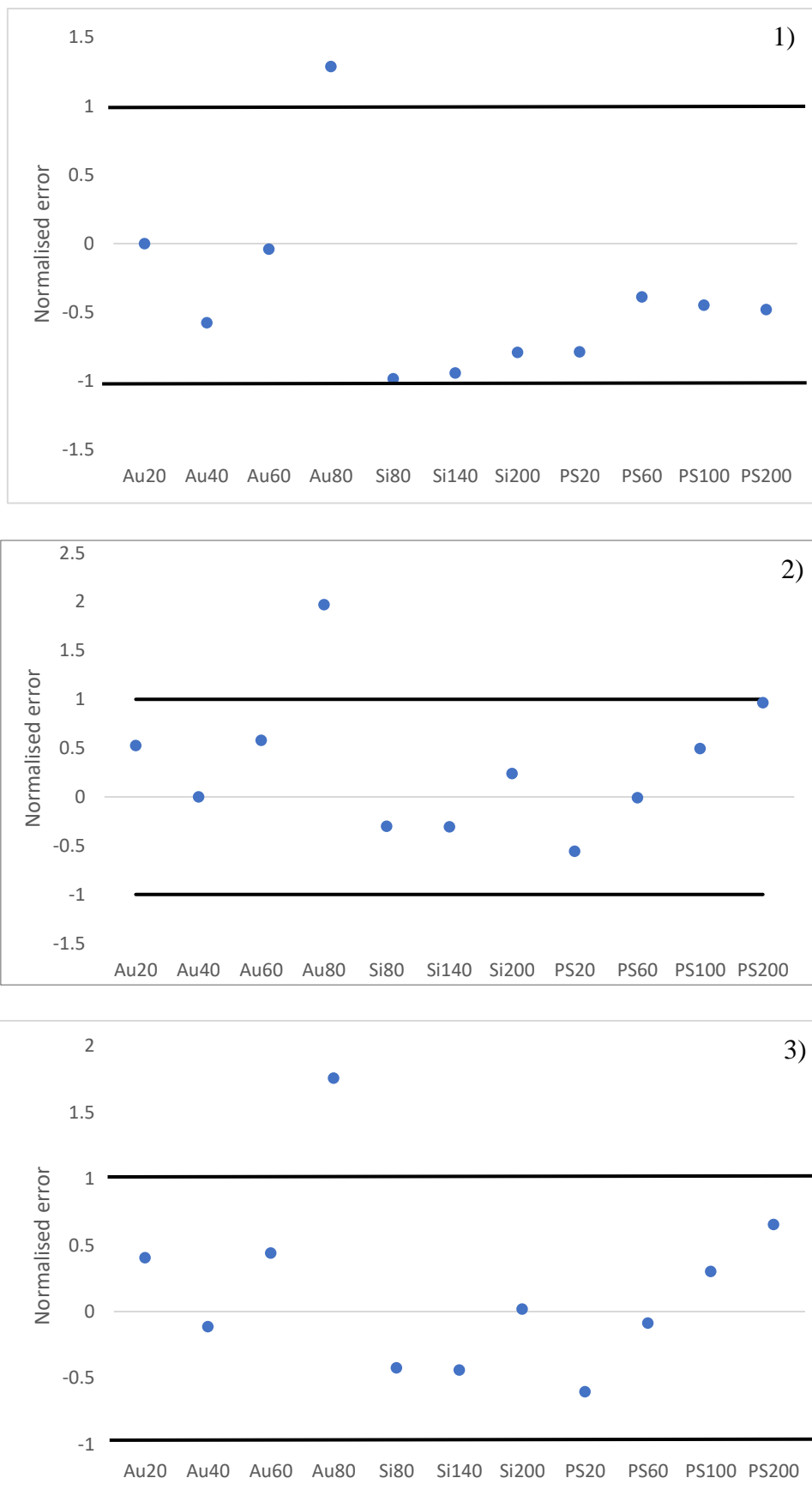


Figure 60. Normalised errors obtained by applying the model on standard nanoparticles with w_{eff} calibrated with 1) the Au20, 2) the PS60 3) the Si200.

4.4. Metrological traceability

According to VIM, the metrological traceability is the “*property of a measurement result whereby the result can be related to a reference through a documented unbroken chain of calibrations, each contributing to the measurement uncertainty. For measurements with more than one input quantity in the measurement model, each of the input quantity values should itself be metrologically traceable and the calibration hierarchy involved may form a branched structure or a network. The effort involved in establishing metrological traceability for each input quantity value should be commensurate with its relative contribution to the measurement result.*” (JCGM 200 : 2008 *International vocabulary of metrology — Basic and general concepts and associated terms (VIM)* Vocabulaire international de métrologie — Concepts fondamentaux et généraux et termes associés (VIM), 2008)

Therefore, the traceability to the International System (SI) of the measurement results obtained with the retention model was evaluated, focussing on those parameters that have a major contribution in the uncertainty budget, namely w_{eff} and t_r . w_{eff} himself mainly depending on r_{het} , t_{ret} and Q_c .

The balances used in these works were calibrated with secondary mass standards. The chronometer and AF4 software time measurement were traceable to the atomic clock. Therefore, the flow rates, ionic strength and retention time measurements were traceable to SI units. The parameters associated with the channel geometry were traceable to the SI by using a calibrated ruler. The standards used to calibrated w_{eff} were traceable to the SI due to the measurement performed on a SEM linked to the SI with a transfer standard calibrated by a metrological atomic force microscope (mAFM)(Feltin *et al.*, 2013). The traceability of the carrier viscosity, the zeta potential of the membrane and the particles as well as their Hamaker constant was not established yet. However, these four parameters contribute to less than 6% to the r_h uncertainty.

Conclusion

In this paper, the validation of an AF4 retention model for the determination of the particle size which takes into account the particle wall interaction has been shown.

The model has been validated for the measurement of PS, SiO₂ and Au nanoparticles in the diameter range between 20 and 200 nm. The estimation of each input quantity contribution on

the final result and the associated uncertainty allowed to have a clear vision on which input quantities need to be improved. It has been established that the channel thickness and the retention time are the main contributors to the uncertainty. To ameliorate the method accuracy the determination of the thickness needs to be improved. However, the accuracy of w_{eff} determination method by using a standard is difficult to improve as it would be challenging to decrease the uncertainty of the three major contributors to w_{eff} uncertainty (t_{ret} , r_{het} and Q_c). A solution would be to find another method which does not rely on the use of a standard to determine the channel effective thickness. It has been shown that the parameters contributing to 94% of the expanded uncertainty were traceable, which allows to consider the method results traceable to the SI.

Acknowledgment

This work has been supported by Ile de France Region through the DIM Analytics program.

References

- Abbate, R. A. *et al.* (2019) ‘Asymmetric flow field flow fractionation for the investigation of caseins cross-linked by microbial transglutaminase’, *Food Hydrocolloids*, 92(August 2018), pp. 117–124. doi: 10.1016/j.foodhyd.2019.01.043.
- Abdolahpur Monikh, F. *et al.* (2019) ‘Development of methods for extraction and analytical characterization of carbon-based nanomaterials (nanoplastics and carbon nanotubes) in biological and environmental matrices by asymmetrical flow field-flow fractionation’, *Environmental Pollution*, 255, p. 113304. doi: 10.1016/j.envpol.2019.113304.
- Allard, A. and Fischer, N. (2018) ‘Sensitivity analysis in practice: Providing an uncertainty budget when applying supplement 1 to the GUM’, *Metrologia*, 55(3), pp. 414–426. doi: 10.1088/1681-7575/aabd55.
- Amarouche, S. (2015) ‘Comparaisons interlaboratoires en étalonnage et en essai-Retour d’expérience’, in *17th International Congress of Metrology, CIM 2015*, pp. 1–5. doi: 10.1051/metrology/20150002006.
- Amde, M., Tan, Z. Q. and Liu, J. (2019) ‘Separation and size characterization of zinc oxide nanoparticles in environmental waters using asymmetrical flow field-flow fractionation’, *Talanta*, 200(March), pp. 357–365. doi: 10.1016/j.talanta.2019.03.074.
- Astefanei, A. *et al.* (2015) ‘Aggregation behavior of fullerenes in aqueous solutions: a capillary electrophoresis and asymmetric flow field-flow fractionation study’, *Analytical and Bioanalytical Chemistry*, 407(26), pp. 8035–8045. doi: 10.1007/s00216-015-8976-8.
- Bae, J. *et al.* (2012) ‘Application of flow field-flow fractionation (FIFFF) for size characterization of carbon black particles in ink’, *Microchemical Journal*, 104(December), pp. 44–48. doi: 10.1016/j.microc.2012.04.007.
- Barber, A. *et al.* (2020) ‘Coupling single particle ICP-MS with field-flow fractionation for

characterizing metal nanoparticles contained in nanoplastic colloids', *Environmental Science: Nano*, 7(2), pp. 514–524. doi: 10.1039/c9en00637k.

Bendixen, N. *et al.* (2014) 'Membrane-particle interactions in an asymmetric flow field flow fractionation channel studied with titanium dioxide nanoparticles', *Journal of Chromatography A*, 1334, pp. 92–100. doi: 10.1016/j.chroma.2014.01.066.

Berstad, D. A. *et al.* (1988) 'Accurate measurements of the viscosity of water in the temperature range 19.5-25.5°C', *Physica A: Statistical Mechanics and its Applications*, 151(2–3), pp. 246–280. doi: 10.1016/0378-4371(88)90015-5.

Bolinsson, H. *et al.* (2018) 'An alternative method for calibration of flow field flow fractionation channels for hydrodynamic radius determination: The nanoemulsion method (featuring multi angle light scattering)', *Journal of Chromatography A*, 1533, pp. 155–163. doi: 10.1016/j.chroma.2017.12.026.

Bukšek, H., Luxbacher, T. and Petrinić, I. (2010) 'Zeta potential determination of polymeric materials using two differently designed measuring cells of an electrokinetic analyzer', *Acta Chimica Slovenica*, 57(3), pp. 700–706.

Caputo, F. *et al.* (2021) 'Measuring particle size distribution and mass concentration of nanoplastics and microplastics: addressing some analytical challenges in the sub-micron size range', *Journal of Colloid and Interface Science*, 588, pp. 401–417. doi: 10.1016/j.jcis.2020.12.039.

de Carsalade du pont, V. *et al.* (2019) 'Asymmetric field flow fractionation applied to the nanoparticles characterization: Study of the parameters governing the retention in the channel', *EDP science*, 23001, p. 23001. doi: 10.1051/metrology/201923001.

Ceria, P. *et al.* (2017) 'Modelling of the X,Y,Z positioning errors and uncertainty evaluation for the LNE's mAFM using the Monte Carlo method', *Measurement Science and Technology*, 28(3), p. 34007. doi: 10.1088/1361-6501/28/3/034007.

Dou, H., Jung, E. C. and Lee, S. (2015) 'Factors affecting measurement of channel thickness in asymmetrical flow field-flow fractionation', *Journal of Chromatography A*, 1393, pp. 115–121. doi: 10.1016/j.chroma.2015.03.025.

Feltin, N. *et al.* (2013) 'CARMEN : une plateforme de caractérisation métrologique dédiée aux nanomatériaux', *Revue française de métrologie*, (31), pp. 41–54. doi: 10.1051/rfm/2012009.

Fraunhofer, W. and Winter, G. (2004) 'The use of asymmetrical flow field-flow fractionation in pharmaceuticals and biopharmaceuticals', *European Journal of Pharmaceutics and Biopharmaceutics*, 58(2), pp. 369–383. doi: 10.1016/j.ejpb.2004.03.034.

Fuentes, C. *et al.* (2019) 'Characterization of molecular properties of wheat starch from three different types of breads using asymmetric flow field-flow fractionation (AF4)', *Food Chemistry*, 298(June), doi: 10.1016/j.foodchem.2019.125090.

Gale, B. K. and Srinivas, M. (2005) 'Cyclical electrical field flow fractionation', *Electrophoresis*, 26(9), pp. 1623–1632. doi: 10.1002/elps.200410296.

Geisler, M. *et al.* (2019) 'Topology Analysis of Chain Walking Polymerized Polyethylene: An Alternative Approach for the Branching Characterization by Thermal FFF', *Macromolecules*, 52(22), pp. 8662–8671. doi: 10.1021/acs.macromol.9b01410.

Giddings, J. C. (1966) 'A New Separation Concept Based on a Coupling of Concentration and

Flow Nonuniformities', *Separation Science*, 1(1), pp. 123–125. doi: 10.1080/01496396608049439.

Giddings, J. C. (1973) 'The Conceptual basis of field flow fractionation', *journal of chemical education*, 50(10), pp. 667–669.

Halabi, A. *et al.* (2020) 'Structural characterization of heat-induced protein aggregates in model infant milk formulas', *Food Hydrocolloids*, 107(December 2019). doi: 10.1016/j.foodhyd.2020.105928.

Hansen, M. E. and Giddings, J. C. (1989) 'Retention Perturbations Due to Particle–Wall Interactions in Sedimentation Field-Flow Fractionation', *Analytical Chemistry*, 61(8), pp. 811–819. doi: 10.1021/ac00183a006.

Hoek, E. M. V. and Agarwal, G. K. (2006) 'Extended DLVO interactions between spherical particles and rough surfaces', *Journal of Colloid and Interface Science*, 298(1), pp. 50–58. doi: 10.1016/j.jcis.2005.12.031.

Hovingh, M. E., Thompson, G. H. and Giddings, J. C. (1970) 'Column Parameters in Thermal Field-Flow Fractionation', *Analytical Chemistry*, 42(2), pp. 195–203. doi: 10.1021/ac60284a003.

JCGM 200 : 2008 International vocabulary of metrology — Basic and general concepts and associated terms (VIM) *Vocabulaire international de métrologie — Concepts fondamentaux et généraux et termes associés (VIM)* (2008) *International Organization for Standardization Geneva* ISBN. Available at: http://www.bipm.org/utls/common/documents/jcgm/JCGM_200_2008.pdf.

Joint Committee For Guides In Metrology (2008) *Evaluation of measurement data — Guide to the expression of uncertainty in measurement*, *International Organization for Standardization Geneva* ISBN. Available at: <http://www.bipm.org/en/publications/guides/gum.html>.

Kavurt, U. B. *et al.* (2015) 'Membranes for separation of biomacromolecules and bioparticles via flow field-flow fractionation', *Journal of Chemical Technology and Biotechnology*, 90(1), pp. 11–18. doi: 10.1002/jctb.4473.

Klein, M. *et al.* (2020) 'Advanced nanomedicine characterization by DLS and AF4-UV-MALS: Application to a HIV nanovaccine', *Journal of Pharmaceutical and Biomedical Analysis*, 179. doi: 10.1016/j.jpba.2019.113017.

Kowalkowski, T., Sugajski, M. and Buszewski, B. (2018) 'Impact of Ionic Strength of Carrier Liquid on Recovery in Flow Field-Flow Fractionation', *Chromatographia*, 81(8), pp. 1213–1218. doi: 10.1007/s10337-018-3551-z.

Leite, F. L. *et al.* (2012) *Theoretical models for surface forces and adhesion and their measurement using atomic force microscopy*, *International Journal of Molecular Sciences*. doi: 10.3390/ijms131012773.

Litzén, A. (1993) 'Separation Speed, Retention, and Dispersion in Asymmetrical Flow Field-Flow Fractionation as Functions of Channel Dimensions and Flow Rates', *Analytical Chemistry*, 65(4), pp. 461–470. doi: 10.1021/ac00052a025.

Loosli, F. *et al.* (2019) 'Dispersion of natural nanomaterials in surface waters for better characterization of their physicochemical properties by AF4-ICP-MS-TEM', *Science of the Total Environment*, 682, pp. 663–672. doi: 10.1016/j.scitotenv.2019.05.206.

- López-Sanz, S. *et al.* (2019) 'Analytical strategy based on asymmetric flow field flow fractionation hyphenated to ICP-MS and complementary techniques to study gold nanoparticles transformations in cell culture medium', *Analytica Chimica Acta*, 1053, pp. 178–185. doi: 10.1016/j.aca.2018.11.053.
- Losert, S. *et al.* (2013) 'Membrane-particle interactions in asymmetric flow field flow fractionation (A4F)-The influence of the zeta-potential', 1, pp. 155–158.
- Marassi, V. *et al.* (2021) 'Characterization of red wine native colloids by asymmetrical flow field-flow fractionation with online multidetection', *Food Hydrocolloids*, 110(July 2020), p. 106204. doi: 10.1016/j.foodhyd.2020.106204.
- Martinez, R. E. *et al.* (2008) 'Surface charge and zeta-potential of metabolically active and dead cyanobacteria', *Journal of Colloid and Interface Science*, 323(2), pp. 317–325. doi: 10.1016/j.jcis.2008.04.041.
- Nilsson, L. (2013) 'Separation and characterization of food macromolecules using field-flow fractionation: A review', *Food Hydrocolloids*, 30(1), pp. 1–11. doi: 10.1016/j.foodhyd.2012.04.007.
- Noskov, S., Scherer, C. and Maskos, M. (2013) 'Determination of Hamaker constants of polymeric nanoparticles in organic solvents by asymmetrical flow field-flow fractionation', *Journal of Chromatography A*, 1274, pp. 151–158. doi: 10.1016/j.chroma.2012.12.001.
- Noskov, S., Scherer, C. and Schupp, W. (2010) 'Determination of Hamaker constants of polymeric nanoparticles by asymmetrical flow field-flow fractionation', 1274, p. 12205.
- Nwoko, K. C. *et al.* (2019) 'Matrix-dependent size modifications of iron oxide nanoparticles (Ferumoxytol) spiked into rat blood cells and plasma: Characterisation with TEM, AF4-UV-MALS-ICP-MS/MS and spICP-MS', *Journal of Chromatography B: Analytical Technologies in the Biomedical and Life Sciences*, 1124(March), pp. 356–365. doi: 10.1016/j.jchromb.2019.06.029.
- Pascotto, K. *et al.* (2020) 'Fractionation and characterization of polyphenolic compounds and macromolecules in red wine by asymmetrical flow field-flow fractionation', *Journal of Chromatography A*, 1629. doi: 10.1016/j.chroma.2020.461464.
- Qu, H. *et al.* (2016) 'Importance of material matching in the calibration of asymmetric flow field-flow fractionation: material specificity and nanoparticle surface coating effects on retention time', *Journal of Nanoparticle Research*, 18(10). doi: 10.1007/s11051-016-3601-0.
- Salgin, S., Salgin, U. and Soyer, N. (2013) 'Streaming potential measurements of polyethersulfone ultrafiltration membranes to determine salt effects on membrane zeta potential', *International Journal of Electrochemical Science*, 8(3), pp. 4073–4084.
- Schimpf, M. (2000) *Field flow fractionation handbook*. Wiley Inte. Edited by M. Schimpf, K. Caldwell, and J. C. Giddings. Wiley Interscience.
- Sikder, M. *et al.* (2019) 'Synthesis, characterization, and environmental behaviors of monodispersed platinum nanoparticles', *Journal of Colloid and Interface Science*, 540, pp. 330–341. doi: 10.1016/j.jcis.2019.01.036.
- Ulrich, A. *et al.* (2012) 'Critical aspects of sample handling for direct nanoparticle analysis and analytical challenges using asymmetric field flow fractionation in a multi-detector approach', *Journal of Analytical Atomic Spectrometry*, 27(7), p. 1120. doi: 10.1039/c2ja30024a.

Wahlund, K.-G. and Giddings, J. C. (1987) 'an Asymmetrical Flow Field-Flow Fractionation Channel Having One Permeable Wall', *Society*, (6), pp. 1332–1339.

Wahlund, K. G. (2013) 'Flow field-flow fractionation: Critical overview', *Journal of Chromatography A*, 1287, pp. 97–112. doi: 10.1016/j.chroma.2013.02.028.

Wang, J. L. *et al.* (2018) 'Theoretical and experimental investigation of the focusing position in asymmetrical flow field-flow fractionation (AF4)', *Journal of Chromatography A*, 1561, pp. 67–75. doi: 10.1016/j.chroma.2018.04.056.

Chapter VII:

**A novel approach to directly determine the
channel thickness: feasibility study**

Chapter VII: A novel approach to directly determine the channel thickness: feasibility study

Abstract

Through the previous chapters the determination of the channel thickness has been identified as a critical step for the implementation of the p-w model. The calibration of the channel thickness with a size standard was the best compromise given the methods available. However, this method provides values that depend upon the retention model applied for the calibration. The values obtained are then injected in the models, which corresponds more to a calibration of the model than to an actual measure of the channel thickness. In this chapter, a novel method to determine the channel thickness using a chromatic confocal sensor will be presented and the feasibility of the method will be demonstrated. The method is independent from the retention models employed and can be used *in situ* giving a value of thickness representative of the real working conditions.

1. On the measurement of the effective channel thickness

The accurate measurement of the channel thickness (w) is required for the determination of the hydrodynamic diameter, d_h . According to AF4 classical model, d_h is inversely proportional to the square of w (Chapter II, Eq. (22)), giving to this parameter higher weight than the other parameters involved in the retention model. On the other hand, the channel thickness affects

the separation resolution as it has been shown that the separation efficiency increases with w , when the cross flow rate is held constant (Dou et al. 2013). The channel thickness is expected to be smaller than the nominal thickness of the channel spacer due to the compressibility of the porous ultrafiltration membrane used as accumulation wall in the AF4 channel (Dou, Jung, and Lee 2015)(Chapter III, Figure 32). This protrusion changes the value of channel thickness, which is then called effective channel thickness, w_{eff} .

Several methods are reported in literature to measure w_{eff} (Bolinsson et al. 2018; Dou et al. 2015; Giddings, Williams, and Benincasa 1992; Häusele, Gindele, and Cölfen 2021). Most of these methods, have been reviewed by *Walhund* in his FFF critical overview (Wahlund 2013). The principal approaches are reported hereafter.

One of the methods consists into inject a low molecular compound in the channel, when no cross flow is applied, and measure its retention time. The void volume is then calculated with the compound retention time and the elution flow rate used for the experiment. After that, the channel thickness is determined by dividing the void volume by the channel area(Wahlund 2013).

Another approach, called “the break-through method”, determine the break-through point (t_b) of the void peak and use this value to calculate the void volume and then the thickness like the previous method. The break through point corresponds to the point of appearance of the peak with the molecules travelling with the fastest streamlines and is equal to (Giddings et al. 1992):

$$t_b = \frac{2}{3} t_0 \quad (VII.1)$$

where t_0 is the void time which corresponds to the mean time of the void peak. This expression is found by knowing that the highest streamlines velocity, v_{max} is equal to the streamlines average velocity, $\langle v \rangle$, multiplied by 3/2. In summary, the experimental measure of the t_0 is used to determine w_{eff} . This method has been recently studied by *Häusele et al.* which concluded that the experimental void time is not suited to w_{eff} determination as it leads to an overestimation of the results which is physically not possible (Häusele et al. 2021).

It is possible to measure the thickness when the membrane is replaced: a micrometer screw is used to measure the difference between the compressed and the uncompressed part of the membrane. This difference corresponds to the membrane part that intrudes in the channel and

is subtracted from the spacer thickness value (Wahlund 2013). Although based on a direct measurement, the results obtained have been questioned as the method cannot be performed *in situ* (Häusele et al. 2021).

Another method commonly used for w_{eff} determination consists in using a particle with a known hydrodynamic diameter (or diffusion coefficient) and measuring its retention time in normal experimental conditions (with the cross flow rate applied). A retention model (generally the classical model) is then used to determine w (Dou et al. 2015). This method has the advantage to be easy to apply. However, *Dou et al.* showed that the w_{eff} values obtained by this method depend on the cross flow applied, the carrier composition (ions and surfactant concentration) and the size of the particle used for the measurement (Dou et al. 2015). *Bolinsson et al.* proposed an alternative by injecting a mixture of particles and calculating the average thickness obtained from each population of the mixture (Bolinsson et al. 2018).

Most of these methods have the disadvantage to be indirect methods and to depend on the retention model equations (whatever the model). Indeed, the methods here presented could not be validated as nowadays no independent method exist to give a reference value of w_{eff} . Furthermore, calibrating the AF4 system with a standard of size, associated to the same unit as the measurand hinders the possibility to establish the FFF method as a primary method².

To overcome these problems, a novel method to directly characterise the channel thickness was conceived and will be presented here. Although the study could not be achieved, the feasibility of the method has been demonstrated.

2. Characteristics of the ideal method for the direct measurement of w_{eff}

To identify the most appropriate experimental approach to measure the channel thickness a set of specifications has been initially defined:

- The method should be able to be used *in situ* under classical experimental conditions used for the fractionation.

² **Primary method:** method having the highest metrological qualities, whose operation can be completely described and understood, for which a complete uncertainty statement can be written down in terms of SI units, and whose results are, therefore accepted without reference to a standard of the quantity being measured (Quinn 1997).

- Measurements should be performed all along the AF4 analysis (focusing, elution) and varying the critical separation parameters (cross flow and channel flow rates, carrier characteristics, ...) in order to monitor the behaviour of the membrane during the analysis and using different sets of parameters.
- Measurements should be performed all along the membrane lifetime in order to monitor the aging of the membrane on the protrusion effect.
- Measurements should be performed at different position in the channel to get an idea on the morphology of the membrane during analyses. This would allow to know if the membrane is deformed uniformly and confirm that the thickness is the same at each point of the channel which is one of the work hypothesis (parallel plate assumption) that needs to be verified in order to apply the retention models.
- The uncertainty associated to the measurement should not exceed 4% of the measured value: indeed, it has been shown in chapter VI that the thickness greatly weights on the uncertainty of the particle diameter. The calibration method used to determine w_{eff} in chapter 6 gave a standard deviation of 4% of the nominal value. A method with a low accuracy would lead to a large uncertainty on the particle diameter reducing the interest for the application of the retention model as a size characterization method.

To fulfil these specifications, it has been decided to implement a measurement system using a chromatic confocal sensor fixed in front of the channel and measuring through the windows present in the channel assembly. The windows are holes in the metallic front plate that allow to observe inside the channel through the plate made of poly(methyl methacrylate) (PMMA, also known as plexiglass). The sensor can be moved along the channel with micrometric precision in order to map the visible channel surface all along the analysis. The principle of the chromatic confocal sensor is presented in the following section.

2.1.Principle of chromatic confocal sensor

The working principle of the chromatic confocal sensor is based on the chromatic aberration, a phenomenon where the focusing point of the light depend on its wavelength (Molesini et al. 1984). Here a source generates a polychromatic light that is focused by a condenser in a small circular pinhole (Figure 61). The light is then reflected by a semi-transparent mirror and propagated through an objective lens that decomposes it in numerous monochromatic lights.

The image of the pinhole is formed at different distances as a function of the wavelength of the monochromatic light. The different beams will be back reflected or back scattered on the object surface, however only the beam that focuses on the object will be able to go through a second pinhole and to attain the photodetector. The distance between the sensor and the target (Figure 61) is then determined from the wavelength registered (Ruprecht et al. 2005)(Miks, Novak, and Novak 2010).

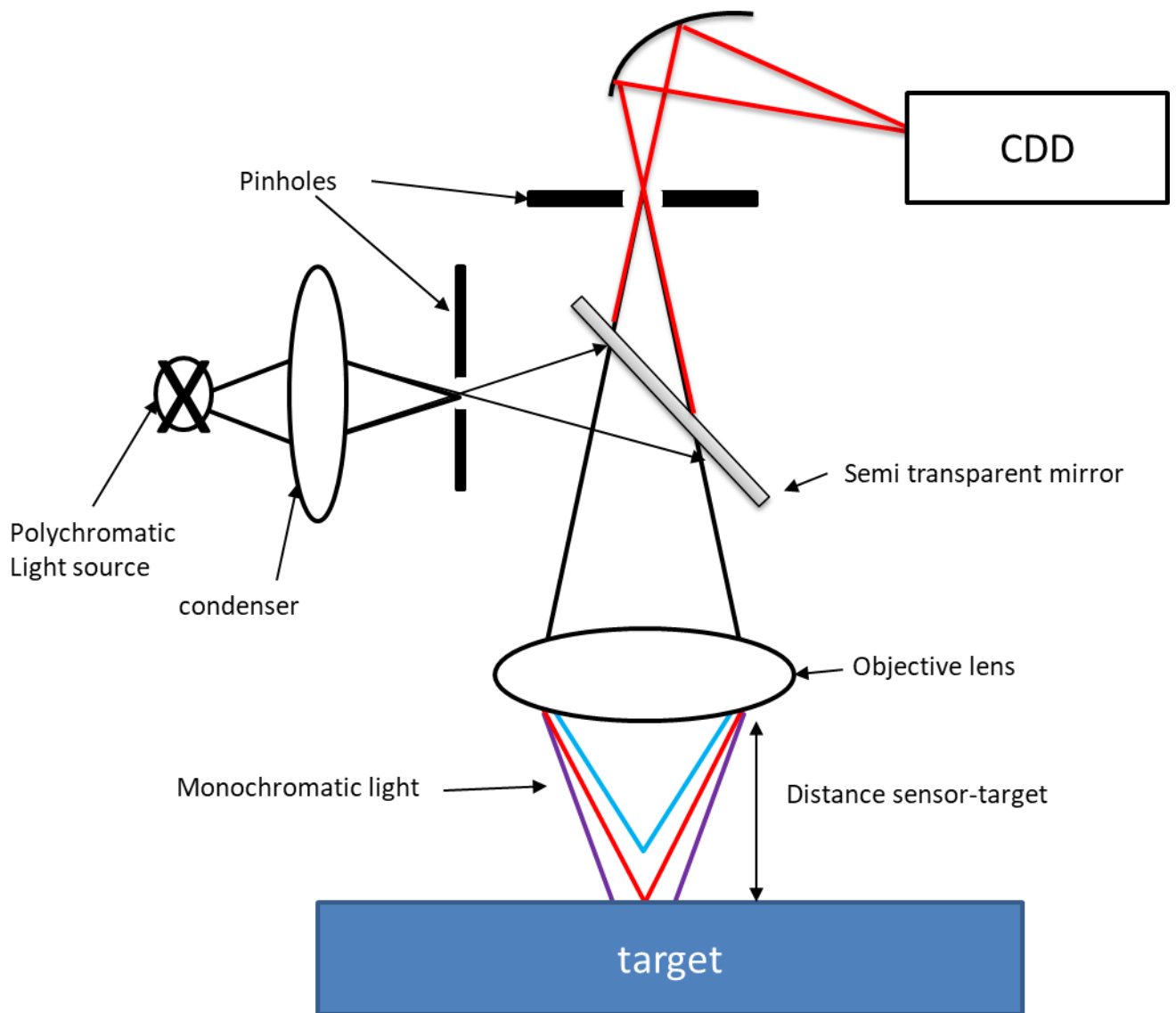


Figure 61. Principle of a chromatic light sensor

In this study, the main difficulty was to find a sensor capable of measuring a micrometric distance between the membrane and the bottom of the PMMA plate (Figure 62). That means the light should be able to pass through the entire thickness of the PMMA plate and through the

liquid carrier. The chromatic confocal sensor presents the appropriate characteristics to overcome these difficulties. Furthermore, the light is reflected whenever there is a change of medium, as long as the previous medium is transparent: in our case, a signal is obtained at the bottom of the PMMA and at the contact of the membrane. A subtraction of the distance sensor-PMMA from the distance sensor-membrane will give a value of the effective thickness, w_{eff} (Figure 62). Depending on the model, the chromatic confocal can either registered the signals obtained by all the different monochromatic beam when refracting on a new medium or just the first signal received.

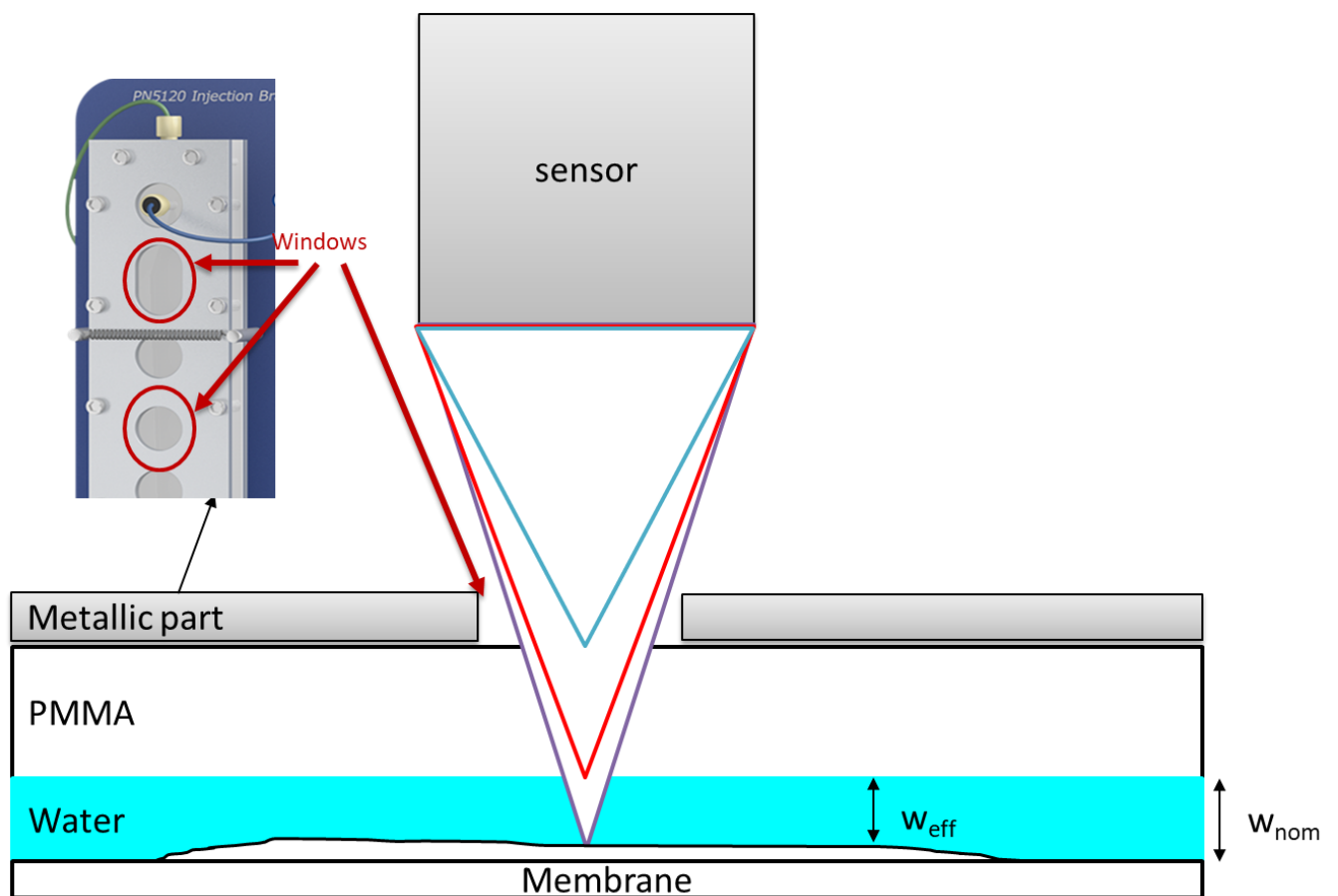


Figure 62. Measurement of the effective thickness with the chromatic confocal sensor.

3. Evaluation of the experimental set-up

The tests were performed with an OP350 chromatic confocal sensor (STIL, Aix-en-Provence, France) which has a working distance of 12.8 mm and measuring range of 350 μm . The working distance is the distance on which the different monochromatic light are not yet focalised and the measurement is not possible. The measuring range represents the maximum length measurable by the sensor (Figure 63). The sensor signal was registered by a controller CHR 450 (STIL, Aix-en-Provence, France), a xenon lamp served as light source.

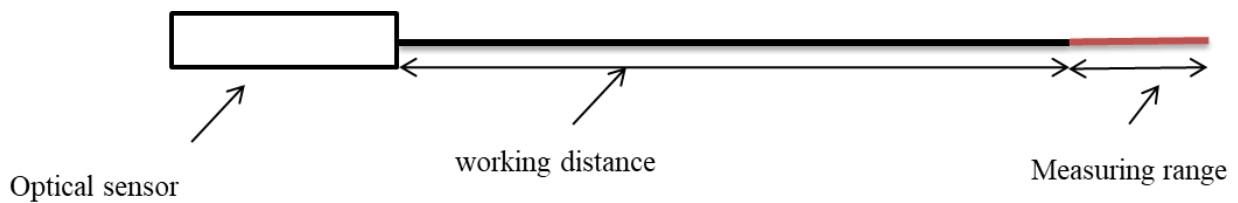


Figure 63. Representation of the working distance and measuring range

This sensor model can only display one signal per measurement. The signal displays correspond to the first object or medium change the light focused on. Therefore, in order to determine the channel thickness the sensor needed to be moved to measure in a first time the distance sensor-PMMA. The sensor position is then readjusted to measure the distance sensor-membrane.

To evaluate the functioning of the system, the linearity of the signal was firstly determined using a simplified set-up. A spacer of 190 μm was placed between two PPMA plates and the space created by the spacer was filled with water to simulate an AF4 channel. Then a micrometer screw with a white adhesive tape stuck at its end, to simulate the membrane, was used to change the distance between the tape and the sensor by a known distance (Figure 64).

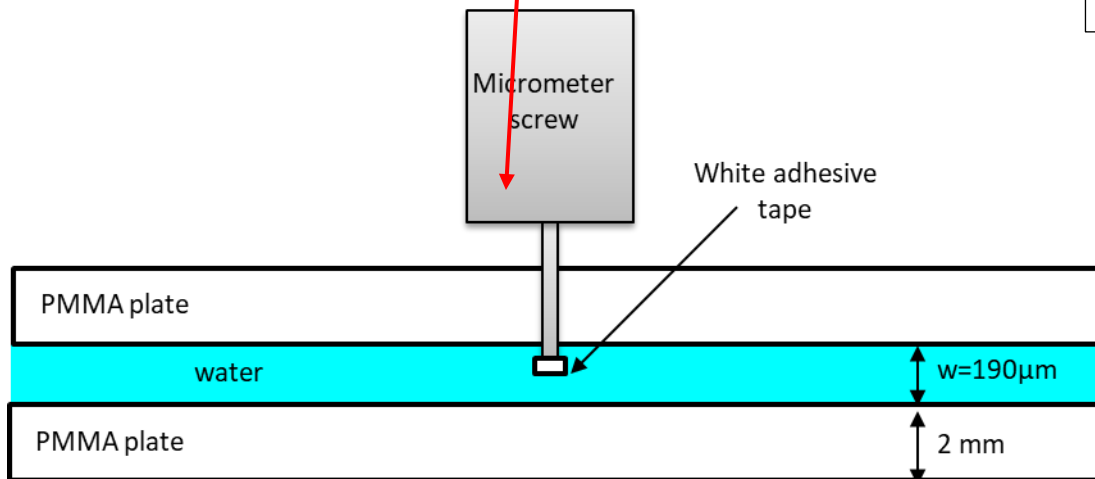
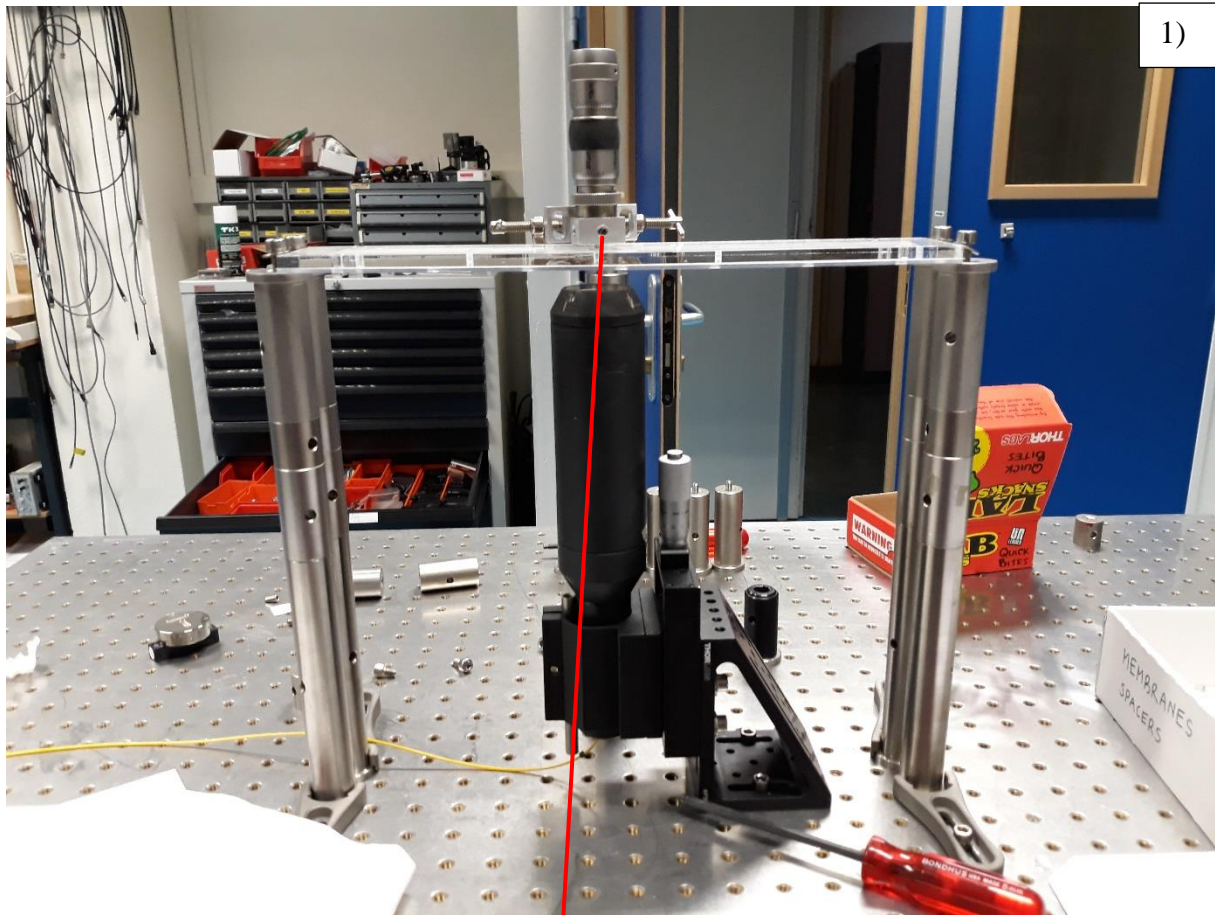


Figure 64. Assembly for testing the linearity of the sensor 1) assemblage picture. 2) Scheme of

The distance sensor-tape was plotted as a function of the displacement of the micrometer screw (Figure 65). The working distance of the sensor was subtracted to each measure realised to have a better vision of the variation

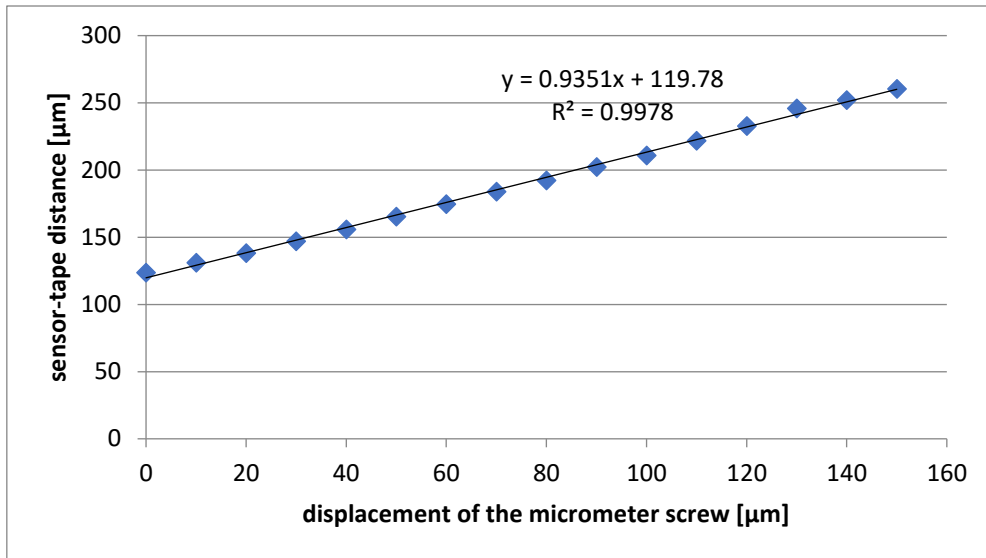


Figure 65. Linearity test of the OP350

The sensor signal proved to increase linearly with the displacement of the micrometer screw. The slope obtained with this linearity test was applied on each measurement. The repeatability of the measurement was established by recording the signal fluctuation each 10 s for a 30 s period. The standard deviation associated to each measurement corresponded to 0.08% of its mean value.

Once verified the linearity of the sensor, the following step was to test the feasibility of the measurement in real conditions. The first obstacle to overcome was the PMMA thickness. As reported before, the sensor has a working range of 12.8 mm and a measuring range of 0.350 mm so the distance between the sensor and its target, the membrane, should be comprise between 12.8 and 13.15 mm. However, the original PMMA bloc of the AF4 channel is 15 mm thick, which oblige the sensor being too far from the target. Consequently, a 2 mm thick PMMA block was customised to replace the original block.

One of the important goal of this study is to perform the measurement in the usual operational conditions. Therefore, first measurements have been performed keeping the channel in the original position (Figure 66). To precisely control the sensor position and to cover a large measurement area, the sensor was elevated using two laboratory scissor jacks and fixed to two manual one-direction moving platforms in order to move the sensor in the three dimensions (Figure 66).

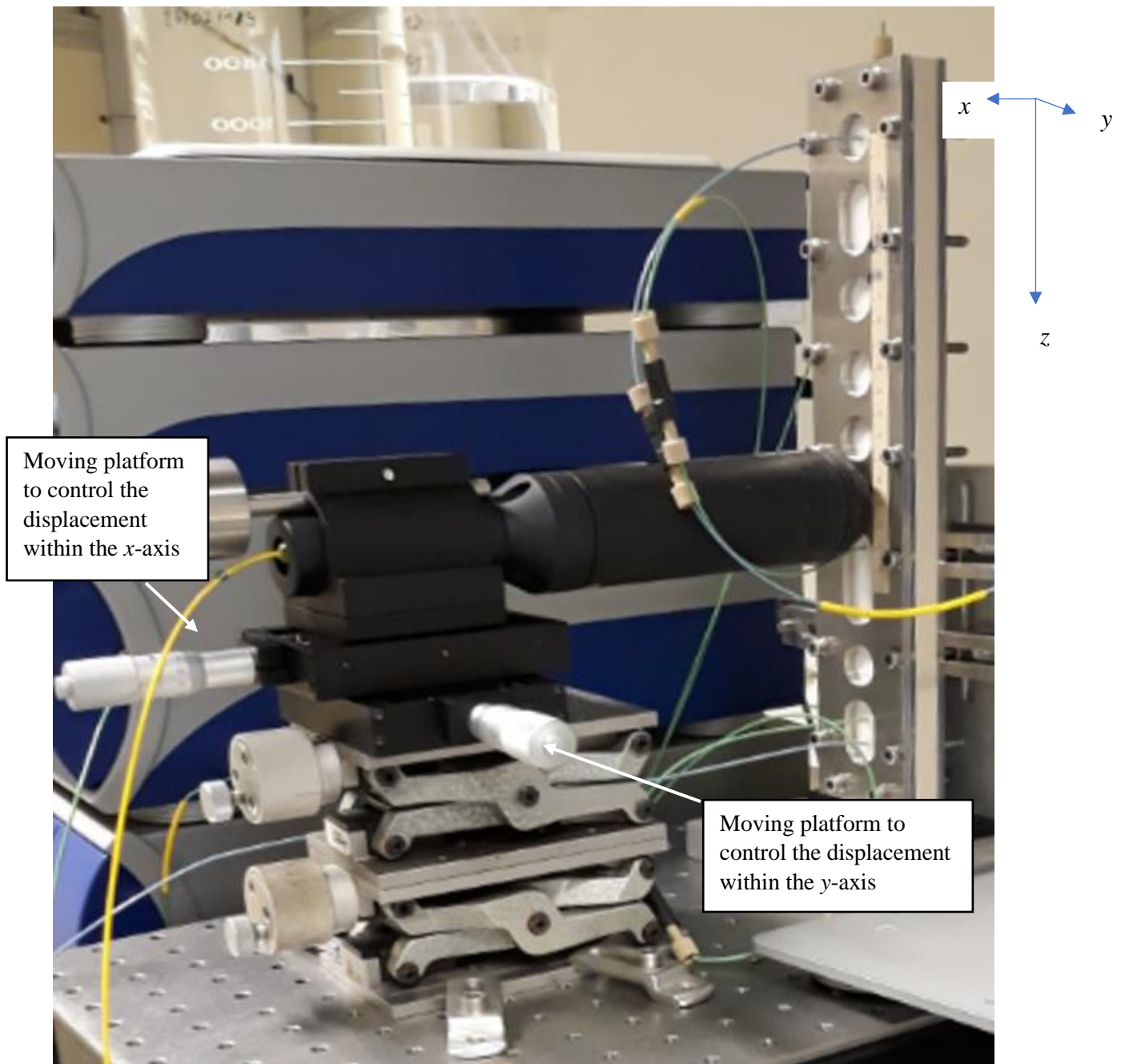


Figure 66. First assembly to measure *in situ* the channel thickness

Despite the fact that the measure is performed only in the channel windows, this assembly allows to access up to 34% of the channel area.

The first measurement consisted to measure **the distance sensor-membrane as a function of the z -axis** (Figure 67). The expected result was a constant distance within the z -axis or with small variations in the case of the swelling was uneven. However, Figure 67 shows a difference of 100 μm between a measure performed at 12.8 cm and the one performed at 13.2 cm, only 4 mm apart. Similar results have been obtained when measuring the distance as a function of **the**

y-axis (data not shown). An inspection with a spirit level on the channel showed that it was inclined by 3 degrees explaining this decreasing trend. It has been concluded that even a small gap from the vertical position may induce evident artefacts on the thickness measurement. It is worth noting that, in case of the use of a sensor which allows the direct measurement of a thickness, this effect could be minimized. Another assembly was conceived to overcome this problem: the channel was put horizontally on four pillars with exactly the same height (Figure 68).

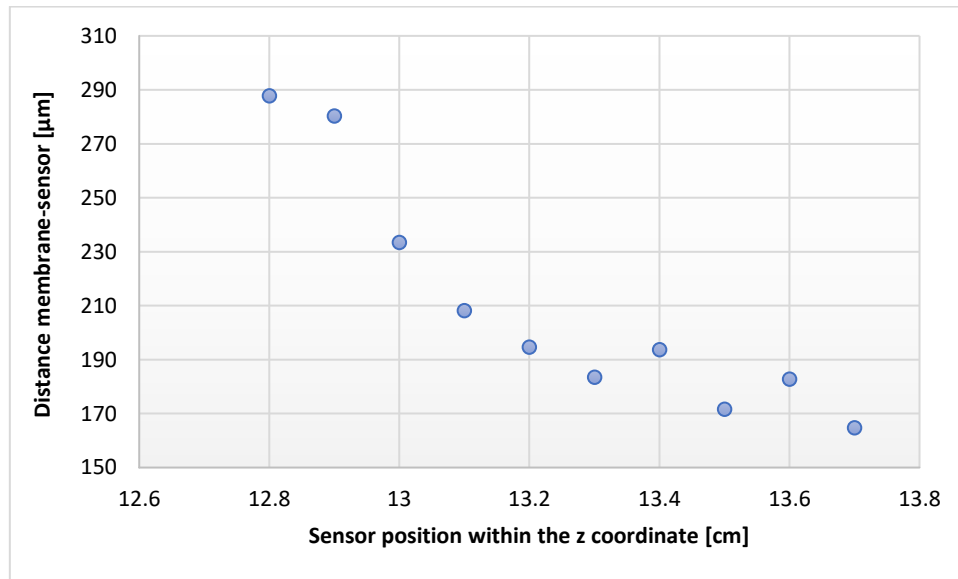


Figure 67. Distance sensor-membrane as a function of the z-axis.

Similarly, to the first the assembly, the sensor was equipped of two Moving platform in order to place the sensor in the correct measuring range and to move it across the channel. Unfortunately, the measurement could not be realized as the CHR 450 broke down and no maintenance was possible because of the obsolescence of the sensor model.

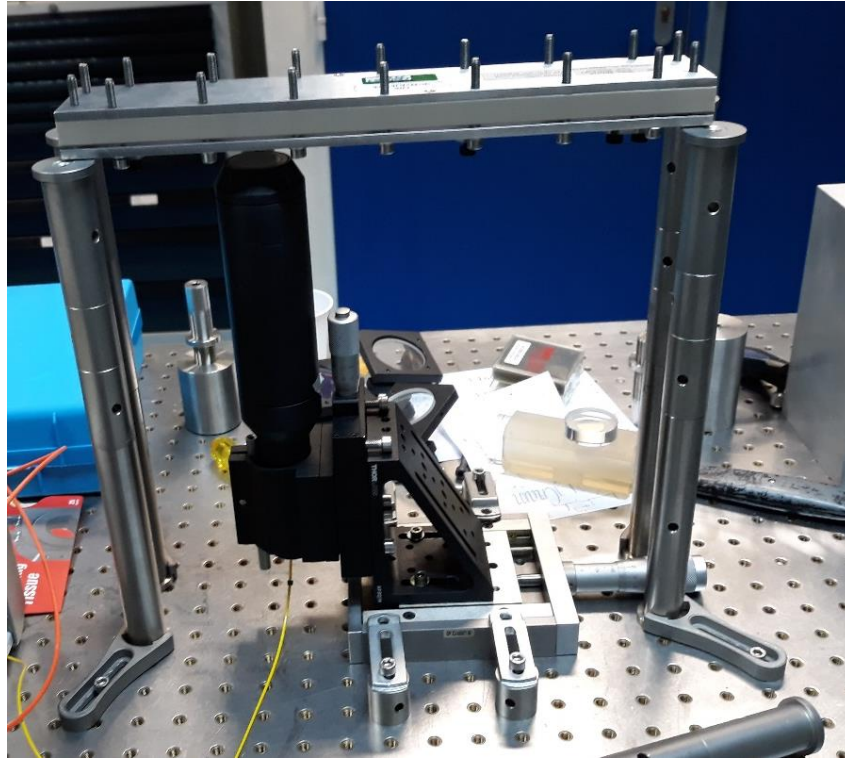


Figure 68. Developed assembly to measure *in situ* the effective channel thickness.

4. Future enhancements of the measurement set-up

The 2 mm thick PMMA block designed to allow the optical measurements was a home-made version. It was possible working with a pressure of about 10 bar inside the channel without leakage problems, neither breaking. The main problem was to fix the flow connections because of the weak thickness of the plate: a glue was used to fix the tubing (Figure 69A). Initially the assembly was waterproof and it was possible to perform properly the first experiments. Unfortunately, the glue weakened the tubing which broke at the basis. After breaking, it was no more possible to repair the prototype.

A new design of the customized PMMA plate was conceived: the idea was to avoid the breaking of the flow connections by using thicker PMMA elements with fittings for the tubing in correspondence of the flow connections (Figure 69B). Unfortunately, it was not possible to build the plate as one piece, and the PMMA elements were stuck on plate, which resulted in leakages under pressure.

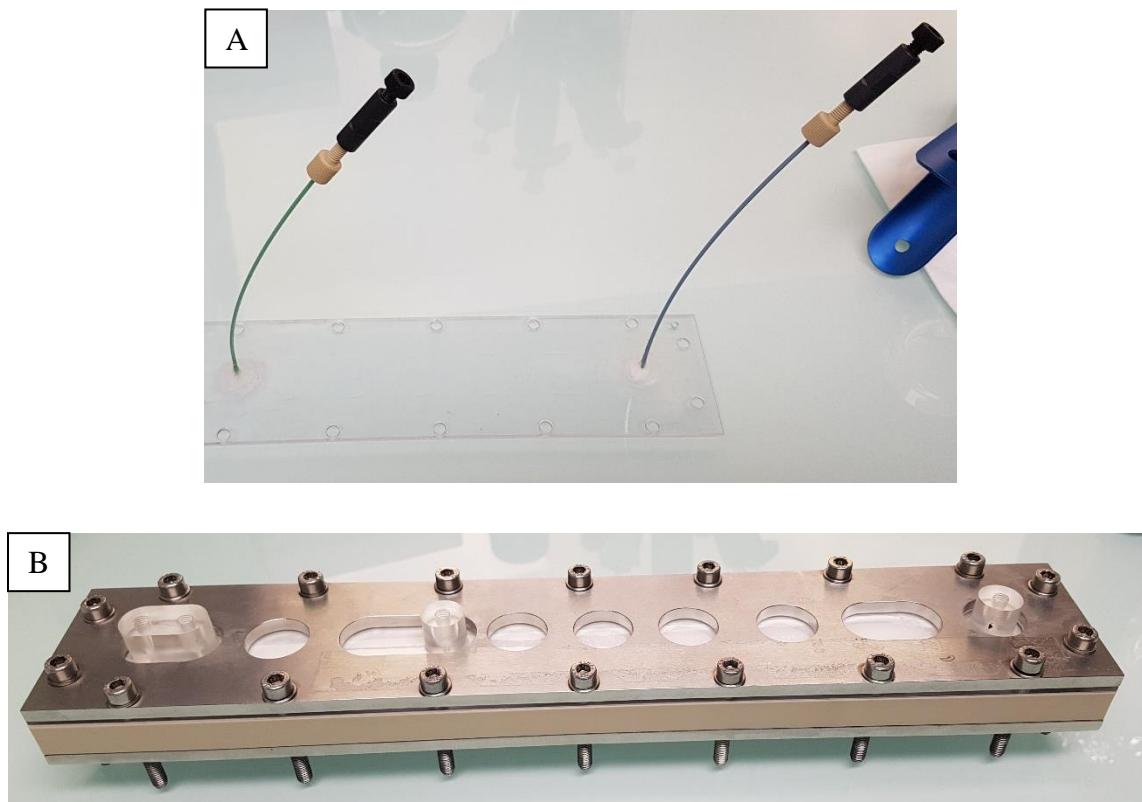


Figure 69. Different channel prototypes adapted to optical sensor measurements.

Based on these experiences a new and more robust prototype has been designed in collaboration with the research and development department of Postnova Analytics in Landsberg (Germany) and may be applied in the future developments of this work.

Concerning the use of prototypes with thin PMMA plates not exceeding 3 mm, it is worth nothing that this may be a critical issue for the w_{eff} measurement, the risk being that the absolute channel height measured would finally not be representative. Indeed, a deformation of the thin PMMA plate is expected under pressurised conditions typical of common AF4 analyses. To overcome this problem, in future measurement campaign the thickness would be measured at different positions in the windows, following the deformation, and w_{eff} would be extrapolated at the edge of the window (Figure 70).

A collaboration with STIL (France) is also envisaged to develop a chromatic confocal sensor able perform the measurement with a standard channel.

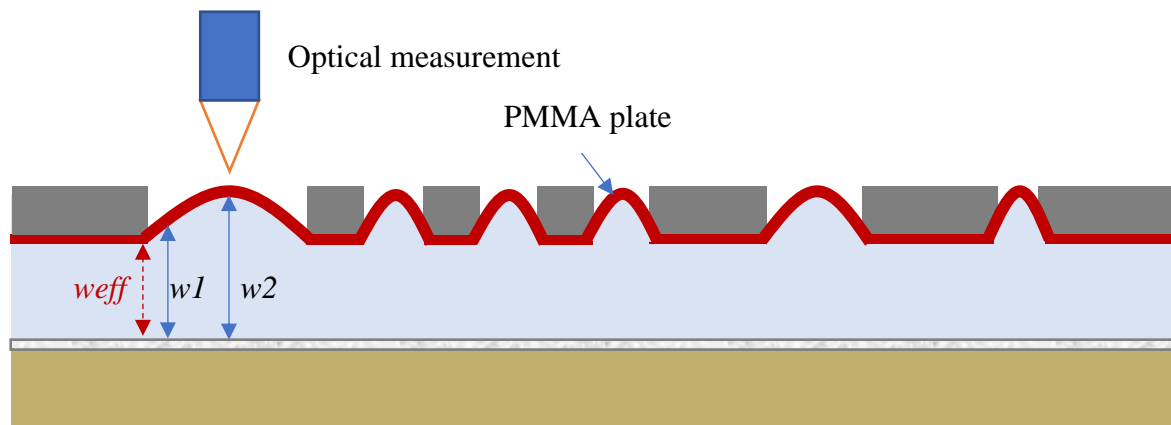


Figure 70. Scheme of the channel thickness measurement in presence of PMMA deformations due to the high pressure.

Conclusion

In this chapter, a new direct method to measure the AF4 channel thickness was presented. This method has the advantages to measure directly the thickness without the need for calibration with standards of size. Even if an unfortunate event prevented from obtaining consistent results about the membrane swelling and real value of the thickness, the preliminary results showed that the sensor light is able to pass through the different mediums composing the channel and to give a consistent signal which makes the measurements achievable. Various PMMA plate prototypes and different set-up assembling have allowed to define a promising configuration for future measurements. The measure of w_{eff} will allow to better understand the retention models used in AF4: the measured value, with associated uncertainty, would represent the solely physical contribution of a geometrical parameter, instead of a correction constant often including the gap between model prediction and experimental reality.

References

- Bolinsson, Hans, Yi Lu, Stephen Hall, Lars Nilsson, and Andreas Håkansson. 2018. "An Alternative Method for Calibration of Flow Field Flow Fractionation Channels for Hydrodynamic Radius Determination: The Nanoemulsion Method (Featuring Multi Angle Light Scattering)." *Journal of Chromatography A* 1533:155–63. doi: 10.1016/j.chroma.2017.12.026.
- Dou, Haiyang, Euo Chang Jung, and Seungho Lee. 2015. "Factors Affecting Measurement of Channel Thickness in Asymmetrical Flow Field-Flow Fractionation." *Journal of Chromatography A* 1393:115–21. doi: 10.1016/j.chroma.2015.03.025.
- Dou, Haiyang, Yong Ju Lee, Euo Chang Jung, Byung Chul Lee, and Seungho Lee. 2013. "Study on Steric Transition in Asymmetrical Flow Field-Flow Fractionation and Application to Characterization of High-Energy Material." *Journal of Chromatography A* 1304:211–19. doi: 10.1016/j.chroma.2013.06.051.
- Giddings, J. ..., P. Stephen Williams, and Maria Anna Benincasa. 1992. "Rapid Breakthrough Measurement of Void Volume for Field-Flow Fractionation Channels." *Journal of Chromatography A* 627(1–2):23–35. doi: 10.1016/0021-9673(92)87183-9.
- Häusele, Benedikt, Maxim B. Gindele, and Helmut Cölfen. 2021. "Revision of the Calibration Experiment in Asymmetrical Flow Field-Flow Fractionation." *Journal of Chromatography A* 1635. doi: 10.1016/j.chroma.2020.461631.
- Miks, Antonin, Jiri Novak, and Pavel Novak. 2010. "Analysis of Method for Measuring Thickness of Plane-Parallel Plates and Lenses Using Chromatic Confocal Sensor." *Applied Optics* 49(17):3259–64. doi: 10.1364/AO.49.003259.
- Molesini, G., G. Pedrini, P. Poggi, and F. Quercioli. 1984. "Focus-Wavelength Encoded Optical Profilometer." *Optics Communications* 49(4):229–33.
- Quinn, T. J. 1997. "Primary Methods of Measurement and Primary Standards." *Metrologia* 34(1):61–65. doi: 10.1088/0026-1394/34/1/9.
- Ruprecht, Aiko K., Christof Pruss, Hans J. Tiziani, Wolfgang Osten, Peter Lucke, Arndt Last, Jurgen Mohr, and Peter Lehmann. 2005. "Confocal Micro-Optical Distance Sensor:

Principle and Design.” *Optical Measurement Systems for Industrial Inspection IV* 5856(0):128. doi: 10.1117/12.612008.

Wahlund, Karl Gustav. 2013. “Flow Field-Flow Fractionation: Critical Overview.” *Journal of Chromatography A* 1287:97–112. doi: 10.1016/j.chroma.2013.02.028.

Conclusions and perspectives

The use of nanoparticles (NPs) is of growing economic importance in several applications in fields like medicine, electronic, construction or even food, due to their properties, which are more attractive than those of the equivalent bulk materials. The principal origin of their unique properties comes from their small size, which makes them adopt a behaviour at the boundary of the quantum and classic mechanic.

The physico-chemical characterization of the nano-objects is complex and rarely exhaustive because it highly depends from the nature of the product. Due to the rapid development of nanotechnologies, it is essential to adopt rigorous methodologies and use combinations of techniques to ensure an adequate characterization of NPs.

Reliable measurements of the size and size distribution as well as the number concentration of nano-objects are essential to understand their properties, fate and behaviour and are now becoming a requirement in the regulatory framework of the characterization of nanomaterials.

Among the existing characterization methods, the hydrodynamic method of separation by asymmetrical flow field-flow fractionation (AF4) has the advantage of being able to be used over a wide range of particle size and nature, fractionating the sample as a function of the hydrodynamic diameter.

A mathematical model, called the classical model in this work, developed by J.C. Giddings in the 1960s describes the particle behaviour inside the channel (Giddings, 1966). The classical model links the particle retention time with hydrodynamic diameter giving the AF4 model the potentiality of being a technique for size characterisation. Moreover, the AF4 model allows the characterisation of the particle size potentially without referring to measurement standards of the same measurement quantity, which gives the AF4 model the characteristics of absolute method.

However, this model is based on four categories of assumptions (Martin, 1999):

- The operating mode and the channel geometry: the particles move under Brownian motion and the channel can be assimilated as two infinite uniform parallel plates.
- The stationarity of the migration process: the field strength applied on the analyte is constant thorough the channel.

- The cross sectional concentration distribution: the steric effect and the interactions between particles and between the particles and the channel walls are considered are negligible compared to the field strength.
- The cross sectional velocity distribution: the elution flow is laminar and the particles go at the same speed as the streamline where the particles is positioned.

The aim of this work was to develop a method for the determination of nanoparticle size based on a mathematical model describing more accurately the mechanisms governing the particles retention behaviour inside the AF4 channel where the listed assumptions are validated in a large range of conditions.

A study was conducted to characterise the effect of the parameters influencing AF4 analyses (i.e. cross flow rate, carrier ionic strength, membrane nature, channel thickness). The effects of the particle hydrodynamic diameter and nature on the retention time were also investigated. The first analyses showed that depending on the carrier used and the particles injected, the membrane surface may change over time and induce changes in the particle retention behaviour. Consequently, a particular attention was paid when the different analyses were performed in order to produce comparable experiments.

Furthermore, this study showed that among the parameters not supposed to influence the particle retention, according to the classical model, it appeared that the carrier ionic strength greatly influences the particles retention behaviour: the assumption of non-interactions between particles and the accumulation wall can difficultly be verified in AF4. In addition, discrepancies in the retention time for two particles with different chemical nature were also observed. The van der Waals forces seem to be one possible cause of this difference. Further studies need to be pursued to get a better understanding of this phenomenon.

Data generated from this study were used as a data set to test the validity of retention models. The first model tested was developed by *Williams et al.* and called “ δ_w model” in this work in reference of the specific approach of this model (*Williams et al.*, 1997). Indeed, the δ_w model includes semi-empirically all the interactions between the particles and the wall by the mean of a parameter called the exclusion distance, δ_w , and determined by calibration. The objectives were (i) to evaluate the applicability of the model to AF4 and (ii) to validate the model as a size characterisation method in the case of AF4. The study demonstrated that δ_w is a good indicator to estimate the interactions inside the channel. However, the sensibility analysis showed that δ_w is the major contributor to the uncertainty and this parameter required a large number of

experiments in order to be determined with a small uncertainty. Since δ_w needs to be calibrated for particle-carrier-wall system, this model may not be attractive as a first choice. Consequently, another retention model tacking the particles wall interactions into account was studied.

Therefore, the model developed by *Hansen and Giddings* (Hansen and Giddings, 1989), which takes into account the particle-wall interactions, was studied. Contrarily to the δ_w model, this model includes into its equation each expected interaction between the particles and the wall that need to be taken into account, namely the electrostatics and van der Waals interactions. For this reason, the model was called particle-wall (p-w) model in this work.

In a first step, the p-w model was compared, using polystyrene standards, with two well-known retention models, the classical model and a model taking the steric effects into account, to see in which conditions the particles-wall interactions absolutely need to be taken into account to determine the particle true diameter (chapter 5). This work has allowed to conclude that the p-w model is interesting to use when the analyses are performed with carrier having an ionic strength below $10^{-4} \text{ mol L}^{-1}$.

In a second step, the p-w model was validated with the use of gold, polystyrene and silicon dioxide nanoparticle standards (chapter 6). It has been demonstrated that the model is applicable in the size range between 20 and 200 nm. The repeatability and reproducibility of the AF4 analysis were estimated. The analysis were replicated using three different suspensions and carrier preparations. The membrane effects on the analysis was also included in the reproducibility. The analysis were performed on three membranes to see if the membrane protrusion is reproducible. The membranes used were not bought at the same time to include the effect due to different fabrication batches. The uncertainty propagation realised with a Monte Carlo approach has indicated an expanded uncertainty of 24% of the diameter value.

The sensibility analysis realized on this model, has revealed that the channel thickness was the biggest contributor to the diameter uncertainty and therefore needed to be accurately determined. Hence, a novel direct method to determine the channel thickness based on a chromatic confocal sensor was developed (chapter VII). A sensor capable of measuring the micrometric distance between the membrane and the PMMA plate was fixed in front of the channel, using precisions tools able to move the sensor in the three dimensions with micrometric precision. Due to technical problems, only the feasibility of the method could be realized. This method has the advantages to measure directly the thickness *in situ* without the need for calibration with standards of size. Measurements may be performed all along the AF4

analysis, varying the critical parameters and monitoring the aging of the membrane on the protrusion effect.

On the basis of these conclusions and considering the contribution that this work brings to the scientific community working in the field of AF4, future developments are suggested on the following aspects:

- 1) **Concerning channel thickness determination:** the channel thickness has been identified as one of the parameters having the biggest influence on the particle retention and consequently on the particle size determination. The development of the chromatic confocal sensor measurement set-up is indispensable to answer many questions, still open, raised through literature and through this work: which is the real extent of the membrane protruding in the channel? The effective channel thickness is a constant value for each membrane or is a varying parameter as a function of the experimental conditions (flows variations, pressure variations)? Is the protruding an instantaneous mechanism due to the strength exerted on the spacer during channel assembling or a smoothly swelling occurring meanwhile membrane wetting?

A new and more robust channel assembly has been designed in collaboration with Postnova Analytics: a measurement strategy has been defined and a future collaboration with STIL has been considered. Further study on the confocal sensor could allow to determine the thickness independently of the retention model. Moreover, these advances would bring size measurements method using the retention theory, nearer to the concept of primary method permitting to avoid the calibration with standards of the quantity being measured (size).

2) **Concerning retention mechanisms**

If the channel thickness is known, the effect of membrane compressibility could be characterised. Further studies could more precisely define which membrane characteristics influence the particle retention.

The effect of particles characteristics, like their coating or Hamaker constant, on their retention are still not fully understood. A better characterisation of their effect on the retention time is critical for size determination methods using the retention time as measurand (retention models or external calibration)

3) **Concerning nanoparticles sphericity and real samples**

This work was performed using spherical nanoparticles of different nature (i.e. Au, SiO₂, PS). The application to non-spherical particles would be an important evaluation of the robustness of the model. The particle shape factor could be used to define the application limit of the model.

At the same time, it will be important to extend the uncertainty estimation to a larger number of samples, particularly real samples in complex matrices, to better check the validity of the developed Monte Carlo approach, and to monitor the potential variations of the uncertainty budget in different experimental conditions.

4) Concerning the feasibility of developing a primary reference procedure

One of the objectives of this work was to evaluate the potentiality of the size measurement approach to be considered as a primary method. In fact, the equation of the p-w model would make it possible to directly relate the retention time of the particle to its hydrodynamic diameter without referring to size standards. However, to this end, the channel thickness should be measured directly and not estimated via the use of standards. Therefore, the finalisation of the study of the thickness determination using a confocal sensor would allow to improve the metrological characteristics of the p-w model.

Publications

1. *Asymmetric field flow fractionation applied to the nanoparticles characterization: Study of the parameters governing the retention in the channel* Valentin de Carsalade du pont, Enrica Alasonati, Sophie Vaslin-Reimann, Michel Martin, Mauricio Hoyos, and Paola Fisicaro. Proceedings of 19th International Congress of Metrology (2019): <https://doi.org/10.1051/metrology/201923001>
2. *Study of mechanism governing the retention behaviour in Asymmetrical Flow Field-Flow Fractionation: taking into account particle-wall interaction.* Valentin de Carsalade du pont, Enrica Alasonati, Sophie Vaslin-Reimann, Mauricio Hoyos, Michel Martin, Clément Guibert and Paola Fisicaro. In preparation for Journal of Chromatography A.
3. *Metrological validation of a retention model taking in account particle-wall interactions for the measurement of nanoparticle hydrodynamic diameter by asymmetrical flow field-flow fractionation.* Valentin de Carsalade du pont, Jabran Zaouali, Enrica Alasonati, Nicolas Fischer, Mauricio Hoyos, Michel Martin and Paola Fisicaro. In preparation for Measurement science and technology.

Oral presentations

1. *Étude des mécanismes qui gouvernent la séparation au sein du canal A4.* Valentin de Carsalade du pont*, Mauricio Hoyos, Michel Martin, Enrica Alasonati, Paola Fisicaro, G4F workshop, October 2018, Paris.
2. *Fractionnement et caractérisation de nanoparticules par une méthode hydrodynamique: modélisation et application aux produits de consommation.* Valentin de Carsalade du pont, annual meeting of the Chemistry and biology division within the Scientific and industrial metrology direction of LNE, April 2019.
3. *Asymmetric flow field-flow fractionation: study of the parameters governing particle retention.* Valentin de Carsalade du pont*, Enrica Alasonati, Sophie Vaslin-Reimann, Michel Martin, Mauricio Hoyos, Paola Fisicaro. Congrès International de Métrologie (CIM) September 2019, Paris.
4. *Étude et mise en équations des mécanismes qui gouvernent la séparation au sein du canal A4.* Valentin de Carsalade du pont*, Mauricio Hoyos, Michel Martin, Enrica Alasonati, Paola Fisicaro, G4F workshop, October 2019, Paris.
5. *Etude de l'agglomération de la TiO2 alimentaire (E171) par A4F-MALS dans les fluides gastro-intestinaux simulés* Enrica Alasonati*, Sara Tomatis, Valentin de Carsalade du pont, Ivana Fenoglio, Paola Fisicaro. Ecole thématique GIENS (Groupe Interdisciplinaire pour l'étude des Effets environnementaux des Nanotechnologie Novembre 2019, Guyancourt.
6. *Study of Mechanism Governing the Retention Behaviour in Asymmetrical Flow Field-Flow Fractionation.* Valentin de Carsalade du pont*, Enrica Alasonati, Sophie. Vaslin-Reimann, Michel Martin, Mauricio Hoyos, Paola Fisicaro. FFF symposium, February 2020, Wien

Price

Price of the best young researcher at the workshop of the French group of field flow fractionation (G4F), June 2019, Toulouse

Résumé étendu en français

1. Introduction

Les nanoparticules manufacturées sont définies comme des matériaux fabriqués par l'homme ayant une taille inférieure ou égale à 100 nm dans au moins une de leurs trois dimensions. Elles peuvent être sous leur forme primaire ou agglomérée. Leur petite taille leur confère des propriétés physico-chimiques différentes comparé au matériau brut. Ces propriétés sont particulièrement intéressantes dans de nombreux domaines (l'électronique, l'optique, la médecine) ce qui a engendré une grande production de nanomatériaux (NMs) ces dernières années. Compte tenu de l'augmentation de l'utilisation des NMs, une meilleure compréhension de leurs propriétés, de leur devenir dans l'environnement et de leur impact sur la santé est devenue nécessaire. A cette fin, une meilleure caractérisation des propriétés des NMs nécessite d'être effectuée.

En 2012, l'ISO et l'OCDE ont proposé une liste de 11 caractéristiques qui ont besoin d'être connues pour définir un nanomatériau :

- sa taille
- sa distribution en taille
- son état d'agglomération/ agrégation
- sa forme
- sa surface/ surface spécifique
- sa composition chimique
- sa pureté
- sa chimie de surface
- sa charge de surface
- sa solubilité
- sa dispersibilité

Parmi ces paramètres, la taille et la distribution en taille des NMs sont des paramètres clés car elles impactent de nombreuses propriétés des nanomatériaux comme leurs propriétés toxicologiques et leur comportement dans l'environnement. De plus, depuis que la définition de NM proposée par la commission Européenne a été adoptée, la taille est devenue un paramètre stratégique dans la réglementation de la caractérisation des NMs. Un large éventail de techniques, basé sur des principes physiques différents, permettent de caractériser la taille et la distribution en taille d'un échantillon donné. Chacune de ces techniques ont leur propre gamme d'application dans laquelle la taille peut être précisément mesurée.

Depuis quelques années les performances des méthodes de mesure, l'assurance qualité et la traçabilité des résultats et les techniques de caractérisation en taille ont été améliorées grâce à de nombreux projets de normalisation. Néanmoins, jusqu'à présent aucune technique ne peut couvrir en une seule mesure la gamme de taille entre 1 et 100 nm et être appliquée à tous les matériaux. Une combinaison de plusieurs techniques est donc nécessaire pour assurer une caractérisation adéquate.

Parmi les techniques de caractérisation en taille, le fractionnement par couplage flux-force asymétrique (AF4) est devenu depuis quelque années, une méthode de choix pour la séparation et caractérisation des nano-objets. La norme CENT/TS 1723 indique l'AF4 comme une des meilleures approches pour détecter et identifier des nano-objets dans plusieurs types de matrices complexes. Malgré le grand nombre d'applications de la méthode FFF pour la caractérisation de NM qu'on trouve dans la littérature, une approche métrologique permettant des mesures fiables, reproductibles et traçables au système international d'unité (SI) n'a pas encore été réalisée.

Le principe de l'AF4 a été décrite par Giddings en 1966. Une équation décrivant le comportement des particules à l'intérieur du canal a été développé en 1970 et permet de déterminer la taille des particules (diamètre hydrodynamique) à partir de leur temps de rétention à l'intérieur du canal AF4. Cependant, la validité de cette équation est basée sur plusieurs hypothèses liées à la géométrie du canal, le processus de migration, le profil de concentration et le profil du flux d'élution qui ont besoin d'être justes pour que l'équation puisse donner des résultats fiables. En pratique, certaines hypothèses comme l'absence d'interactions entre les particules et la paroi du canal ne sont pas vérifiées. Ces interactions peuvent influencer la rétention des particules ce qui peut engendrer un biais allant jusqu'à 40% lorsque la taille de la particule est déterminée. Améliorer le modèle de rétention permettrait d'avoir une méthode simple à utiliser pour déterminer la taille des particules. De plus, cette approche a le potentiel de caractériser la taille des particules sans se référer à un étalon de la même unité que le mesurande, ce qui donne à la méthode FFF la possibilité d'avoir les caractéristiques d'une méthode primaire.

La méthode FFF serait également complémentaire avec la caractérisation par diffusion de la lumière (MALS) puisque le rapport des mesurandes de chaque méthode est égale au facteur de forme qui permet d'avoir une indication sur la forme de la particule.

L'objectif de cette thèse est par conséquent de développer une méthode de caractérisation en taille basée sur la théorie de la rétention de l'AF4 et d'évaluer sa capacité à devenir une méthode primaire. Pour ce faire, dans un premier temps une étude sur les mécanismes gouvernant la rétention au sein du canal AF4 a été réalisée. Chaque paramètre faisant partie d'une analyse AF4 a été étudié. Cette étude a permis de générer une base de donnée permettant de tester deux modèles de rétention, le premier ayant été développé par *Williams et al.* et le deuxième par *Hansen et al.* Chaque modèle utilise une approche différente pour estimer les interactions présentes dans le canal. Les avantages et les limites de chaque modèle ont été évalués dans le but de proposer des améliorations.

2. Principe de fractionnement par couplage flux force (FFF)

Le concept de la FFF a été développé par J.C Giddings en 1966. La FFF représente une grande famille de technique de séparation dont le principe consiste à appliquer un champ de force perpendiculairement au flux d'élution (Figure R1). Les composés de l'échantillon sont soumis à deux forces opposées : le champ de force les poussant vers la partie basse du canal appelé paroi d'accumulation et la diffusion Brownienne. Les composés de l'échantillon vont se placer à une hauteur différente en fonction de leur coefficient de diffusion. Ces composés s'élueront à des vitesses différentes grâce au profil laminaire, puisque les composés proches de la paroi d'accumulation iront moins vite que les composés éloignés de la paroi.

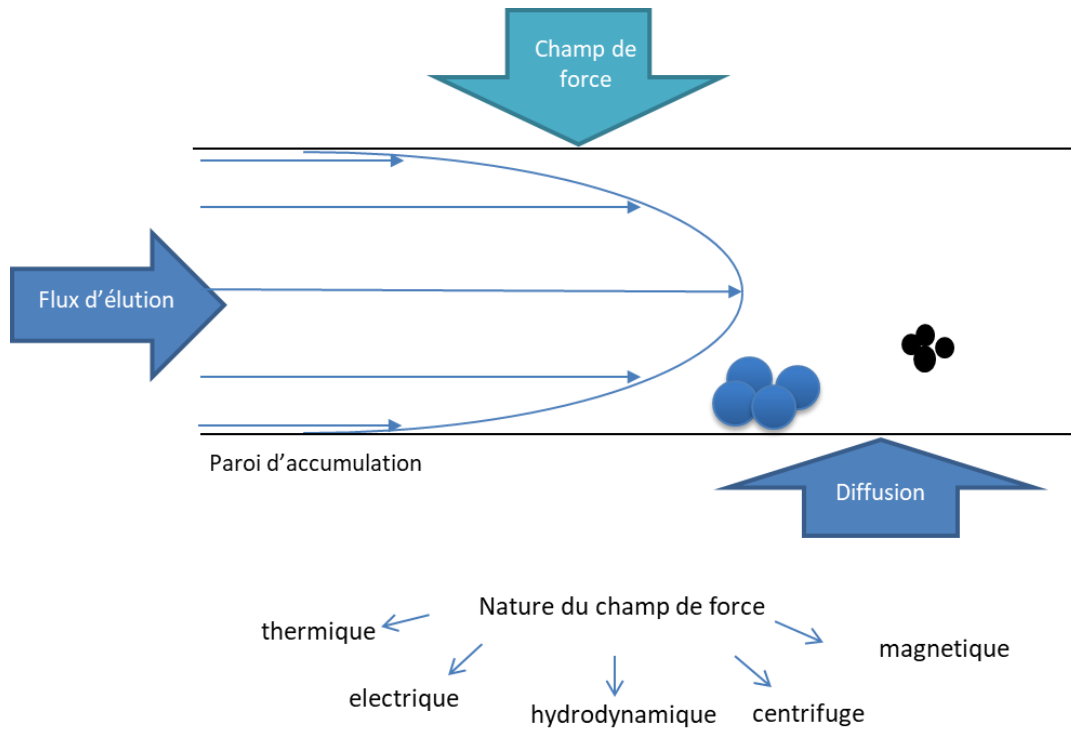


Figure R1. Principe du fractionnement par FFF

Le champ de force peut être de différentes natures (électrique, hydrodynamique, thermique...). Les différents types de FFF sont classés en fonction de la nature du champ de force appliqué.

3. Formalisation théorique

Un modèle décrivant la rétention des particules au sein du canal a été développé dans les années 1960 par Giddings (Eq. 1).

$$R = 6\lambda \coth\left(\frac{1}{2\lambda}\right) - 12\lambda^2 \quad \text{modèle classique (1)}$$

où R est le rapport entre le temps mort, t_0 , et le temps de rétention, t_r , et λ le paramètre de rétention égal à kT/F avec k la constante de Boltzmann, T la température et F le champ de force appliqué dont l'expression dépend du type de FFF utilisée. Dans ce manuscrit l'Eq. 1 est appelée modèle classique. Si $\lambda < 0,02$ l'Eq.1 peut être approximée par

$$R = 6\lambda \quad (2)$$

Le modèle classique est basé sur plusieurs hypothèses qui peuvent être classées en 4 catégories :

1) Hypothèses liées à la géométrie du canal et au modus operandi : le modèle assume que les particules se déplacent selon le mode brownien. Le canal doit être rectilinéaire avec une géométrie à plans parallèles et bidimensionnelle.

2) Hypothèses liées au processus de migration : le modèle s'applique seulement lorsque l'élution est isocratique. C'est-à-dire que le champ de force appliqué, le flux croisé dans le cas de l'AF4, est constant. Le fractionnement est également sensé débiter après la relaxation totale des particules.

3) Hypothèses liées au profil de distribution de la concentration des particules dans le canal : le profil de concentration est supposé décroître exponentiellement tout au long du canal. Cette hypothèse implique que les particules soient assimilables à un point matériel pour que les effets stériques soient négligeables. L'effet des interactions électrostatiques et de van der Waals entre les particules et la paroi d'accumulation doit également être négligeable par rapport à celui du champ de force appliqué.

4) Hypothèses liées au profil de distribution de la vitesse dans le canal : le profil de la vitesse est supposé suivre une loi parabolique tout au long du canal. Cela implique que l'analyse se fasse dans des conditions isothermes. L'effet Faxén est également considéré comme négligeable.

La validité des hypothèses 1, 2 et 4 a été vérifiée en littérature. La validité de l'hypothèse n°3 dépend, quant à elle, des conditions dans laquelle se déroule l'expérience. Plusieurs articles ont montré que les interactions électrostatiques ne pouvaient pas être négligées lorsque la force ionique de la phase mobile était inférieure à 10^{-3} mol. L⁻¹. De plus certains effets non expliqués par le modèle classique, par exemple, un temps de rétention, t_r dépendant de la nature chimique des particules analysées ou encore un t_r différent en fonction de l'enrobage des particules ont été observés dans la littérature. Plusieurs modèles ont donc été développés en parallèle pour avoir une meilleure représentation des différents phénomènes se passant dans le canal.

Williams et al. ont développé un modèle appelé ici, le modèle δ_w , qui prend en compte de façon semi-empirique la somme des interactions particules-paroi par le biais du paramètre δ_w . Si la somme des forces est répulsive, δ_w représente la distance à laquelle les particules n'ont pas accès à cause des interactions particule-paroi. Si la somme des forces est attractive, δ_w sera négatif et signifie que les particules sont plus proches de la paroi que prévu par le modèle classique. Le rapport de rétention R devient égal à

$$R = 6\alpha(1 - \alpha) + 6\lambda \left((1 - 2\alpha) \coth \frac{1 - 2\alpha}{2\lambda} - 2\lambda \right) \left(1 + \frac{\delta_w}{l} \right) \quad \text{modèle } \delta w \quad (2)$$

avec α le rapport entre le rayon de la particule et l'épaisseur du canal et l le produit entre λ et l'épaisseur du canal. La valeur de δ_w est obtenue en mettant l'Eq. (2) sous la forme suivante

$$Y = \frac{R - 6\alpha(1 - \alpha)}{6\lambda \left((1 - 2\alpha) \coth \frac{1 - 2\alpha}{2\lambda} - 2\lambda \right)} = \left(1 + \frac{\delta_w}{l} \right) \quad (3)$$

Sous cette forme δ_w est égal à la pente de $Y = f(l/l)$. La valeur absolue de δ_w dépend de l'intensité des interactions particules-paroi. Elle dépend donc de la composition et des propriétés de surface de l'étalon et de la paroi, ainsi que de la composition et concentration de la phase mobile.

Un deuxième modèle, nommé dans cette thèse modèle p-w, développé par *Hansen et Giddings* prend en compte les interactions particules-paroi en ajoutant les forces de van der Waals et les interactions électrostatiques dans l'Eq. (1). L'équation prend donc la forme suivante :

$$R = \frac{6 \int_{r_h}^{w-r_h} \exp \left(- \frac{(W_F(x) + W_{el(p-w)}(x) + W_{vdW(p-w)}(x))}{kT} \right) \left(\frac{x}{w} - \frac{x^2}{w^2} \right) dx}{\int_{r_h}^{w-r_h} \exp \left(- \frac{(W_F(x) + W_{el(p-w)}(x) + W_{vdW(p-w)}(x))}{kT} \right) dx} \quad \text{modèle } p - w \quad (4)$$

Avec $W_F(x)$, $W_{el(p-w)}(x)$ et $W_{vdW(p-w)}(x)$ les énergies potentielles liées au champ de force appliqué, aux interactions électrostatiques et aux forces de van der Waals entre les particules et la membrane.

Le type de FFF utilisé dans cette thèse est une AF4. Le canal de l'AF4 est composé d'un fritté pour permettre l'écoulement de la phase mobile perpendiculairement au flux d'élution. Une membrane d'ultrafiltration est posée sur le fritté pour retenir les particules à l'intérieur du canal (Figure R2). Ici le fractionnement est effectué en appliquant une force hydrodynamique, le flux croisé, sur l'échantillon. L'expression de cette force est égale à :

$$F_{A4F} = \frac{Q_c w 3\pi\eta d_h}{V^0} \left(1 - \frac{3x^2}{w^2} + \frac{2x^3}{w^3} \right) \quad (5)$$

Avec Q_c le flux croisé, w l'épaisseur du canal, η la viscosité de la phase mobile, d_h le diamètre hydrodynamique de la particule et V^0 le volume mort. Les composés présents au sein du canal sont donc séparés uniquement en fonction de leur diamètre hydrodynamique.

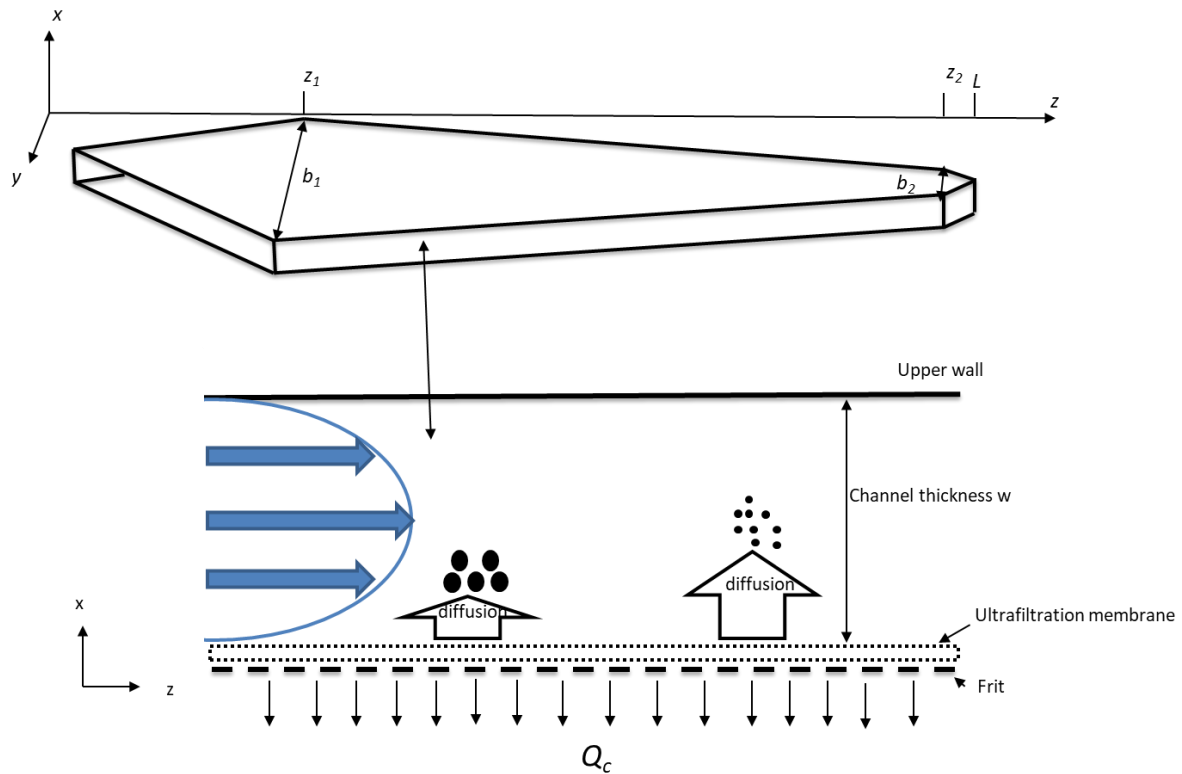


Figure R2. Géométrie d'un canal AF4 et principe de fonctionnement

4. Objectif de la thèse

La littérature montre que les modèles de rétentions qui existent ne sont pas toujours adaptés pour décrire le comportement d'élution des particules dans le canal AF4. La nature chimique, l'enrobage des particules, les caractéristiques de la membrane (nature chimique, potentiel zêta) sont des exemples de facteurs qui peuvent affecter le temps de rétention de l'échantillon.

Pour mieux représenter l'élution des particules et avoir une relation précise entre leur temps de rétention et leur taille, une étude sur l'influence des interactions entre les particules et la paroi sera réalisée en suivant les approches de *Williams et al.* et *Hansen et al.* qui ont inclus ces interactions en suivant deux approches différentes. Si l'aspect théorique avait déjà été décrit par ces auteurs, l'applicabilité du modèle δ_w et p-w à l'AF4 a été évaluée au cours de cette thèse pour la première fois. Le modèle le plus adapté à l'AF4 a ensuite été validé à travers de l'évaluation de ses performances ce qui inclut l'établissement d'un bilan de l'incertitude de mesure et de la traçabilité métrologique de ses résultats au système international.

5. Etude des mécanismes gouvernant la rétention des particules sphériques dans un canal d'AF4

La première étape de ce travail a été d'étudier les mécanismes qui gouvernent la rétention des particules dans un canal AF4. L'étude a consisté à observer l'effet de plusieurs paramètres sur le temps de rétention de l'étalon injecté et son taux de recouvrement (Tableau R1). Les possibles covariances entre les paramètres ont également été étudiées.

Tableau R1. Liste des paramètres étudiés. La gamme de travail dans laquelle chaque paramètre a été étudié est indiquée.

	Paramètres	Gamme de travail
tiré du modèle classique	flux croisé, Q_c	0,5-2 mL min ⁻¹
	épaisseur du canal, w	190-500 µm (nominal)
	diamètre hydrodynamique, d_h	20-200 nm
paramètres fréquemment optimisés	force ionique	eau ultrapure ($\sim 10^{-7}$)- 10^{-3} mol L ⁻¹
	nature de la membrane	cellulose régénérée (RC), Polyethersulfone (PES)
	composition chimique des particules	polystyrène, or et dioxyde de silice

La reproductibilité des analyses a été réalisée en parallèle pour estimer l'incertitude sur le temps de rétention et savoir si le temps de rétention risque d'engendrer une grande incertitude ou non dans les modèles de rétentions.

Il a été constaté que selon les conditions expérimentales la surface de la membrane pouvait se modifier avec le temps et/ou le nombre d'injections ce qui influençait le temps de rétention des

échantillons (Figure R3). Ce phénomène est défini dans la littérature comme le vieillissement de la membrane.

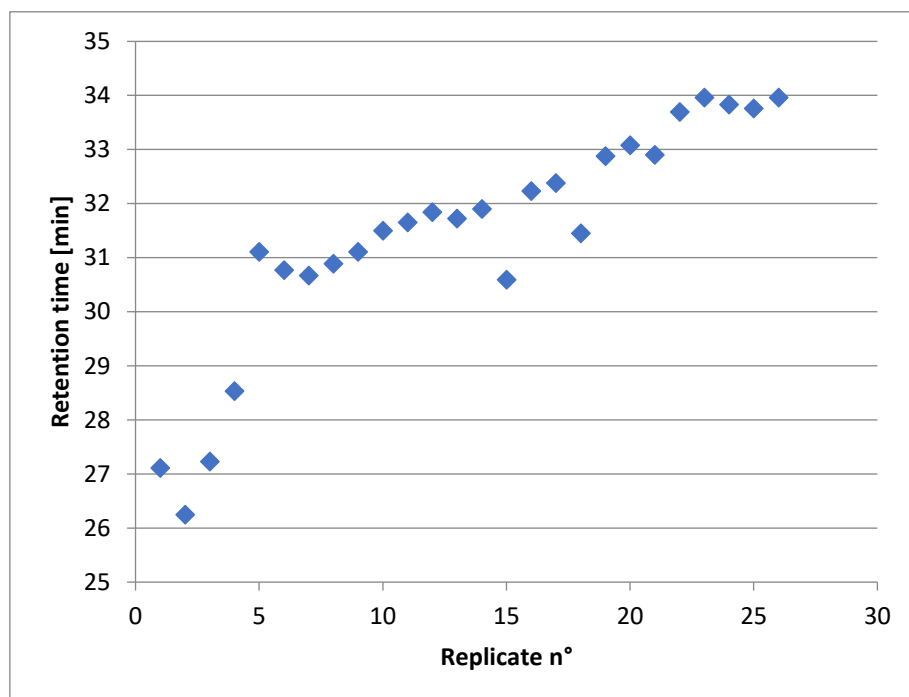



Figure R3. Temps de rétention d'un étalon de polystyrène de 60 nm en fonction du nombre de répliques. Phase mobile : NaCl à 10^{-4} mol. L $^{-1}$; membrane RC 10 kDa ; flux croisé et flux d'élution : 0,5 mL. min $^{-1}$.

Pour surmonter ce problème, la séquence d'analyses a été modifiée pour prendre en compte le vieillissement de la membrane dans la répétabilité. Pour expliquer cette approche un exemple est présenté dans le Tableau R2. Lorsque 3 différents flux croisés (Q_{c1} , Q_{c2} , Q_{c3}) sont testés, au lieu d'injecter l'échantillon 3 fois dans les mêmes conditions (Q_{c1}) puis passer à la deuxième condition (Q_{c2}), un premier réplica de chaque condition a été réalisé avant de passer au deuxième réplica de la condition n°1 (Q_{c1}). Cette séquence augmente l'écart type de chaque expérience mais permet d'obtenir une valeur moyenne plus représentative de la vie de la membrane. La répétabilité présentée dans la Figure R3 est un cas extrême qui n'est arrivé qu'une seule fois sur les 70 membranes utilisées pendant cette thèse. La séquence d'injection a cependant été gardée par mesure de précaution.

Tableau R2. Séquence d'injection utilisée lorsque différentes conditions (ici flux croisé) sont testées

Analysis n°	Typical sequence		Sequence applied in this study
1	replicate 1 Q_{c1}		replicate 1 Q_{c1}
2	replicate 2 Q_{c1}		replicate 1 Q_{c2}
3	replicate 3 Q_{c1}		replicate 1 Q_{c3}
4	replicate 1 Q_{c2}		replicate 2 Q_{c1}
5	replicate 2 Q_{c2}		replicate 2 Q_{c2}
6	replicate 3 Q_{c2}		replicate 2 Q_{c3}
7	replicate 1 Q_{c3}		replicate 3 Q_{c1}
8	replicate 2 Q_{c3}		replicate 3 Q_{c2}
9	replicate 3 Q_{c3}		replicate 3 Q_{c3}
Standard deviation obtained	$u(t_r) \approx 0.2 \text{ min}$		$u(t_r) \approx 0.7 \text{ min}$

Cette première étude a montré l'influence des interactions particules-membrane sur le temps de rétention des particules et leur taux de recouvrement en faisant varier la force ionique de la phase mobile ainsi que la composition de la membrane et des particules. Il a été montré que la force ionique a une grande influence sur le temps de rétention (Figure R4). La répulsion due à la force ionique, I , s'atténue lorsque $I=10^{-3} \text{ mol. L}^{-1}$ et l'on retrouve le comportement prédit par le modèle classique. Cependant les analyses ont un faible taux de recouvrement ce qui rend cette force ionique inadaptée aux analyses (Figure R5). Un modèle prenant en compte les interactions est donc nécessaire pour fournir des résultats justes.

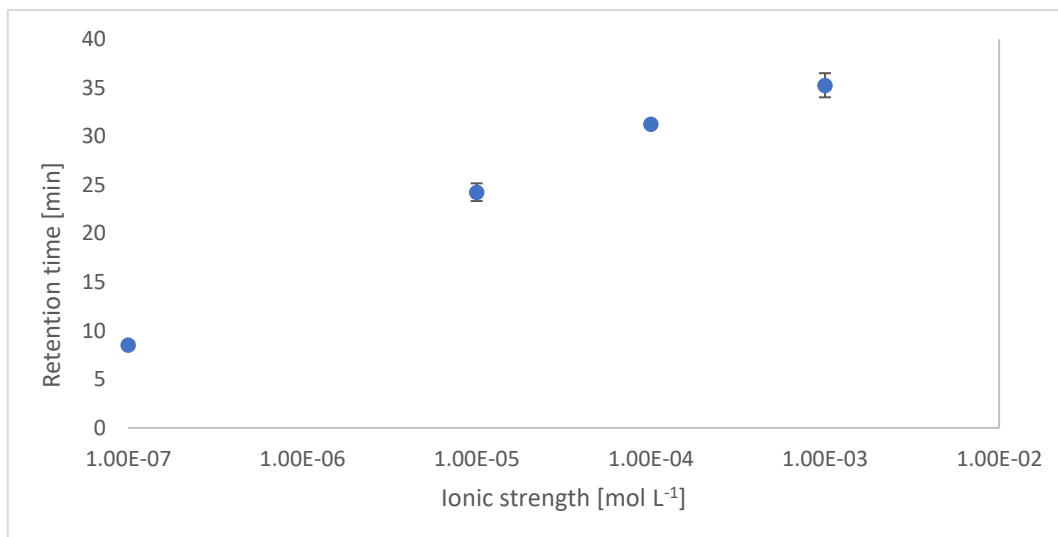


Figure R4. Influence de la force ionique sur le temps de rétention d'un étalon de polystyrène à 60 nm.
 $Q_c=1 \text{ mL.min}^{-1}$; $w=350 \text{ }\mu\text{m}$; membrane : RC 10kDa.

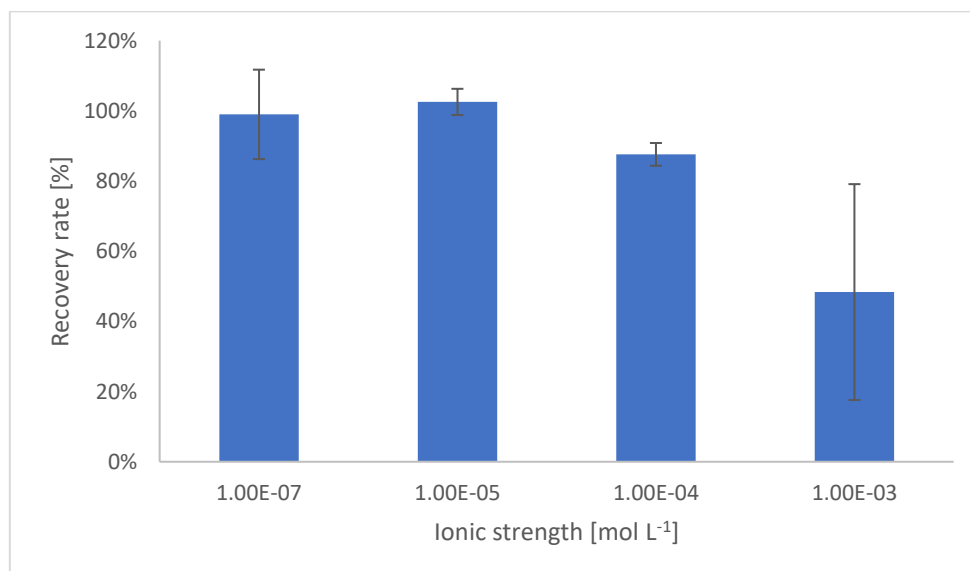


Figure R5. Influence de la force ionique sur le taux de recouvrement d'un étalon de polystyrène à 60nm.
 $Q_c=1 \text{ mL.min}^{-1}$; $w=350 \text{ }\mu\text{m}$; membrane : RC 10 kDa.

L'ensemble des analyses montrent que dans des conditions de reproductibilité, la méthode AF4 donne des temps de rétention avec des écart types entre 0,7 et 1,5 min, pour des valeurs moyennes allant de 6 à 80 min. L'ordre de grandeur des écarts types est suffisamment bas pour appliquer des méthodes se basant sur le temps de rétention.

6. Application du modèle δ_w à l'AF4 pour la caractérisation en taille des particules.

La validité du modèle δ_w a été testée pour la première fois par *Williams et al.* avec la FFF à sédimentation pour une gamme de taille sub micrométrique (197-742 nm). Des tests ont été par

la suite réalisés par *Du et Schimpf* en AF4 dans une gamme plus large allant de 64 à 1000 nm. Cependant les auteurs ont remarqué une différence entre le δ_w déterminé par l'étalon de 64 nm et les δ_w déterminés par les autres étalons en taille. La valeur de δ_w doit être indépendante de la taille de l'étalon pour que le modèle soit intéressant à utiliser comme méthode de caractérisation en taille. Une étude a donc été effectuée pour savoir si δ_w se comporte différemment dans le domaine nanométrique ou si la différence observée par *Du et Schimpf* est négligeable.

Le comportement de δ_w a été évalué en faisant varier la force ionique de la phase mobile et en le déterminant à l'aide d'étalons de polystyrène de diamètre compris entre 23 et 185 nm. δ_w a suivi le comportement prévu par le modèle lorsque la force ionique a été variée : sa valeur diminuait lorsque la force ionique augmentait. Il a également été montré que la valeur de δ_w est indépendante de la taille de l'étalon utilisé. La justesse du modèle δ_w en tant que méthode de caractérisation en taille a ensuite été évaluée. Pour ce faire le diamètre des étalons de PS a été comparé à celui calculé par le modèle. L'équation étant difficile à résoudre analytiquement, un programme en langage Python a été utilisé pour résoudre la fonction numériquement. La méthode de Monte Carlo (MCM) a été appliquée pour réaliser la propagation des incertitudes. Le Tableau R2 montre les résultats obtenus sur 4 étalons de polystyrène. Le δ_w a été déterminé en utilisant le PS à 60 nm. 5 flux croisés différents ont été utilisés pour la droite d'étalonnage. Chacun des points a été répété 3 fois. Les distributions obtenues étant asymétriques les résultats sont présentés sous forme d'intervalle [d_h min- d_h max]. Le d_h min correspond au d_h pour lequel 95% des valeurs de la distribution sont supérieures. Le d_h max correspond au d_h pour lequel 5% des valeurs de la distribution sont supérieures. Le diamètre médian de la distribution a été rajouté pour donner une idée de la forme de la distribution. Le tableau R3 montre que toutes les valeurs de référence et les intervalles déterminés par MCM se recoupent et que les résultats obtenus par le modèle δ_w sont justes. Cependant, il est intéressant de constater que, contrairement aux incertitudes des étalons déterminés par microscopie électronique, l'intervalle calculé avec le modèle devient de plus en plus large au fur et à mesure que la taille de la particule augmente alors que l'écart type de la distribution du seul paramètre entrant, propre à chaque échantillon (temps de rétention) est similaire pour chaque échantillon (0,7-1 min). Ce phénomène est expliqué par le principe de la méthode. Comme δ_w représente une distance d'exclusion qui empêche les particules d'atteindre une certaine zone du canal, les particules devraient à partir d'une certaine taille être éluées sur la même ligne de flux. La relation entre le diamètre hydrodynamique des particules et leur temps de rétention deviendrait asymptotique ce qui engendrerait une large distribution lorsque la MCM est appliquée.

Tableau R3. Evaluation de la justesse du modèle δ_w sur des étalons de PS. Les analyses ont été réalisées dans du NH_4NO_3 à $10^{-5} \text{ mol. L}^{-1}$; $w=350 \text{ }\mu\text{m}$; membrane : RC 10 kDa; $Q_c=0.8 \text{ mL.min}^{-1}$; $\delta_w=0.8 \text{ }\mu\text{m}$.

étalon	diamètre de l'étalon $\pm U$ ($k=2$)[nm]	d_h min - d_h max [nm]		d_h médian [nm]	Résultats significativement différent
PS20	23 \pm 10	12.2	13.8	13.1	Non
PS60	60 \pm 8	49.3	59.8	53.8	Non
PS100	99 \pm 8	86.8	114.3	99.0	Non
PS200	186 \pm 6	172.3	328.7	224.1	Non

La contribution de chaque paramètre à l'incertitude du d_h a été déterminée en utilisant les coefficients de corrélations de Spearman. La Figure R6 montre que le δ_w et le t_r sont les deux paramètres les plus influents sur l'incertitude. Cependant l'incertitude de mesure de ces deux paramètres est difficilement améliorable si l'on considère l'attention portée sur ces deux paramètres pour réaliser cette propagation d'incertitude.

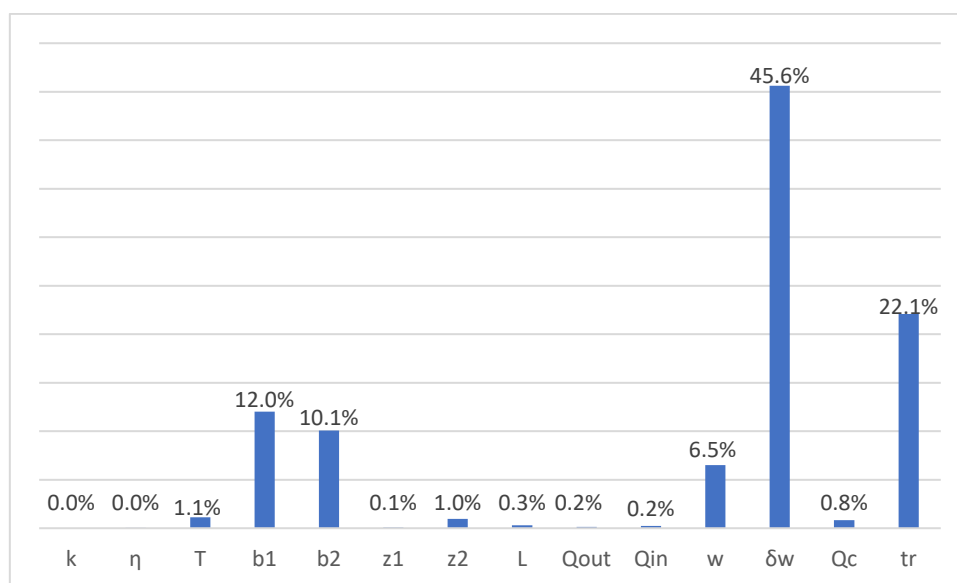


Figure R6. Contribution relative de chacun des paramètres entrants sur l'incertitude du d_h

Le modèle δ_w permet grâce au paramètre δ_w d'estimer qualitativement les interactions présentes au sein du canal. Cependant le paramètre δ_w nécessite un grand nombre d'analyses pour être étalonné et avoir une faible incertitude. Cette approche n'est pas très attractive si l'on veut se servir du modèle comme d'une méthode de détermination en taille. Un autre modèle a donc été étudié.

7. Application du modèle $p-w$ à l'AF4 pour la caractérisation en taille de particules

L'avantage du modèle $p-w$ par rapport au modèle δ_w est qu'il permet de savoir précisément quelle force influence le plus le temps de rétention vu que chaque force est ajoutée dans l'équation. Le premier test a consisté à voir comment le modèle prend en compte l'effet de la force ionique sur le temps de rétention. Le diamètre hydrodynamique prédit par le modèle $p-w$ en fonction du temps de rétention pour une force ionique donnée a été comparé au diamètre prédit par le modèle classique ainsi qu'aux données expérimentales obtenues dans les mêmes conditions (Figure R7). Il a été constaté que le modèle $p-w$ donnait des résultats plus justes que le modèle classique particulièrement lorsque les interactions électrostatiques sont importantes (force ionique $< 10^{-4}$ mol. L $^{-1}$)

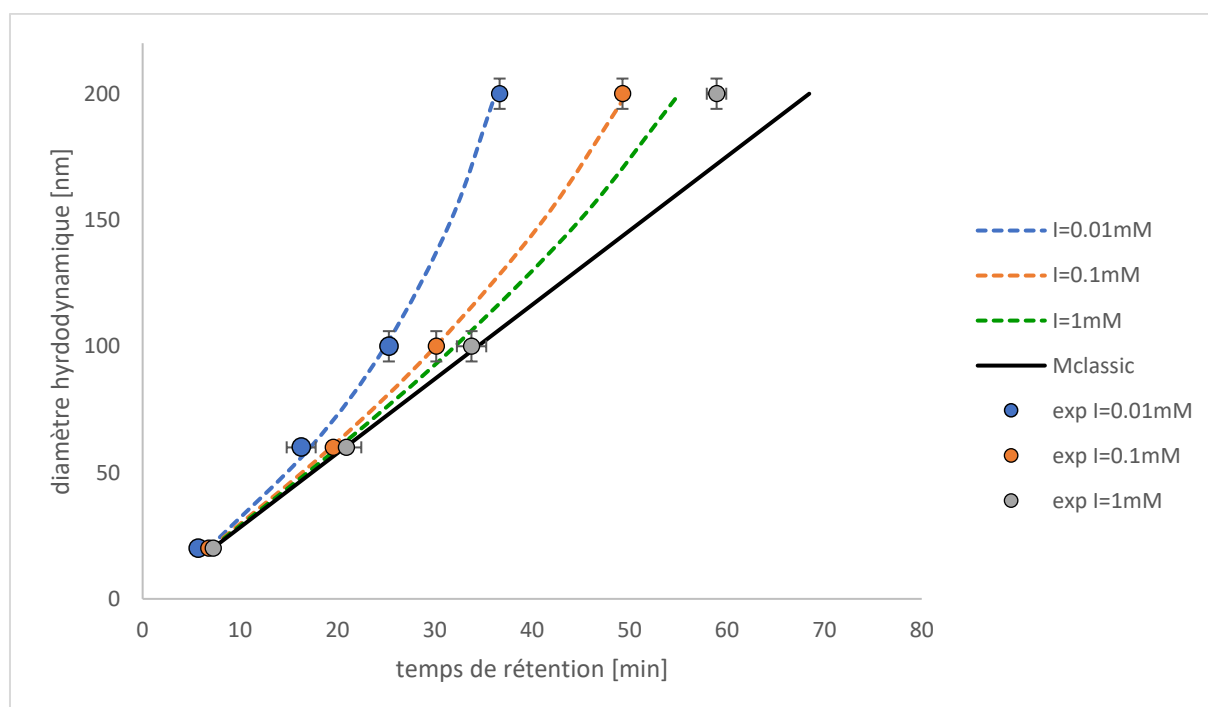


Figure R7. Diamètre hydrodynamique prédit par le modèle classique (ligne continue noire) et le modèle $p-w$ pour des forces ioniques allant de 10^{-5} à 10^{-3} mol. L $^{-1}$. $Q_{out} = 0,5$ mL min $^{-1}$, $Q_c = 0,8$ mL min $^{-1}$, $w = 350$ μ m.

Une propagation des incertitudes a ensuite été réalisée en utilisant l'approche Monte Carlo. Pour cela, une loi de distribution a été attribuée à chaque paramètre (Tableau R4). Deux types de loi de distributions ont été choisis : la loi normale et la loi uniforme. Une loi de distribution normale désigne une distribution gaussienne, quant à la loi uniforme elle désigne une distribution rectangulaire ce qui augmente l'incertitude associée au paramètre par rapport à une loi normale. Les paramètres ont également été classés en 2 catégories, type A et type B. Un paramètre de type A est un paramètre dont la valeur et son incertitude ont été déterminées

expérimentalement, tandis qu'un paramètre de type B est un paramètre dont la valeur a été prise depuis la littérature. Un des paramètres entrant du modèle, l'épaisseur du canal, a été déterminée en appliquant le modèle $p-w$ sur un étalon connu. Les caractéristiques de l'étalon ont donc été rajoutées dans le tableau R4 en tant que paramètres entrants. La Figure R8 représente la distribution obtenue à partir des valeurs du tableau R4. L'échantillon analysé était du dioxyde de silice à 70 nm de rayon. Dans la configuration utilisée on obtient une valeur moyenne de 65,5 nm, un écart type représentant 11,7% de la valeur moyenne et un intervalle de recouvrement à 95% égale à [$r_{hmin} = 54,8$ nm ; $r_{hmax} = 7,5$ nm].

Tableau R4. Paramètres entrants utilisés pour la méthode Monte Carlo

	paramètre	type	valeur moyenne	incertitude	loi de distribution	unité
Constantes physiques	k	B	$1.38065 \cdot 10^{-23}$	0	normale	J K ⁻¹
	ε_0	B	$8.85419 \cdot 10^{-12}$	0	normale	F m ⁻¹
	ε_r	B	78.5	0	normale	
	Na	B	$6.02214 \cdot 10^{23}$	0	normale	mol ⁻¹
	e	B	$1.60218 \cdot 10^{-19}$	0	normale	C
Paramètres constants pour toutes les expériences	η	B	$1.00103 \cdot 10^{-3}$	$1.3 \cdot 10^{-7}$	normale	kg m ⁻¹ s ⁻¹
	T	A	293.15	0.5	normale	K
	b_1	A	0.02	$5.0 \cdot 10^{-4}$	normale	m
	b_2	A	0.005	$5.0 \cdot 10^{-4}$	normale	m
	z_1	A	0.033	$5.0 \cdot 10^{-4}$	normale	m
	z_2	A	0.268	$5.0 \cdot 10^{-4}$	normale	m
	L	A	0.277	$5.0 \cdot 10^{-4}$	normale	m
	Q_{out}	A	0.55	$1.5 \cdot 10^{-4}$	normale	mL min ⁻¹
	Q_{in}	A	0.21	$2.1 \cdot 10^{-4}$	normale	mL min ⁻¹
	Q_c	A	0.5	0.02	normale	mL min ⁻¹
	ζ_w	A	-0.051	0.004	normale	V
	I	A	10^{-5}	$2.5 \cdot 10^{-8}$	normale	mol L ⁻¹
Paramètres associés à l'étalon pour déterminer w_{eff}	A_{123et}	B	$4.26 \cdot 10^{-20} - 8 \cdot 10^{-20}$		uniforme	J
	ζ_{pet}	A	-0.069	$5 \cdot 10^{-3}$	normale	V
	r_{het}	A	$3 \cdot 10^{-8}$	$1 \cdot 10^{-9}$	normale	m
	tr_{et}	A	976	48	normale	s
w_{eff} déterminé	w_{eff}	A	336	10	normale	μm
Paramètres associés à l'échantillon	A_{123}	B	$0.85 \cdot 10^{-20}$	$0.95 \cdot 10^{-20}$	uniforme	J
	ζ_p	A	-0.069	$5 \cdot 10^{-3}$	normale	V
	tr	A	28.05	1	normale	min

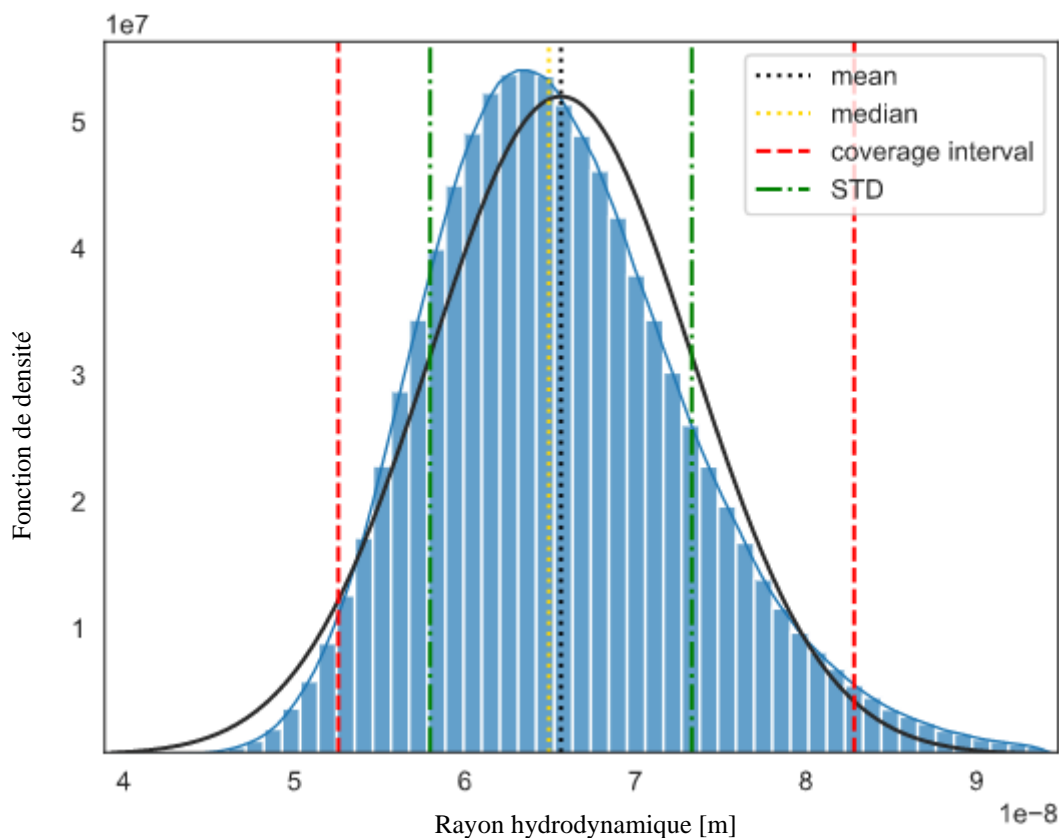


Figure R8. Fonction de densité d'un étalon de dioxyde de silice à 140 nm.

Le modèle p - w a ensuite été appliqué sur plusieurs types de particules (Au, SiO₂ et polystyrène latex) dans un intervalle de taille compris entre 20 et 200 nm de diamètre. La justesse des résultats a été évaluée en utilisant l'écart normalisé. Sur les 11 particules analysées, le modèle p - w a donné des résultats justes sur toutes les particules sauf sur l'échantillon d'or de 80 nm de diamètre.

Une analyse de sensibilité a ensuite été réalisée pour savoir quels paramètres doivent être mesurés plus précisément pour diminuer l'incertitude associée au rayon hydrodynamique, r_h (Figure R9). La Figure R9 montre que les paramètres contribuant majoritairement à l'incertitude sont l'épaisseur du canal et le temps de rétention. Une attention particulière étant portée depuis le début au temps de rétention, l'expérience montre que son incertitude ne peut pas être diminuée. L'épaisseur du canal a également l'incertitude minimale que la méthode actuelle utilisée pour le caractériser peut donner. La traçabilité au SI des résultats provenant du modèle a été établie en suivant les recommandations du guide pour l'expression des incertitudes de mesures (GUM) concernant les modèles ayant plusieurs paramètres entrants. La traçabilité

des paramètres contribuant le plus à l'incertitude du mesurande a donc été établie en priorité. La traçabilité au SI du potentiel zêta des particules et de la membrane, de la viscosité ainsi que de la constante d'Hamaker du système n'a pas pu être établie. Cependant ces paramètres contribuent à moins de 6% de l'incertitude sur le rayon hydrodynamique ce qui est acceptable.

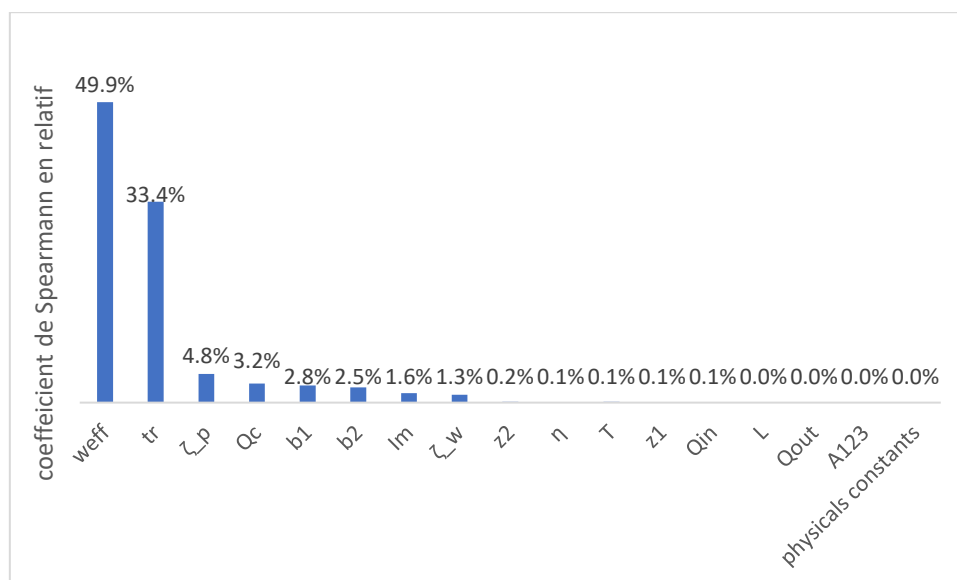


Figure R9. Analyse de sensibilité réalisée à partir des données du tableau R4.

8. Développement d'une nouvelle méthode pour mesurer l'épaisseur du canal

L'analyse de sensibilité a montré que l'épaisseur du canal est un paramètre important lorsque l'on applique le modèle. La méthode utilisée pour le déterminer doit donc être la plus précise possible. La méthode utilisée actuellement consiste à appliquer un modèle de rétention sur un étalon de taille connue ce qui permet de retrouver l'épaisseur. Le fait que l'épaisseur soit déterminée par le même modèle qui est ensuite utilisé pour déterminer la taille ressemble plus à un étalonnage du modèle qu'à une mesure indépendante de l'épaisseur. Cet étalonnage empêche d'évaluer correctement les performances du modèle $p-w$. Une méthode directe pour mesurer l'épaisseur indépendamment du modèle $p-w$ a donc été développée.

Cette méthode utilise un capteur chromatique confocal pour la mesure. Le capteur génère une lumière polychromatique qui est ensuite décomposée en plusieurs rayons monochromatiques à l'aide d'une lentille. Chaque rayon monochromatique se focalise à une distance propre à sa longueur d'onde. Si un rayon se focalise au contact de l'objet visé, un signal est envoyé au détecteur et la distance est déterminée selon la longueur d'onde du rayon concerné. Les premiers tests ont consisté à évaluer la linéarité du capteur. Un montage simulant le canal AF4

a donc été réalisé (Figure R10). Pour évaluer la linéarité du capteur, un ruban adhésif blanc a été collé sur une vis micrométrique. La pointe de cette vis a ensuite été placée entre 2 plaques de poly(méthacrylate de méthyle) (PMMA) séparées par une entretoise de $190\text{ }\mu\text{m}$. L'espace séparant les 2 plaques a été rempli d'eau pour simuler la configuration d'un canal AF4. La position du ruban adhésif a ensuite été déplacée grâce à la vis micrométrique et la variation du signal a été tracée en fonction du déplacement de la vis.

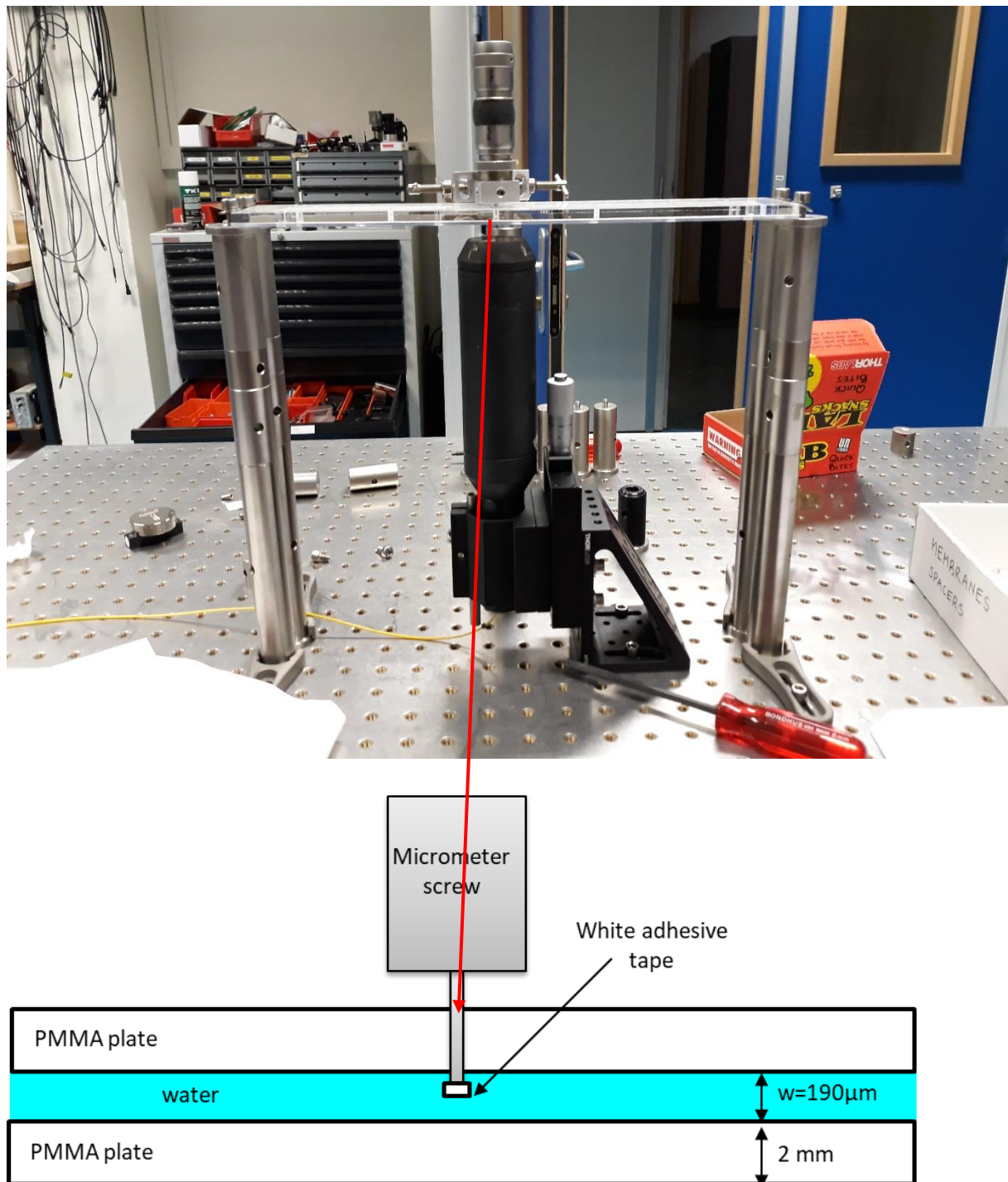


Figure R10. Montage pour tester la linéarité du capteur chromatique confocal.

Une fois que la linéarité du capteur a été évaluée un montage a été développé pour mesurer l'épaisseur du canal (Figure R11). Le montage a été pensé pour pouvoir mesurer l'épaisseur du canal en chaque point du canal. Le capteur a donc été placé sur 2 platines de déplacement pour pouvoir le bouger selon les axes x et y . Le tout a été fixé sur deux élévateurs pour déplacer le canal selon l'axe z . Le montage a permis d'accéder à 34% de l'aire du canal. Les premières mesures ont montré que le montage n'était pas adapté car le canal penchait légèrement vers l'arrière ce qui a entraîné un biais dans les mesures. Un autre montage a donc été développé pour palier à ce problème, mais un problème technique au niveau du capteur a empêché toutes mesures. Seul la faisabilité de la méthode a pu être établie.

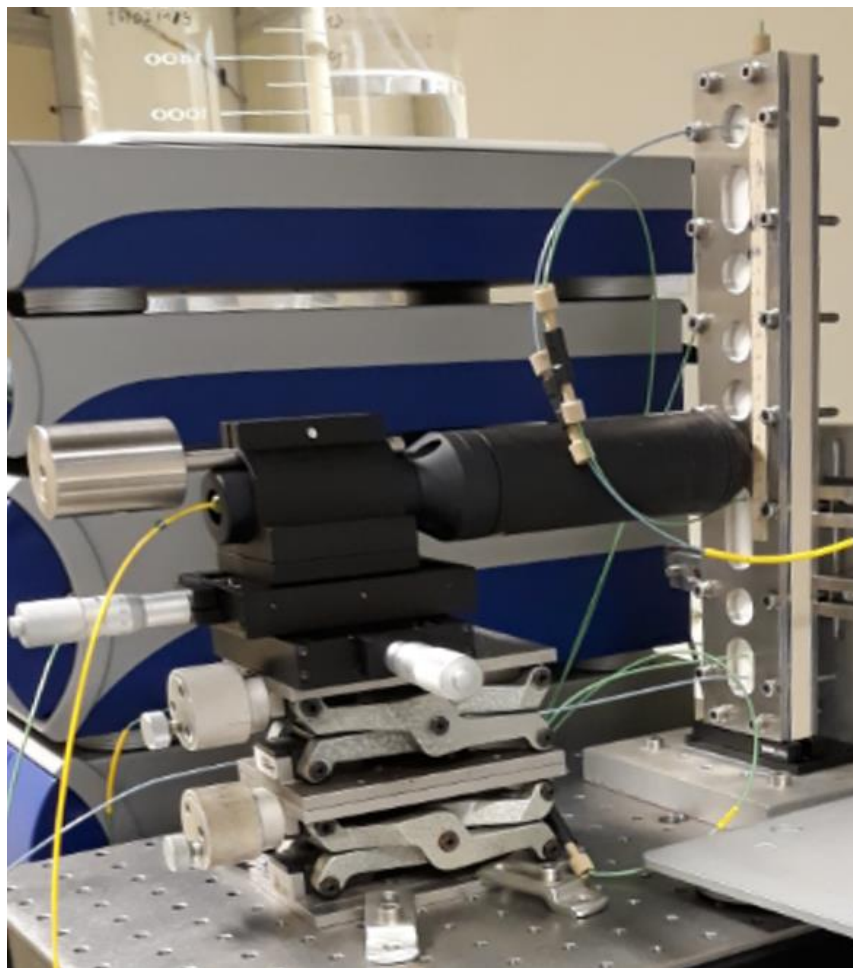


Figure R11. Montage pour mesurer l'épaisseur du canal AF4.

9. Conclusion

L'objectif de cette thèse était de développer une méthode de caractérisation en taille basée sur un modèle physique décrivant précisément les mécanismes gouvernant la rétention des particules au sein d'un canal AF4 et pour lequel les hypothèses de travail sont validées pour une large gamme de conditions.

Une étude a été réalisée pour caractériser l'effet des paramètres influençant le temps de rétention (exemple : le flux croisé, la force ionique, la nature de la membrane, la taille des particules). Les premières expériences ont montré que selon la phase mobile et les particules injectées, la surface de la membrane peut changer au cours du temps et induire un changement dans le comportement de rétention des particules. Par conséquent, les différentes analyses ont été faites dans un ordre précis pour pouvoir avoir des résultats comparables.

Cette étude a également montré que parmi les paramètres qui, selon le modèle classique, ne sont pas censés influencer la rétention des particules, la force ionique influence grandement le temps de rétention des particules. L'hypothèse supposant que les interactions particules-paroi sont négligeables est donc difficilement vérifiée en AF4. De plus des différences entre des particules de même taille, mais de nature chimique différente, ont aussi été observées. Les forces de van der Waals semblent influencer cette différence entre les temps de rétention cependant elles n'expliquent pas à elles seules cette différence. D'autres études devront être menées pour avoir une meilleure compréhension de ce phénomène.

Les données générées par cette étude ont été utilisées pour tester la validité de deux modèles de rétention. Le premier modèle développé par *Williams et al.* est appelé modèle δ_w dans cette thèse en référence à l'approche spécifique de ce modèle qui inclue les interactions particule-paroi dans l'équation à l'aide du paramètre δ_w . L'objectif était (i) d'évaluer l'applicabilité du modèle à l'AF4 et (ii) de réaliser la validation de ce modèle en tant que méthode de caractérisation en taille. Cette étude a montré que le paramètre δ_w est un bon indicateur pour estimer les interactions dans le canal. Cependant l'analyse de sensibilité a montré que δ_w contribue de façon majeure à l'incertitude et ce paramètre demande un grand nombre de mesure afin d'être déterminé avec une faible incertitude. Par conséquent un autre modèle de rétention prenant en compte les interactions particules-paroi a été étudié.

Le deuxième modèle développé par *Hansen et Giddings*, appelé modèle $p-w$ dans cette thèse, prenait en compte chaque interaction en les incluant directement dans l'équation. Les

interactions prises en compte sont les interactions électrostatiques et les forces de van der Waals.

Dans un premier temps, le modèle *p-w* a été comparé à un autre modèle de rétention très connu, le modèle classique, pour savoir dans quelles conditions les interactions particules-paroi ont absolument besoin d'être pris en compte pour déterminer correctement le diamètre des particules. Ce travail a permis de voir que le modèle *p-w* est intéressant lorsque les analyses sont réalisées dans des phases mobiles avec une force ionique inférieure à 10^{-4} mol. L⁻¹.

Dans un deuxième temps, le modèle *p-w* a été validé sur différentes particules d'or, de polystyrène et de dioxyde de silice. Il a été démontré que le modèle est applicable dans la gamme de taille entre 20 et 200 nm. La répétabilité et reproductibilité des analyses AF4 ont également été estimées. Les analyses ont toutes été réalisées 3 fois en utilisant 3 préparations de suspensions et de phases mobiles différentes. L'effet de la membrane sur les analyses a également été pris en compte. Une séquence d'injection spéciale permettait de prendre en compte le vieillissement de la membrane. La reproductibilité de la protrusion de la membrane à l'intérieur du canal a été évaluée en reproduisant les analyses sur 3 membranes différentes. Les membranes choisies provenaient de batch différents pour inclure l'effet de la fabrication dans la reproductibilité. La propagation des incertitudes, réalisée en utilisant la méthode de Monte Carlo, a indiqué une incertitude élargie équivalent à 24% de la valeur moyenne.

L'analyse de sensibilité réalisée sur ce modèle a montré que l'épaisseur du canal contribue de façon majeure à l'incertitude sur le diamètre et doit par conséquent être déterminé de façon précise. Une nouvelle méthode basée sur l'utilisation d'un capteur chromatique confocal a été développée pour mesurer l'épaisseur du canal de façon directe. Un montage permettant de faire bouger le capteur dans les 3 dimensions a été développé, cependant due à un problème technique au niveau du capteur, seule la faisabilité de la méthode a pu être établie. Cette méthode a l'avantage de pouvoir mesurer l'épaisseur *in situ* sans besoin d'utiliser d'étalon ce qui permet de caractériser l'importance de la protrusion de la membrane dans le canal.

Perspectives

En se basant sur les conclusions de la thèse, les aspects suivants peuvent être approfondis :

1) Détermination de l'épaisseur du canal. L'épaisseur du canal a été identifiée comme un des paramètres ayant le plus d'influence sur le temps de rétention et par conséquent sur la détermination de la taille des particules. Une méthode de mesure directe a été développée pour

déterminer l'épaisseur du canal, cependant seule la faisabilité de la méthode a pu être réalisée. Des mesures de l'épaisseur du canal permettraient d'avoir une mesure indépendante des modèles de rétention. Cela permettrait de vérifier les valeurs d'épaisseur trouvées par les différents modèles de rétention et par conséquent de valider ou invalider les modèles de rétention. Le fait d'avoir une mesure d'épaisseur indépendante d'un étalon en taille donnerait également aux deux modèles les caractéristiques d'une méthode primaire.

2) Mécanismes gouvernant la rétention. Une fois que l'épaisseur du canal est connue, la compressibilité des membranes le sera également. D'autres études pourraient définir avec plus de précision quelles caractéristiques des membranes influencent la rétention des particules.

L'effet de certaines caractéristiques des particules comme leur enrobage ou la constante d'Hamaker sur leur temps de rétention n'est pas encore bien compris. Une meilleure caractérisation de leurs effets est nécessaire pour développer des modèles de rétention plus précis.

3) Particules sphériques et échantillons réels. Les différentes études réalisées au cours de cette thèse ont été conduites en utilisant des particules sphériques de différentes natures (Au, SiO₂, PS). L'application du modèle à des particules non sphériques permettrait d'évaluer la robustesse du modèle. Le facteur de forme pourrait être un bon indicateur pour délimiter le domaine d'application du modèle.

**Annex I: Conference paper 19th
International Congress of Metrology -
CIM2019**

Asymmetric field flow fractionation applied to the nanoparticles characterization: Study of the parameters governing the retention in the channel

*Valentin de Carsalade du pont*¹, *Enrica Alasonati*¹, *Sophie Vaslin-Reimann*¹, *Michel Martin*², *Mauricio Hoyos*², and *Paola Fisicaro*²

¹ Department of Biomedical and Inorganic Chemistry, Laboratoire National de Métrologie et d'Essai (LNE), 1 rue Gaston Boissier, Paris, 75015, France

²Laboratoire de Physique et Mécanique des Milieux Hétérogènes (PMMH), ESPCI Paris, CNRS, 10 rue Vauquelin, 75231, Paris Cedex 05, France

Abstract. In this work we study the parameters which are often modified to optimize the separation in asymmetrical field flow fractionation, and we observe their impact on the retention behavior of the analyte. The aim of the work is to improve our knowledge of the phenomena which govern the behavior of the analytes in the channel and to have a better understanding of the limits of the actual theoretical model in order to improve it. Results illustrate that the ionic strength influences the effect of the cross flow rate on the retention time of the particle. The question of the determination of the channel thickness was also addressed.

1. Introduction

Since some years, researchers are interested in nanoscience to understand the original properties of nano-objects, design new nanomaterials for various applications like electronics, cosmetics or medicine, or to study the fate of nanoparticles (NPs) in the environment. The fast development of nanotechnologies created the need for analytical methodologies able to characterize the nanoparticles. The size and the size distribution are key parameters of NPs which have been included in (ISO/TS 80004-2, 2015). One of the analytical methods used to determine the size distribution of nanoparticles is the field flow fractionation (FFF).

FFF is a family of techniques which belongs to the category of separation technique like chromatography. The technique consists in the application of a field force perpendicularly to a laminar elution flow rate, allowing the particles to be separated according to the nature of the force applied. The main difference between chromatography and FFF is that the separation is not based on the affinity between the analytes and the stationary phase but on the interaction between the analytes and a force applied perpendicularly to the elution flow (Figure 1).

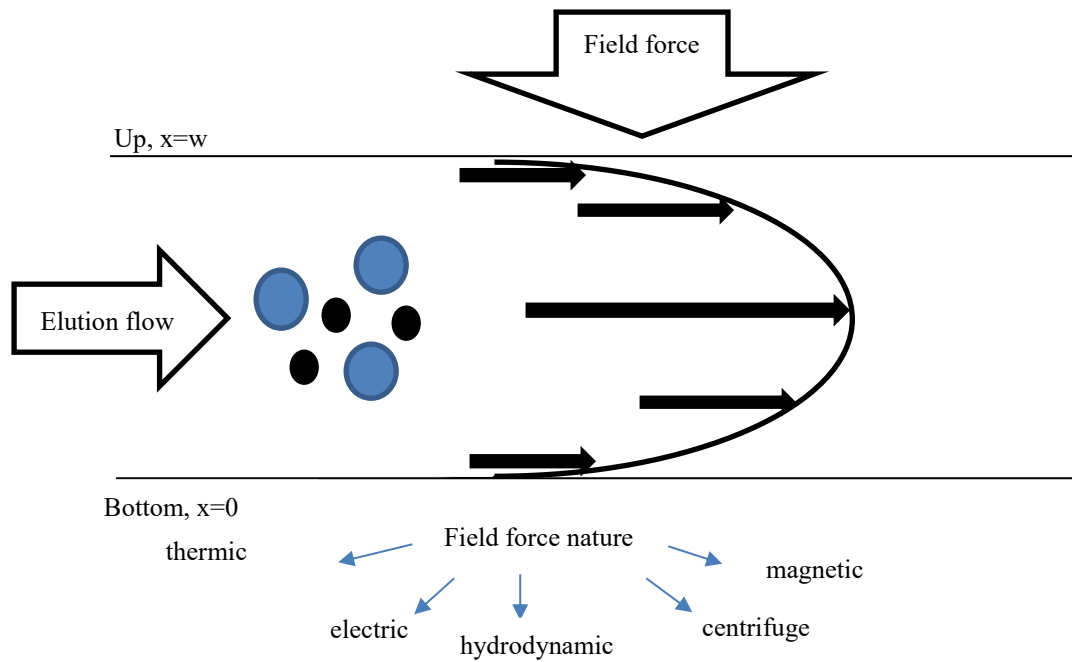


Figure 1. Separation principle of FFF

The sub techniques of FFF are distinguished by the nature of the force applied. Flow field flow fractionation (FI-FFF) is a sub technique which fractionates the sample by applying a hydrodynamic force on the sample. This force is generated by a secondary flow, the cross flow, applied perpendicularly to the main one. The channel is constituted of two porous walls and a semi permeable membrane that covers one of them. Another version of the FI-FFF was developed by Granger et al.[1] in which the channel had only one porous wall. This model has the advantage to decrease the perturbation from the cross flow generated by the heterogeneous permeability of the two porous walls. This version was called asymmetrical flow field flow fractionation (A4F)[2]. To ensure that the cross flow and the carrier velocity are constant thorough the channel, the channel was modified from a rectangular to a trapezoidal shape.

2. theory

In FFF there are different types of elution depending on the size of the analyte. In the nanoscale the elution mode followed by the nano-objects is the Brownian mode (or normal mode). A theoretical model was developed in 1960s by Giddings[3] to predict the behavior of an analyte in a FFF channel.

The measurand in FFF, like in chromatography, is the retention time (t_r) of the eluting peak. The model defines a retention ratio R which corresponds to the ratio between the velocity of the analyte zone and the velocity of the carrier. In practice it is equal to the ratio of the void peak (t_0) and the retention time[4]:

$$R = \frac{t_0}{t_r} = \frac{v_{analyte}}{v_{carrier}} \quad (1)$$

Due to the large ratio width/thickness (y/x) of the channel, generally larger than 60, the channel can be assimilated to two parallel plates so that the velocity ratio can be expressed only in function of the x axis:

$$\frac{v_{analyte}}{v_{carrier}} = \frac{\int_0^w c(x)v(x)dx}{\langle v(x) \rangle \int_0^w c(x)dx} \quad (2)$$

where w is the thickness of the channel and $v(x)$ and $c(x)$ are respectively the velocity of the flow rate and the concentration profile in the transversal axe, x . For the expression of $v(x)$ a laminar flow has been assumed.

$$v(x) = 6\langle v(x) \rangle \left(\left(\frac{x}{w} \right) - \left(\frac{x^2}{w^2} \right) \right) \quad (3)$$

The expression of $c(x)$ has been made with the assumption of an analyte cloud in a steady state regime where only two opposite forces are applied on the analyte: the field force and the diffusion. This leads to equation (4):

$$c(x) = c_0 \exp\left(-\frac{Fx}{kT}\right) \quad (4)$$

where c_0 is the analyte concentration at the accumulation wall, F is the strength applied on the analyte, k the Boltzmann constant and T the temperature. Equation 3 and 4 are then introduced in equation 2, which gives

$$R = 6\lambda \coth\left(\frac{1}{2\lambda}\right) - 12\lambda^2 \quad (5)$$

with λ a dimensionless retention parameter equal to kT/Fw . When $\lambda < 0.02$ an approximation of equation 5, accurate within 5%, can be made:

$$R = 6\lambda \quad (6)$$

These conditions are easy to obtain when the analyte is retained in the channel. Therefore, most of the users use equation 6. In A4F the force applied on the channel can be approximated by:

$$F_{A4F} = \frac{3\pi\eta d_h V_c w}{kTV_0} \quad (7)$$

With η the carrier viscosity, d_h the hydrodynamic diameter of the particle, V_c the cross flow and V_0 the channel volume. Combining equation 7 and 6 we obtain an expression between the retention time and the hydrodynamic diameter of the particle.

$$d_h = \frac{2kTV_0 t_r}{\pi V_c \eta t_0 w^2} \quad (8)$$

Among the hypotheses made to obtain equation 8, the hypothesis about the concentration profile implies that the interaction within the analytes and between the analytes and the accumulation wall are negligible with respect to the applied field. However, several works[5–7] showed that these interactions are not negligible which reduce the model validity. To overcome the model limitations for size determination of (nano)particles, macromolecules or proteins, nowadays FFF is coupled online with size detectors like multi angle light scattering (MALS)[8–10]. In this work we propose to investigate the main parameters usually optimized by the users, namely the carrier composition, the cross-flow rate and the channel thickness. Moreover, their influence on the retention time is

compared to the retention time predicted by the model in order to have a better understanding of the model deviations and of possible improvements.

3. Material and methods

3.1. A4F instrumentation

Experiments were carried out in this study using an A4F system (AF2000 Postnova Analytics, Landsberg Germany) coupled to a UV detector (Shimadzu, Kyoto Japan) set at 254 nm. The A4F channel was 27.7 cm long and narrowing in width from 2.0 to 0.5 cm. A 350 μm thick spacer and membrane in regenerated cellulose (RC) at 10 kDa cut-off (Postnova Analytics) were used for the experiments.

3.2. Chemical and samples

Polystyrene latex nanosphere (PS) size standards of 23, 60 and 100 nm of diameter (Thermo-Scientific) were used to study the effect of the particle size on the retention time. The samples were prepared by diluting the commercial solution in the carrier to obtain a solution at 13 $\mu\text{g/g}$. The carrier was ultrapure water filtered through a 0.1 μm RC filter (Postnova Analytics). The ionic strength of the carrier was adjusted by adding sodium chloride, NaCl (Sigma Aldrich). The injection volume was 60 μL .

4. Results and discussion

4.1. Methodology of the study

One particularity of the FI-FFF is the use of a semi permeable membrane at the bottom of the channel. The role of this membrane is to keep the sample inside the channel and allows at the same time the carrier to flow out thorough the accumulation wall. Unfortunately, the membrane gradually ages with the number of injections. The phenomenon is well known [11,12] and can be detected in two different ways: following the decrease of the fractogram area, in this work the UV peak integral, or following the variation of the retention time. Most users use a size detector (as light scattering detectors) coupled to the A4F to determine the particle's size and in this case, they are not affected by the variation of the retention time between the injections. In our case the retention time is our measurand so we have included the membrane aging in our uncertainty budget to be able to compare different sets of data (Figure 2).

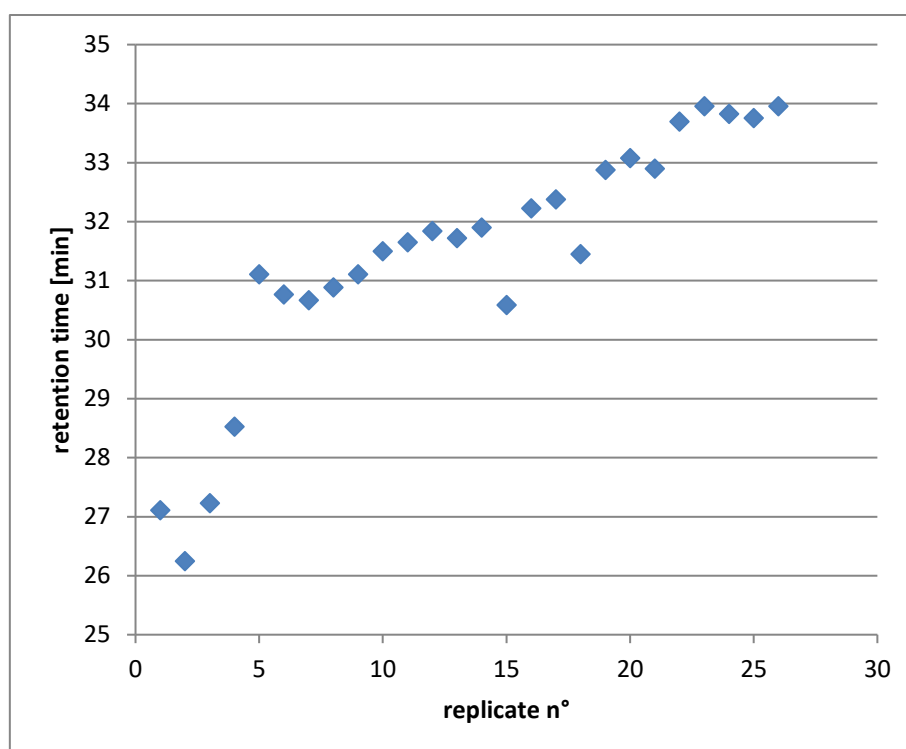


Figure 2. Retention time of the PS standard 60nm as diameter in function of the number of replicates. Carrier: NaCl 10^{-4} mol/L; membrane: RC 10 kDa; cross flow rate and elution flow rate: 0.5mL/min.

Figure 2 represents the repeatability in NaCl 10^{-4} mol/L. If we want to test 5 five different parameters in 3 consecutive replicates, there will be 13 injections between the first and the last parameter tested which could create a significant bias larger than the repeatability of three replicates. To take the aging into account in the uncertainty budget, one series of parameters was tested first (example three different cross flow, V_{c1} , V_{c2} , V_{c3}), followed by 2 replicates of the same series (Table 1). This experiment plan increases the uncertainty associated to the retention time but allows the comparison between two set of data acquired at different ages of the membrane.

Table 1. Experiment planning for three different values of cross flow (V_c) with 3 replicates

Analysis n°	sequence usually applied		sequence applied in this study
1	replicate 1 V_{c1}	=>	replicate 1 V_{c1}
2	replicate 2 V_{c1}		replicate 1 V_{c2}
3	replicate 3 V_{c1}		replicate 1 V_{c3}
4	replicate 1 V_{c2}		replicate 2 V_{c1}
5	replicate 2 V_{c2}		replicate 2 V_{c2}
6	replicate 3 V_{c2}		replicate 2 V_{c3}
7	replicate 1 V_{c3}		replicate 3 V_{c1}
8	replicate 2 V_{c3}		replicate 3 V_{c2}
9	replicate 3 V_{c3}		replicate 3 V_{c3}
standard deviation obtained	$u(t_r) \approx 0.4\text{min}$	<	$u(t_r) \approx 2.6\text{min}$

4.2. Impact of the ionic strength and cross flow on the retention time

The equation 8 is based on the assumption that the interactions among analytes and between analytes and the membrane are negligible compared to the cross flow force. But this implies that the model can be only used with particular experimental conditions and, in practice, a carrier optimized for a good fractionation isn't necessarily adapted for the model (Figure 3). In the Figure 3 we show the influence of the carrier ionic strength (I) on a 60 nm standard retention time. The retention time was measured for different cross flow rates. We can see that, depending on the carrier ionic strength, the retention time can triple. This increase limits the application of the model. Independently of the ionic strength effect on retention time, the ionic strength of the carrier also changes the effect of the cross flow on the retention. We can see that the slope of the curve change depending on the carrier ionic strength while it should be the same. According to *Kato et al.*, the slope difference can be explained by a diminution of the electrostatic repulsions between the membrane and the particles due to the diminution of the length of Debye[13].

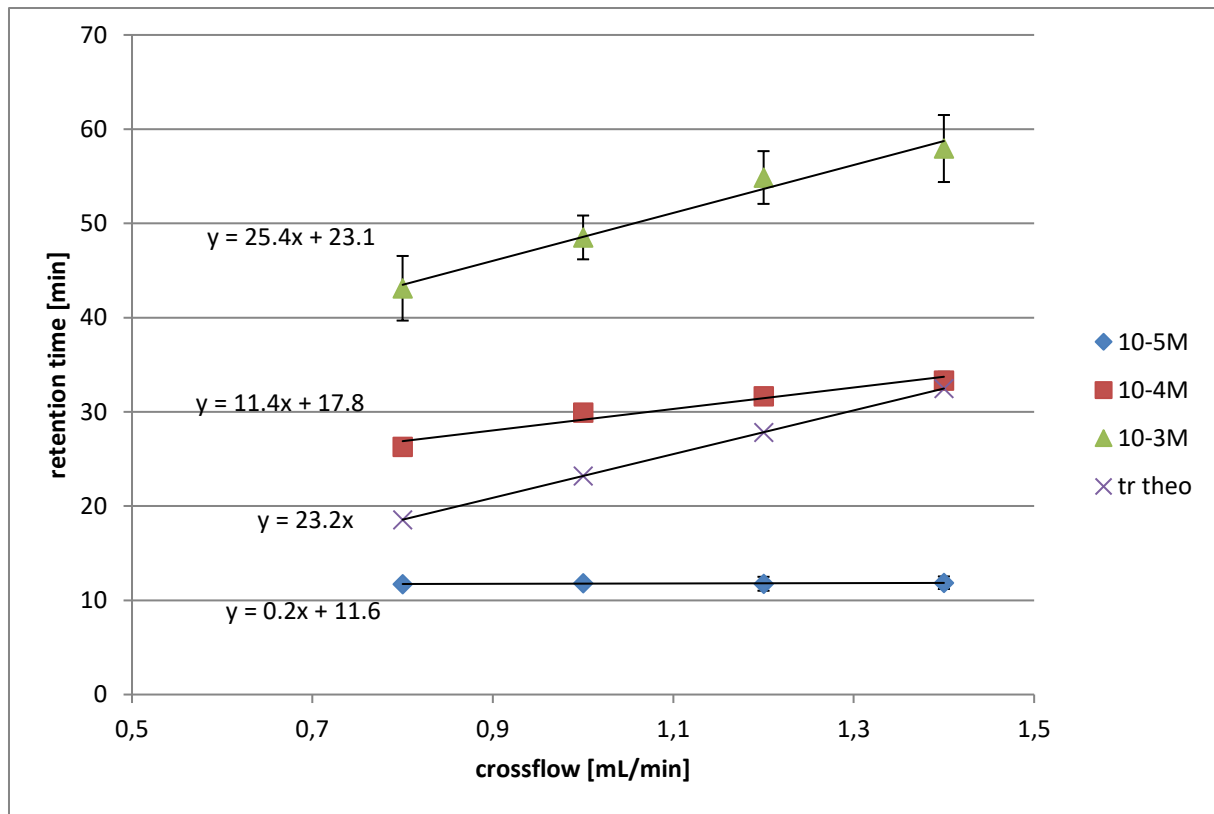


Figure 3. Retention time of PS60 in function of the cross flow for a given ionic strength. The experiment have been realized with a $V_{out}=0.5\text{mL/min}$

To show the difference, the retention time predicted by the model ($t_{r,theo}$) for a 60 nm particle was added in Figure 3. The parameters used for the calculation are listed in Table 2

Table 2. Value of the parameters used for the equation 8

$d_h [m]$	$V_o [m^3]$	$\eta [kg\ m^{-1}\ s^{-1}]$	$T [K]$	$t_o [min]$	$w[m]$
6.00E-08	1.15E-06	1.00E-03	293	1.4	3.50E-04

V_o , t_o , d_h and T were measured and the viscosity of the carrier was assumed equal to the viscosity of water at 293K. The channel thickness was assumed equal to the nominal spacer thickness even if these two values may be different in the experimental reality. This can explain the differences between the theoretic and experimental values. The theoretical curve could fit with experimental curves having the same slope, like e.g. the curve at $I=10^{-3}\text{mol/L}$. if these thicknesses were equal. This inequality leads to the second principal limit in the model, the channel thickness measurement

4.3. Channel thickness measurement

The second principal limit of the model is the determination of the channel thickness. Indeed, when a spacer is placed in the channel, the spacer nominal thickness (w_{nom}) is known. However, two phenomena are suspected to reduce the channel thickness, each one linked with the membrane below the spacer. The first hypothesis is that the

membrane slightly invades the spacer because of the pressure applied on the membrane when the channel is built[14]. The second supposes that, in presence of the carrier the membrane swells which also reduces the channel thickness[15]. To determine the effective channel thickness (w_{eff}) a calibration is done based on equation 8 using particles or protein standards with a known hydrodynamic diameter or diffusion coefficient[16]. To evaluate the effect of the cross flow and the ionic strength of the carrier on the effective channel thickness calibration, w_{eff} was calculated using a polystyrene standard of 60 nm as diameter by using the retention time obtained in Figure 3 (Figure 4). Each couple of conditions (cross flow and ionic strength) apart for $I=10^{-5}$ mol/L, give a different w_{eff} . The equation 8 doesn't take interactions into account, hence the w_{eff} were expected to vary depending on the carrier ionic strength. The cross-flow rate effect is taken into account in the calibration (equation 8) so the calculated thickness shouldn't vary with the used cross flow. However, we saw that the ionic strength also influences the effect of the cross flow rate on the particles retention time (Figure 3). So, the fact that w_{eff} varies depending on the cross flow applied is not surprising (Figure 4).

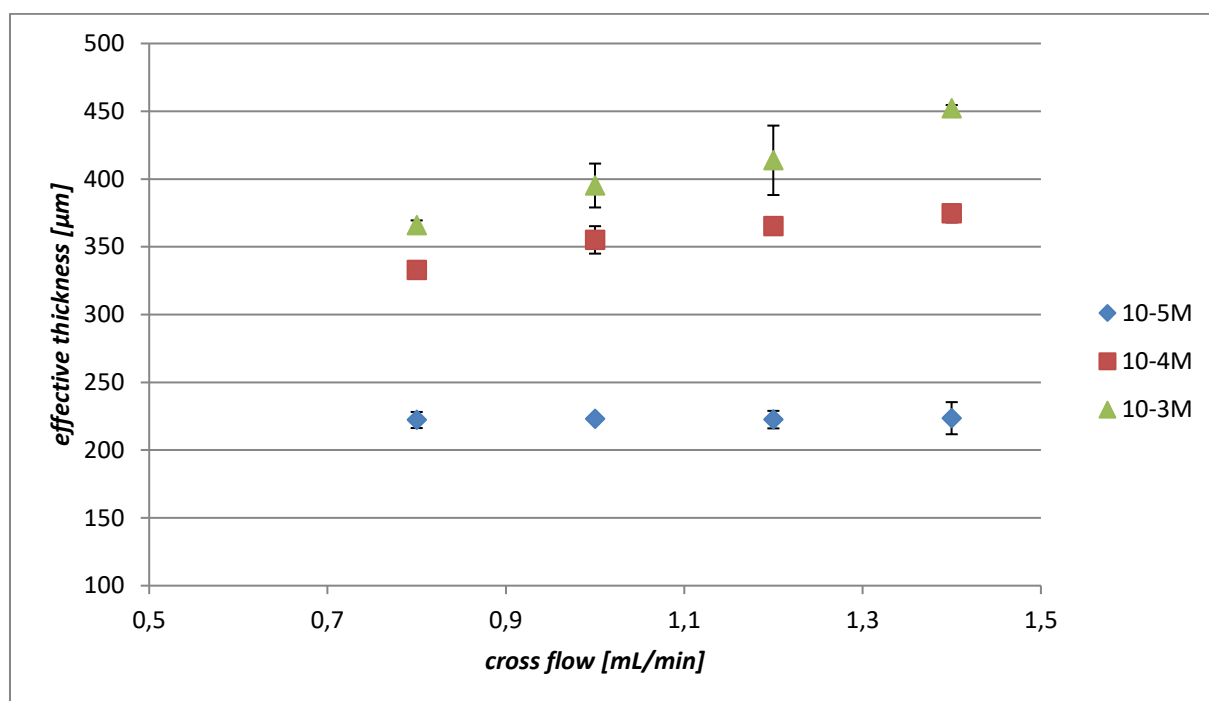


Figure 4. Determination of the effective channel thickness by using a PS standard of 60 nm diameter. The calibration has been performed using different carrier concentrations and different cross flow rates. The nominal channel thickness was 350 μ m.

Depending on the experimental conditions we obtained a w_{eff} which can go from 250 μ m to 450 μ m. The fact that we obtain a larger or smaller w_{eff} with a significant increase or decrease compared to w_{nom} makes us think about the physical meaning of the w_{eff} value. The two hypotheses cited above can explain the thickness decrease but not the increase. Moreover w_{eff} increased proportionally with the ionic strength and the cross flow rate applied during the calibration. It could be said that the calibration approach used to determine the effective thickness of the channel results in fact in a determination of a kind of correction constant taking in account particles and membrane interactions in the model, more than an evaluation of the channel thickness.

5. Conclusion

In this work we have identified, experimentally measured and discussed two main problems of the model representing the particle retention in A4F: the impact of the ionic strength and the measurement of the effective channel thickness. Ideally, particle-particle and particle-membrane interactions should be included in the forces applied on the particle: this should allow representing the different retention time tendency observed in function of the ionic strength.

The challenge due to the thickness can be solved in multiple ways. One possibility could be to assume the non-knowledge of the actual thickness and to use the effective thickness as a correction factor or apply a correction factor to the nominal thickness. Another way will be to find another method to measure the channel thickness.

References

1. J. Granger, J. Dodd, D. Leclerc, and N. Midoux, (1986)
2. K.-G. Wahlund and J. C. Giddings, *Society* 1332 (1987)
3. J. C. Giddings, *Sep. Sci.* **1**, 123 (1966)
4. J. C. Giddings, **50**, 667 (1973)
5. J. Gigault and V. A. Hackley, *Anal. Bioanal. Chem.* **405**, 6251 (2013)
6. M. Martin, *J. Chromatogr. A* **831**, 73 (1999)
7. Y. Mori, K. Kimura, and M. Tanigaki, *Anal. Chem.* **62**, 2668 (1990)
8. E. Bolea, J. Jiménez-Lamana, F. Laborda, and J. R. Castillo, *Anal. Bioanal. Chem.* **401**, 2723 (2011)
9. M. Correia and K. Loeschner, *Anal. Bioanal. Chem.* **410**, 5603 (2018)
10. S. Schachermeyer, J. Ashby, M. Kwon, and W. Zhong, *J. Chromatogr. A* **1264**, 72 (2012)
11. K. Hungerbühler, J. Ebert, A. Ulrich, B. Nowack, C. Adlhart, N. Bendixen, H. Hagedorfer, S. Losert, M. Lattuada, and A. Al-Kattan, *J. Anal. At. Spectrom.* **27**, 1120 (2012)
12. S. Losert, N. Bendixen, K. Hungerbühler, and A. Ulrich, **1**, 155 (2013)
13. H. Kato, A. Nakamura, H. Banno, and M. Shimizu, *Colloids Surfaces A Physicochem. Eng. Asp.* **538**, 678 (2018)
14. K. G. Wahlund, *J. Chromatogr. A* **1287**, 97 (2013)
15. M. E. Schimpf and Q. Du, *Anal. Chem.* **74**, 2478 (2002)
16. H. Dou, E. C. Jung, and S. Lee, *J. Chromatogr. A* **1393**, 115 (2015)

RÉSUMÉ

L'augmentation de l'utilisation des nanoparticules au fil des années rend nécessaire une meilleure compréhension de leurs propriétés, leur devenir dans l'environnement ainsi que leur impact sur la santé. A cette fin, de meilleures techniques de caractérisation nécessitent d'être développées. Parmi les différentes propriétés des nanoparticules, la taille est particulièrement importante car elle influence de nombreuses propriétés (comme, par exemple : la réactivité, la toxicité ou leur capacité de migration dans l'environnement). Parmi les nombreuses techniques de caractérisation en taille existantes, le fractionnement par couplage flux force asymétrique (AF4) est une technique qui permet de séparer les différentes populations de nanoparticules présentes dans l'échantillon en fonction de leur diamètre hydrodynamique avant de les envoyer à un détecteur en taille. Ce fractionnement permet de simplifier le travail du détecteur.

Dans les années 1960, un modèle (appelé dans la thèse modèle classique) reliant le temps de rétention des nanoparticules au sein de l'AF4 à leur diamètre hydrodynamique a été développé. Cependant la validité du modèle repose sur des hypothèses de travail qui ne sont pas toujours respectées dans certaines conditions expérimentales.

Ces travaux ont consisté, dans un premier temps, à étudier les mécanismes gouvernant la rétention au sein de l'AF4. Il a été montré que des interactions entre les nanoparticules et la paroi du canal biaisent les résultats prédits par le modèle classique. Un autre modèle (appelé dans la thèse modèle p-w) prenant en compte les interactions électrostatiques et de van der Waals a été étudié. Le modèle p-w s'est montré plus robuste que le modèle classique. Une validation de ce modèle a été conduite et un bilan d'incertitude a été développé en utilisant la méthode de Monte- Carlo. La traçabilité métrologique des résultats de mesure a également été démontrée.

MOTS CLÉS

AF4, FFF Théorie, nanoparticules, validation de méthode

ABSTRACT

Due to the increasing use of nanoparticles, a better understanding of their properties, their environmental fate, and their impact on the human health becomes mandatory. To this end, reliable methods for the characterization of nanomaterials' properties need to be developed. Among the different properties of nanoparticles, the size is particularly important as it influences several other properties (e.g. the reactivity, the toxicity or their behavior in the environment). The asymmetrical flow field flow (AF4) is a technique that fractionates the different populations inside the sample as a function of their hydrodynamic diameter. In the 1960s, a model (thereafter called classical model) relying the retention time of a nanoparticle with its hydrodynamic diameter has been developed. However, the model validity is based on work hypothesizes which are not always respected depending on the experimental conditions.

The work of this PhD thesis has consisted firstly in the study of the mechanisms governing the nanoparticles retention inside the AF4 channel. Notably it has been shown that interactions between the nanoparticles and the accumulation wall of the AF4 biased the results predicted by the classical model. Another model (thereafter called p-w model), which takes electrostatic and Van de Walls interactions into account, has been developed. Tests realized with particle standards for size showed that the p-w model give results with a better trueness than the classical model and that it can be applied for a larger range of experimental conditions. A validation of this model has been conducted and an uncertainty budget has been developed by following the Monte Carlo method. The metrological traceability of the measurement results has also been demonstrated.

KEYWORDS

AF4, FFF theory, nanoparticles, method validation